



THE HONG KONG
POLYTECHNIC UNIVERSITY

香港理工大學

Pao Yue-kong Library

包玉剛圖書館

Copyright Undertaking

This thesis is protected by copyright, with all rights reserved.

By reading and using the thesis, the reader understands and agrees to the following terms:

1. The reader will abide by the rules and legal ordinances governing copyright regarding the use of the thesis.
2. The reader will use the thesis for the purpose of research or private study only and not for distribution or further reproduction or any other purpose.
3. The reader agrees to indemnify and hold the University harmless from and against any loss, damage, cost, liability or expenses arising from copyright infringement or unauthorized usage.

IMPORTANT

If you have reasons to believe that any materials in this thesis are deemed not suitable to be distributed in this form, or a copyright owner having difficulty with the material being included in our database, please contact lbsys@polyu.edu.hk providing details. The Library will look into your claim and consider taking remedial action upon receipt of the written requests.

Pao Yue-kong Library, The Hong Kong Polytechnic University, Hung Hom, Kowloon, Hong Kong

<http://www.lib.polyu.edu.hk>

**PERFORMANCE ASSESSMENT OF
COVER SHIELD-ASSISTED RADIANT COOLING SYSTEM
FOR OUTDOOR URBAN ENVIRONMENT**

DHARMASASTHA KUMAR

PhD

The Hong Kong Polytechnic University

2025

The Hong Kong Polytechnic University

Department of Building Environment and Energy Engineering

**PERFORMANCE ASSESSMENT OF
COVER SHIELD-ASSISTED RADIANT COOLING SYSTEM
FOR OUTDOOR URBAN ENVIRONMENT**

DHARMASASTHA KUMAR

A thesis submitted in partial fulfillment of the requirements for the

Degree of Doctor of Philosophy

August 2024

Certificate of Originality

I hereby declare that this thesis is my own work and that, to the best of my knowledge and belief, it reproduces no material previously published or written, nor material that has been accepted for the award of any other degree or diploma, except where due acknowledgement has been made in the text.

(Signed)

Dharmasastha Kumar (Name of Student)

Department of Building Environment and Energy Engineering

The Hong Kong Polytechnic University

Hong Kong, China

August 2024

Abstract

Abstract of the thesis entitled: Performance assessment of cover shield-assisted radiant cooling system for outdoor urban environment

Submitted by: Dharmasastha Kumar

For the Degree of: Doctor of Philosophy

at The Hong Kong Polytechnic University in August 2024.

Extreme heat is a growing global threat that requires urgent action to care for vulnerable populations in outdoor environments and protect workers. The year 2023 was considered one of the hottest on record in many cities around the world, but 2024 has proven to be even more scorching, indicating an increasing trend in heat waves across the globe. The more vulnerable groups affected by these heatwaves include bus commuters, daily labourers working outdoors, road workers and the homeless. Deadly heat stress and heat strokes are experienced as dire consequences of the heat waves sweeping through communities. With temperatures rising, there is a critical need to implement measures that shield these at-risk populations from the dangers of extreme heat.

Localised outdoor cooling hubs have the potential to address this problem and can protect the public in the outdoors from heat waves. In the current situation of record-breaking temperatures every year, i.e., for instance, crossing 52°C in China, and India, the common passive cooling strategies such as shading, fan cooling, green roofs and blue-green infrastructure, are questionable to protect people from extreme heat. The evaporative cooling, mist cooling, and air conditioning have been utilized in the outdoors in some cities, but they are ineffective and energy-intensive, especially in hot and humid climates.

The cover shield-assisted radiant cooling system is one of the alternative potential cooling solutions for outdoor cooling applications. It can treat the radiant load directly and reduce convective heat loss to the surroundings. An infrared-transparent cover shield, such as a low-density polyethylene (LDPE) membrane is used to cover the radiant panel. The cover shield allows infrared radiation from the surroundings but reduces convective heat transfer to the ambient.

This technology has been proven to be effective in semi-outdoor environments. However, outdoor cooling using this technology has yet to be investigated. In this research, the localised cooling hub integrated with the cover shield-assisted radiant cooling system is investigated using Computational Fluid Dynamics (CFD) modelling. It aims to investigate the thermal and comfort performance of the proposed localised cooling hub for the urban outdoor environment.

A three-dimensional, steady-state CFD model of the proposed cooling system has been developed for an outdoor urban environment. The thermal performance of the localised outdoor cooling hub system is investigated for an open space in the hot and humid climate of Hong Kong. The heat transfer characteristics of the proposed cooling system are analyzed for various cover shield materials under realistic ambient conditions of the summertime in Hong Kong. It was found that the sky-window selective membrane outperforms other materials. However, this membrane is still in the development stage. In situations where there is no direct solar exposure, a non-selective membrane can be preferred over a mid-infrared selective membrane, as the non-selective membrane can provide the same cooling performance in the absence of direct solar radiation.

In order to overcome the limitations of the existing outdoor comfort models, a methodology to couple the CFD simulation with the human body thermoregulation system has been developed. The skin temperature obtained from the coupling method is used to determine the human

thermal sensation in the outdoor environment using the updated CBE comfort model. The thermal sensation obtained from this method has been compared with the thermal comfort survey conducted in the experimental facility of a localised outdoor cooling hub employed with membrane assisted radiant cooling system.

The thermal and comfort performance has been investigated for the street canyons of Hong Kong, in terms of the heat extraction rate of the cooling system and thermal sensation experienced by the occupants. The obtained thermal sensation has been compared with the thermal sensation experienced by the people standing in the shaded spot without any cooling. The results are more promising that the proposed cooling system performs well in the typical summer weather of Hong Kong.

The present research has identified that the proposed radiant cooling system is a suitable solution for outdoor applications. However, the current structure design of the system requires optimization to improve the heat exchange between the cooling panel and the human body, as well as to reduce the impact of solar radiation. Optimizing the system design will not only enhance its energy efficiency but also provide better comfort for users. Future work should focus on integrating the proposed cooling system with low-grade energy sources, such as waste heat or renewable energy, to develop a more sustainable and livable cooling solution for outdoor urban environments.

By addressing the design limitations and exploring the integration of low-grade energy sources, the proposed radiant cooling system has the potential to become a more comprehensive and effective solution for mitigating the challenges of extreme heat in outdoor spaces.

List of Research Publications

Publications Arising from the Thesis

Journal Publications

- **Dharmasastha, K.**, Zhong, Z., Niu, J., & Liang, H. (2023). A Comprehensive review of cover-shield-assisted radiant cooling system. *Energy and Buildings*, 113121. <https://doi.org/10.1016/j.enbuild.2023.113121>
- **Dharmasastha, K.**, Zhong, Z., Niu, J., & Liang, H. (2024). Thermal performance investigation of membrane-assisted-radiant cooling system for localised outdoor cooling hub. *Sustainable Cities and Society*, 101, 105173. <https://doi.org/10.1016/j.scs.2024.105173>
- **Dharmasastha, K.**, Liang, H., Junwei, L., Xie, Y., Yu, Y., & Niu, J. (2024). Evaluating thermal sensation in outdoor environments - different methods of coupling CFD and radiation modelling with a human body thermoregulation model. *Building and Environment*, 266, 112081. <https://doi.org/10.1016/j.buildenv.2024.112081>

Conferences

- **Dharmasastha, K.**, & Niu, J., (2022). Parametric analysis of the condensation-free radiant cooling system, Proceedings of 11th international conference on indoor air quality, ventilation & energy conservation in buildings, Tokyo, Japan.
- **Dharmasastha, K.**, Shin-ichi Tanabe & Niu, J., (2024) Sensitivity Analysis of Cooling Panel Temperature on the Thermal and Comfort Performance of Outdoor Radiant Cooling System, Proceedings of 18th International Conference of the International Society of Indoor Air Quality & Climate, Honolulu, Hawaii.
- **Dharmasastha, K.**, Liang, Y., Yang, J., & Niu, J., (2024). A localised cooling hub for urban outdoor environment: a sustainable solution for hot and humid climates, Proceedings of 8th National and 2nd International Conference on Refrigeration and Air Conditioning, Chennai, India.

Other Publications

Journal Publications

- Yang, J., Liang, Y., Zhong, Z., **Dharmasastha, K.**, Xie, Y., & Niu, J. (2024). Thermal comfort investigation of membrane-assisted radiant cooling in outdoor settings. *Sustainable Cities and Society*, 113, 105634. <https://doi.org/10.1016/j.scs.2024.105634>
- Liang, Y., Yang, J., Zhong, Z., Xie, Y., **Dharmasastha, K.**, & Niu, J. (2024). Thermal Performance and Energy Efficacy of Membrane-Assisted Radiant Cooling Outdoors. *Sustainable Cities and Society*, 114, 105787. <https://doi.org/10.1016/j.scs.2024.105787>

Conferences

- Yang, J., Liang, Y., Zhong, Z., **Dharmasastha, K.**, & Niu, J. (2023). A study of the cooling efficacy and thermal comfort performance of membrane-assisted radiant cooling panels under outdoor air conditions. Proceedings of 3rd international conference for global Chinese academia on energy and built environment, Shanghai, China.
- Liang, Y., Yang, J., Zhong, Z., **Dharmasastha, K.**, & Niu, J. (2024). Assessment of thermal comfort performance of membrane-assisted radiant cooling outdoors, Proceedings of Roomvent 2024, Stockholm, Sweden.

Acknowledgements

First, I would like to express my sincere gratitude to my supervisor, Prof. Jianlei Niu, for his invaluable guidance, unwavering support, and the numerous opportunities he has provided for my career growth and network development. He has been a constant source of support, readily available to listen to my problems, provide technical advice to tackle them and offer motivating guidance. He has also generously spent his valuable time reviewing my papers and reports, which has been instrumental in improving the quality of my work.

I would like to express my heartfelt thanks to the Research Grant Council of the Hong Kong SAR, China (Project No. 15206620) for funding this project. I also extend my gratitude to The Hong Kong Polytechnic University for supporting my participation in conferences and funding my Research Student Attachment Program, both of which have been invaluable experiences for my academic and professional development.

A special note of appreciation goes to Prof. Chengwang Lei for the exceptional opportunity to continue my research at the University of Sydney and for his dedicated guidance throughout my exchange program, which has broadened my perspectives and enriched my research experience.

More importantly, I would like to acknowledge the invaluable support and collaboration of my project colleagues, Dr. Zhong Ziwen, Liang Yan, Junran Yang, and Dr. Haobin Liang. Their contributions to the same project have been instrumental in the progress of my thesis work. I also extend my gratitude to Kenny Huang for his assistance in preparing the indoor chamber tests, which were crucial for the project. Furthermore, I would like to thank Dr. Xie Yongxin, Lin Junwei, and Dr. Yu Yichen for their expertise and support in the assessment of human thermal sensation, which has been a vital aspect of this research.

I would like to express my heartfelt appreciation to all my friends and colleagues at PolyU, who have made my entire PhD journey a truly rewarding and fulfilling experience. A special mention goes to my "research family" including Dr. Li Jianong, Jiang Ying, Zhou Siqi, Wang Jiawei, Xu Xinzi, Peiyang Du, Wang Jue, Hou Yunge, Zhao Cheng, Dr. Huang Taiyang, as well as my Indian friends, Aswin Kumar, Nandini, Mohana Das, Mohammed Yousuf, Vasundra, Subash, Ramakanth, and Gokula Manikandan, for their unwavering support and camaraderie throughout this journey.

Last, but certainly not least, I would like to express my deepest gratitude to my beloved wife, Durgadevi, for her constant support, understanding, and companionship, which have been invaluable throughout this endeavor. I also extend my heartfelt thanks to my mom Amsavalli, sister Dharani, and my adorable nephew Aadav Kumar for their unconditional love, encouragement, and unwavering support, without which I would not have been able to reach this point of success.

**Dedicated to Prof. Jianlei Niu
and in Loving Memory of My Father**

Table of Contents

Certificate of Originality	i
Abstract.....	ii
List of Research Publications.....	v
Acknowledgements	vii
List of Tables	xv
List of Figures.....	xvi
Nomenclature	xxi
Abbreviations	xxi
Variables	xxiii
Subscripts.....	xxvi
CHAPTER 1.....	1
Introduction.....	1
1.1 Cover Shield-Assisted Radiant Cooling System.....	3
1.2 Research Gaps and Objectives	5
1.3 Thesis Outline	6
CHAPTER 2.....	8
Literature Review	8
2.1 Outdoor Cooling.....	8
2.2 Membrane-Assisted Radiant Cooling System.....	10
2.2.1 Design Considerations	12

2.2.2	Cover Shield Selection Factors	15
2.2.3	Critical Air Gap Thickness for Membrane-Assisted RCS	23
2.2.4	Heat Transfer Modelling	26
2.2.5	CFD Simulations	36
2.2.6	Thermal Comfort and Energy	39
2.2.7	Discussions	46
2.3	Condensation Issues	47
2.4	Outdoor Applications	49
2.5	Urban Outdoor Environment Modelling	50
2.6	Heat Loss from Human Body in Outdoors	52
2.7	Outdoor Thermal Comfort Models	55
2.8	Human Thermoregulation Model	58
2.9	Coupling Numerical Modelling and Human Thermoregulation Systems	60
2.10	Summary	63
CHAPTER 3		66
Thermal Modelling of Membrane-Assisted Radiant Cooling System		66
3.1	Membrane-Assisted RCS in the Outdoor Environment	66
3.2	Model Set-Up and Framework	71
3.2.1	Mathematical Model	75
3.3	Results and Discussion	78
3.3.1	Validation of Modelling Method	78

3.3.2	Heat Transfer Performance Analysis of Membrane-Assisted RCS in the Outdoor Environment.....	80
3.3.3	Impact of Membrane Material	84
3.3.4	Practical Implications of the Prototype Design	90
3.4	Summary	91
CHAPTER 4.....		93
Thermal Sensation Assessment - Coupling CFD and Radiation Modelling with Human Body Thermoregulation Model		93
4.1	Research Background.....	93
4.2	Methodology	96
4.2.1	Coupling of Environment Modelling and Human Thermoregulation Model ...	96
4.2.2	JOS-3 Thermoregulation Model	99
4.2.3	Thermal Sensation Assessment.....	101
4.3	Thermal Sensation Assessment in Localised Outdoor Cooling Hub	104
4.3.1	CFD Modelling of Localised Outdoor Cooling Hub	104
4.4	Result and Discussion	107
4.4.1	Convective and Radiative Heat Transfer	108
4.4.2	Thermal Sensation Assessment using the CFD-CTM-JOS-3 Coupling Method...	109
4.5	Comparison of Thermal Sensation Vote between CFD-CTM-JOS-3 Coupling Method and Thermal Comfort Survey	111
4.6	Impact of Wind Velocity on the CFD-CTM-JOS-3 Coupling Method	114

4.7	Comparison of the CTM-Free Simplified Approach and the CFD-CTM-JOS-3 Coupling Method	117
4.8	Summary	120
CHAPTER 5.....		122
Thermal and Comfort Performance Analysis of Outdoor Radiant Cooling System		122
5.1	Methodology	122
5.2	Model Validation with Chamber Test.....	127
5.2.1	Monitoring Facility	128
5.2.2	Comparison of Model Results and Chamber Test Results	129
5.3	Results and Discussion.....	131
5.3.1	Thermal Performance of the System.....	132
5.3.2	Comfort Performance of the System.....	134
5.3.3	Cooling Effect Comparison: LOCH Bus Stop and Conventional Bus Stop	140
5.4	Summary	143
CHAPTER 6.....		146
Conclusions and Recommendations for Future Study		146
6.1	Cover Shield-assisted Radiant Cooling System	147
6.2	Thermal Performance Assessment in the Outdoor Urban Environment.....	148
6.3	Thermal Sensation Assessment (Coupling of CFD and Human Thermoregulation)....	150
6.4	Thermal and Comfort Performance of the Cooling System.....	151
6.5	Scope of Future Research.....	152

Appendix A Thermal Efficiency and Efficacy Analysis	155
Results and Discussion	156
Sensitivity Analysis – Cooling Panel Temperature	156
Appendix B - Computational Thermal Manikin (CTM) Validation	160
References.....	162

List of Tables

Table 2.1 Summary of the cover shield-assisted radiant cooling studies	11
Table 2.2 Transmissivity of the cover shield through the thermal radiation channel (J. Zhang et al., 2021)	16
Table 2.3 Various nomenclature for the optical properties of semi-transparent material	17
Table 2.4 Parametric studies of optical properties of the membrane.....	18
Table 2.5 Details of heat transfer studies of CS-RCS.....	28
Table 2.6 Details of coupling methods reported in the literature	60
Table 3.1 Details of the critical air gap thickness analysis reported in the literature	68
Table 3.2 Transmissivity of the cover shield through the thermal radiation channel (J. Zhang et al., 2021)	70
Table 3.3 Ambient and solar parameters inputs for the CFD modelling for various times of the day.....	72
Table 3.4 Boundary conditions for the CFD modelling	74
Table 4.1 Null zone skin temperature range and coefficients of body parts for the updated CBE comfort model (Xie et al., 2020; Y. Zhao, Zhang, Arens, & Zhao, 2014)	103
Table 4.2 Description of local body parts of CTM.....	106
Table 4.3 Boundary conditions of the CFD model	107
Table 4.4 Details of participants and ambient conditions of the comfort survey	113
Table 4.5 Wind parameters of the different cases (Zou et al., 2021).....	115
Table 5.1 Ambient factors and ground and building surface temperatures of the investigated times of the day.....	124
Table 5.2 Boundary conditions of the computational domain.....	125

List of Figures

Figure 1.1 The radiant cooling system proposed by Morse (Morse, 1963).....	4
Figure 2.1 Historical view of CS-RCS research	10
Figure 2.2 Schematic of (a) Single layer (Xing et al., 2020), (b) double layer (Du et al., 2021), (c) Multi-layer membrane-assisted RCS (Gu et al., 2023), (d) aerogel-assisted radiant cooling (Y. Liang et al., 2021) studies.....	13
Figure 2.3 (a) Pictorial view of the outer side and (c) inner side of CS-RCS experiment setup (b) Structure of the membrane-assisted radiant panel, and (d) schematic of the experiment setup (K. W. Chen et al., 2020; Teitelbaum et al., 2020; Teitelbaum, Chen, et al., 2019)	14
Figure 2.4 Variation of heat transfer coefficient with respect to air gap thickness (Xing et al., 2020; N. Zhang et al., 2021)	25
Figure 2.5 Heat transfer components of (a) membrane and (b) aerogel-assisted radiant cooling system (Sheppard, 2020).....	28
Figure 2.6 Thermal radiation heat transfer model of membrane-assisted RCS (Xing et al., 2021)	31
Figure 2.7 Heat transfer process considered for the two-heat flux model (N. Zhang et al., 2021)	33
Figure 2.8 Radiative heat transfer for double skin membrane-assisted RCS (Du et al., 2021)	35
Figure 2.9 Radiative heat transfer process in aerogel layer in the aerogel-assisted radiant panel (Y. Liang et al., 2021; Y. Liang et al., 2022).....	39

Figure 2.10 Comparison of cooling capacity between the various cover shield configurations of CS-RCS (Du et al., 2021; Gu et al., 2023; Guo et al., 2023; Y. Liang et al., 2021; N. Zhang et al., 2021)	43
Figure 2.11 Parameters considered for the urban modelling	51
Figure 3.1 (a) Schematic of localised outdoor cooling hub prototype (b) Heat transfer components of the membrane-assisted RCS in the outdoor environment (Roshan, Moghbel, & Attia, 2020)	67
Figure 3.2 Spectral transmittance of LDPE, Polyolefin (POF), PEA, and STATIC (He et al., 2021; A. Leroy et al., 2019; Torgerson & Hellhake, 2020; N. Zhang et al., 2023).....	70
Figure 3.3 Framework for the LOCH modelling in the outdoor environment	71
Figure 3.4 Schematic of the computational domain and radiant cooling structure	74
Figure 3.5 (a) Computation domain and boundary conditions of CFD model (b) schematic of experiment setup	79
Figure 3.6 (a) velocity vector, (b) temperature contour of air domain, and (c) CFD Model validation of membrane-assisted RCS for heat extraction rate.....	80
Figure 3.7 View factors of ceiling and wall panels to the surroundings.....	82
Figure 3.8 Heat extraction rates and heat transfer coefficients of ceiling panel at different cooling panel temperatures ($T_{\text{air}} = 31.6^{\circ}\text{C}$ at 13:00 hr, MIR-selective membrane).....	83
Figure 3.9 Heat extraction rates and heat transfer coefficients of wall panel at different cooling panel temperatures (($T_{\text{air}} = 31.6^{\circ}\text{C}$ at 13:00 hr, MIR-selective membrane)	84
Figure 3.10 Sun position and shading on the cooling panels at different times on 21st July ..	85

Figure 3.11 Heat flux comparison of the radiant cooling panel with various cover shield configurations at (a) 9:00 (b) 11:00 (c) 13:00 and (d)15:00 hrs.	86
Figure 3.12 Variation of ceiling and wall panels' membrane temperature, and their corresponding ambient air and dew point temperatures at different times of the day	89
Figure 3.13 Comparison of panel heat extraction rate of the three membrane types at different times of the day	91
Figure 4.1 Flow chart of coupling methods (i) CFD-CTM-JOS-3 method (Both one-way and two-way coupling) (ii) CTM-free simplified approach (one-way coupling only).....	98
Figure 4.2 Schematic of human thermoregulation model (Takahashi et al., 2021b).....	101
Figure 4.3 Schematic of the computational domain and radiant cooling structure	106
Figure 4.4 Local heat transfer coefficients, MRT and air temperature variation for the one-way and two-way coupling method.....	109
Figure 4.5 (a) Local and overall skin temperature and (b) predicted thermal sensation from one-way and two-way coupling methods (CFD-CTM-JOS-3 coupling).....	111
Figure 4.6 (a) Comparison of local and overall TSV between predicted by the CFD-CTM-JOS-3 coupling method and default JOS-model with thermal comfort survey (b) onsite survey of the human subject (Yang et al., 2024)	113
Figure 4.7 Annual Wind Rose Diagram for Hong Kong (Betti et al., 2022) (weather file: Kowloon weather station).....	115
Figure 4.8 Local CHTCs (W/m^2K) for the wind velocities of 0.5, 1.0 and 1.5 m/s	116

Figure 4.9 Local and mean skin temperatures assessed for the wind velocities of 0.5, 1.0 and 1.5 m/s.....	117
Figure 4.10 Local and overall (a) skin temperature and (b) thermal sensation vote predicted by CFD-CTM-JOS-3 coupling method and CTM-free simplified approach.....	119
Figure 4.11 Different wind direction and manikin orientation configurations of the outdoor radiant cooling hub	120
Figure 5.1 Framework of the methodology to assess the heat extraction rate and thermal sensation.....	123
Figure 5.2 Street orientation and respective solar path diagram of Hong Kong.....	124
Figure 5.3 Schematic of the computational domain and boundary condition of Street Canyon	126
Figure 5.4 (a) Schematic of the chamber test environment and (b) Pictorial view of experiment setup	129
Figure 5.5 Comparison of total heat extraction rate between chamber test and CFD	130
Figure 5.6 Comparison of skin temperatures of local body parts between simulation and chamber test	131
Figure 5.7 Solar exposure of the LOCH for NS (East-facing hub) and WE (South-facing hub) orientations for 9:00, 11:00, 13:00 and 15:00 hr	132
Figure 5.8 Comparison of heat load components between WE and NS orientation cases	134
Figure 5.9 Solar heat flux contour of CTM and radiant cooling panel (a) NS and (b) WE orientation cases.....	135

Figure 5.10 Local and overall (a) skin temperature and (b) thermal sensation vote in the LOCH for the case of NS orientation	136
Figure 5.11 Local and overall (a) skin temperature and (b) thermal sensation vote in the LOCH for the case of WE orientation	138
Figure 5.12 Comparison of (a) skin temperature and (b) thermal sensation vote between LOCH and conventional bus stop for NS orientation case (East-facing bus stops) at 13:00 hr.....	141
Figure 5.13 Comparison of radiative heat flux contour for (a) conventional bus stop and (b) LOCH for NS orientation case (East-facing bus stops) at 13:00 hr.....	142
Figure 5.14 Comparison of total heat flux contour for (a) conventional bus stop and (b) LOCH for NS orientation case (East-facing bus stops) at 13:00 hr.....	143
Figure A.1 Variations of local and overall (a) skin temperature and (b) thermal sensation vote for different cooling panel temperatures and no-cooling case.....	158
Figure A.2 Variation of heat extraction rate, overall thermal sensation vote and energy efficacy for different cooling panel temperature	159
Figure B.1 Convective and radiative heat flux validation of CTM against the wind tunnel experiments for the velocities of (a) 0.5 m/s (b) 1.0 m/s and (c) 2.0 m/s	161

Nomenclature

Abbreviations

AFTPU	Aerogel-Functionalized Thermoplastic Polyurethane
AIJ	Architectural Institute of Japan
AT	Apparent Temperature
AVA	Arteriovenous Anastomoses
CBE	Center for Built Environment
CFD	Computational Fluid Dynamics
CHTC	Convective Heat Transfer Coefficient
COST	European Cooperation in the Field of Scientific and Technical Research
CS-RCS	Cover Shield Assisted Radiant Cooling System
CTM	Computational Thermal Manikin
DES	Detached Eddy Simulation
DI	Discomfort Index
DO	Discrete Ordinates
DOAS	Dedicated Outdoor Air Systems
DPT	Dewpoint Temperature
EVA	Ethyl Vinyl Acetate
HDPE	High-Density Polyethylene
HI	Heat Index
IR	Infrared Radiation
IRT	Infrared Radiation Transparent
JOS	Jointed Circulations System

LDPE	Low-Density Polyethylene
LES	Large Eddy Simulation
LLDPE	Linear Low-Density Polyethylene
LOCH	Localised Outdoor Cooling Hub
MIR	Mid-Infrared Radiation
MRT	Mean Radiation Temperature
NS	North-South
NST	Non-Shivering Thermogenesis
OUT_SET*	Outdoor Standard Effective Temperature
PAU	Primary Air Unit
PCM	Phase Change Material
PCT	Partially Transparent Polycarbonate
PDMS	Poly Dimethyl Siloxane
PE	Polyethylene
PEA	Polyethylene Aerogel
PET	Physiologically Equivalent Temperature
PMV	Predicted Mean Vote
PP	Poly Propylene
PPD	Predicted Percentage Of Dissatisfied
PRESTO	Pressure Staggering Option
PVC	Polyvinyl Chloride
RANS	Reynolds Averaged Navier Stokes
RCS	Radiant Cooling System
RHTC	Radiative Heat Transfer Coefficient
SET	Standard Effective Temperature

SRANS	Steady Reynolds Averaged Navier-Stokes
SST	Shear Stress Transport
STATIC	Spectrally Tuned All-Polymer Technology for Induced Cooling
TI	Turbulence Intensity
TLS	Turbulent Length Scale
TSV	Thermal Sensation Vote
TSV	Thermal Sensation Vote
TWL	Thermal Work Limit
UHI	Urban Heat Island
UTCI	Universal Thermal Comfort Index
WBGT	Wet Bulb Globe Temperature
WE	West-East

Variables

i_{cl}	Clothing vapour permeation efficiency
\vec{s}	Scattering direction vector
C_1, C_2 and C_3	Constants
E_b	Blackbody emissive power (W/m ²)
G_b	Turbulent kinetic energy due to buoyancy (m ² /s ²)
G_k	Turbulent kinetic energy due to velocity gradient (m ² /s ²)
$I_{b\lambda}$	Black body intensity (W/m ²)
I_{cl}	Clothing insulation (clo)
I_λ	Spectral intensity (W/m ² /μm)
L_R	Lewis ratio

P_a	Saturated water vapour pressure at ambient air (kpa)
P_{ssk}	Saturated water vapour pressure at skin temperature (kpa)
Q_c	Convective heat flux (W/m ²)
Q_{cond}	Conductive heat flux (W/m ²)
Q_r	Radiative heat flux (W/m ²)
Q_t	Total heat transfer (W/m ²)
Q_T	Solar heat flux (W/m ²)
S_k and S_ϵ	User-defined source terms
Y_M	Fluctuating dilatation compressible turbulence to the overall dissipation rate
f_{cl}	Clothing area factor
g_i	Gravity (m/s ²)
q_{in}	Incident radiative heat flux (W/m ²)
\vec{r}	Position vector (m)
\vec{s}	Direction vector
u_i	Air velocity component along the i-axis (m/s)
u_j	Air velocity component along the j-axis (m/s)
Ω'	Solid angle (sr)
α_T	Thermal diffusivity (m ² /s)
α_λ	Spectral absorption coefficient (m ⁻¹)
λ_1 and λ_2	Wavelength boundaries for a band (μm)
μ_t	Turbulent viscosity (kg/ms)
ρ_{ref}	Reference density (kg/m ³)
σ_k	Prandtl numbers for k

σ_s	Scattering Coefficient (m^{-1})
σ_ϵ	Prandtl numbers for ϵ
ϵ_ω and $\epsilon_{\omega\lambda}$	Wall emissivity
B	Heat exchange by blood flow (W)
BSA	Body surface area (m^2)
C	Heat exchange by convection (W)
C, C1, C2, D1, and D2	Constants in terms of reflectivity, emissivity, and panel temperature
Cap	Heat capacity (J/K)
D	Thickness of the membrane (m)
D	Heat exchange by conduction (W)
E	Evaporation (W)
$F(0 \rightarrow n\lambda T_\omega)$	Fraction of radiant energy emitted by a blackbody
G	Incident radiant flux onto a surface (W/m^2)
h	Heat transfer coefficient ($\text{W}/\text{m}^2\text{k}$)
H	Incident radiant flux across a membrane (W/m^2)
I	Radiation intensity (W/m^2)
J	Radiosity (W/m^2)
k	Thermal conductivity of air (W/mk)
L	Air gap thickness (m)
n	Refractive index
Nu	Nusselt number
P	Pressure (pa)
Q	Heat production
R	Thermal resistance ($\text{m}^2\text{k}/\text{W}$)

R	Heat exchange by radiation (W)
Ra	Raleigh number
RES	Heat loss by respiration (W)
s	Path length (m)
T	Temperature (K)
t	Time (s)
Ω	Scattering albedo
a	Absorption coefficient (or) Attenuation coefficient (m^{-1})
w	Skin wittedness
Φ	Phase function (1/sr)
α	Absorptivity
β	Thermal expansion coefficient (1/K)
ε	Emissivity
λ	Wavelength (μm)
μ	Extinction Coefficient (m^{-1})
μ	Dynamic viscosity (kg.m/s)
ρ	Reflectivity
ρ	Density (kg/m^3)
σ	Stephen Boltzmann constant (W/m^2k^4)
τ	Transmissivity

Subscripts

j	adjacent body tissues
atm	atmosphere

c	cooling surface
c	convective
c-m	heat transfer between the cooling panel and membrane
cse	cover shield external surface
et	total evaporative
g	geometrical resistance based on the view factor between the surfaces
h	heating panel surface
hs	heat sources
i	segment number
j	tissues
m	membrane surface
m,e	membrane to external ambient
me	membrane exterior surface
mi	membrane internal surface
o	operative temperature
r	radiative
s	surface radiant resistance
sk	skin
sol	solar radiation
surr	surrounding indoor surfaces
t	total
t	total
$r\varepsilon$	radiant energy resulting from emissivity

CHAPTER 1

Introduction

Global warming and urban heat waves are marked by an increase in the frequency, intensity, and duration of hot days. In recent years, many cities all around the world have suffered heat wave attacks (Kotharkar & Ghosh, 2022). For instance, India (Goyal, Singh, & Jain, 2023), China (Lei et al., 2024; Tan et al., 2010), Europe (Sola-Caraballo, Lopez-Cabeza, Roa-Fernández, Rivera-Gomez, & Galan-Marin, 2024) and USA (Issa & Alrusayni, 2024) have faced extremely high temperatures, exceeding 45°C, 42°C, 46.8°C and 49°C respectively. This shift could have detrimental effects on both physical and psychological well-being, and in extreme cases, it may contribute to an uptick in mortality rates (Ballester et al., 2023; Dodla, Satyanarayana, & Desamsetti, 2017; Knowlton et al., 2009; Robine et al., 2008). The urban heat island (UHI) effects (Mirzaei & Haghghat, 2010; Mattheos Santamouris, Ding, & Osmond, 2019) i.e., the combination of anthropogenic heat release and trapped solar radiation, and weakened wind flow due to blockages by buildings of the urban environment worsen the summer thermal conditions for human comfort (M. Santamouris, 2020). The number of hot days and nights increased drastically due to the UHI effect (Edward, 2009). This phenomenon is occurring in parallel with the rapid pace of urbanization. Predictions indicate that by 2050, urban dwellers are expected to constitute two-thirds of the global population, a significant increase from the 57% recorded in 2022 (Desa, 2014). Elevated temperatures in urban environments are likely to result in greater indoor-centric lifestyles among city residents. People become aware of the importance of the outdoors for fresh air and a healthy lifestyle during the COVID pandemic (Stock, Bu, Fancourt, & Mak, 2022). Moreover, bus commuters and people working outdoors, road workers, construction workers and the homeless are

supposed to spend a long day time in the outdoors and thus, are more vulnerable to the UHI and heat waves.

The outdoor shelters such as bus stops with current infrastructure standards and material options mostly failed to protect the occupants in summer days of hot climates (Dzyuban, Hondula, Coseo, & Redman, 2022). Regrettably, some major cities did not even have shelter for suburban bus stops ("Sydney's Busted Bus Stops: Read our Campaign Report," 2024). There are several passive methods proposed to improve the thermal comfort of outdoor shelters such as adaptive structure design (Lin, Matzarakis, & Huang), alternate constructive materials, roof vegetation (Iqbal, 2019), and trees (Cheung & Jim, 2018). While these passive cooling concepts can provide thermal comfort (Iqbal, 2019), their effectiveness during extreme urban heat waves remains questionable.

Mechanical air-conditioners are used in bus stops in some hot cities such as Delhi (India), Lahore (Pakistan), Antalya (Turkey), and Dubai (UAE) ("Waiting for a bus becomes cool," 2017). The "Green Air Conditioner" based on evaporative mist cooling is implemented in bus stops in Japan ("Keeping Bus Stops Cool," 2017). Most of the abovementioned air-conditioned bus stops are enclosed by glass facades, but waiting in a confined space is not safe as it can accelerate the spread of infectious pathogens (Mokhtari & Jahangir, 2021). Kyogoku et al. (Kyogoku & Takebayashi, 2023) reported that the evaporative mist cooling system for the open space in Japan failed to provide chillness to the human body. In middle-east countries, outdoor air conditioning has been implemented for an open stadium (Sofotasiou, Hughes, & Calautit, 2015) and open jogging tracks (Post, 2021). When it comes to a humid environment, could become energy-intensive, and energy will be wasted for treating the latent heat of outdoor ambient air.

On the other hand, the heat imbalance between the human body and the thermal environment causes discomfort, i.e., cold or hot. The heat generated from the human body is continuously transferred to the surroundings through convection, radiation, conduction and evaporation, to maintain the body core temperature between 36.1 to 37.2°C, in turn, achieve thermal comfort. The conventional air conditioning system helps attain the heat balance by enhancing convective heat transfer, by blowing the cold air over the skin. It is energy-intensive for outdoor applications. Instead of enhancing the convection, increasing the radiation loss by using a heat sink would be the better alternate solution. Enhancing the radiative heat transfer by using a heat source or sink is called radiant heating or cooling technology. For the outdoor application, the cover shield-assisted radiant cooling system could be a potential option, as the system directly treats the radiant load, with reduced convective heat loss to the ambient. Teitelbaum et al. (Teitelbaum, Chen, et al., 2019) performed an experimental study on membrane-assisted radiant cooling in a semi-outdoor environment. The results revealed that it can provide better thermal comfort as it provides cooling energy through radiative heat transfer. Condensation is a major issue for conventional radiant cooling technology, especially in hot and humid climates (Tang, Zhang, Liu, & Li, 2021; Teufl, Schuss, & Mahdavi, 2021; Xing, Li, Zhang, & Heiselberg, 2021). However, the membrane cover shield on the radiant panel protects the panel from ambient convection while transmitting infrared (IR) radiation (Du, Wu, Huang, Xu, & Liu, 2021; Guo, Wu, Du, Huang, & Xu, 2023; N. Zhang et al., 2021).

1.1 Cover Shield-Assisted Radiant Cooling System

In the Cover Shield-Assisted Radiant Cooling System (CS-RCS), the radiant cooling surface is decoupled from the ambient air by the infrared-radiation transparent (IRT) membrane. The transparency of the cover shield in the infrared region allows thermal radiation from occupants and heat sources. The concept of the CS-RCS was initially proposed by Morse in 1963 for the hot and humid climates of Australia (Morse, 1963). In the proposed system, the radiant cooling

panel is covered using a 0.1 mm transparent polythene sheet with 25 mm spacing between them to prevent contact between the cooling surface and external humid air (Figure 1.1). To maintain the outer surface temperature of the polythene cover above the dewpoint temperature (DPT) of the surrounding air, a small heater is provided between the cover and the radiant panel. However, it is not economical and increases the cooling load of the radiant cooling system. Morse also proposed to increase the number of polythene covers but each additional cover reduces 17% of the cooling effect. The proposed cooling system was not getting much attention due to its inefficiency and also the unavailability of the appropriate material.

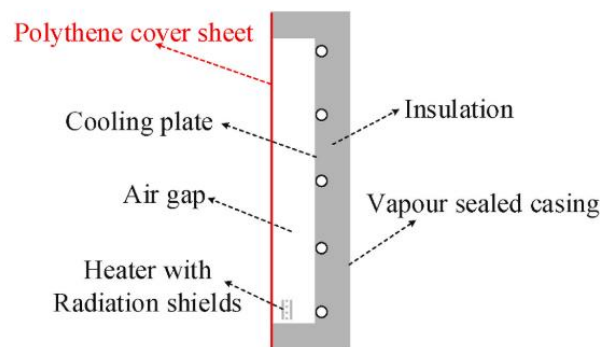


Figure 1.1 The radiant cooling system proposed by Morse (Morse, 1963)

In 2005, Wang (J. Wang, 2005) replicated the Morse model and the air gap-based radiant cooling system is mutated from the original concept. Instead of a polythene sheet, an aluminium sheet was used. It will act as the radiation shield, i.e., a barrier for the radiation exchange between the heat source and cooling pipes (Ning, Chen, Liu, & Zhang, 2016; Su et al., 2019; Teitelbaum, Rysanek, et al., 2019; Xing & Li, 2021). Later, the original concept was revived in 2018 (Teitelbaum, Rysanek, et al., 2019) with an IRT membrane, i.e., a convection shield between heat sources and a cooling panel. And this concept grabbed momentum in academics and various researchers showed interest in this concept (Aviv et al., 2021; K. W. Chen, Teitelbaum, Meggers, Pantelic, & Rysanek, 2020; Teitelbaum et al., 2019; Teitelbaum et al., 2020). The IRT aerogel is also used as the cover shield for CS-RCS applications (Y.

Liang et al., 2021; Y. Liang et al., 2022). In the membrane-based CS-RCS, the heater is not used to maintain the membrane temperature above DPT, as the well-designed air gap thickness serves this purpose. The air gap between the membrane and radiant cooling panel reduces convective heat transfer between them and keeps the membrane temperature comparatively higher than the cooling panel. In aerogel-based CS-RCS, highly insulative and transparent aerogels are preferred to serve the purpose of air layer in the membrane-based CS-RCS.

The principle of the CS-RCS is almost similar to that of the nighttime radiative sky cooling system (N. Zhang et al., 2021). In the radiative sky cooling system, the panel exposed to the sky absorbs the radiation from outer space, which is around 258 K, through the atmospheric window (8-13 μ m). In the membrane-assisted radiant cooling system, the membrane acts as an atmospheric window between the radiant panel and the heat source. Advancement in the membrane design makes the radiative sky cooling work in the daytime also. Inspired by daytime radiative sky cooling which uses a selective IRT membrane that is only transparent in infrared radiation regions and highly reflective to the solar radiation wavelength opens the opportunity to use the membrane-assisted RCS for outdoor/semi-outdoor applications. Wind effects enhance convective heat loss from the human body in outdoor environments, while radiant cooling improves radiative heat loss.

1.2 Research Gaps and Objectives

Studies reported on outdoor cooling are seldom found in the literature. However, conventional air conditioning-based outdoor cooling systems have been installed in some cities, they were used for transparent enclosed spaces and their performance has not been reported yet. Compared to indoor space cooling, outdoor cooling has to deal with several undesirable load components such as solar radiation, radiation from surrounding surfaces etc. On the other hand, the outdoor ambient conditions are uncontrollable and transient. Due to the convective heat

loss to the outdoor environment, it is challenging to design conventional air conditioning for open outdoor spaces.

As a relatively less explored alternative, cover shield-assisted radiant cooling systems avoid convective losses while addressing radiative loads. Previous studies on the membrane-assisted radiant cooling system have investigated indoor and semi-outdoor applications, and not adequately investigated for outdoor applications. It is important to address the challenges for its usage in outdoor applications. To advance understanding and implementation of outdoor radiant cooling systems, this research aims to address three key questions:

1. To what extent does the radiant cooling system enhance human thermal comfort in outdoor environments?
2. What are the system's energy consumption and energy efficiency?
3. What system design considerations are necessary to meet both thermal comfort and energy efficiency?

Answering these will support the overarching goal of developing sustainable and climate-resilient urban centers. Outdoor populations worldwide would benefit from improved thermal conditions and expanded use of public spaces.

1.3 Thesis Outline

This chapter (Chapter 1) presents the problem statement, the proposed solution of the membrane-assisted radiant cooling system, research gaps, objectives and the outline of the thesis.

Chapter 2 covers the literature review based on the aspects of outdoor cooling systems, outdoor environment modelling and outdoor thermal sensation assessment. It provides a comprehensive review of the membrane-assisted radiant cooling system, outdoor modelling using Computational Fluid Dynamics (CFD) techniques, and the coupling methods between CFD

and thermoregulation models. Additionally, the design considerations regarding the membrane material have been discussed.

Chapter 3 provides the thermal performance investigation of a Localised Outdoor Cooling Hub (LOCH) employed with the membrane-assisted radiant cooling system. It analyses the impact of membrane material on the thermal performance of the cooling system and presents the result and discussion to address the second and third research questions concerning energy consumption, and design parameters.

Chapter 4 explores the different coupling methods between CFD and the human thermoregulation model to assess the thermal sensation in the outdoor environment. This methodology is applied to the proposed LOCH to investigate the first research question on the thermal comfort provided by the outdoor radiant cooling system.

Chapter 5 presents the thermal and comfort performance of the outdoor radiant cooling system for the hot and humid climate of Hong Kong. It compares the thermal sensation experienced under the cooling system with that of a shaded spot representing a conventional bus stop, evaluating the performance of the cooling system in a real-world scenario and addressing the first and third research questions.

The last chapter, Chapter 6 provides the concluding remarks from the present research work and provides the recommendation for future studies. The energy efficiency and efficacy analysis of the current structure design on a typical summer day in Hong Kong and the validation of the computational thermal manikin utilized in the simulation are discussed in the appendices.

CHAPTER 2

Literature Review

This chapter presents a literature review on key topics related to membrane-assisted radiant cooling systems for outdoor applications and the assessment of outdoor thermal comfort. It first examines the membrane-assisted radiant cooling system designs, highlighting impactful design factors, heat transfer models developed, and evaluations of thermal comfort levels and cooling capacity achieved. A comprehensive understanding of this emerging cooling technology was sought through this review.

Numerical modelling is central to achieving the research objectives. Therefore, the literature review also examines previous work on outdoor environment modelling techniques. When assessing thermal sensation in outdoor settings, focus is given to studies investigating outdoor thermal comfort models, human thermoregulation models, and efforts to couple numerical simulations with thermoregulation system representations. This review aims to build upon prior work to design and modelling of membrane-assisted radiant cooling hubs, while effectively evaluating the systems' impacts on occupants' perceived thermal comfort within varying outdoor contexts. Additionally, gaps and opportunities for further research are identified.

2.1 Outdoor Cooling

The asymmetrical and transient outdoor environment makes outdoor cooling more challenging. The outdoor cooling system must treat the undesired ambient factors including solar radiation, long wave radiation, wind speed, air temperature and humidity. The purpose of outdoor cooling is to provide comfortable outdoor space, especially during hot summer days. There are several strategies implemented to mitigate the intense urban heat waves and to provide comfortable

outdoor spaces. Passive cooling strategies such as urban morphology designs (Lai, Maing, & Ng, 2017; Taleghani, Kleerekoper, Tenpierik, & Van Den Dobbelsteen, 2015), solar reflective coating on surfaces (Chatzidimitriou & Yannas, 2015; Taleghani, Sailor, Tenpierik, & van den Dobbelsteen, 2014; Jiachuan Yang, Wang, Kaloush, & Dylla, 2016), and blue and green infrastructure (Gobatti, Bach, Scheidegger, & Leitão, 2023) are commonly used for urban spaces to provide shading, reduce solar, ground surface temperature, and air temperature, and enhance wind speed. Particularly in outdoor public places, including bus stops and train stations, shading, and mechanical fans most commonly used passive cooling strategies, and green roofs are seldom located. However, during intense urban heat waves or hot summer days in tropical climate zones, the benefit of a passive cooling system to protect public health from heat exposure is questionable.

There are some active cooling systems implemented for outdoor spaces. Air conditioning and mist cooling have been implemented in the bus stops with enclosed glass facades ("Keeping Bus Stops Cool," 2017; Kyogoku & Takebayashi, 2023; "Waiting for a bus becomes cool," 2017). However, the performance of the air-conditioned bus stops has not been reported yet. Although there are difficulties and limitations to designing and implementing air conditioning in outdoor settings, air-conditioned stadiums (Sofotasiou et al., 2015) and jogging tracks (Post, 2021) have been implemented in middle east countries. In tropical climates, the air conditioning system outdoors has to deal with a high latent load, which becomes energy intensive. Adding mist in an enclosed space may increase the chances of virus spread, and also increase the humidity in the space.

Radiant cooling technology can be used for outdoor cooling as it directly provides cooling energy to humans by radiative heat transfer, instead of conditioning the air. Conventional radiant cooling systems have limited cooling capacity due to their condensation issue in humid climates. Therefore, to reduce the convective heat loss from the panel, as well as to isolate the

panel from humid ambient air, the membrane-assisted radiant cooling system is reported to be a feasible option for outdoor cooling applications.

2.2 Membrane-Assisted Radiant Cooling System

In the past two decades, studies regarding conventional radiant cooling systems have attracted a lot of interest (Hu & Niu, 2012; Karmann, Schiavon, & Bauman, 2017; La, Dai, Li, Wang, & Ge, 2010; Rhee & Kim, 2015; Saber, Tham, & Leibundgut, 2016; Xing et al., 2021; K. Zhao, Liu, & Jiang, 2016). With the IR transparent membrane, the radiant cooling system can be quite different from those traditional radiant cooling systems which have been studied (N. Zhang et al., 2021). The cover shield-assisted radiant cooling technology was initiated in 1963 in Australia (Morse, 1963). Due to the lack of appropriate materials and inefficient operation techniques, it has not gained much attention. In recent years, it has gained attention again in academia due to its potential to deal with condensation in hot and humid climates (Dharmasastha, Zhong, Niu, & Liang, 2023). The historical journey of CS-RCS is shown in Figure 2.1, and a detailed summary of the studies is provided in Table 2.1.

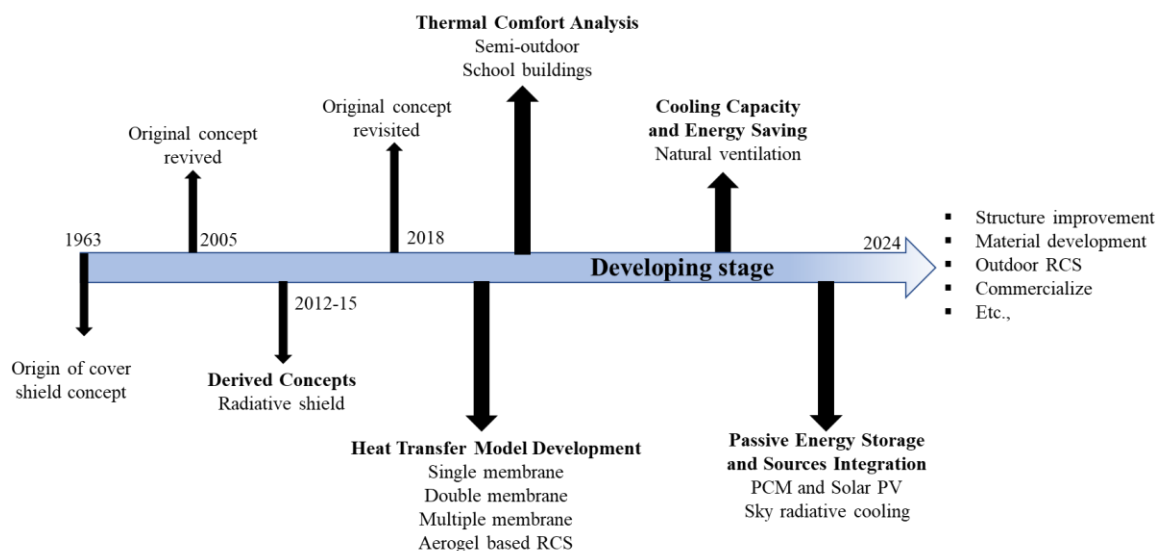


Figure 2.1 Historical view of CS-RCS research

Table 2.1 Summary of the cover shield-assisted radiant cooling studies

S. No	Author	Location of authors	Covering material	Research methods
1	Morse, 1963	Australia	Polythene	Experimental
2	J. Wang, 2005	China	Wide range	Experimental
3	Teitelbaum, Rysanek, et al., 2019	USA	PP, LDPE, HDPE	Experimental
4	Teitelbaum, Chen, et al., 2019	Singapore & USA	LDPE	Experimental, Semi-outdoor
5	Sheppard, 2020	Singapore & Canada	LDPE	Experimental, Numerical
6	Xing, Li, Cui, Zhou, & Liu, 2020	China	Wide range	Numerical
7	Teitelbaum et al., 2020	USA, Singapore & Canada	LDPE	Experimental
8	Teitelbaum et al., 2021	USA, China & Canada	Polyethylene	Experimental, Numerical
9	Y. Liang et al., 2021	China	PE Foam and PE Aerogel	Experimental, Numerical
10	N. Zhang et al., 2021	China	Polyethylene	Experimental, Numerical
11	K. W. Chen et al., 2020	USA, Singapore & Canada	LDPE	Numerical
12	Du et al., 2021	China	LLDPE	Experimental, Numerical
13	Aviv et al., 2021	USA, Canada & Belgium	IRT membrane	Numerical

S. No	Author	Location of authors	Covering material	Research methods
14	He et al., 2021	China & Singapore	PE Aerogel	Numerical, Experimental
15	Y. Liang et al., 2022	China	PE Aerogel	Numerical
16	Du et al., 2022	China	IRT membrane	Numerical
17	Riffat, Kutlu, Tapia-Brito, Su, & Riffat, 2022	UK	IRT Plastic Sheet	Experimental
18	Mokhtari, Ulpiani, & Ghasempour, 2022	Iran & Italy	Polyethylene	Numerical
19	Albuja, Foliaco, Bula, & Gonzalez-Quiroga, 2022	Columbia	IRT membrane	Numerical
20	Guo et al., 2023	China	IRT membrane	Numerical
21	Gu et al., 2023	China	IRT membrane	Numerical
22	N. Zhang et al., 2023	China	Wide range	Experiment – Chamber test
Note: PP- Polypropylene, LDPE - Low-density polyethylene, HDPE - High-density polyethylene and PE - Polyethylene				

2.2.1 Design Considerations

Structure design of CS-RCS

The structures illustrated in Figure 2.2a were applied in most of the studies related to the CS-RCS. In some numerical studies, mini prototypes were built to validate the numerical models (Du et al., 2021; Gu et al., 2023; Y. Liang et al., 2021; Xing et al., 2020). The cover shield configurations of these prototypes are based on material and number of layers, i.e., single, double, and multilayer membrane-assisted, and aerogel-assisted radiant cooling systems, as shown in Figure 2.2 (a) (b) (c) and (d) respectively. The first-ever full-scale structure of membrane-assisted RCS namely the “cold tube” was built in Singapore (K. W. Chen et al.,

2020; Teitelbaum et al., 2020; Teitelbaum, Chen, et al., 2019). The structure of the membrane-assisted radiant panel and pictorial and schematic of the pavilion cooled by a membrane-assisted radiant cooling system are shown in Figure 2.3. The capillary tube radiant cooling panel covered with LDPE membrane has been used. A semi-enclosed space designed with 8 wall radiant panels is tested for the cooling performance of the system. Do et al., (Do, Luther, Amirkhani, Wang, & Martek, 2022) proposed a similar membrane-assisted radiant cooling panel design for retrofitting radiant cooling panels.

The difficulty in adopting the membrane concept in the radiant cooling application is the infiltration of the humid air in the air gap region. Hence, the structure should be designed carefully to seal the air gap perfectly. Even in the tightly packed air gap, the water vapor can penetrate through the membrane, as the commonly used membrane materials are water vapor permeable (Tock, 1983). To absorb the water vapors, water vapor absorbents such as desiccants, and silica gel packets, can be kept in the air layer. And these packets need to be replaced often once they are saturated. Therefore, it should be considered when designing the structure.

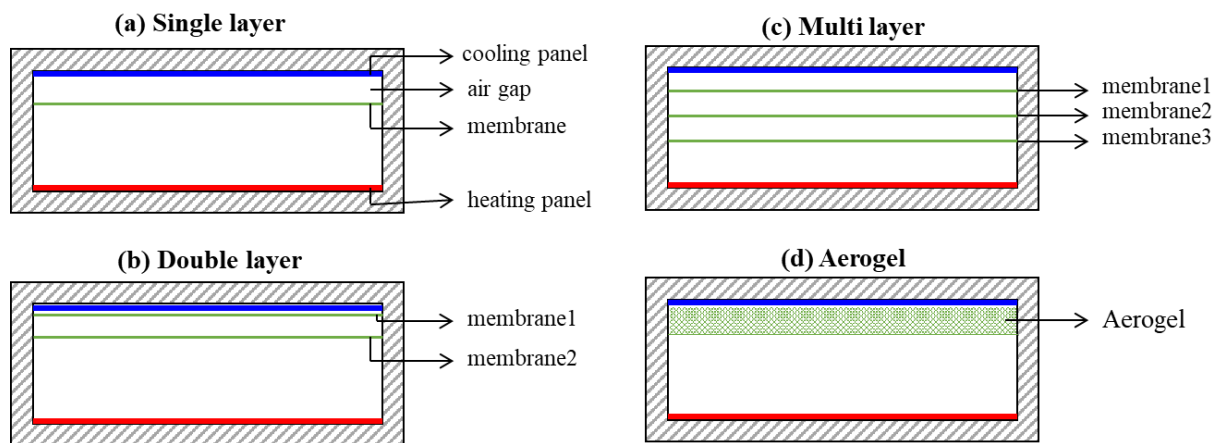


Figure 2.2 Schematic of (a) Single layer (Xing et al., 2020), (b) double layer (Du et al., 2021), (c) Multi-layer membrane-assisted RCS (Gu et al., 2023), (d) aerogel-assisted radiant cooling (Y. Liang et al., 2021) studies

The backside of the panel is insulated to prevent heat transfer in that direction. The frame structure can be made of plastic material such as PVC, UPVC, etc., as it conducts less heat and is also light in weight. In the CS-RCS, the radiant panel will be maintained at a temperature lower than the DPT of the ambient. In this case, the use of aluminium or metal frame structure should be insulated from the cooling panels, as the conduction from the panel to the frame may cause condensation on frame surfaces. The chilled water circuit to the cooling panels is the same as the conventional radiant cooling system.

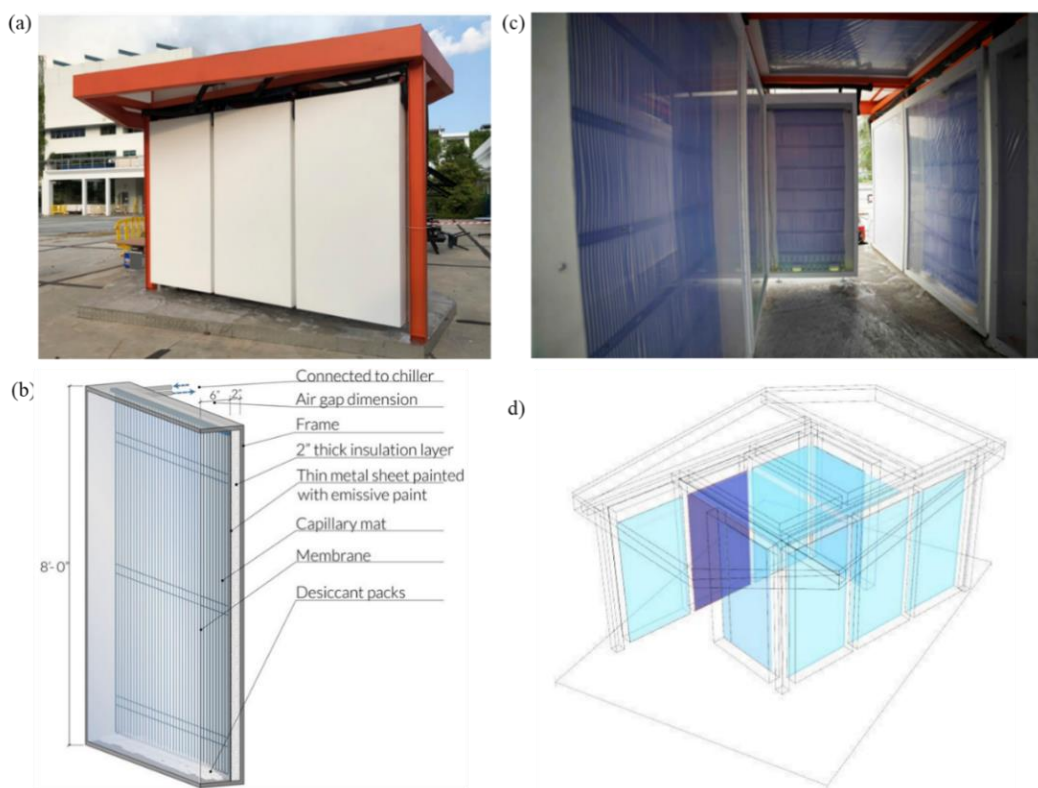


Figure 2.3 (a) Pictorial view of the outer side and (c) inner side of CS-RCS experiment setup (b) Structure of the membrane-assisted radiant panel, and (d) schematic of the experiment setup (K. W. Chen et al., 2020; Teitelbaum et al., 2020; Teitelbaum, Chen, et al., 2019)

The main difference between the CS-RCS and the conventional radiant cooling systems is the cover shield. There are several factors involved in the selection of the cover shield, such as optical properties and thermal conductivity, which are primarily discussed in this section.

Depending on the cover shield, whether it is membrane or aerogel, the design parameters and structure will vary, as their heat transfer characteristics are different.

2.2.2 Cover Shield Selection Factors

Selecting the cover shield material for a radiant cooling application is a crucial element and many factors need to be considered. The most important factors include the optical, thermal, and mechanical properties of membranes. For practical applications, other factors like availability, cost, and manufacturability should also be considered. These factors associated with membrane selection are critically reviewed in this section.

Optical Properties of cover shield

The requirements of the optical property of the cover shield are stringent for the better performance of the system. To treat the sensible heat load effectively by radiative heat transfer, an ideal cover shield should be 100% transparent to infrared radiation. Typically, the radiation emitted by humans (8 -14 μm) (Hsu et al., 2016; Ignatov, Mosin, & Drossinakis, 2014) and indoor heat sources is within the Mid-Infrared (MIR) region (3-50 μm) (Iso, 2015).

The cover shield property that indicates the transmittance variation with respect to the wavelength is spectral transmittance. According to the spectral transmittance in different thermal radiation channels, the cover shield used for CS-RCS can be categorized into non-selective, MIR-selective, and sky window selective (J. Zhang et al., 2021). Table 2.2 indicates the spectral transparency of each type of cover shield. The non-selective membranes can be used for indoor applications as the shortwave radiation exchange is less considered for the cooling load. MIR selective cover shield which can reflect most solar radiation but is transparent in the MIR region is considered as an ideal cover shield for daytime radiative sky cooling (Zizhong Li, Chen, Song, Zhu, & Zhu, 2020; Naghshine & Saboonchi, 2018). It is also preferable for outdoor and semi-outdoor radiant cooling applications to eliminate the solar heat

load on radiant cooling. Sky window selective cover shield only allows infrared radiation between 8-13 μm , which covers the radiation from the human body. It is suitable for outdoor environments, and it will only allow IR radiation from humans and block the radiation from surrounding buildings and ground surfaces. Hence, the performance of the radiant panel can be effectively utilized in an outdoor environment.

Table 2.2 Transmissivity of the cover shield through the thermal radiation channel (J. Zhang et al., 2021)

Cover Shield	Thermal Radiation Channels			
	Solar (0.25 - 2.5 μm)	Atmosphere (2.5 - 8 μm)	Sky Window (8 - 13 μm)	Atmosphere (>13 μm)
Non-Selective	✓	✓	✓	✓
MIR Selective	✗	✓	✓	✓
Sky Window Selective	✗	✗	✓	✗

Note: ✓ and ✗ symbols in the column indicate the transparent and opaque on the specific channel

There are significant parametric studies related to membrane optical properties to analyze the cooling performance of CS-RCS. It is important to understand various optical properties used in the literature, and it is listed in Table 2.3. The cooling performance was usually represented by cooling capacity and the cover shield's air contact surface temperature to avoid the condensation risk. An increase in transmittance allows more IR radiation between the source and sink. An increase in transmissivity increases the cooling capacity significantly (Du et al., 2021; Xing et al., 2020), while it has comparatively less impact on membrane surface temperature. An increase in reflectivity decreases the cooling capacity and air contact surface

temperature of the membrane linearly (Du et al., 2021). However, the impact of reflectivity on the cooling performance and membrane temperature is comparatively lower than that of transmissivity.

Table 2.3 Various nomenclature for the optical properties of semi-transparent material

S. No	Property	Nomenclature	Unit	Definition
1	Transmissivity	τ	-	Transmitted radiation/incident radiation
2	Absorptivity	α	-	Absorbed radiation/incident radiation
3	Reflectivity	ρ	-	Reflected radiation/incident radiation
4	Emissivity	$\varepsilon = \alpha$	-	absorptivity = Emissivity (Kirchoff's law)
5	Absorption coefficient (or) Attenuation coefficient	k	m^{-1}	Decrease in radiation due to absorption/thickness
6	Scattering Coefficient	σ_s	m^{-1}	Decrease in radiation due to scattering/thickness
7	Extinction Coefficient	$\mu = (k + \sigma_s)$	m^{-1}	Combined effect of absorption and scattering loss
8	Scattering Albedo	$\Omega = \frac{\sigma_s}{(k + \sigma_s)}$	-	Fraction of scattering loss to total loss
9	Refractive Index	n	-	Speed of light in vacuum/speed of light in membrane

The reduction of radiation across the thickness of the cover shield is indicated by the absorption and scattering coefficient. The parametric study on its derived coefficients, scattering, and extinction coefficient of membrane material is performed by Zhang et al. (N. Zhang et al., 2021), using a validated theoretical model. At a lower extinction coefficient, the cooling capacity of the radiant cooling system is higher, as the absorption and scattering losses are lower. The membrane surface temperature is maintained as constant, i.e., 17°C which is above DPT to avoid condensation risk. An increase in extinction coefficient 10 to 3000 m^{-1} increases

the cooling capacity as the panel temperature can be reduced to 0.25°C, for the constant membrane temperature. The radiant panel temperature is decreased by 90.6%, and the cooling capacity is increased by 5.9% when the scattering albedo increases from 0.1 to 0.9. The scattering loss has no impact on the radiative heat flux of the radiant panel, it varies less than 5% throughout this range. The extinction coefficient and the refractive index have a comparatively great influence on the cooling capacity. An increase in the refractive index from 1.01 to 1.91 increases the panel temperature by 96.8% and reduces the cooling capacity by 26%. Lower refractive index membranes are comparatively better and enhance the radiative heat exchange. The detailed variation of cooling capacity and membrane temperature of various parametric studies on the optical properties are summarized in Table 2.4. The influence of aerogel optical properties on the radiant cooling performance is yet to be analyzed.

Table 2.4 Parametric studies of optical properties of the membrane

Ref.	Parameters	Range	Default	Variation in cooling capacity (W/m ²)	Variation in membrane temp. (°C)	Panel temp. (°C)
(N. Zhang et al., 2021)	Scattering albedo	0.1 - 0.9	0.5	97.1 - 102.9	17.0 (constant)	2.68 - 0.25
	Extinction Coefficient	10-3000	500	107.9 - 89.4	17.0 (constant)	-0.44 - 3.13
	Refractive Index	1.01-1.9	1.51	124.5 - 91.8	17.0 (constant)	1.25 - 2.46
(Xing et al., 2020)	Transmissivity	0.1-0.8	0.5	24.8 - 61.7	Order of 10 ⁻²	14.25 (constant)
	Emissivity	0.05-0.8	0.2	43.2 - 54.6	Order of 10 ⁻¹	14.25 (constant)
(Du et al., 2021)	Reflectivity	0-0.1	0.87	101-104.7	17.3-17.9	7.0 (constant)
	Transmittance	0.05-0.95	0.04	75.5-105.4	17.2-18	7.0 (constant)

Thermal properties of the cover shield

The thermal resistance associated with convection and conduction, which is offered by the transparent layer above the cooling surface, should be designed as high as possible to 1) reduce the convective and conductive heat transfer, and 2) to maintain the temperature of the cover shield above DPT.

In membrane-assisted RCS, thermal resistance is offered by the membrane and the air gap layer. The thermal resistance offered by the membrane is negligible compared to the thermal resistance offered by the air gap, due to the micro-size thickness of the membrane (N. Zhang et al., 2021). In other words, the impact of the thermal conductivity of the membrane on the cooling performance of CS-RCS is insignificant. Hence, the thickness of the air gap layer should be carefully designed to provide higher thermal resistance.

In the aerogel-assisted RCS, the aerogel works like an air gap layer in membrane-assisted RCS. It should be highly insulative to achieve the two targets mentioned above. Thermal resistance offered by the aerogel depends not only on thermal conductivity but also its thickness. However, an increase in aerogel layer thickness reduces the IR transmissivity. The thickness of the widely used aerogel material, i.e., PE aerogel, is limited, typically less than 8 mm for radiant/radiative cooling applications for adequate IR transparency (He et al., 2021). An increase in PE Aerogel thickness reduces the IR transmittance in the MIR region. The PE Aerogel thickness of less than 6 mm thickness has transmittance above 0.9, and it gradually decreases when its thickness increases further (A. Leroy et al., 2019). Hence, the tradeoff between the aerogel thickness and IR transmissivity must be taken care of.

Mechanical properties of cover shield

The mechanical strength of materials may need to be considered for cover shield selection in practical applications. The IRT membranes with high transmissivity would have poor

mechanical strength. Typically, the membrane thickness is in the order of microns to enhance its IR transparency, which also makes it vulnerable to damage and puncture. An increase in the thickness of the membrane reduces its transparency and in turn reduces the cooling performance of the radiant cooling system (Teitelbaum et al., 2020; J. Zhang et al., 2021). An increase in the thickness of the membrane from 0.05 to 3 mm, reduces the cooling capacity from 105.34 to 93.37 W/m², assuming constant membrane temperature (N. Zhang et al., 2021). The average transmissivity of the PE membrane reduces from 0.9 to 0.75 when its thickness increases from 10 to 100 μm (J. Zhang et al., 2021). Widely used LDPE membranes are known for being soft, flexible, lightweight, and having low toughness. LDPE films have a high chance of getting cracked and wrinkled easily (Xing et al., 2021). The practical application of using LDPE films for radiant cooling applications tends to fail shortly (Xing & Li, 2021; Xing et al., 2020; Xing et al., 2021). There are several studies related to the mechanical stability enhancement of membranes for radiative sky-cooling applications, such as corrugated structures (Nilsson, Eriksson, & Granqvist, 1985), PE meshes (Gentle, Dybdal, & Smith, 2013), windshields (Golaka & Exell, 2007), etc. These studies can be valid for membrane-assisted RCS applications, as their structure is similar to that of a sky radiative cooling system (Xing et al., 2020). However, all the methods to improve mechanical stability have their drawbacks which affect the cooling capacity of the radiant cooling systems. An experimental study on CS-RCS used wooden frames to hold the LDPE membrane (Guo et al., 2023). And the study suggested that the influence of the wooden frames could be ignored for the results. The cover shield used for outdoor radiant cooling applications should withstand the worst ambient conditions such as high wind, dust, rain, etc. Especially when it is easily accessible, it should have considerable mechanical strength to resist external forces. Hence, suitable materials with better mechanical strength with favorable optical properties need to be developed. As the properties of the cover shield, i.e., membrane or aerogel, for both radiant

and radiative cooling are similar, hopefully, appropriate material will be developed in the near future.

Availability of cover shield material

The non-selective membranes such as LDPE, and LLDPE, are commercially available as they are used for a wide range of applications. The application area of the PE membrane is limited to 0.06 to 0.08 m² (Gentle et al., 2013) due to its stiffness and structural strength. However, some experimental studies on the membrane-assisted radiant cooling system used the 2.52 m² (1.2 x 2.1 m) of LDPE membrane for a single (Teitelbaum et al., 2020; Teitelbaum, Chen, et al., 2019). The application area limitation is not considered in this study, it may have an issue in the long term.

Teitelbaum et al. (Teitelbaum, Rysanek, et al., 2019) used commercially available plastic materials which are transparent to the IR wave, i.e., HDPE trash bags, LDPE, and PP bottles. The transmissivity measured using Fourier-transform infrared spectroscopy (FTIR) analysis for HDPE (t:0.76 mm), LDPE (t:3.4 mm), and PP (t:0.05 mm) are 0.247, 0.298, and 0.587 respectively. Due to the higher transmittance of PP, it was concluded that suitable for radiant cooling applications, but the thicknesses of the membranes were different. However, in the later studies (Teitelbaum et al., 2020; Teitelbaum, Chen, et al., 2019), the LDPE (0.05 mm thickness) membrane was used rather than PP due to its excellent optical properties.

Zhang et al., (N. Zhang et al., 2021) developed a method for the selection of IRT membrane in CS-RCS. Two criteria for determining the availability of membrane materials were proposed, which include that the cooling capacity should be higher than the conventional radiant cooling system with a radiant panel temperature of 17°C, and the outer surface temperature of the membrane should be higher than 17°C. Among the investigated materials including polyethylene (PE), PE aerogel, KCl crystal, KBr crystal, and ZnSe crystal, polyethylene, all

materials satisfy both selection criteria. It was suggested that PE and PE aerogel could be better options when considering cost and stability. Xing et al., (Xing et al., 2020) provided a list of several available membranes and their optical properties, which can be suitable for CS-RCS. The list consists of several variants of PE, i.e., LDPE and HDPE, ethyl vinyl acetate (EVA), polyvinyl chloride (PVC), partially transparent polycarbonate (PCT), and PP.

Despite so many available membranes, most relevant studies chose LDPE membranes in their experiments due to their low cost, high availability, and high IR transparency. There are several materials commercially available at low costs, such as polyethylene terephthalate (PET) and polyolefin (POF), etc. (Abdel-Bary, 2003), though they were seldom considered for CS-RCS before.

As for aerogel-assisted RCS applications, there were two materials ever used, including PE foam and PE aerogel (Y. Liang et al., 2021). The PE aerogel provides better cooling performance compared to PE foam (Y. Liang et al., 2021). The PE aerogel is getting attention for daytime radiative cooling applications. Various derivatives of PE aerogel, such as zinc sulfide-pigmented PE aerogel (Arny Leroy, Bhatia, Njike, Vaartstra, & Wang, 2021), polydimethyl siloxane (PDMS) film laminated PE aerogel (M. Yang et al., 2020), and aerogel-functionalized thermoplastic polyurethane (AFTPU) (Shan et al., 2022) have been developed to improve the performance of radiative cooling devices. These Aerogel materials may be a potential choice for future CS-RCS applications. To realize that the cooling performance and the condensation risk of aerogel-assisted RCS need to be further analyzed.

More than cost and availability, favourable optical properties, mechanical strength, and application area need to be considered for cover shield selection. The selective cover shields which provide better cooling performance in radiant cooling applications are also used for daytime sky radiative cooling (Zizhong Li et al., 2020; J. Zhang et al., 2021), and cloth fabrics

for personal thermal management applications (Hsu et al., 2016; Shan et al., 2022). Hence, the development of an advanced cover shield with all favourable parameters is the need of the hour.

2.2.3 Critical Air Gap Thickness for Membrane-Assisted RCS

The heat transfer between the radiant cooling panel and membrane should be the lowest possible. The insulative nature of the air reduces the heat transfer between them. However, the lesser thickness restricts the air movement, hence the conduction heat transfer dominates over convective heat transfer. An increase in air gap thickness allows air movement due to the buoyancy effect. The air gap thickness at which maximum thermal resistance is nearly achieved is called critical air gap thickness. Beyond the critical air gap thickness, the influence of thermal resistance on membrane temperature is negligible.

The perception of critical air gap thickness is reviewed and reported by each researcher differently. The critical air gap thickness is at which the effect of radiant panel temperature on the membrane surface temperature became insignificant. Teitelbaum et al., (Teitelbaum, Rysanek, et al., 2019) reported the critical air gap thickness through experiments. It was reported that for the 99 mm of air gap thickness, the membrane surface temperature will be the same for all orientations of the radiant cooling panel. An increase in air gap thickness beyond this equilibrium point, i.e., 99 mm, does not influence the membrane temperature.

Xing et al., (Xing et al., 2020) obtained the critical air gap thickness through the membrane surface temperature calculation through the heat transfer model developed. It was found that the critical air gap thickness is 14 mm at which the natural convection dominates the heat transfer over conduction. The maximum membrane temperature achieved at the critical air gap thickness for the investigated radiant panel temperature is 22.5°C. Designing the air gap thickness beyond this critical limit will improve the anti-condensation. Panel depth causes pure

conduction to natural convection resulting in the highest membrane temperature when analyzing panel depth of 0-50 mm. This study failed to explain the membrane temperature when the pipe depth is above 50 mm (Figure 2.4). The researcher also suggested that a vacuum-filled gap between the panel and membrane will only allow the radiative heat transfer and it can maintain relatively lower air gap thickness. Even though the vacuum-filled air gap is the perfect insulator for convective heat transfer, it involves several issues when applied in practical applications.

Zhang et al. (N. Zhang et al., 2021) reported the critical air gap thickness through Raleigh Number. The theoretical analysis of the heat transfer coefficient will be minimal at the Raleigh Number for the air gap larger than 3.5×10^5 . The minimum heat transfer coefficient and its corresponding critical air gap thickness were calculated for the fixed panel temperature (0°C) and membrane temperature (18°C), i.e., $2.01 \text{ W/m}^2\text{K}$ and 55 mm (Figure 2.4).

Du et al. (Du et al., 2021) considered the air gap thickness of 10 mm for the analysis as the corresponding calculated thermal resistance of the air gap is attained maximum. This study failed to report the thermal resistance beyond 30 mm of air gap thickness and the temperature difference between the cooling panel and membrane assumed for the calculation is impractical. As the previous studies are reporting a critical air gap thickness of more than 50 mm, the range of air gap thickness analyzed could have been extended.

Gu et al. (Gu et al., 2023) analyzed the air gap thickness for the multilayer membrane-assisted RCS using CFD techniques. The air gap thickness at which the heat transfer transition occurs from conduction to natural convection provides the maximum thermal resistance. The simulation results concluded that the air gap thickness of 10 mm has negligible convective heat transfer in the air gap region. And it provides the optimal cooling capacity and higher air contact surface temperature. An increase in the number of layers with a critical air gap thickness

of 10 mm will not increase the convective heat transfer. Designing the air gap thickness around the critical range will enhance the air contact surface temperature for the multi-air-layer or membrane concept. However, it has a great risk of condensation for single and double-membrane-assisted RCS.

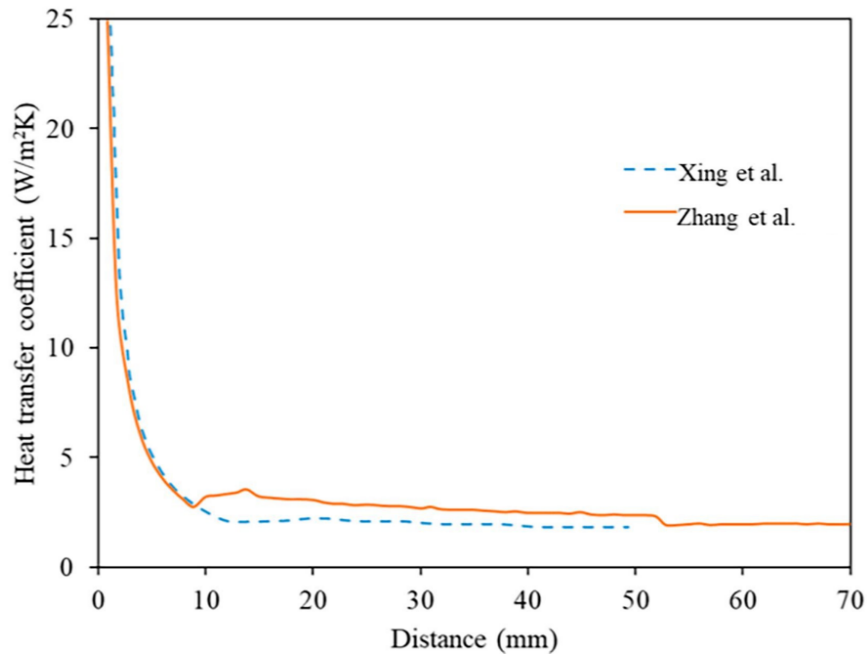


Figure 2.4 Variation of heat transfer coefficient with respect to air gap thickness (Xing et al., 2020; N. Zhang et al., 2021)

The air gap thickness is the function of radiant panel temperature, membrane surface temperature, and its orientation (Horizontal, vertical, and inclined). Hence, it should be analyzed for the range of possible radiant panel temperatures and membrane temperatures. The critical air gap thickness at the worst-case condition should be considered for the calculation. The first-ever full-scale membrane-assisted radiant cooling system was experimentally investigated, and the air gap thickness used is 152 mm (Teitelbaum, Chen, et al., 2019).

2.2.4 Heat Transfer Modelling

Theoretical analysis

The concept of CS-RCS evolved into different types depending on the cover shield material and the number of cover shields over the radiant panels. As per the panel design and its applications, the heat transfer methods and heat load components will vary. As the CS-RCS can be used for both indoor and outdoor applications, the heat transfer components will be slightly different. This is due to the various heat source exposures.

In indoor applications, the exposed heat loads are limited to occupants, indoor heat sources, and non-radiant surfaces. Hence, a non-selective cover shield, i.e., transparent for all thermal radiation channels, is suitable for this application. For outdoor applications, the MIR and sky window selective cover shields are preferred to eliminate the solar radiation falling on the cooling panel. The heat transfer components of both membrane and aerogel-assisted RCS are shown in Figure 2.5. The solar load component can be neglected for indoor applications.

In the membrane-assisted RCS, the components of convective heat transfer are due to the natural convection in the air gap region, external convection between the ambient and membrane surface, conduction across the membrane layer, solar radiation, and radiation from surrounding heat sources. The heat balance equation at steady state conditions for both indoor and outdoor applications of membrane-assisted radiant cooling systems is given below (Eqns. 2.1-2.3).

$$Q_{t, \text{indoor}} = Q_{r, \text{human}} + Q_{r, \text{surr.}} + Q_{c, \text{mi}} \quad [2.1]$$

$$Q_{t, \text{outdoor}} = Q_{r, \text{human}} + Q_{r, \text{atm}} + Q_{c, \text{mi}} + Q_{r, \text{sol}} \quad [2.2]$$

Where,

$$Q_{c, \text{mi}} = Q_{\text{cond, m}} = Q_{c, \text{me}} \quad [2.3]$$

Where, Q_t is total heat transfer, Q_r is the radiative heat transfer, Q_c is the convective heat transfer and Q_{cond} is the conductive heat transfer, and the subscripts hs is the heat sources, $surr$ is the surrounding indoor surfaces, mi is the membrane internal surface, me is the membrane exterior surface, sol is the solar radiation and atm is the atmospheric radiation. The atmosphere radiation ($Q_{r,atm}$) heat transfer involves radiation from the ground surface and surrounding buildings.

In an aerogel-assisted RCS, the conduction occurs across the aerogel layer, instead of natural convection in membrane-assisted RCS. Thus, in the heat transfer components for aerogel-assisted RCS, the conduction ($Q_{\text{cond-Aerogel}}$) component replaces internal natural convection ($Q_{c,mi}$). The heat transfer components of aerogel radiant cooling components are shown in Figure 2.5b. The heat balance equations at the steady state condition for the indoor and outdoor applications of aerogel radiant cooling systems (Y. Liang et al., 2021) can be expressed as,

$$Q_{t, \text{indoor}} = Q_{r, \text{human}} + Q_{\text{cond-Aerogel}} + Q_{c, \text{cse}} \quad [2.4]$$

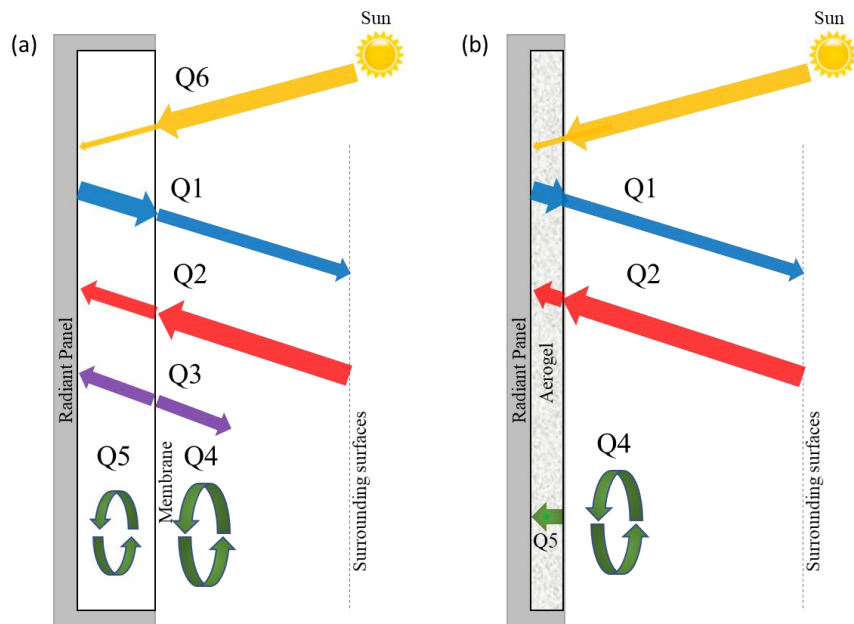
$$Q_{t, \text{outdoor}} = Q_{r, \text{hs}} + Q_{r, \text{atm}} + Q_{\text{cond-Aerogel}} + Q_{r, \text{sol}} \quad [2.5]$$

$$Q_{\text{cond-Aerogel}} = Q_{c, \text{cse}} \quad [2.6]$$

Where the $Q_{c, \text{cse}}$ represents the convective heat transfer on the cover shield surface.

Denon et al. (Sheppard, 2020) proposed the heat transfer model to determine the equilibrium membrane temperature. The model involves the heat balancing of individual convective and radiative terms (Eq. 2.1) which affects the membrane temperature. The membrane temperature obtained from the heat transfer model is validated against the data collected in cold tube experiments. The heat transfer model is integrated with TRNSYS, and it is used to analyze the CS-RCS coupled with natural ventilation. Various heat transfer models were developed for CS-RCS using different methods. The list of the heat transfer models developed, and the

corresponding cover shield configurations are shown in Table 2.5. Notable heat transfer models for the CS-RCS are discussed in this section.



- Q1: Radiation emitted by the chilled surface and absorbed by the membrane/aerogel
- Q2: Radiation emitted by the surrounding surfaces and absorbed by the membrane/aerogel
- Q3: Radiation emitted by the membrane
- Q4: External convection
- Q5: Membrane - Internal natural convection /Aerogel - Conduction
- Q6: Solar radiation (direct or diffused)

Figure 2.5 Heat transfer components of (a) membrane and (b) aerogel-assisted radiant cooling system (Sheppard, 2020)

Table 2.5 Details of heat transfer studies of CS-RCS

Author	Cover Shield	Model Type	Study Type	Environment
Single Membrane Layer				
Sheppard, 2020	membrane - LDPE	Energy modelling - TRNSYS	Energy saving	Semi outdoor
Xing et al., 2020	membrane	Thermal radiation model	Model development and parametric study	Indoor space

Author	Cover Shield	Model Type	Study Type	Environment
Teitelbaum et al., 2021	membrane -PE	Grasshopper+ Rhino 3D modelling environment	Model for cover shield MRT	Semi outdoor
Aviv et al., 2021	membrane	Energy Plus	Global analysis, energy saving, and thermal comfort	Indoor space
N. Zhang et al., 2021	membrane -PE	Thermal radiation model - Two heat flux model	Model development and parametric study	Indoor space
K. W. Chen et al., 2020	membrane -LDPE	Simple thermal model	Thermal comfort analysis	Indoor space
Mokhtari et al., 2022	membrane -PE	Grasshopper+ Rhino 3D modelling environment	Energy saving, and feasibility of outdoor application globally	Semi outdoor
Albuja et al., 2022	membrane	Energy Plus	Thermal comfort assessment	Indoor space- school building
Double Membrane Layer				
Du et al., 2021	membrane -LLDPE	Theoretical model - Double skin Membrane	Model development and parametric study	Indoor space
Du et al., 2022	membrane	Theoretical model - Double skin membrane	Improving cooling capacity and feasibility analysis for indoors	Indoor space
Multiple Membrane Layer				
Gu et al., 2023	membrane	CFD-Ansys FLUENT	Improving cooling capacity and	Indoor space

Author	Cover Shield	Model Type	Study Type	Environment
			reducing condensation risk	
Aerogel-Assisted RCS				
He et al., 2021	PE Aerogel	Heat transfer model	Energy Saving and feasibility analysis for indoor and outdoors	Indoor and outdoor space
Y. Liang et al., 2022	PE Aerogel	CFD-Ansys FLUENT	Cooling load characteristics	Indoor space
Y. Liang et al., 2021	PE Foam and PE Aerogel	CFD-Ansys FLUENT	CFD model development and thermal comfort analysis	Indoor space

Thermal radiation model

Xing et al., (Xing & Li, 2021; Xing et al., 2020) developed a thermal radiation model of membrane-assisted radiant cooling and extended the model for indoor space equipped with the membrane-assisted RCS (Figure 2.6). A thermal radiation model of an enclosed opaque space containing a transparent surface was developed (Dai, Xing, Fang, & Zhao, 2017). This model is extended for indoor space, containing one cooling opaque surface and other opaque indoor wall surfaces. The model is validated against the experimental data obtained by Wang (J. Wang, 2005). In Wang's experiment, the gap between the cooling/heating panels and the membrane is 8 mm. The heat transfer in the air gap region, for both the heating panel-membrane and radiant panel-membrane, is dominated by the conduction component. The validated model is used to analyze the anti-condensation performance of the membrane in an office building. To simplify the model, the indoor space is modelled with no door, window, and heat sources.

Also, the mean radiation temperature (MRT) method is proposed to simplify the model further (Xing & Li, 2021), as it is less than a 10% deviation from the current model.

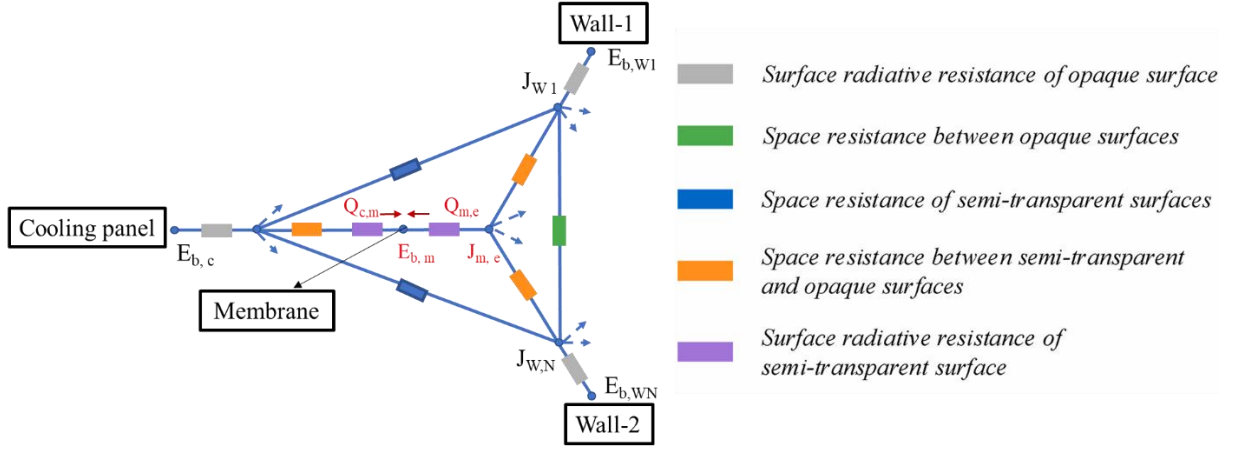


Figure 2.6 Thermal radiation heat transfer model of membrane-assisted RCS (Xing et al., 2021)

At steady state conditions,

$$Q_{r,c-m} + Q_{mi} + Q_{me} + Q_{r,m-i} = 0 \quad [2.7]$$

$$\frac{J_c - \sigma T_m^4}{R_{c,m} - R_m} + Nu \frac{kA_m}{L} (T_c - T_m) + 2.13A_m |T_a - T_m|^{0.31} (T_a - T_m) + \frac{J_{m,e} - \sigma T_m^4}{R_m} = 0 \quad [2.8]$$

The total cooling capacity (q_t) of the radiant cooling system can be calculated by,

$$q_t = \left| \frac{\sigma T_c^4 - J_c}{R_c A_m} - \frac{Q_{mi}}{A_m} \right| \quad [2.9]$$

Where, $Q_{r,c-m}$ is the radiative heat transfer between the cooling panel and membrane, Q_{mi} is the convective or conductive heat transfer inside the air gap, Q_{me} is the convective heat transfer between the membrane and the external environment, $Q_{r,m-i}$ is the radiative heat transfer between the membrane and indoor heat sources. R, T, and A represent the resistance, temperature, and surface area respectively. The subscripts c, m, and a represent the radiant

cooling surface, membrane, and indoor air respectively. J_c and $J_{m,e}$ are the radiosity of the cooling surface and the radiosity between the membrane and external environment respectively. Nu is the Nusselt number, k is the thermal conductivity of air, L is the air gap thickness and σ is the Stephen Boltzmann constant.

In the thermal radiation model, the thickness of the membrane is not considered, assuming that the surface temperature on both sides is equal. However, in the Teitelbaum et al., (Teitelbaum, Rysanek, et al., 2019) experiment, there was a difference in membrane surface temperature between the interior and exterior. The assumptions made for the thermal radiation model are only suitable for thin membranes. However, a new membrane may arise to address the mechanical strength issue with the larger thickness and improved IRT properties. In such cases, the proposed thermal radiation model needs to be modified. Depending upon the radiant panel orientation, the internal and external convection equations have to be modified.

Two-heat flux heat transfer model

Zhang et al. (N. Zhang et al., 2021) developed a two-heat flux model (Siegel, 1996; Siegel & Spuckler, 1996) for the membrane-assisted RCS which considered the conduction heat transfer across the membrane. The radiation heat transfer model which is coupled with the heat conduction inside the membrane is solved to get the temperature distribution of a membrane. In the two heat flux methods, the radiant heat flux is defined as q_r^+ (positive direction) and q_r^- (negative direction) with respect to the heat flow direction (Figure 2.7).

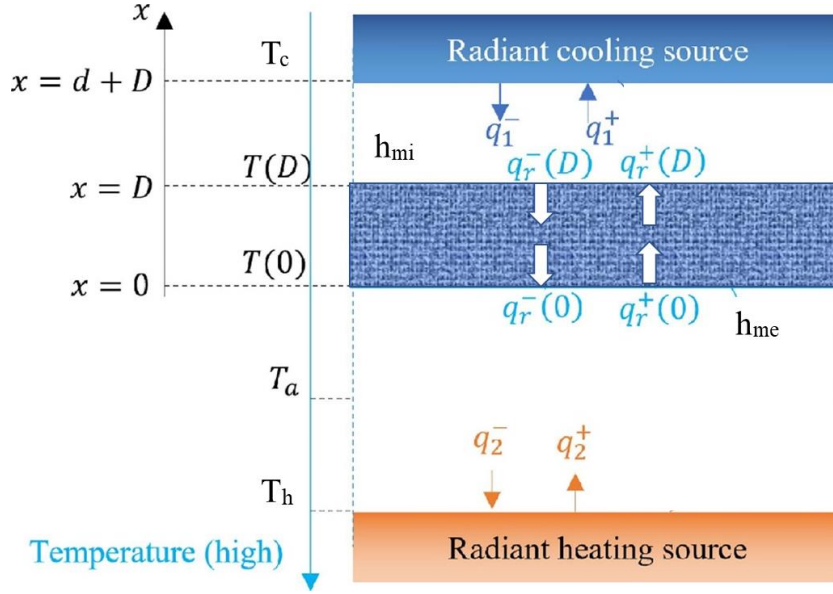


Figure 2.7 Heat transfer process considered for the two-heat flux model (N. Zhang et al., 2021)

The energy equation at the steady state condition is defined by Eq. 2.10, which considers the conduction and radiation of the membrane. The energy equations are reformulated in terms of the radiation heat flux (q_r) and quantity (G), which are defined with the two heat fluxes, i.e., q_r^+ and q_r^- .

$$q_t = -k \frac{dT(x)}{dx} + q_r(x) \quad [2.10]$$

$$\frac{dq_r(x)}{dx} = K(1 - \Omega)[4n^2\sigma T^4(x) - G(x)] \quad [2.11]$$

$$\frac{dG(x)}{dx} = -3Kq_r(x) \quad [2.12]$$

Where, q_t is total cooling capacity, q_r is the radiant heat flux, K is the extinction coefficient, Ω is the scattering albedo and n is the refractive index of the membrane layer.

The two-heat flux method transforms the energy equation into a single integration form.

Applying the boundary conditions, the energy equations transform into Eq. 2.13.

$$k \frac{d^2T(x)}{dx^2} = K(1 - \Omega)[4n^2\sigma T^4(x) + 3KkT(x) + 3Kq_t x - 3KC] \quad [2.13]$$

$$q_t = \frac{\{3Kk[T(0)-T(D)]+C_1-C_2+2D_1h_{me}[T_a-T(0)]+2D_2h_{mi}[T(D)-T_c]\}}{3KD} + 2D_2 + 2D_1 \quad [2.14]$$

Where, C, C1, C2, D1, and D2 are constants in terms of reflectivity, emissivity, and panel temperature, T(0) and T(D) represent the internal and external surface temperature of the membrane, and D is the thickness of the membrane, h_{me} and h_{mi} are the heat transfer coefficients at membrane external and internal surfaces respectively. Eqns. 2.13 and 2.14 represent the heat transfer model. They will be solved for the heat capacity and membrane surface temperature using the Runge-Kutta Method. The numerical model is validated against the experimental results obtained from a small-scale experiment. For the validation, the optical properties, i.e., extinction coefficient and scattering albedo, are referred from the literature. However, the result of the experiment has a good match with the model. As the heat transfer model considers the conduction within the membrane, it also can be used for thick membranes.

Double membrane-assisted RCS

Du et al., (Du et al., 2022; Du et al., 2021), establish a heat transfer model to evaluate the cooling capacity of radiant cooling assisted with two membranes, and the results are validated against a reduced-scale experimental setup. The membrane temperature is assumed to be the same throughout the membrane, as the membrane thicknesses are smaller than 2 μm . The heat transfer components are divided into convective and radiative terms. The radiative heat flux is calculated based on the thermal resistances and input parameters. The radiative heat transfer process of the double skin membrane-assisted RCS is shown in Figure 2.8. The air contact surface temperature of membrane-2 is predicted from the radiative heat flux calculation directly. Then it is used to calculate the convective heat flux in the air gap region using a

conventional way of heat flux calculation where the heat transfer coefficient is found by Nusselt number calculation.

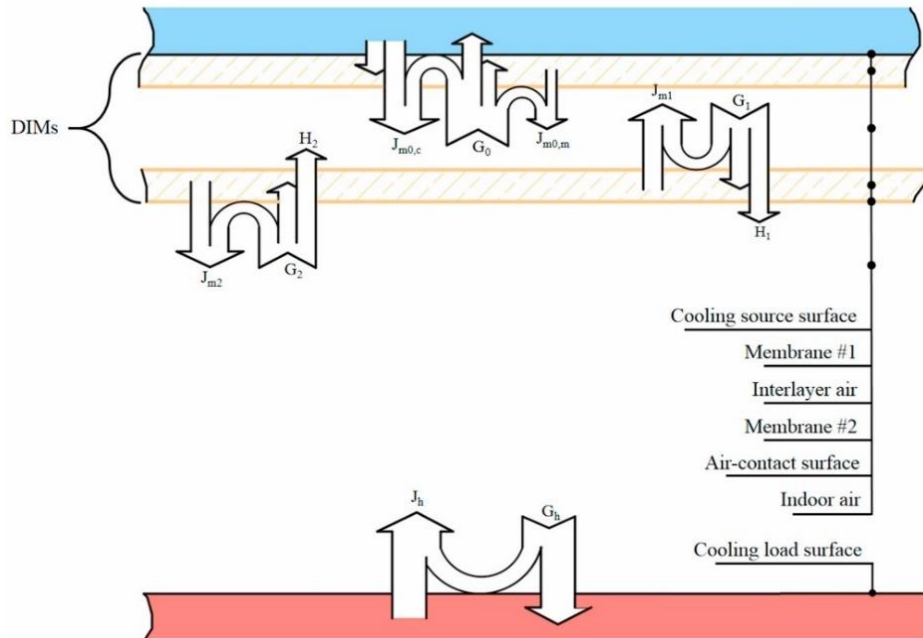


Figure 2.8 Radiative heat transfer for double skin membrane-assisted RCS (Du et al., 2021)

The radiant heat flux on the lower surface of membrane-1 (q_{r1}) and through the membrane-2 (q_{r2}) are calculated using the Eqns. 2.15 and 2.16 respectively.

$$q_{r1} = \frac{J_{m0} - E_{bc}}{R_{s,m-c}} \quad [2.15]$$

$$q_{r2} = \frac{J_h - J_{m0}}{R_t} \quad [2.16]$$

Net radiation between the cooling panel and heating panel (q_r) is

$$q_r = \frac{E_{bh} - E_{bc}}{R_{s,m-c} + R_t + R_{s,h}} \quad [2.17]$$

Where, E_b is the blackbody emissive power, G is the incident radiant flux onto a surface, H is the incident radiant flux across a membrane, J is the outgoing radiant heat flux, and R is the

resistance. The subscripts h is the heating panel surface, c is the radiant cooling surface, m is the membrane surface, and t is the total.

The membrane temperature (T_m) can be calculated by the following equations.

$$E_{bm} = J_{m0} + \frac{qr\epsilon(R_{s,m} + R_{g,c-m})}{1-\tau_m} \quad [2.18]$$

$$T_m = \sqrt[4]{\frac{E_{bm}}{\sigma}} - 273.15 \quad [2.19]$$

Where, τ transmittance, the subscripts g is geometrical resistance based on the view factor between the surfaces, s is the surface radiant resistance and $r\epsilon$ is the radiant energy resulting from emissivity.

The radiative heat transfer is not a function of ambient air temperature and air properties. In this case, the membrane temperature obtained only through radiative heat flux calculation may lead to an inaccurate prediction of membrane temperature. Zhang et al. (N. Zhang et al., 2021) reported that the external heat transfer coefficient has a significant impact on the membrane temperature and cooling capacity of the system. Du et al., (Du et al., 2022; Du et al., 2021) have not provided a clear explanation of the convective heat flux observed from the surroundings which is also one of the vital parameters to predict the membrane surface temperature.

2.2.5 CFD Simulations

Compared with general heat transfer models, CFD techniques can provide more details on the air flow and heat transfer, such as detailed air flow in the air gap layer of the membrane-assisted RCS (Teitelbaum et al., 2021). Liang et al., (Y. Liang et al., 2021; Y. Liang et al., 2022) developed models for coupling CFD and radiation heat transfer simulation for indoor

application of CS-RCS, indicating the detailed air flow and temperature distribution in indoor spaces. Further, the manikin was sometimes included in the CFD model to simulate the thermal comfort of indoor environments applied with CS-RCS (Y. Liang et al., 2021). As the radiation across the semi-transparent medium is involved in the CS-RCS, the discrete ordinates (DO) radiation model provides better accuracy in solving intricate optical problems.

Teitelbaum (Teitelbaum et al., 2021) simulated the air temperature stratification in the air layer. The membrane-assisted radiant panel (1.2 x 0.25 x 2.5 m) in a vertical orientation was simulated in the Rhino-CFD plugin into the Rhino 3D modelling software. The constant temperature boundary condition is provided in all walls (membrane, radiant panel, and surrounding frames). Radiative heat transfer is neglected in this study as it focuses only the air stratification. The air in the enclosed air gap is considered with the atmospheric pressure. Chen-Kim k- ϵ turbulence model has been used, which is a sub-variant of the standard k- ϵ model, and the standard wall function is adopted for near-wall treatment. In this study, the CFD simulation is supporting evidence to find the pattern of MRT based on the view factor, to predict the condensation using simulation techniques. And the author concluded that the combined results of MRT prediction and cold air stratification prediction helped to identify the condensation pattern, however, the combined effect is yet to be analyzed.

Multiple membrane-assisted RCS

The heat transfer from the radiant panel to the surroundings through the multiple layers of the air gap and membrane will be different from the single-layer membrane. Gu et al., (Gu et al., 2023), developed a 2D steady-state CFD model of the CS-RCS with various layers of the membrane using Ansys Fluent. The uniform surface temperature has been provided as the boundary conditions for the radiant panel and heating panel surface, and the remaining surfaces are considered to be adiabatic. The laminar flow and discrete ordinates model were used for

the flow and radiation modelling. The Discrete Ordinates (DO) is the only radiation model used to solve the radiation across the semi-transparent medium, i.e., membrane. The radiative transfer equation (RTE) for solving the radiative heat transfer through the membrane layers is shown in Eq. 2.20, The simulation results of single and double membrane layer CS-RCS are validated with the experimental results. The validated model is extended for multilayer membrane layer CS_RCS and is used to analyze the air gap thickness, cooling capacity, and temperature distribution of air contact surface temperature.

$$\frac{dI(\vec{r},\vec{s})}{ds} + (a + \sigma_s)I(\vec{r},\vec{s}) = \frac{an^2\sigma T^4}{\pi} + \frac{\sigma_s}{4\pi} \int_0^4 I(\vec{r},\vec{s}')\Phi(\vec{s} \cdot \vec{s}')d\Omega' \quad [2.20]$$

Where I is the radiation intensity, a is the absorption coefficient, σ_s is the scattering coefficient, σ is the Stephen Boltzmann constant and T is the temperature. The vectors \vec{r} , \vec{s} and \vec{s}' are the position, direction, and scattering direction vectors respectively. Φ and Ω' represent phase function and solid angle respectively.

Aerogel-assisted RCS

Liang et al., (Y. Liang et al., 2021; Y. Liang et al., 2022) developed a 3D steady-state model of aerogel-assisted radiant cooling using a commercial CFD tool, i.e., ANSYS Fluent. The heat transfer process in the aerogel-assisted radiant cooling system and the radiative heat transfer across the aerogel layer are shown in Figure 2.9. The DO radiation model is used for the analysis as it is suitable to solve the energy equation across the semitransparent aerogel layer. Realizable k- ϵ with enhanced wall function treatment is considered for the turbulence model. A simple enclosed CFD model (200 x 200 x 50 mm) consisting of a PE foam-covered cooling panel and heating panel has been validated against the experimental results. The model was extended to study the thermal comfort of indoor space with PE aerogel-assisted ceiling radiant cooling. The computation domain of indoor space consists of the numerical thermal manikin

in a sitting position, with the provision of a fresh air inlet and outlet. No doors and windows were considered for the simplification of the model.

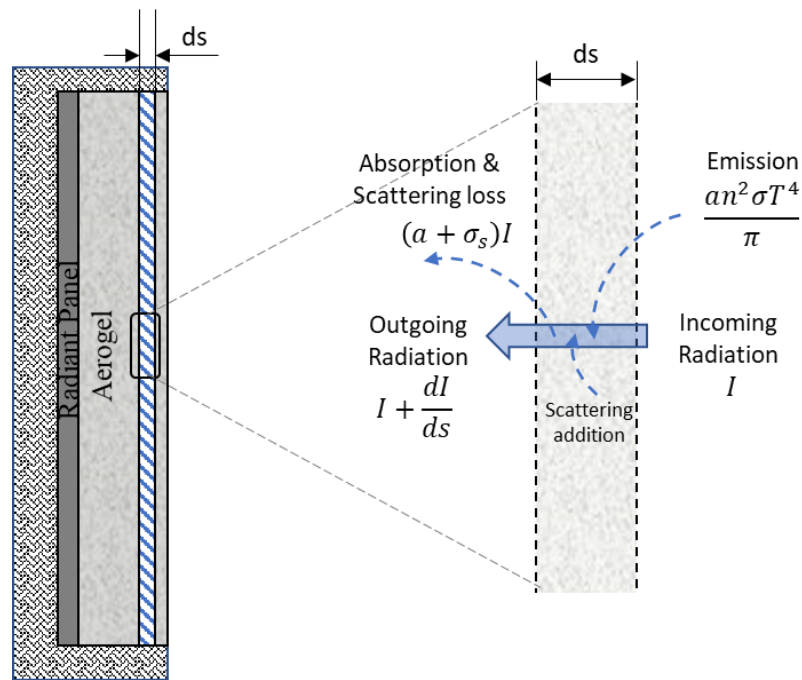


Figure 2.9 Radiative heat transfer process in aerogel layer in the aerogel-assisted radiant panel (Y. Liang et al., 2021; Y. Liang et al., 2022)

2.2.6 Thermal Comfort and Energy

Thermal comfort

The CS-RCS can provide a lower MRT compared with conventional radiant cooling systems for indoor spaces, as the surface temperature can be controlled lower but without condensation concern. In this way, an acceptable thermal comfort level can be achieved in environments with higher air temperatures. It was indicated by a subject thermal comfort survey in Singapore (Teitelbaum et al., 2020) that 80% of the 37 participants felt satisfied in an enclosed pavilion with a mean radiant temperature between 22°C and 24°C, air temperature between 28°C and 32°C, and humidity between 60% and 80%. The pavilion was constructed by using several membrane-assisted radiant cooling wall panels, and chilled water with a temperature between

10°C and 15°C was supplied to the panels to maintain MRT. No condensation was observed on the radiant panel surfaces.

This means more degrees of freedom for comfort design in buildings can be achieved by applying CS-RCS to provide more flexible combinations of air temperature, MRT, and air velocity (Teitelbaum, 2019). Teitelbaum et al., (Teitelbaum et al., 2019) developed a comfort design tool by solving the objective function of human body heat losses and metabolic rates. The thermal comfort zone was derived and plotted in a psychrometric chart by matching MRT, air temperature, humidity, air speed, metabolic rate, and skin wettedness to achieve the heat balance between body heat loss and metabolic rates. According to the study, even when the air temperature went up to 35°C, thermal comfort could be achieved when MRT was kept close to 5°C. In another study (Y. Liang et al., 2021), it was found that when the area ratio of CS-RCS was shrunk to 60% of the total ceiling area, the level of Predicted Mean Vote (PMV) and Predicted Percentage Dissatisfied (PPD) needed to meet the requirement of the ASHRAE 55 standard (ANSI/ASHRAE, 2013) could still be maintained. The panel surface temperature was controlled at 9.7°C, almost 8°C lower than the DPT of supply air. Another study (Mokhtari et al., 2022) on the semi-enclosed bus shelters equipped with the CS-RCS was reported to have the potential to reduce the Universal Thermal Comfort Index (UTCI) by 10°C, and MRT to 15°C. The system performed better in hot arid climates. Albuja et al., (Albuja et al., 2022) modelled a school building with CS-RCS located in a hot and humid climate, using Energy Plus software. It was found that the CS-RCS was capable of reducing the annual discomfort hours by 3-6%, compared to that of conventional radiant cooling systems.

An increase in air velocity improves the convective heat transfer of occupants, thereby improving thermal comfort. Mechanical fans can be combined with CS-RCS to increase air velocity in a semi-open environment (Aviv et al., 2021). It was proposed to retrofit naturally ventilated classrooms in Singapore with the decentralized membrane-assisted RCS and ceiling

fans, as it was believed to be a viable option (K. W. Chen et al., 2020; Wong & Khoo, 2003). It was reported that 80% comfort acceptability was achieved compared to conventional air conditioning systems. However, the maximum indoor air velocity was limited to 0.9 m/s (Gong et al., 2006).

The lack of thermal comfort data on the CS-RCS, despite the subject survey in Singapore (Teitelbaum et al., 2020), has hindered an understanding of the potential of CS-RCS to achieve thermally comfortable environments. The potential local discomfort can be caused by radiant asymmetry. As per the ASHRAE handbook – fundamentals (2017), occupants are more sensitive to the asymmetry caused by a cold wall, and higher radiant asymmetry leads to less thermal comfort while a cold ceiling has less impact on comfort. Fanger et al., (P. O. Fanger et al., 1985) reported that the radiant asymmetry has an insignificant impact on the operative temperature experienced by the occupants and suggested allowable radiant asymmetry of 14 and 10°C for the cold ceiling and wall respectively. Hence, it is important while designing the CS-RCS for the indoor space, as it has to deal with low temperatures. The potential application of the CS-RCS in an open outdoor environment and for various climatic conditions is yet to be analyzed. The thermal comfort in complex outdoor environments with unpredictable wind conditions, and shortwave and longwave radiation has not been investigated so far.

Cooling capacity

The cooling capacity of the CS-RCS can be improved compared to the conventional radiant cooling system. Since the air gap reduces the condensation risk on the radiant panel, the lowest radiant panel temperature can be further reduced to enhance the radiation loss of occupants. In typical ambient air conditions of 26°C, 60% RH, and DPT of 17.5°C, the maximum cooling capacity achieved by the conventional radiant cooling system was 70.3 W/m² as the radiant

panel temperature, i.e., 17.5°C, is limited to prevent condensation (Du et al., 2021). Similarly, the membrane temperature of CS-RCS is limited to the DPT of the ambient air.

The lowest possible radiant panel temperature to maintain the membrane temperature above DPT is 7°C and its corresponding cooling capacity of CS-RCS was reported to be 105.8 W/m² (N. Zhang et al., 2021). Xing et al., (Xing et al., 2020) reported a cooling capacity of 103.2 W/m² for the same radiant cooling temperature, i.e., 7°C. The double membrane-assisted RCS reported a maximum cooling capacity of 104 W/m² for the same radiant panel temperature (Du et al., 2021). On the other hand, another experimental study on the same reported a cooling capacity of 105.5 W/m² for the radiant surface temperature of 8°C (Guo et al., 2023). The cooling capacity reported by different studies for the same membrane configurations and radiant panel temperature will vary depending on the ambient conditions, membrane properties, and radiant panel emissivity. The cooling capacity of the membrane-assisted RCS was noted to be improved by 24.4 to 50.5% compared to the conventional radiant cooling system. It was reported that the aerogel-assisted RCS (Y. Liang et al., 2021) had a maximum cooling capacity of 162.3 W/m² at 4°C of panel temperature when PE aerogel was used. It improved significantly by 130% when compared to the conventional radiant cooling system, without visible condensation on the aerogel surface.

Figure 2.10 shows the comparison of cooling capacity between the various cover shield configurations of CS-RCS found in the literature (Du et al., 2021; Gu et al., 2023; Guo et al., 2023; Y. Liang et al., 2021; N. Zhang et al., 2021). The heating load configurations for the studies carried out by Liang et al. (Y. Liang et al., 2021), Zhang et al. (N. Zhang et al., 2021) and Gu et al. (Gu et al., 2023) were the same, i.e., the heating panel was maintained at 32°C. Hence, the comparison between these three studies will provide valid findings. Due to the insufficient data availability, the cooling capacity of the PE aerogel configuration was plotted only for the radiant panel temperature of 4°C, where the PE aerogel maintained the air contact

surface temperature of 17°C. The PE aerogel cover shield configuration provided the maximum cooling capacity, i.e., 162.3 W/m², compared to the single and double membrane configurations, without any condensation issues. For the double membrane configurations studies carried out by Du et al. (Du et al., 2021) and Guo et al. (Guo et al., 2023), different heat load configurations were adopted. An increase in the number of membrane layers with an air gap between them helps to reduce the radiant panel temperature, for the constant outer membrane temperature, i.e., above DPT. An increase in membrane layers from single to four increases the cooling capacity from 134.72 W/m² to 200.19 W/m², for the corresponding reduction of cooling temperature from 5 to -21°C (Gu et al., 2023). It was concluded that an increase in the membrane layers beyond two layers had less impact on the cooling capacity. Hence, a maximum of two layers of the membrane was recommended to obtain an optimal cooling capacity of 169.42 W/m² for the radiant panel temperature of -5°C.

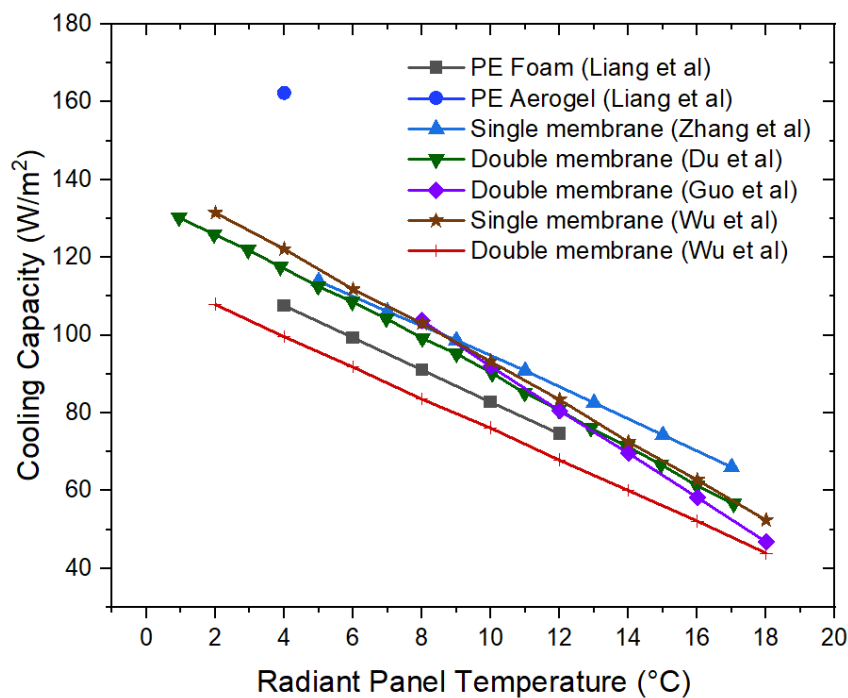


Figure 2.10 Comparison of cooling capacity between the various cover shield configurations of CS-RCS (Du et al., 2021; Gu et al., 2023; Guo et al., 2023; Y. Liang et al., 2021; N. Zhang et al., 2021)

In the experiment performed in a semi-outdoor environment (Teitelbaum et al., 2020), the heat flux between the human body and the ambient environment and CS-RCS was measured by heat flux sensors installed on the occupant's wrist. The occupant was standing at a distance of 0.8 m from the panel. The heat flux was 89.8, 131, and 156.8 W/m² for the supply water temperatures of 26, 17, and 13°C, respectively. The ratio of radiative to the net heat exchange increases as the decrease in cooling water temperature.

Other than the impact of the cover shield and air gap design, there are several ambient parameters, such as air temperature, velocity, solar radiation, and humidity, that have a significant influence on the cooling capacity. The airflow affects the convective heat transfer coefficient of air contact membrane surfaces. Airflow can be induced either by fans or by natural ventilation. An increase in external heat transfer coefficient from 1 to 9 W/m²K had the potential to reduce the radiant cooling panel temperature from 9.8 to -6°C, assuming constant external surface temperature. Consequently, it could improve the cooling capacity from 61.49 to 135.14 W/m² as the panel surface temperature was lower (N. Zhang et al., 2021). The relative humidity of the ambient air greatly impacts the cooling capacity, as it is responsible for condensation. The cooling capacity was reduced from 104 to 38 W/m² when the ambient RH increased from 65 to 90% (Xing et al., 2020).

Energy saving

Compared to the conventional radiant cooling system, the cooling water temperature can be reduced further in the CS-RCS with less condensation concern. The heat transfer through thermal radiation can be improved by radiant surfaces with lower temperatures. Although reducing the cooling water temperature will reduce the coefficient of performance of the chiller plant, CS-RCS provides a possibility to couple with natural ventilation. This reduces the requirement of low-temperature air supply in the ventilation system and hence energy saving

can be potentially achieved. CS-RCS can be coupled with passive energy sources, such as radiative sky cooling, solar photovoltaic (PV), and geothermal cooling.

Passive cooling sources such as earth tunnel cooling, nocturnal cooling, evaporative cooling, and geothermal cooling, can be integrated along with the conventional radiant cooling system. In addition to the cooling sources, cooling energy storage methods such as phase change material (PCM)-assisted radiant cooling panels, and PCM storage tanks are also gaining the attention of the research community (L. Liu, Zhang, Liang, Niu, & Wu, 2022). Recent studies have quantified the thermal performance of CS-RCS which is integrated with passive energy sources, such as solar PV panels and sky radiative cooling, and passive energy storage concepts using PCM.

Riffat et al. (Riffat et al., 2022) proposed the incorporation of the PCM with the membrane-assisted radiant cooling panel to store the excessive cooling energy, to be utilized during the needy time. The power required to run the water chiller was harvested from the solar PV panel. A small-scale experiment was performed to analyze the performance of the RCS with or without PCM. The results revealed that the PCM-based membrane-assisted RCS could sustain the panel at a temperature of 2-2.5°C lower than that without a PCM, for up to 4.5 hours after switching off the system. The study reported that the panel temperature was maintained at 11°C without any visible condensation on panel surfaces.

Mokhtari et al. (Mokhtari et al., 2022) studied the membrane-assisted RCS for cooling bus stops in Tehran, Iran; the cooling water required for the radiant panel was produced from sky radiative cooling application. A simulation-based study analyzed the feasibility of the proposed passive cooling structure to provide thermal comfort in an outdoor environment. The shape of the bus stop was optimized by analyzing its maximum view factor between the occupants and the radiant surfaces and outdoor surfaces. The bus stop orientation was also optimized to reduce

the solar heat gain. The obtained results showed that the UTCI by 10%. The proposed design maintained the MRT at 15°C during the end of July, whereas it was 40°C at a typical bus stop. The study location was extended to analyze its feasibility for various climatic zones during summertime. It revealed that the proposed system had significant potential to perform in hot and arid climates, with significant energy saving. Mokhtari et al. (Mokhtari & Ghasempour, 2023) also examined the feasibility of the proposed integration for single-family households using numerical modelling. The results revealed that the proposed integration could provide comfortable conditions for 99% of the hours in summer.

2.2.7 Discussions

System design

In general, the RCS is mostly used for indoor applications. However, the impact on the cover shield in indoor applications needs to be taken care of, as it is vulnerable to physical damage and tears easily. Hence, ceiling installation is a practical and viable option, as it is not accessible by the occupants. It cannot be used for floor cooling applications as the membrane or aerogel on the radiant surface gets damaged when people walk over it. For indoor applications, the membrane-assisted RCS performs better regardless of climatic conditions.

In outdoor applications, the parameters impacting the CS-RCS are quite high, particularly the membranes. Membrane-assisted radiant panel predominantly provides transfer of the cooling energy to the occupants through radiative heat transfer. It is always beneficial for the radiant panels to have high view factors for the occupants and radiant and non-radiant surfaces (Houchois, Teitelbaum, Chen, Rucewicz, & Meggers, 2019; Teitelbaum et al., 2021). In the outdoor application, the radiation from the human, ground, adjacent buildings, and direct solar radiation needs to be handled by the RCS if the structures are not properly designed. Hence, the structure of the outdoor system should be designed such that the view factor of the radiant

panel should focus dominate the occupants rather than the outside, i.e., ground, buildings, etc. (Mokhtari et al., 2022). Some studies proposed maintaining a vacuum in the air gap layer (Z. Chen, Zhu, Raman, & Fan, 2016). However, it involves several practical issues and may require a rigid membrane.

As of now, selective membranes and aerogels are fabricated mostly only for lab-scale studies. There are certain issues in fabricating the selective cover shield in large sizes and it is expensive. The thin membranes tend to damage easily. Hence, a material with improved mechanical strength and without compromising IR transparency is the need of the hour.

2.3 Condensation Issues

Condensation is one of the major limitations of the conventional radiant cooling system, especially in hot and humid climates. Several methods and control strategies have been proposed to control the condensation risk on panel surfaces (Xing et al., 2021). Integrating dehumidification systems and dedicated outdoor air systems (DOAS) are commonly used technologies to avoid condensation problems. There are several strategies proposed in the literature such as ventilation management, cooling water temperature adjustment, and humidity control techniques, to avoid condensation issues (Xing et al., 2021). Recent studies suggested coating the radiant panel surface with a hydrophobic or superhydrophobic material (Su et al., 2019; Tang, Liu, Li, Zhou, & Jiang, 2016; Zhong, Ma, Yao, Xu, & Niu, 2022). Another concept is to cover the radiant cooling panel with another metal panel as a radiant shield (Ning et al., 2016; Xing & Li, 2021). There are certain drawbacks to each method such as high initial cost, energy cost, inefficient cooling, etc. Furthermore, these proposed methods are inefficient for outdoor cooling applications.

The CS-RCS is one of the feasible options to eliminate condensation risk with enhanced cooling capacity. The air contact surface temperature of the cover shield is the indicator for condensation, and it should be maintained above DPT. The heat transfer equilibrium between the radiant panel and the ambient air will result in the cover shield surface temperature. The external heat transfer coefficient and internal thermal conductance are important influencing parameters for the cover shield surface temperature. A higher external heat transfer coefficient and internal thermal resistance will be favorable for the cooling system to keep the cover shield temperature higher. Designing the air gap thickness by considering the critical thickness (Xing et al., 2020; N. Zhang et al., 2021) and highly insulative aerogel helps to enhance the internal thermal resistance. The heat transfer coefficient on the air contact surface of the cover shield can be improved by enhancing the contact air velocity in indoor applications. The wind velocity serves this purpose in outdoor applications; however, a part of the cooling energy from the cooling source will be carried away by the wind.

In practical systems, the lowest applicable panel surface temperature of CS-RCS should be carefully selected to prevent condensation on both the panel surface and the air contact surface of the cover shield. This would be affected by many factors, like the moisture content in the air layer and the thermal resistance of the transparent layer covering the panel. The moisture content of the air layer is highly dependent on the sealing between the cover shield and panel frame, the water vapour transmission rate of the cover shield, and the quantity of desiccant in the air layer. The relation between the temperatures of the water, ambient air, and dew point was investigated in an experimental study (Teitelbaum et al., 2019). In the experiment, chilled water, ambient air, membrane, and dew point temperatures were recorded when signs of condensation were observed. A correlation was proposed to identify the appropriate supply water temperature to eliminate condensation. This correlation was application-specific.

$$T_{DPT} - T_{water} = 2.0 (T_{air} - T_{DPT}) \quad [2.21]$$

Teitelbaum et al., (Teitelbaum et al., 2021) reported that membrane condensation was a function of heat transfer equilibrium between the cold air stratification in the air gap region and the view factor to the hot external environment. The view factor changed across the membrane surface due to the difference in heat transfer and the cold air present in the air gap accumulated at the bottom side of the cooling unit. Consequently, the condensation formed only on certain portions of the bottom side of the membrane surface. Combining the CFD simulation of cold air stratification in the air gap region and the MRT prediction could help to forecast the condensation pattern.

The DPT of the ambient air has a significant impact on the radiant panel temperature and its cooling capacity. An increase in relative humidity increases the DPT of the ambient air. Hence, the cooling capacity of the radiant panel is limited to the humidity level of atmospheric air, to avoid condensation on the membrane surface. The cover shield-assisted radiant panel temperature can be reduced up to 7°C, 14.4°C, and 19.3°C without condensation, for the atmospheric humidity conditions of 65%, 80%, and 90%, respectively (N. Zhang et al., 2021). An experimental study on the double-layer CS-RCS recommended the maintenance of the cooling water temperature at 8°C and above for safe operation without condensation problems (Guo et al., 2023).

2.4 Outdoor Applications

The outdoor environmental conditions have an adverse impact on the cover shield and the overall cooling performance of the system. For outdoor applications where the radiant panels expose to solar radiation, non-selective membranes are not recommendable, as the panel starts to absorb the solar heat instead of transferring cooling energy to the occupants. The plastic film

allows the water vapour to transmit through it at a certain temperature (Coles, McDowell, & Kirwan, 2003). High ambient humidity speeds up the water vapour transmission towards the dry air in the air gap region. Hence, it is recommended that solid desiccants, i.e., silica gel, be used in the air gap region, to maintain the dry air. Some silica gels change colour when they get saturated by adsorbing water vapour (Du et al., 2021; Teitelbaum et al., 2020). This is a visible indicator to replace or regenerate the silica gel by heating (Du et al., 2021).

The stiffness, durability, lifetime, and degradation of optical properties of the cover shield need to be considered especially when it is exposed to sunlight. Mostly, the optical properties of polymers tend to deteriorate when they are exposed to solar radiation (Balocco, Mercatelli, Azzali, Meucci, & Grazzini, 2018; Coles et al., 2003). The ageing of PE film was reported to downgrade the transmissivity, i.e., 72% (0th day) to 42% (100th day) (Ali, Saito, Taha, Kishinami, & Ismail, 1998). The membrane exposed to the outdoor ambience tends to be affected by dust in the air. The deposition of dust particles on the membrane surface impacts the transmissivity of the membrane (Pieters & Deltour, 1997). Dew formation on the membrane surface also affects the transmissivity of the membrane. Condensation was observed to deteriorate the transmissivity of the PE membrane by 9-19% (Pieters & Deltour, 1997; Pollet & Pieters, 2000). This issue could be addressed by designing the air gap thickness beyond the critical thickness. Studies on the impact of exposure to sea breeze on the cover shield materials are not found in the literature, this aspect should be duly considered when the study location is located in proximity to the sea.

2.5 Urban Outdoor Environment Modelling

CFD is the most recognized tool for urban environment modelling and is used for a wide range of studies related to thermal comfort analysis. The computational model of the outdoor environment involves different scales such as meso, local, and micro scales for urban modelling

(Potsis, Tominaga, & Stathopoulos, 2023). The mesoscale encompasses the entirety of the metropolitan city, whereas the local scale pertains to the neighbourhood, and the microscale encompasses individual elements such as buildings, roads, and trees. Microscale modelling is suitable to analyse the pedestrian level thermal comfort. Several environmental factors need to be considered for the modelling, such as solar radiation, longwave radiation from surroundings, wind velocity and ambient temperature. The parameters needed to be considered for the modelling are shown in Figure 2.11. The influencing factors affecting the prediction accuracy can be identified by comparing the wind tunnel experiments, and field measurements with the CFD simulation results. For the wind environment modelling, Reynolds Averaged Navier Stokes (RANS) equations models, and Large Eddy Simulation (LES) are widely used. The turbulence model plays an important role in outdoor wind flow modelling as it has a significant influence on the numerical results. For instance, Liu et al., (J. Liu & Niu, 2016), reported that LES and Detached Eddy Simulation (DES) models predict the wind flow around an isolated building with a better match with the experiment results, compared to Steady Reynolds Averaged Navier-Stokes (SRANS) and RNG k- ϵ models. However, LES and DES provide more accurate results, but their computational cost is higher.

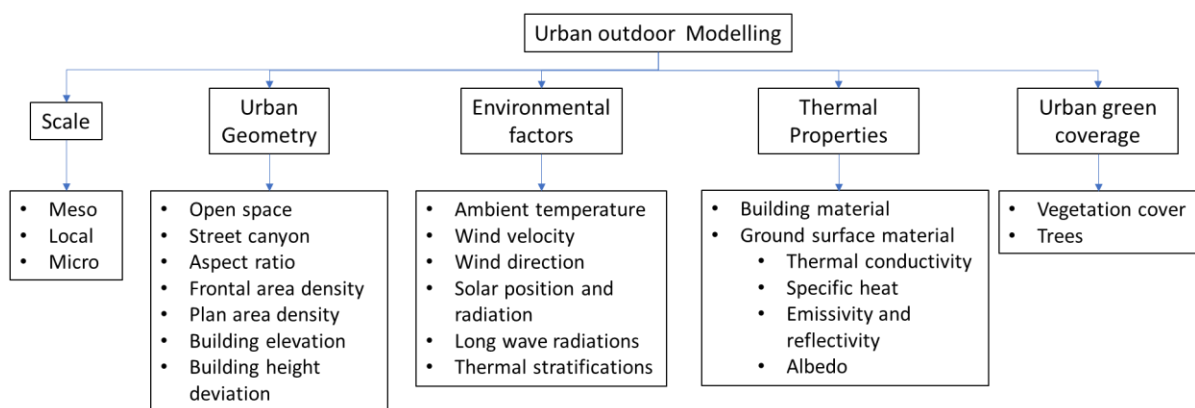


Figure 2.11 Parameters considered for the urban modelling

There are some guidelines for the CFD techniques to assess the wind environment at the pedestrian level. They are proposed by the European Cooperation in the Field of Scientific and Technical Research (COST) and the Architectural Institute of Japan (AIJ) (Tominaga et al., 2008). AIJ guidelines are based on the CFD simulation performed for seven different cases, i.e., square building, rectangular building, simple city blocks, high-rise buildings in a city, simple building shapes in actual urban areas, complex building shapes in actual urban areas and 2D pine trees. To assess thermal sensation in a specific zone, it is essential to capture the environmental conditions at the pedestrian level. A microscale approach is adequate for simulating these conditions effectively.

2.6 Heat Loss from Human Body in Outdoors

The Computational Thermal Manikin (CTM) is utilized primarily to calculate the convective (h_c) and radiative (h_r) heat transfer coefficients for localised body segments. To determine these coefficients accurately, one should consider the micro-environmental conditions, as previously described, as well as the human body's geometry. While traditional thermal manikin studies have provided empirical data for local h_c and h_r values (de Dear, Arens, Hui, & Oguro, 1997; Ichihara, Saitou, Nishimura, & Tanabe, 1997), these experiments are often prohibitively expensive and time-consuming. Moreover, it is impractical to conduct such experiments for every possible scenario. Therefore, the CTM emerges as a valuable tool, offering a more efficient alternative for assessing thermal exchanges in various contexts.

The numerical modelling based on human physiological responses and thermal sensation assessment will reduce the cost and time associated with the human trial studies considering several ambient and human factors. Considering the complexity of the human body shape, there were several simplified shapes to represent the human subject as a heat source reported in previous studies (Joshi, Wang, Kang, Yang, & Zhao, 2022). However, the shapes of each local

body part to evaluate the local heat transfer are important as it has a significant impact on human physiological responses (Kilic & Sevilgen, 2008; Xu, Psikuta, Li, Annaheim, & Rossi, 2019). Hence, CTM to represent the human subject needs to be included in the numerical model.

There were several wind tunnel experiments reported in the literature to analyse the convective heat flux from each local body part of thermal manikin for different wind conditions (S. Gao, Ooka, & Oh, 2019; Ichihara et al., 1997). The factors that affect the convective heat transfer coefficient (CHTC) of humans in the outdoor environment are wind parameters, i.e., wind velocity, temperature, wind turbulence, human parameters orientation of the human body relative to wind directions, surface area, clothing, gender, physical activity and posture, and surrounding parameters, buildings or other structure affecting the flow. In the outdoor environment, the dynamic wind parameters are the dominant factors influencing the CHTC, and they are more complex in both time and space. The wind parameters, i.e. mean wind velocity, turbulence intensity, and turbulent length scale, are extensively used to assess the convective heat loss from humans through experimental and CFD techniques (de Dear et al., 1997; S. Gao et al., 2019; Yu, Liu, Chauhan, de Dear, & Niu, 2020). The studies related to local CHTCs considering all the outdoor wind environments are rarely found in the literature. Yu et al.'s correlation (Yu et al., 2020) (eq.2.22), developed using experimental techniques, is limited to front-facing direction cases in outdoor environments. Zou et al., (Zou, Liu, Niu, Yu, & Lei, 2021) developed the correlation (eq.2.23) for all the human orientations relative to wind direction using CFD techniques. These studies are limited to standing posture and immediate surrounding disturbance has not been considered. For special cases such as humans standing at a bus stop or under a tree, correlation cannot be used, as the immediate surrounding disturbs the wind flow parameters.

$$h_c = Au^n(1 + B.TI.u^{0.5}) \quad [2.22]$$

$$h_c = Au^n(1 + B.TI.u^{0.5}).(L/D)^\beta. \quad [2.23]$$

Where, h_c represents the heat transfer coefficients, A, B, n and β are the constants. D is the diameter of the human body. u, L, and TI represent wind velocity, turbulence length scale and turbulent intensity respectively.

The challenges of turbulence modelling for the outdoor environment include the inability to fully reproduce wind flow, which leads to substantial discrepancies in local convective heat flux when comparing simulation results and experimental data. Ito et al., (Kazuhide et al., 2015) compared the various turbulence models including SST k- ω , realizable k- ϵ , low-Re k- ϵ , and v2-f models for the human body convective heat loss prediction. In their works, the SST k- ω model predicted a comparatively accurate value than other models. Li et al. (C. Li & Ito, 2014), compared the different turbulence models for extreme wind velocities and reported SST k- ω has best agreement with the experimental results. Liang et al., (H. Liang, Yu, & Niu, 2023) reported that the LES has better agreement with experiment results in human convective heat loss prediction, reducing the error from 22 to 8% compared to the RANS model. However, the RANS model is widely used for outdoor environment studies as the meshing and computational cost is comparatively lesser than LES.

The local radiative heat transfer coefficient (RHTC) for each body segment was reported mostly for the indoor environment (de Dear et al., 1997; S. Gao et al., 2019) and seldom found for the outdoor environment. In the outdoor environment, the radiative heat loss from the human body is influenced by human factors (skin temperature, posture, sex and surface area), and ambient factors (solar radiation, long wave radiation from the surroundings, emissivity of the surface).

2.7 Outdoor Thermal Comfort Models

Thermal comfort is a critical aspect of human comfort and well-being, particularly in outdoor environments. In the urban outdoor environment, thermal comfort is influenced by a variety of ambient factors such as wind velocity, solar radiation, longwave radiation from surroundings, air temperature and humidity. As these factors are constantly changing in outdoor environments, the assessment of thermal comfort in outdoor environments is a complex and challenging task. Thermal comfort indices were developed to assess indoor thermal comfort. Later stage, some of the indices were modified for the outdoor environment. There are several outdoor thermal comfort indices have been developed namely Standard Effective Temperature (SET) (Gagge, Fobelets, & Berglund, 1986), Heat Index (HI), Wet Bulb Globe Temperature (WBGT) (Yaglou & Minaed, 1957), Universal Thermal Climate Index (UTCI) (Blazejczyk, Epstein, Jendritzky, Staiger, & Tinz, 2012), Predicted Mean Vote (PMV) (Cheng, Ng, Chan, & Givoni, 2012) and Predicted Percentage of Dissatisfied (PPD), Discomfort Index (DI) (Thom, 1959), Physiologically Equivalent Temperature (PET) (Höppe, 1999), modified Physiologically Equivalent Temperature (m-PET) (Chen & Matzarakis, 2018), Outdoor Standard Effective Temperature (OUT_SET*) (Pickup & de Dear, 2000), Thermal Work Limit (TWL) (Brake & Bates, 2002), Humidex (Masterton & Richardson, 1979), Thermal Sensation Vote (TSV), Apparent Temperature (AT) (Steadman, 1984) to represent the thermal comfort in outdoor environment. Despite the importance of thermal comfort assessment in outdoor environments, there are still several limitations and gaps in the existing methods. Traditional methods for assessing thermal comfort, such as the PMV and the PPD (Poul O. Fanger, 1970), were developed primarily for indoor environments and have limitations when applied to outdoor spaces. Even later developed outdoor targeted indices, such as UTCI, PET, and OUT SET were not able to provide accurate quantification of asymmetric solar radiation and

dynamic wind outdoors (Huang, Li, Xie, Niu, & Mak, 2017). As a result, there is a need for more accurate and comprehensive methods for assessing thermal comfort in outdoor spaces.

The traditional outdoor thermal comfort evaluations are field measurements, subject surveys and thermo-physiological modelling. The ambient parameters for the outdoor thermal comfort assessment can be obtained by microclimate simulation and field measurements. In field measurements, the environmental parameters are directly measured by the different kinds of measuring instruments, such as air temperature and humidity sensors, globe thermometers, radiometer, and anemometers, etc. In a comfort survey, along with the field measurement of ambient conditions, a set of questionnaires related to thermal sensation and thermal perception was asked to the subject after spending 10 to 20 minutes in the corresponding study location (Huang et al., 2017). In recent studies, physiological parameters such as skin and body core temperatures can be measured using i-button thermocouples (Jiang, Xie, & Niu, 2024), and ingestible core temperature capsules (Hui Zhang, 2003) respectively. However, the outdoor thermal comfort survey is subjective, and its reliability greatly depends on the sample size, contextual factors, thermal history, thermal comfort index chosen, and practical constraints such as limited environmental parameters etc. In the simulation method, ambient factors such as wind, air temperature, solar radiation, and longwave radiation can be obtained based on the input urban geometries and boundary conditions. Simplified geometries, incorrect boundary conditions and physical processes increase the uncertainties of the required output parameters. Though this limits the application of simulation results to practical cases, the simulation methods are cost- and time-effective compared to the field measurements.

The existing methods for assessing thermal comfort in outdoor environments have several limitations that need to be addressed. One of the main limitations of these methods is their inability to precisely account for the effects of complex thermal environmental factors such as solar radiation and wind. Solar radiation, for example, creates highly asymmetric radiation

conditions for humans. The input of a simple MRT to existing models introduces an assumption of using a uniform index to represent complex radiation conditions, therefore resulting in inaccurate predictions. Turbulent and gusty winds outdoors result in a much higher rate of convective heat transfer between the human body and the outer environment than indoors (Yu et al., 2020). Besides, the complex thermal environment exposed to different segments of the body may also be aggravated by thermal stratification. Thus, each body segment experiences different local thermal conditions and thus different local thermal sensations. In the traditional methods, localised environment parameters for each body segment were not considered. Single or mean input parameters used in the traditional outdoor thermal comfort models may lead to incorrect prediction. Due to different exposures to solar radiation or other ambient factors in the outdoors, humans can experience different local thermal sensations. Traditional methods failed to capture the local thermal sensation of body parts.

Furthermore, the majority of traditional comfort models overlook the human thermoregulation system and the adaptation of skin temperature to ambient conditions. Manikins equipped with thermoregulation systems for outdoor thermal comfort assessments possess the advantage of accounting for both the impacts of the thermal environment and human thermoregulation. The interface between the human thermoregulation system and the ambient environment can be established by coupling CFD simulation and the human thermoregulation system, where the CFD captures the local ambient conditions and heat exchange to the ambient. There were several studies reported on the coupling method for indoor applications, which are discussed in the subsequent sections. However, the comprehensive performance of these integrated systems has yet to be evaluated for the complex outdoor urban environment.

2.8 Human Thermoregulation Model

The human body continuously produces heat and to maintain the body core temperature, the skin will respond to the ambient conditions through active and passive systems. There were several thermoregulation models to simulate the heat transfer within the body and to the surroundings. Among the various human thermoregulation models developed over the last six decades, Stolwijk's multimodal model (Stolwijk, 1971) is one of the most recognized models developed in 1971. This model considered 6 body segments with core, muscle, fat and skin layers. It becomes a fundamental origin of the algorithm for many multimodal models. Continuing this model, there were many models have been developed such as those of the Gagge 2 nodes model, 65 multinodal models, Gordon model, Fiala model, and CBE model (Fiala, Lomas, & Stohrer, 1999; Gagge et al., 1986; Gordon, Roemer, & Horvath, 1976; Huizenga, Hui, & Arens, 2001; Tanabe, Kobayashi, Nakano, Ozeki, & Konishi, 2002). The thermoregulation models were widely used for non-uniform and unsteady environments. These models consider the heat conduction in the body tissue, heat exchanges between the skin and environment, sweating, vasodilation, vasoconstriction, and shivering. In Fiala's model (Fiala et al., 1999; Fiala, Lomas, & Stohrer, 2001), the improvement of the vasomotion model enhances the accuracy of core temperature prediction. The CBE comfort model (Hui Zhang, Arens, Huizenga, & Han, 2010) which is based on Stolwijk's and Tanabe's model (Tanabe et al., 2002), is improved over Stolwijk's in terms of increased body segments, improved blood flow model, addition of clothing node, and conduction heat transfer with the skin contact surfaces. The model considered 16 body segments with four layers from core to skin tissues and a clothing layer. The model improved the precision of skin and core temperature predictions. Smith's (Smith & Twizell, 1984) developed a distributed parameter model considering the vascular system, and the heat exchange of the human body was simulated using the finite element method. Following by Smiths model, Fu et al., (Fu et al., 2014) improved the

Smiths model by considering the transient heat transfer of clothing. Joshi et al. (Joshi et al., 2022), Park et al. (Park et al., 2024) and Yang et al. (Yang et al., 2017) integrated the clothing model considering air layers and thermos-physical properties of clothing into the thermoregulation model. THERMODE-2023 model (Alfano et al., 2024) considered a more refined partition with 193 nodes and accounts for the spatial distribution of microclimate parameters, effects of body movements and air action on the thermo-physical properties of clothing, and sweating efficiency. Takemori (Takemori, Nakajima, & Shoji, 1996) developed the model based on the Smiths model considering the arteriovenous anastomoses (AVA) blood flow control. Takemori's AVA model has greater accuracy in local skin temperature prediction than Smith's model. The THERMOSEM model (Boris R. M. Kingma, 2012; B. R. M. Kingma, Schellen, Frijns, & van Marken Lichtenbelt, 2012) adopted the neurophysiological skin blood flow model to regulate the skin blood flow by the autonomous nervous system. Further, the passive system in the thermoregulation models improved through the consideration of anatomically and geometrically better human thermoregulation models based on medical images (M. P. Castellani et al., 2023; Michael P. Castellani, Rioux, Castellani, Potter, & Xu, 2021; Unnikrishnan et al., 2021).

Tanabe's research group has developed a 65-modal thermoregulation system (Tanabe et al., 2002) also known as Jointed Circulations System (JOS) with 16 body segments and 4 layers. This model can be used for women and the elderly. To improve the accuracy of the JOS model, JOS-2 (Kobayashi & Tanabe, 2013) has been developed with 17 body segments, considering a detailed vascular system with veins and AVA, and all thermoregulatory mechanisms. The recently developed JOS-3 model (Takahashi et al., 2021a) has included the age factors on thermoregulation, shivering and non-shivering thermogenesis (NST), and an estimation method for heat production. The prediction accuracy of the mean skin temperature in the JOS-3 model is improved over the JOS-2 model.

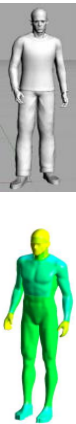
2.9 Coupling Numerical Modelling and Human Thermoregulation Systems

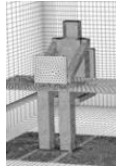
To comprehensively evaluate the human physiological response across various environmental conditions, an interface between the human thermoregulation model and the environmental model is essential. In the coupling method, the environmental parameters such as heat transfer coefficients, and air temperatures, simulated in the CFD are used as inputs for the thermoregulation system, and the resulting physiological response is fed back to the simulation until convergence criteria are met. Numerous attempts have been made to couple CFD with thermoregulation models for different applications, such as automobile cabins (Kornev, 2016), flight cabins, and indoor environments. The coupling methods reported in the literature are listed briefly in Table 2.6. Most of these coupling methods focused on indoor environments, taking into account updated thermoregulation models, human shapes, clothing, activity, pose, and steady or transient conditions in the CFD and radiation modelling. They were primarily applied to indoor scenarios such as personal ventilation, natural ventilation, radiant cooling/heating systems, and cabin comfort. The studies related to outdoor applications are limited. Liang et al. (H. Liang, Tanabe, & Niu, 2023), explored the coupling method for the outdoor application using the JOS-3 thermoregulation model but did not account for short-wave and long-wave radiation effects important in outdoor environments.

Table 2.6 Details of coupling methods reported in the literature

Reference	Thermoregulation Model	Manikin Details		Application details
Murakami, Kato, & Zeng, 2000	Gagge's 2-node model	Vase-shaped human figure – Standing, h: 1.65 m, BSA: 1.688 m ² , 1.7 met		Indoor environment, t_a : 26°C, RH:40-50%

Reference	Thermoregulation Model	Manikin Details		Application details
Tanabe et al., 2002	65-node thermoregulation model	Realistic human shape – Unclothed male - Standing-17 body segments, h: 1.75 m, BSA: 1.72 m ² , 0.6 clo, 1 met		Indoor with solar radiation through the window and Radiant ceiling cooling, panel capacity: 220 W/m ² , RH:50%, t_a : 29 – 30°C, solar radiation: 302 - 406 W/m ²
Al-Mogbel & Chaturvedi, 2003	Gagge's 2-node model	6 cylinders in human shape – Standing – Unclothed, 1.7 met		Indoor environment, Supply air temp.: 10-30°C, RH: 20-80%
Omori, Yang, Kato, & Murakami, 2004	Fanger model	Realistic Unclothed female body	-	Indoor environment
N. Gao, Niu, & Zhang, 2006	CBE comfort model	Scanned manikin - Unclothed Female – Sitting, BSA: 1.568 m ²		Indoor- Personalized Air (PA) ventilation , t_a : 23°C, PA temperature: 20-25°C
Jie Yang, Ni, & Weng, 2017	Yang's multi-node thermal model – 81 nodes	Manikin Newton – Unclothed - Standing - 20 body segments		Indoor environment, t_a :19-45°C, RH: 40%

Reference	Thermoregulation Model	Manikin Details		Application details
Y. Zhang & Yang, 2008	IESD-Fiala model	Scanned manikin – Clothed male – Standing, h:1.75 m, BSA: 1.83m ² ,1.2 met, 1.7 clo		Indoor environment, Ta: 28°C, RH: 60%
Streblow, Müller, Gores, & Bendfeldt, 2008	65 MN Tanabe Model – 16 body segments	-	-	aircraft cabin (complex indoor environment), thermal sensation assessed by CBE comfort model
Zhu, Kato, Ooka, Sakoi, & Tsuzuki, 2008	Sakoi's model	Scanned manikin - unclothed female – Sitting, 16 body segments, BSA: 1.837 m ²		Indoor – non-uniform thermal environment, with radiant wall cooling t_a : 28°C, RH:40-45°C, v_a : 0.05 m/s
Cook, Yang, & Cropper, 2011; Cropper, Yang, Cook, Fiala, & Yousaf, 2010	IESD-Fiala model	Scanned standing manikin -Standing - both clothed and unclothed male, 19 body segments, ,h: 1.73 m, BSA: 2.019 m ²		Cross-ventilated classrooms, and naturally-ventilated room, t_a : 25-34°C, RH: 50%

Reference	Thermoregulation Model	Manikin Details		Application details
Schellen et al., 2013	ThermoSEM model	Humonoid – Sitting		Indoor environment, t_a : 22.2-24.2°C, RH: 32.7-47.7%
Turnow J., 2016	Fiala’s Model	Simplified 3D Geometry – Sitting, h:1.75 m, BSA: 1.85 m ²		Vehicle cabin, t_a : 22.6°C
Choudhary & Udayraj, 2022	JOS-3 thermoregulation model - 85 nodes, 17 segments	Virtual scanned manikin, Clothed, Met: 1.2 – 3.2 met		Air ventilation clothing, t_a : 27-38°C, RH: 30-65%
Ramesh Babu, Sebben, Chronéer, & Etemad, 2024		Scanned manikin – Male - Sitting – clothed - physical activity ratio:1.6		Vehicle cabin, t_a : -20°C – 0°C, RH: 50-90%
Liang et al., 2023		Scanned manikin – Unclothed female, h: 1.6 m, BSA: 1.317 m ²		Wind tunnel simulation, t_a : 30°C, v_a : :1 m/s

2.10 Summary

The membrane-assisted radiant cooling system is a potential choice for future outdoor cooling technology for thermal comfort applications. LDPE membrane is the commonly used low-cost material that has excellent IR transparency for radiant cooling applications. However, thin membranes have poor mechanical properties, and they tend to tear and wrinkle easily. Hence,

IRT membranes with good mechanical properties need to be developed to make the cooling system for real-world use. The provision of thin wire mesh over the membrane can be a viable option to protect the membrane from the ambient condition, for a short while. As the membrane-assisted RCS has more resemblance to the daytime radiative sky cooling, the membrane or aerogel material used for that application can be utilized for the radiant cooling application. However, these materials are still developed for laboratory models and hope to be available commercially in the future.

Several heat transfer models were developed and they are sufficient to prove their cooling capacity improvement over conventional radiant cooling systems. Meanwhile, an in-depth energy model is yet to be developed. The whole system energy analysis of the membrane-assisted RCS needs to be explored.

The application of membrane-assisted RCS is not limited to indoor and semi-outdoor applications. However, outdoor applications such as bus shelters, and shelters in community parks need to be explored more, as outdoor thermal comfort is getting more attention in recent days. The operative temperature of cooling water for the membrane-assisted RCS is comparatively lower than the conventional radiant cooling system. The possibility of integrating the membrane cooling system with passive cooling options is limited and it is to be explored in the future.

In outdoor modelling, the microscale approach is adequate for capturing the environmental conditions at the pedestrian level to assess thermal sensation. The literature indicate that developed correlations for the human convective heat loss in the outdoor environment is not only the function of velocity but also the turbulence intensity and the turbulent length scale. The literature reported that the SST $k-\omega$ turbulence model provides high accuracy in convective heat loss prediction from the human body surfaces.

There were numerous thermoregulation models reported in the literature. Among them, the recently developed JOS-3 model is gaining popularity as it is available in open source as well and it provides greater accuracy compared to its previous versions. It helps to predict the physiological responses, including skin and core temperature for each body part. Coupling with environment modelling helps to evaluate the ambient factors in the vicinity of the local body parts, which aids in accurately predicting the skin temperature. The coupling of CFD and human thermoregulation systems has been attempted for various indoor applications. However, very limited attempts reported on the outdoor application, as well as they have not adequately considered all outdoor ambient factors.

CHAPTER 3

Thermal Modelling of Membrane-Assisted Radiant Cooling System

This chapter presents a numerical investigation of the Localised Outdoor Cooling Hub (LOCH) utilising a membrane-assisted RCS, designed to provide relief from heat stress. The thermal performance of the LOCH is investigated under typical summer conditions in subtropical Hong Kong using CFD techniques. The objectives of this chapter include (i) simulating the heat extraction rates of the cooling hub prototype over a summer day, (ii) analysing and comparing the impact of different membrane materials on thermal performance, and (iii) evaluating the influence of solar radiation on heat extraction at various times of the day. By assessing heat extraction rates, effects of membrane selection, and solar impacts throughout the day, this present chapter aims to provide insights into optimizing the design and operation of membrane-assisted radiant cooling for outdoor applications in terms of energy consumption.

3.1 Membrane-Assisted RCS in the Outdoor Environment

The schematic of the LOCH prototype shown in Figure 3.1 is inspired by the design of bus stop structures in Hong Kong. The cooling hub consists of ceiling and wall radiant cooling panels assisted with IR transparent membranes. As the prototype is designed for a single person standing in it and considering the standard height of the man (1.6 m), the structure was designed for 2 m height and 1.2 m width. The proposed cooling panel consists of copper pipes arranged in a serpentine pattern attached to the aluminium sheet. The back side of the panel will be thermally insulated using nitrile rubber insulation. The front side of the panel is covered by an IR transparent membrane with a certain air gap thickness between them. The cooling water

needs to be circulated through the panel to maintain the cooling panel at the required temperature. Desiccant accommodation in the air gap assists in adsorbing the water vapour in that layer and ensures low humidity.

The thermal load components of the membrane-assisted RCS in outdoor environments are significantly different than those indoors. Typical thermal load components of the membrane-assisted RCS in the outdoor ambient environment are shown in Figure 3.1b. In the outdoor environment, the radiative heat load components include, solar load, i.e., both direct and diffuse components, reflected solar radiation, long wave radiation from the human, ground surface, and adjacent building surfaces. The wind velocity and air temperature are responsible for the convective heat transfer at the exterior surface of the membrane. The design of an appropriate air gap thickness helps to reduce convective heat loss from the panel to the ambient environment. Additionally, the use of a suitable membrane assists in controlling the radiation incident on the panel. Hence, it is important to understand the air gap thickness design and spectral transmissivity of the membranes.

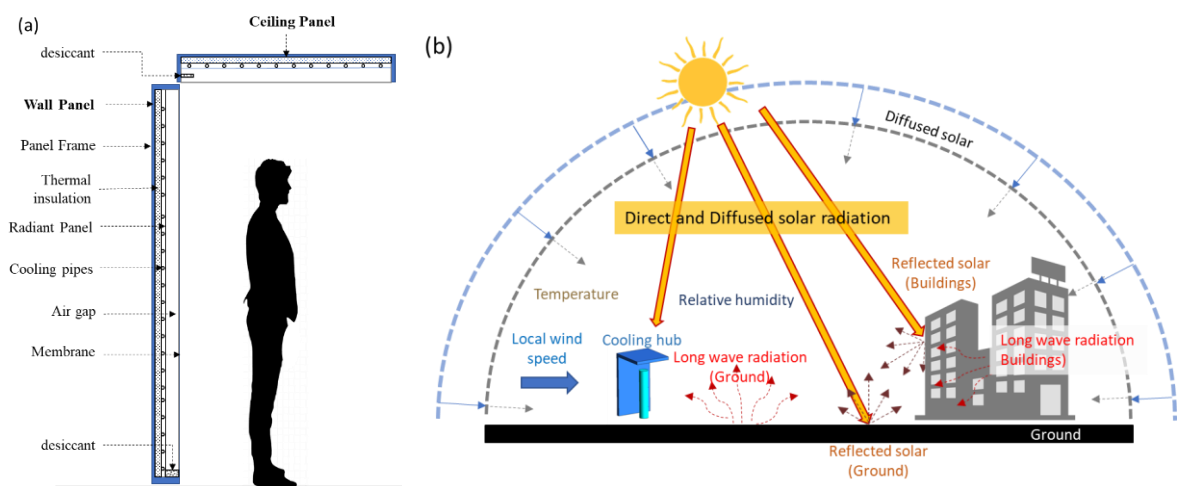


Figure 3.1 (a) Schematic of localised outdoor cooling hub prototype (b) Heat transfer components of the membrane-assisted RCS in the outdoor environment (Roshan, Moghbel, & Attia, 2020)

The air gap thickness between the panel and membrane plays a crucial role in minimizing the convective heat transfer. It should be highly insulative to reduce the convective heat loss from the panel. The critical air gap thickness at which the impact of conductive or convective heat transfer between the panel and membrane is negligible. Therefore, it is advisable to design the air gap thickness beyond the critical air gap thickness. The details of the critical air gap thickness analysis reported in the literature are listed in Table 3.1. The perceptions and factors to determine the critical air gap thickness reported in each study are different, such as equilibrium membrane temperature (Teitelbaum, Rysanek, et al., 2019), thermal performance change (Xing & Li, 2021), the transition from conduction to natural convection (Xing et al., 2020), heat transfer coefficient (Du et al., 2021), and condensation resistance (Gu et al., 2023). The critical air gap thickness reported in the literature deviated from one another, i.e., ranging from 6 to 99 mm, as the assumptions, perceptions, calculation methods, and temperature considerations are different. However, to accommodate the desiccant in the air gap to adsorb the water vapour penetrating to the air gap, and also considering the maximum critical air gap thickness reported in the literature, the air gap thickness is designed to be 100 mm. It ensures a relatively lower CHTC and higher membrane surface temperature for safe operation.

Table 3.1 Details of the critical air gap thickness analysis reported in the literature

Ref. /Membrane config.	Critical airgap thickness/Analysed range	Criteria for critical air gap thickness	Method
Teitelbaum, Rysanek, et al., 2019/ Single	99 mm / 40-120 mm	Equilibrium membrane temperature for different orientations	Experiment

Ref. /Membrane config.	Critical airgap thickness/Analysed range	Criteria for critical air gap thickness	Method
Xing & Li, 2021 / Single	11 mm/0-50 mm	Minimum change in thermal performance	Numerical
Xing et al., 2020/ Single	14 mm/0-50 mm	Transition from conduction to natural convection	Numerical
N. Zhang et al., 2021/ Single	55 mm/0-70 mm	Minimum heat transfer coefficient, (Raleigh number $>3.5 \times 10^5$)	Numerical
N. Zhang et al., 2023 /Single	6 mm/0-100 mm	Minimal heat transfer in the air gap for all orientations	Experiment
Du et al., 2021/ Double	10 mm/0-30 mm	High thermal resistance	Numerical
Gu et al., 2023) Multilayer	10 mm/0-45 mm	Optimum thickness for best condensation resistance	CFD

As per the transparency of the membrane, the radiation falling on the radiant cooling panel is controlled. The membrane material can be categorized as non-selective, mid-infrared (MIR) selective, and sky-window selective, each with different transparency characteristics. The transparency of these membranes for different wavelength regimes is shown in Table 3.2. In the present study, the thermal performance of the membranes-assisted RCS is analysed for the abovementioned membrane configurations. The spectral transmissivity of the available membrane materials is shown in Figure 3.2. The non-selective membranes, i.e., LDPE, are transparent for all wavelength regions. Hence, it allows solar radiation to the panel surface. The MIR selective membrane blocks the solar radiation but allows IR radiation in MIR (2.5-50 μ m) (International Organization for, 2007). The sky window selective membrane, i.e., Polyethylene Aerogel (PEA) (He et al., 2021) and Spectrally Tuned All-Polymer Technology for Induced Cooling (STATIC) (Torgerson & Hellhake, 2020), selectively allows IR radiation in the 8-15

μm range (J. Zhang et al., 2021). The human emits heat mainly in the wavelength of 8-14 μm (Hsu et al., 2016; Ignatov et al., 2014). Hence, undesirable heat loads can be eliminated by using this membrane.

Table 3.2 Transmissivity of the cover shield through the thermal radiation channel (J. Zhang et al., 2021)

Cover Shield	Thermal Radiation Channels			
	Solar (0.25 - 2.5 μm)	Atmosphere (2.5 - 8 μm)	Sky Window (8 - 15 μm)	Atmosphere (>13 μm)
Non-Selective	✓ (α :0.1, τ :0.8)	✓ (α :0.1, τ :0.8)	✓ (α :0.1, τ :0.8)	✓ (α :0.1, τ :0.8)
MIR Selective	✗ (α :0.1, τ :0.1)	✓ (α :0.1, τ :0.8)	✓ (α :0.1, τ :0.8)	✓ (α :0.1, τ :0.8)
Sky Window Selective	✗ (α :0.1, τ :0.1)	✗ (α :0.1, τ :0.1)	✓ (α :0.1, τ :0.8)	✗ (α :0.1, τ :0.1)

Note: ✓ and ✗ symbols in the column indicate the transparent and opaque on the specific channel, *boundary condition value for CFD modelling

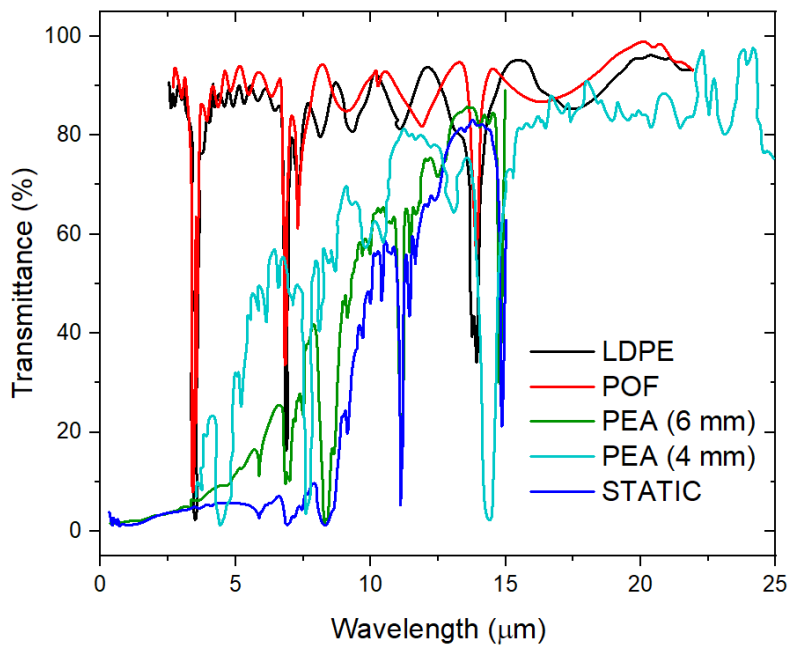


Figure 3.2 Spectral transmittance of LDPE, Polyolefin (POF), PEA, and STATIC (He et al., 2021; A. Leroy et al., 2019; Torgerson & Hellhake, 2020; N. Zhang et al., 2023)

3.2 Model Set-Up and Framework

Numerical modelling is employed to analyse the thermal performance of the proposed LOCH in terms of heat extraction rate. The numerical model should consider the effects of wind, solar radiation, and long-wave radiation from humans and the surrounding environment. It is important to accurately define the boundary conditions for the numerical modelling to replicate the real ambient environment. Most previous numerical studies reported for outdoor urban environments often made assumptions regarding boundary conditions such as an isothermal ground surface with the same ambient air temperature (Allegrini & Carmeliet, 2017; G. Chen, Rong, & Zhang, 2020; H. Chen, Ooka, Huang, & Tsuchiya, 2009), and convection with predefined heat transfer coefficients (Zhengtong Li, Zhang, Wen, Yang, & Juan, 2020; A.-S. Yang, Juan, Wen, & Chang, 2017). To effectively assess the thermal performance of the proposed cooling system in a real-world condition, the developed framework (Figure 3.3) intended to define the boundary conditions that replicate the actual outdoor environment of the study location. In the present study, the ambient data extracted from the corresponding location’s weather file and the ground surface temperature were obtained from the energy and radiation modelling using Rhino-Grasshopper software (Step 1). The obtained data from Step 1 ensures the real ambient condition and they are used as the boundary conditions for the numerical modelling (Step2).

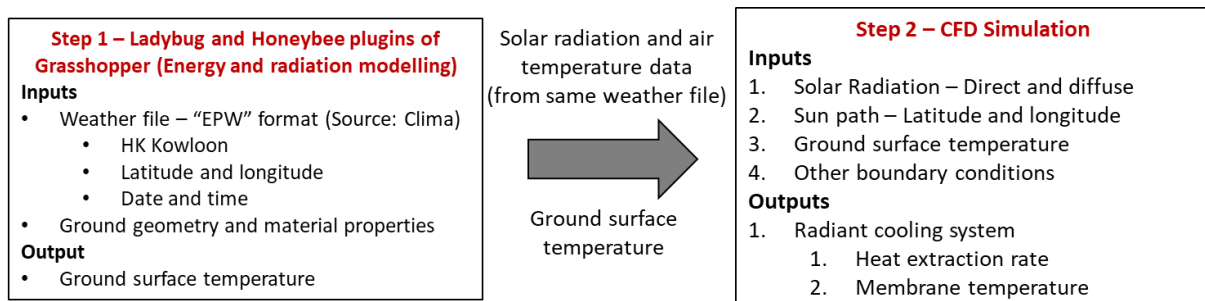


Figure 3.3 Framework for the LOCH modelling in the outdoor environment

The study location considered for the modelling is Hung Hom bus station, Hong Kong (latitude: 22.3056° N, Longitude: 114.1887° E, humid subtropical climate (Peel, Finlayson, & McMahon, 2007)), which represents an unshaded open space environment. The weather file is based on the weather station in Kowloon, Hong Kong considered for the study (Betti, Tartarini, Nguyen, & Schiavon, 2022). The weather file consists of an hourly average of 50 years of data, i.e., solar radiation and air temperature. The plugins of Rhino-Grasshopper, i.e., Honeybee and Ladybug, extract the required input data from the weather file and process it for the ground surface temperature (Crawley, Lawrie, Pedersen, & Winkelmann, 2000). The thermal properties and albedo of the ground surface material have a significant influence on the ground surface and mean radiant temperature. Hence, the thermal properties of the concrete were considered for the ground surface. Hourly-based ground surface temperature is obtained from the modelling results for the typical summer day in Hong Kong, i.e., July 21. The solar radiation and air temperature data needed for the CFD simulation are extracted from the same weather file. Steady-state CFD simulation aims to be performed for 4 different time points on July 21, i.e., 9:00, 11:00, 13:00, and 15:00 hrs, on July 21. The ambient and solar parameters inputs for the CFD modelling of investigated times of the typical summer day are listed in Table 3.3.

Table 3.3 Ambient and solar parameters inputs for the CFD modelling for various times of the day

Time (hr)	Ground surface temp. (°C)	Solar Radiation (W/m²)		Air temp. (°C)
		Direct	Diffused	
9:00	43.2	402	350	29.3
11:00	52.3	613	326	30.8
13:00	54.9	591	266	31.6
15:00	50.5	388	200	31.9

A CFD model of a bus stop structured cooling hub equipped with the membrane-assisted RCS in an open space environment has been developed using Ansys Fluent. The geometry and hexahedral meshing were created using ICEM software. The computation domain size is modelled based on the COST Action 732 (Franke, Hellsten, Schlünzen, & Carissimo) and the AIJ guidelines (Potsis et al., 2023; Tominaga et al., 2008), considering the height of the radiant cooling structure as the base height. The computational domain and geometry of the membrane-based radiant cooling structure are shown in Figure 3.4. Mesh independence test results revealed that the minimum number of mesh elements to achieve grid independence is 4M. Since the objective of this chapter focuses solely on the cooling system, the human thermal manikin has not been included in the simulation, due to the complex mesh generation process. A cylindrical heat source is included to approximate the standard female height, i.e., 1.6 m, and surface area, i.e., 1.588 m² (Arens & Zhang, 2006). Considering the heat load received from the surrounding surfaces by the panels, the difference in heat load between the manikin and the cylindrical heat source is negligible. The difference Constant heat flux boundary conditions are assigned for the heat source, considering the heat flux emitted by a human body, i.e., 58.15 W/m² (Y. Wang, Huang, Lu, Zhao, & Li, 2013). The radiant panel temperature is considered to be at a constant uniform temperature, i.e., 10°C. The ground surface temperature extracted from Step 1 is specified as an isothermal boundary condition. The uniform wind speed at the inlet has been assumed to be 1.5 m/s. The air temperature at the inlet and direct and diffused solar radiation for the investigating date and time are extracted from the Hong Kong weather file. The sun position vector is calculated by the solar calculator in the Ansys Fluent. The solar ray tracing approach is employed for solar incident radiation. The solar radiation load of the exposed surface will be added to the energy equation as a source term. The boundary conditions of the modelling are listed in Table 3.4.

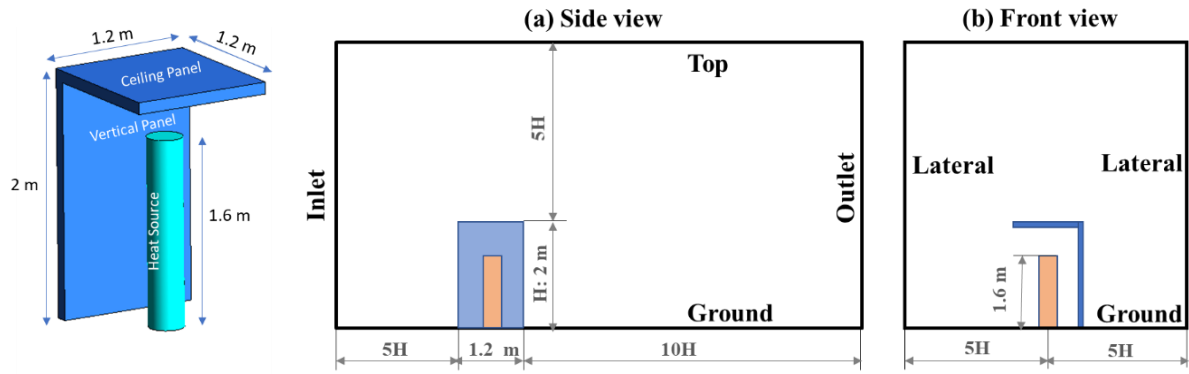


Figure 3.4 Schematic of the computational domain and radiant cooling structure

Table 3.4 Boundary conditions for the CFD modelling

Boundaries	Boundary Condition	Description
Inlet	Velocity inlet	V: 1.5 m/s, Turbulent Intensity(TI): 29 %, Turbulent Length Scale (TLS): 6.6 (Zou et al., 2021) (Zou et al., 2021), T_{air} : BES*, ϵ : 0.95
Ground	Isothermal	T: BES*, ϵ : 0.9 (Jinxin Yang, Wong, Menenti, & Nichol, 2015)
Radiant panel	Isothermal	T: 10°C, ϵ : 0.95
Membrane	Coupled	semi-transparent, ϵ : 0.124
Heat source (cylinder)	Isoflux	q: 58.15 W/m ² , ϵ : 0.95 (Y. Wang et al., 2013)
Top surface	Isothermal	T_{sky} : 258 K (Gliha, Kruczek, Etemad, & Thibault, 2011). ϵ : 0.7 (Pandey, Lee Iii, & Paden, 1995)
Lateral surfaces	Symmetry	-
Outlet	Outflow	-

* BES- Input from building energy simulation (from Rhino-Grasshopper (Step 1))

3.2.1 Mathematical Model

Governing equations

Numerical analysis is based on the conservation of mass, momentum, and energy equations. A 3D steady-state numerical model has been developed using Ansys Fluent 19.0. The most commonly used Reynolds-Averaged Navier-Stokes (RANS) modelling approach is used for flow analysis. The governing equations of the CFD simulation are shown in eqns. 3.1 - 3.3.

$$\text{Continuity Equation: } \frac{\partial u_i}{\partial x_i} = 0 \quad [3.1]$$

$$\text{Momentum Equation: } \frac{\partial \rho u_i u_j}{\partial x_i} = -\frac{\partial p}{\partial x_i} + \frac{\partial}{\partial x_j} \left[(\mu + \mu_t) \left(\frac{\partial u_i}{\partial x_j} + \frac{\partial u_j}{\partial x_i} \right) \right] + \rho_{ref} g_i \beta (T - T_{ref}) \quad [3.2]$$

$$\text{Energy Equation: } \frac{\partial u_i T}{\partial x_i} + \frac{\partial}{\partial x_i} \left(\alpha_T \frac{\partial T}{\partial x_j} \right) = Q_T \quad [3.3]$$

Where, u_i and u_j is the air velocity component along the i and j axes respectively, P is pressure, ρ is density, μ is dynamic viscosity, μ_t is turbulent viscosity, ρ_{ref} is reference density, g_i is gravity, β is thermal expansion coefficient, T is temperature, and T_{ref} is the reference temperature. α_T and Q_T represents the thermal diffusivity and solar heat flux.

Boussinesq approximation is adopted for the air density in the buoyancy term within the momentum equation for the buoyancy-driven flow analysis. The Raleigh number in the air gap thickness is in the range of 10^6 , where the critical Raleigh number is 3×10^5 . The computational domain consists of two air zones, i.e., ambient air and dry air in the air gap layer. As the turbulence flow is predicted for both air domains, a realizable $k-\epsilon$ model with an enhanced wall treatment method is used for the turbulence modelling. The transport equations of the turbulent kinetic energy (k) and dissipation rate (ϵ) are shown in eqns. 3.4 and 3.5 (FLUENT, 2009).

$$\frac{\partial}{\partial t}(\rho k) + \frac{\partial}{\partial x_j}(\rho k u_j) = \frac{\partial}{\partial x_j} \left[\left(\mu + \frac{\mu_t}{\sigma_k} \right) \frac{\partial k}{\partial x_j} \right] + G_k + G_b - \rho \epsilon - Y_M + S_k \quad [3.4]$$

$$\frac{\partial}{\partial t}(\rho \epsilon) + \frac{\partial}{\partial x_j}(\rho \epsilon u_j) = \frac{\partial}{\partial x_j} \left[\left(\mu + \frac{\mu_t}{\sigma_\epsilon} \right) \frac{\partial \epsilon}{\partial x_j} \right] + \rho C_1 S \epsilon - \rho C_2 \frac{\epsilon^2}{k + \sqrt{\nu} \epsilon} + C_{1\epsilon} \frac{\epsilon}{K} C_{3\epsilon} G_b + S_\epsilon \quad [3.5]$$

$$C_1 = \max \left[0.43, \frac{\eta}{\eta + 5} \right], \eta = S \frac{k}{\epsilon}, S = \sqrt{2 S_{ij} S_{ij}}$$

Where, G_k and G_b represent turbulent kinetic energy due to velocity gradient and buoyancy respectively. Y_M denotes the contribution of the fluctuating dilatation compressible turbulence to the overall dissipation rate, C_1 , C_2 and C_3 are constants, and σ_k and σ_ϵ represent the Prandtl numbers for k & ϵ respectively. S_k and S_ϵ denote the user-defined source terms.

The DO radiation model is employed for solving the Radiative Transfer Equation (RTE) (Eqns. 3.6 & 3.7). DO model has better accuracy in solving complex optical problems and is suitable for radiation through semi-transparent medium problems (Moghimi, Craig, & Meyer, 2015; Qu, Milliez, Musson-Genon, & Carissimo, 2012). It can make a close coupling between wall temperature and radiative heat transfer, which is effective for solving energy equations (Dugaria, Bortolato, & Del Col, 2018). As the membrane thickness is in the range of microns, the thickness of the membrane has not been considered in the study.

In the simulation, the membrane is defined as a semi-transparent boundary type, and the transmissivity and absorptivity for the solar radiation regime are defined. The transparency of non-selective and MIR-selective, only differ in the solar radiation regime. As both membranes are transparent for longwave radiation, they are considered to be grey surfaces. For the sky window selective regime simulations, the non-grey model is used. The wavelength for three bands, i.e., band 0 (2.5-7 μm), band 1 (8 - 15 μm), and band 2 (16 - 100 μm) is defined and the radiative heat transfer in band 2 (8-15 μm) is considered for the post-processing. The RTE

equation for the radiation intensity of the grey surface radiation and spectral intensity of the non-grey surface radiation is shown in eqns. 3.6 and 3.7 respectively.

$$\nabla \cdot (I(\vec{r}, \vec{s})\vec{s}) + (\alpha + \sigma_s)I(\vec{r}, \vec{s}) = \alpha n^2 \frac{\sigma T^4}{\pi} + \frac{\sigma_s}{4\pi} \int_0^{4\pi} I(\vec{r}, \vec{s}') \Phi(\vec{s}, \vec{s}') d\Omega' \quad [3.6]$$

$$\nabla \cdot (I_\lambda(\vec{r}, \vec{s})\vec{s}) + (\alpha_\lambda + \sigma_s)I_\lambda(\vec{r}, \vec{s}) = \alpha_\lambda n^2 I_{b\lambda} + \frac{\sigma_s}{4\pi} \int_0^{4\pi} I_\lambda(\vec{r}, \vec{s}') \Phi(\vec{s}, \vec{s}') d\Omega' \quad [3.7]$$

Where I is radiation intensity, \vec{r} is the position vector, \vec{s} is direction vector, s is path length, α is absorption coefficient, σ_s is scattering coefficient, n is refractive index, σ is Stephen Boltzmann constant, T is temperature, \vec{s}' is scattering direction vector, Φ is phase function and Ω' is the solid angle. The net radiative heat flux (q_{net}) of the grey and non-grey surface models is calculated by Eqns. [3.8&3.9] respectively.

$$q_{net} = (1 - \epsilon_\omega)q_{in} + n^2 \epsilon_\omega \sigma T_\omega^4 - \int_{\vec{s} \cdot \vec{n} > 0} I_{in} \vec{s} \cdot \vec{n} d\Omega \quad [3.8]$$

$$q_{net,\lambda} = (1 - \epsilon_{\omega\lambda})q_{in,\lambda} + \epsilon_{\omega\lambda} [F(0 \rightarrow n\lambda_2 T_\omega) - F(0 \rightarrow n\lambda_1 T_\omega)] n^2 \sigma T_\omega^4 - \Delta\lambda \int_{\vec{s} \cdot \vec{n} > 0} I_{in} \vec{s} \cdot \vec{n} d\Omega \quad [3.9]$$

Where λ denotes the wavelength, α_λ is the spectral absorption coefficient, I_λ is the spectral intensity, $I_{b\lambda}$ is the black body intensity, q_{in} is the incident radiative heat flux, ϵ_ω and $\epsilon_{\omega\lambda}$ represent the wall emissivity, $F(0 \rightarrow n\lambda T_\omega)$ represents the fraction of radiant energy emitted by a blackbody from 0 to λ wavelength interval. λ_1 and λ_2 denotes the wavelength boundaries for a band.

Solver settings

The governing equations are discretized by the finite volume scheme. The coupled algorithm was adopted for the pressure-velocity coupling. Second-order discretization was used for the convective and diffusion terms of the governing equations and DO radiation. The PRESTO discretization was adopted for the pressure terms. A double-precision solver was selected for the simulation. The convergence criteria of the normalized residual errors were set to be 10^{-8}

for the energy and 10^{-5} for other equations. Additionally, the key parameters of the simulation, i.e., heat extraction rate was monitored for stable values to ensure convergence.

3.3 Results and Discussion

3.3.1 Validation of Modelling Method

The experimental result reported by Gu et al. (Gu et al., 2023; N. Zhang et al., 2021) is used to validate the developed CFD model. The experiment setup (Figure 3.5) size of 200 x 200 x 50 mm, has the cooling and heating panel on the top and bottom sides respectively. The cooling and heating panel has an emissivity of 0.95 and other surfaces are coated with thin nickel film to have high reflectivity, i.e., 0.95. An LDPE film is used as a membrane with an air gap thickness of 10 mm. The whole experiment setup was insulated from the ambient heat transfer using polyurethane foam. In the experiment, the heating panel was maintained at 32°C, and the cooling panel temperature varied from 6 to 16°C.

The computational domain (Figure 3.5) consists of an aluminium cooling panel on the top surface and an aluminium heating panel on the bottom surface. The emissivity of the cooling and heating panels is assumed to be 0.95. The membrane used to cover the cooling panel is assumed to be transparent for the IR radiation in the MIR wavelength (2.5-50 μm) region. In the simulation study, the membrane thickness has been neglected as the available membrane thicknesses are in the range of microns. The vertical surfaces of the computational domain are assumed to be adiabatic surfaces with an emissivity of 0.05.

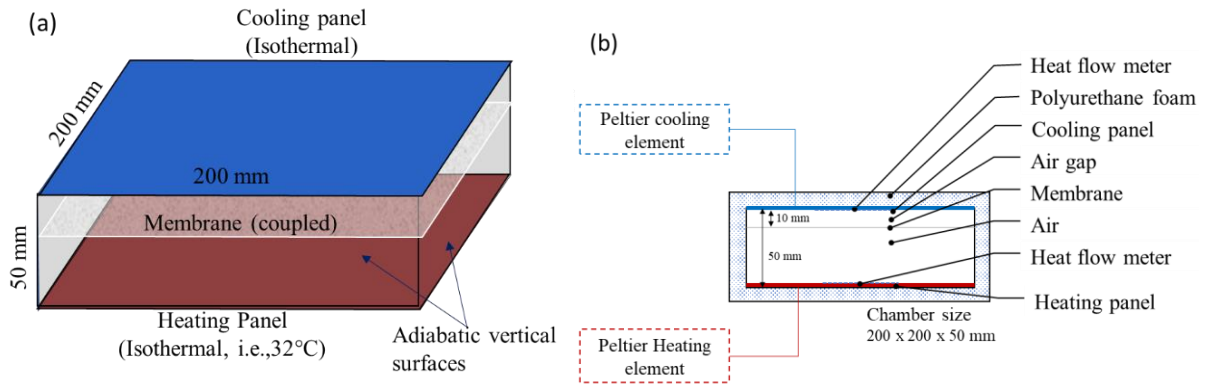


Figure 3.5 (a) Computation domain and boundary conditions of CFD model (b) schematic of experiment setup

The model has two zones, i.e., a dry air zone between the membrane and radiant panel, and an air zone between the membrane and heating panel. The dry air zone is considered as the pure conduction region, i.e., $Nu=1$, and there is no convection. The Raleigh number for the air zone falls below 1.2×10^5 , indicating the laminar flow, whereas turbulent flow occurs when $Ra > 3 \times 10^5$. Hence, the laminar model is employed for the simulation. The velocity vector and the temperature contour of the cross-section of the domain are shown in Figure 3.6 a and b. The buoyancy effect in the air region between the membrane and heating panel induces the airflow and forms the Bernard cells. The corresponding temperature contour explains the temperature variation in the air domains. The heat extraction rates obtained from the CFD heat transfer model were compared with experiment results (Figure 3.6c). An increase in the radiant panel temperature from 6 to 16°C decreases the heat extraction rate from 140.27 to 89.0 W/m^2 , and the results have good agreement with the experimental results, i.e., within 5% error limits.

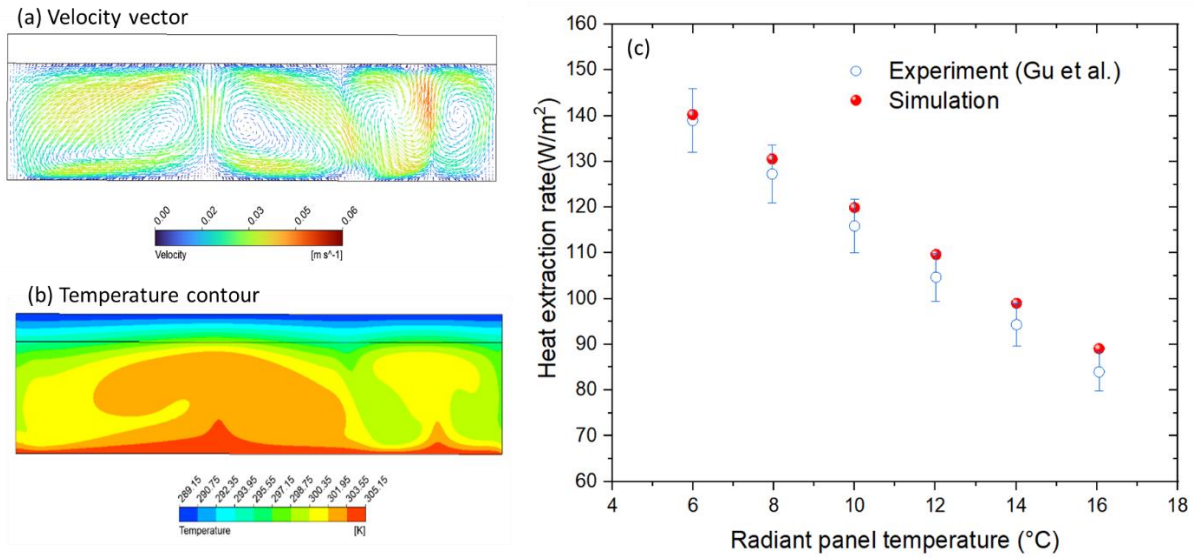


Figure 3.6 (a) velocity vector, (b) temperature contour of air domain, and (c) CFD Model validation of membrane-assisted RCS for heat extraction rate

3.3.2 Heat Transfer Performance Analysis of Membrane-Assisted RCS in the Outdoor Environment

The heat transfer characteristics of the membrane-based RCS are analysed for the various panel surface temperatures at the time of 13:00 hr and the MIR selective membrane is considered for the cover shield material. The panel surface temperature is varied between 2 to 10°C at the interval of 2°C. Figure 3.8 and Figure 3.9 illustrate the variations in convective, radiative, and total heat extraction rates of the ceiling and wall panels as a function of panel surface temperature. As the convective shield, i.e., membrane, reduces the convective heat transfer to the surroundings, radiative heat transfer dominates the total heat transfer. The total heat extraction rate of wall panels considering heat loads from humans, surroundings, and solar radiation is 382.1 W/m² for panel temperature 2°C. While the wall panel absorbs 346 W/m². The total heat extraction of the ceiling panel is 10 to 14% higher than the wall panel for the investigated panel temperature range. The reason is that the view factor of the ceiling panel shares 70% with the ground surface while the wall panel shares 40% (Figure 3.7). The long

wave radiation from the ground surface which has a relatively higher surface temperature causes a higher heat load on the ceiling panels. A decrease in the panel temperature from 10°C to 2°C increases the radiative heat transfer by 15% and 20% and convective heat transfer by 23% and 31% for the ceiling panel and wall panel respectively. As the study is analysed for the time of 13:00 hr, both panel surfaces are self-shaded. Therefore, the direct solar radiation component is eliminated, and the diffused solar radiation component contributes to the solar heat flux. The diffused solar heat flux falling on the ceiling and wall panels is constant, i.e., 88.18 W/m². In the solar heat load model used, the total diffused load calculated by the model will be distributed to all the surfaces participating in the solar radiation. Therefore, the diffused load on the ceiling and wall panels are same if the panel is not exposed to direct solar radiation.

Several studies explored the convective and RHTC for the conventional RCS for indoor applications (Shinoda, Kazanci, Tanabe, & Olesen, 2019). In the conventional RCS, the reference temperatures used for the convective and radiative heat transfer calculations are the air temperature and Average Unheated/cooled Surface Temperature (AUST) respectively. With a membrane in between, the CHTC as calculated by Eq. 3.10 is an equivalent one, having taken into account the increased resistance of the air gap. The MRT is considered for the reference temperature in the RHTC calculation (Eq.3.11) (Kántor & Unger, 2011; Rakha & Zhandand Christoph Reinhart). The MRT is calculated using the absorbed radiation heat flux and solar heat flux obtained from CFD simulation. The first term in Eq. 3.12 represents the heat absorbed by the surface and the second and third terms represent the diffused and direct solar components. In the current simulation, the radiation from the inlet and outlet boundaries, ground surface, and sky are considered. The view factor percentages of the ceiling and wall panels are shown in Figure 3.7.

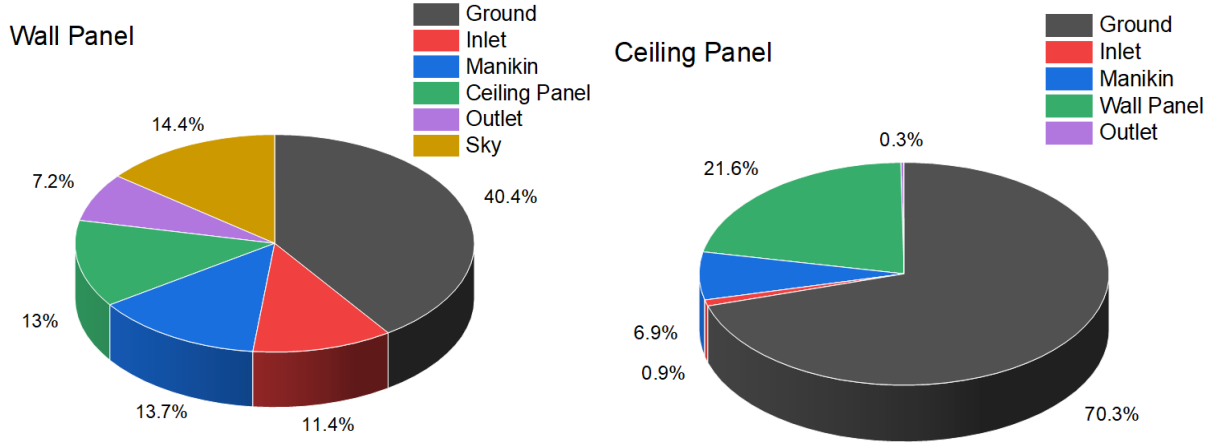


Figure 3.7 View factors of ceiling and wall panels to the surroundings

$$h_c = \frac{Q_c}{(T_p - T_m)} \quad [3.10]$$

$$h_r = \frac{Q_r(lw + Solar)}{(T_p - T_{mrt})} \quad [3.11]$$

Where,

$$T_{mrt} = \sqrt[4]{\frac{\sum_{i=1}^n F_i \cdot a_l \cdot E_i}{\epsilon \cdot \sigma} + \frac{\sum_{i=1}^n F_i \cdot a_k \cdot D_i}{\epsilon \cdot \sigma} + \frac{f_p \cdot a_k \cdot I^*}{\epsilon \cdot \sigma}} \quad [3.12]$$

Where, Q and h represent the heat flux and heat transfer coefficient respectively, and the subscripts r and c represent radiative and convective heat transfer respectively. T_{mrt} mean radiant temperature, F_i is the view factor, and E_i is long-wave emission. a_l and a_k are the absorption coefficients due to long-wave and short-wave radiation respectively. D_i and I^* are the diffused radiation and direct solar intensity respectively.

The variation of the CHTC and RHTC of the ceiling and wall panels for the investigated panel surface temperatures is shown in Figure 3.8 and Figure 3.9 respectively. The CHTC for the panel surface is the function of the surface temperatures of the radiant panel surface and membrane, and air gap thickness. The natural convection in the air gap layer caused by buoyancy force is different for ceiling and wall panels due to their orientations, i.e., horizontal

and vertical respectively. The CHTC of the cooling panels The CHTC for the investigated panel surface temperature range is 2.6 W/m²K for the ceiling panel and 2.2 W/m²K for the wall panel. Variation in the panel surface temperature has an insignificant impact on the CHTC. The RHTC for both ceiling and wall panels are almost the same, i.e., RHTC for the ceiling panel increases from 5.7 to 6.2 W/m²K while for the wall panel increases from 5.6 to 6.1 W/m²K. The RHTC is always higher than the CHTC for both ceiling and wall panels. It indicates that radiative heat transfer dominates over convective heat transfer.

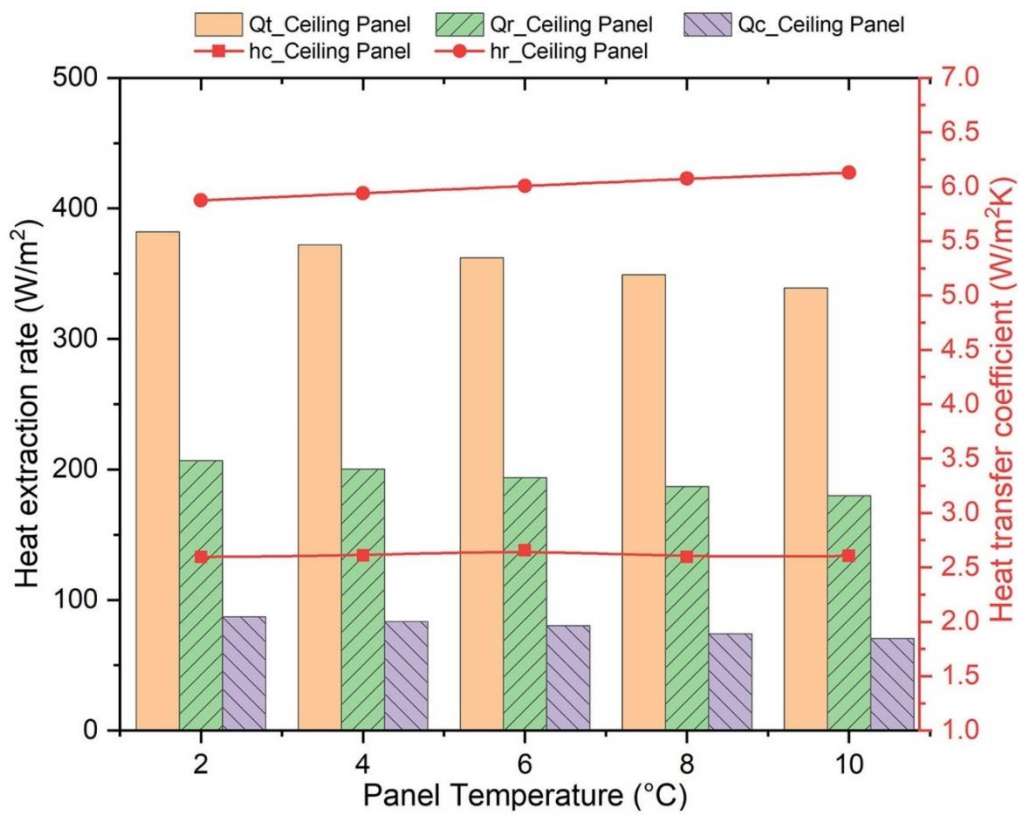


Figure 3.8 Heat extraction rates and heat transfer coefficients of ceiling panel at different cooling panel temperatures ($T_{\text{air}} = 31.6^{\circ}\text{C}$ at 13:00 hr, MIR-selective membrane)

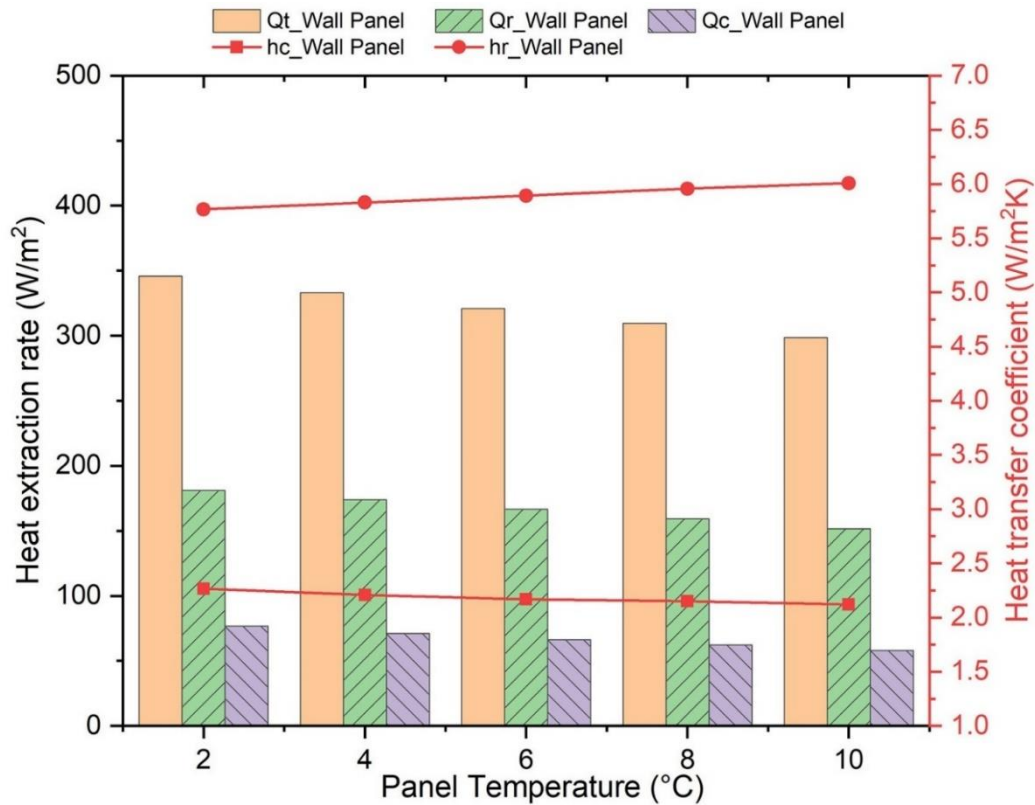


Figure 3.9 Heat extraction rates and heat transfer coefficients of wall panel at different cooling panel temperatures ($T_{\text{air}} = 31.6^{\circ}\text{C}$ at 13:00 hr, MIR-selective membrane)

3.3.3 Impact of Membrane Material

In the present study, the different cover shield materials, i.e., non-selective, MIR-selective, and sky-selective cover shields, are analysed for the thermal performance of the cooling system. The direct and diffused solar radiation, and ground surface temperature, are the major influencing parameters of the thermal performance of the cooling system. As these parameters vary from morning to evening, it is important to evaluate the thermal performance of the system over the day. Hence, the impact of ambient and solar parameters on the heat load components of panels during different times of the day, i.e., 9:00, 11:00, 13:00, and 15:00 hr, is analysed. The solar path and associated shading on the cooling hub of the investigating timings of July 21st are shown in Figure 3.10, for a better understanding of direct solar radiation exposure.

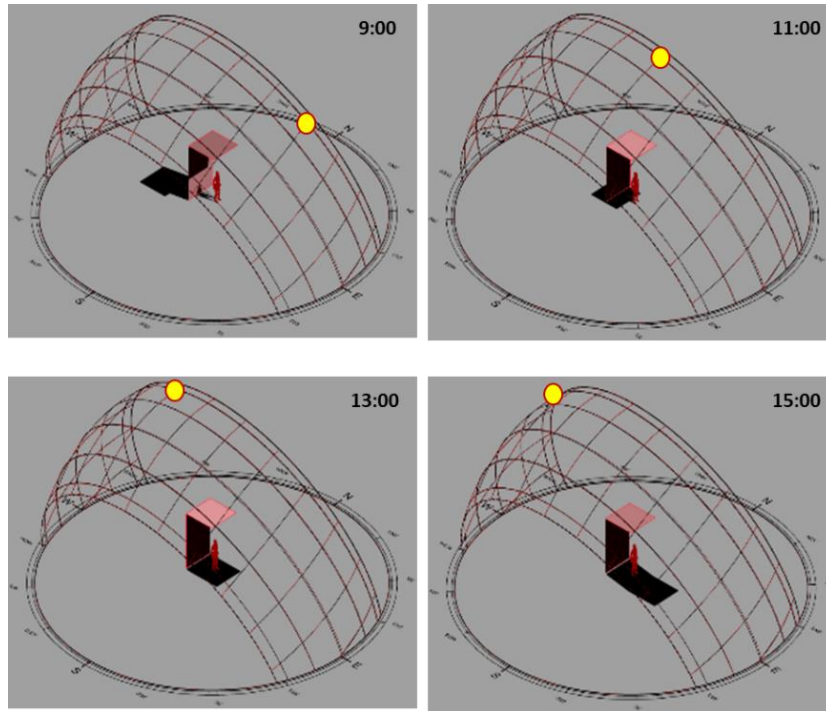


Figure 3.10 Sun position and shading on the cooling panels at different times on 21st July

Figure 3.11 shows the convective, radiative, solar, and total heat flux of the cooling panels for the different membrane configurations at different times of the day. The total heat extraction rate of the cooling panel depends on the radiative heat transfer from the surroundings, solar heat flux, and convective heat transfer from the ambient. Solar heat flux is one of the significant contributors to total heat extraction and varies depending on the transmittance of the membrane and, direct and diffused solar radiation components. As the cooling hub structure is oriented east-facing, there is direct solar radiation falling on the wall panel during morning hours, i.e., 9:00 hr. The non-selective covers allow 80% IR and visible parts of solar heat flux, while MIR and sky-window selective allow only 10%. Hence, the wall panel with a non-selective cover shield has comparatively higher solar heat flux at 9:00 hr, i.e., 100.4 W/m^2 and it is 1.27 times higher than other membranes. Consequently, the total heat extraction of the wall panel is 30% and 97% higher than the MIR and Sky-window selective panels respectively. The ceiling panel is not affected by direct solar radiation always, as it is facing downwards. It can be concluded that the wall panel with the non-selective membrane is not recommended where direct solar

radiation falls on the panel. For the remaining studied hours, i.e., 11:00 to 15:00 hrs, panel surfaces provide self-shading, thus diffused and reflected solar radiation loads participating.

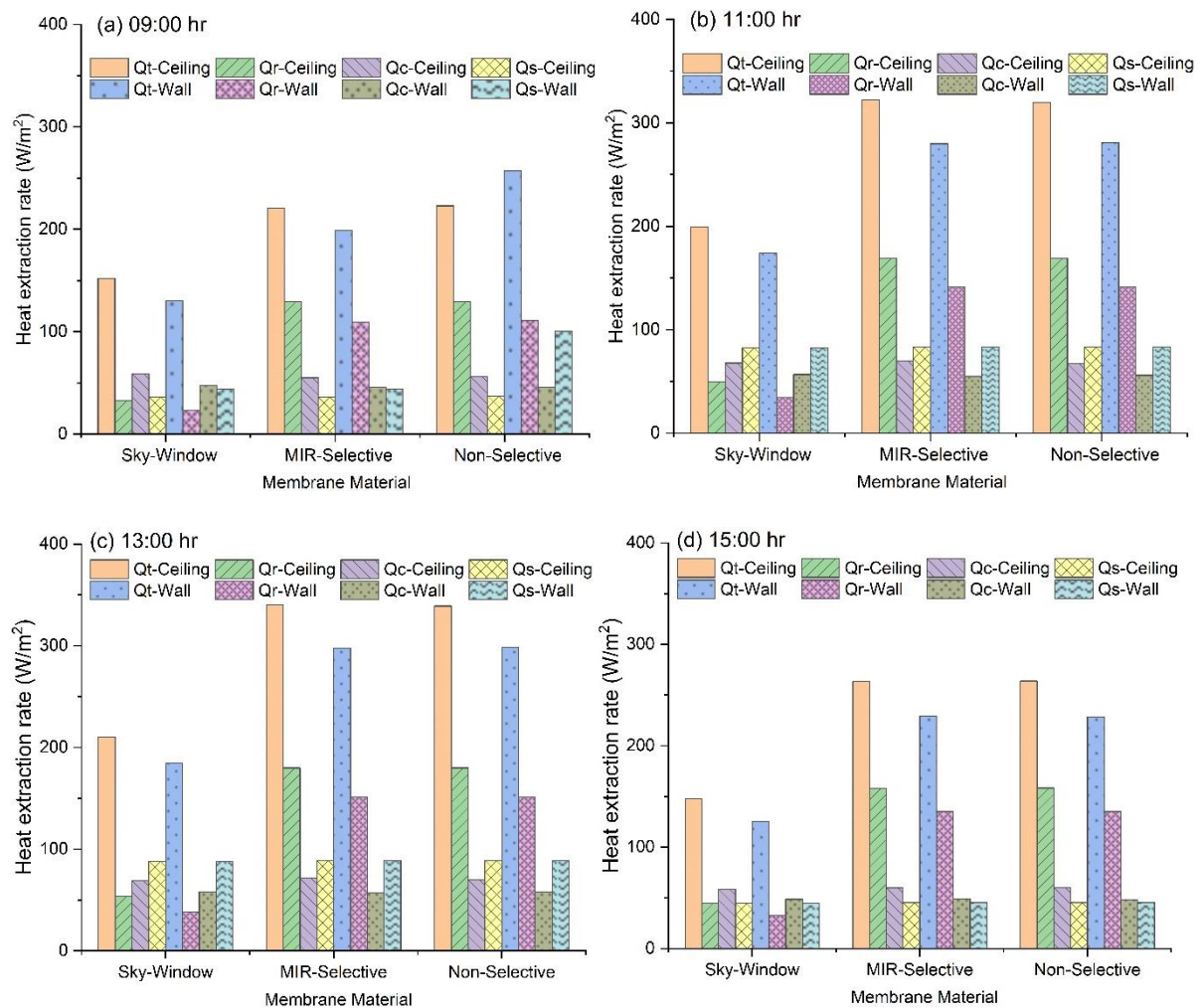


Figure 3.11 Heat flux comparison of the radiant cooling panel with various cover shield configurations at (a) 9:00 (b) 11:00 (c) 13:00 and (d) 15:00 hrs.

The radiative heat transfer from the panel varies with the membrane's optical properties. As the MIR and non-selective allow around 80% of longwave radiation, the radiative heat flux of both configurations is the same all the time. Hence, non-selective membranes can be preferred over MIR-selective, wherever the direct solar radiation is not directly falling on the radiant panel, as it is economical. For instance, the MIR selective membrane serves no benefits over non-selective membranes for the ceiling panels. However, the sky-window selective membrane

outperforms other membranes by selectively allowing the IR radiation within the 8-15 μ m wavelength range, which covers the radiation emitted by the human body. It serves the purpose of absorbing the heat from selective sources, i.e., humans, while minimising the heat absorption from undesired thermal loads. The peak and nadir of the total heat extraction rate over the day are observed at 13:00 and 9:00 hr respectively, for all the configurations. Compared to the MIR and non-selective membranes, sky-window selective membrane configuration reduces the radiative heat flux of ceiling panels by 96.2 and 126.4 W/m² at 9:00 hr and 13:00 hr respectively. The ceiling panel assisted with sky-window selective membrane absorbs 152 and 210.5 W/m² of total heat extraction rate at 9:00 and 13:00 hr respectively, which is 31 and 38% lower than that of MIR-selective membrane assisted ceiling panels. While the wall panel with sky-window selective membrane absorbs the total heat extraction rate of 184.5 W/m² at 13:00 hr.

The large radiative heat transfer potential between the ground surface and the radiant cooling panel has a significant impact on the heat extraction rate. As shown in Figure 3.7, the view factor shared by the ceiling panel to the ground surface is 0.7, while the wall panel to the ground surface is 0.4. The variation of radiative heat flux of panels follows the same trend as ground surface temperature variation over the day. However, the impact of the ground surface temperature observed on the radiative heat flux is minimal for the sky-window selective configuration as the incident radiation is controlled. The highest radiative heat flux of the ceiling and wall panels observed is 180 and 151.5 W/m² at 13:00 hr, in the MIR and non-selective membrane configurations. Due to the higher view factor to the ground surface, the radiative heat flux of the ceiling panel is always higher than that of wall panels. The view factor of the ceiling and wall panels shared with the manikin is 7 and 13%. Typically, the human core temperature will be 36.1 to 37.2°C, which is lower than the ground surface temperature during the daytime (Table 3.3). Hence, the heat absorbed by the MIR and non-selective membrane-

assisted panels from the human will be much less than the ground surface which is undesired cooling and costs a huge energy. It can be controlled by structure design and membrane configurations. Improving the cooling structure design to improve the view factors between the humans and panels, while reducing between the ground surface and panel will be more effective for the cooling.

The convective heat flux of the ceiling panel is consistently higher than the wall panels, due to their orientations and the buoyancy effect. For the MIR-selective membrane configuration, the difference in convective heat flux between the ceiling and wall cooling panel is 9.5 W/m^2 at 9:00 hr and increased to 14.7, 14.5, and 10.8 for the time of 11:00, 13:00, and 15:00 hr respectively. The convective heat flux of the panel is greatly influenced by the natural convection and membrane temperature. The observed difference in convective heat flux between the investigated membrane configurations for a given time is found to be insignificant. The reason is that the membrane temperature is almost the same for all the membrane configurations (Figure 3.12) for a corresponding panel and time. For the MIR-selective configuration, the convective heat transfer of the ceiling panel is 55.5 W/m^2 at the time of 9:00 hr, and it reaches the peak at 13:00 hr, i.e., 71.5 W/m^2 . It follows a similar trend as the corresponding membrane temperature variation. It can be concluded that the membrane materials have an insignificant influence on the convective heat flux irrespective of the time. Overall, the radiative heat transfer contributes more to the total heat extraction rate, i.e., varies from 50 to 60%. While the convective and solar heat flux contribute 19 to 24 and 17 to 30% respectively.

The membrane temperature is an indicator of condensation, and it should be maintained above the dew point temperature of the ambient to reduce condensation risk. The variation of ceiling and wall panels' membrane temperature, and their corresponding ambient air and dew point - temperatures are shown in Figure 3.12. The membrane surface temperature is influenced by

interior and exterior surface convective heat transfer and absorptivity of membrane material. For all the membrane configurations, the absorptivity of the membrane is 0.1, while transmissivity and reflectivity vary. Hence, absorption of incident solar radiation is the same for all the membrane configurations, resulting in minimal variation in the respective panel membrane's temperature at a given time. The membrane temperature varies in the range of 31.8 to 37.4°C, over the day, and they are higher than the respective ambient air temperature, as the absorption of solar radiation significantly impacts the membrane temperature. However, due to its optical properties, i.e., high transmissivity and low emissivity, the effect of heat emission from the membrane is not significant. The wall panel's membrane temperature is slightly higher than that of the ceiling panel membrane, and the difference is noticeably higher at 9:00 hr, due to direct solar radiation exposure on the wall panel membrane.

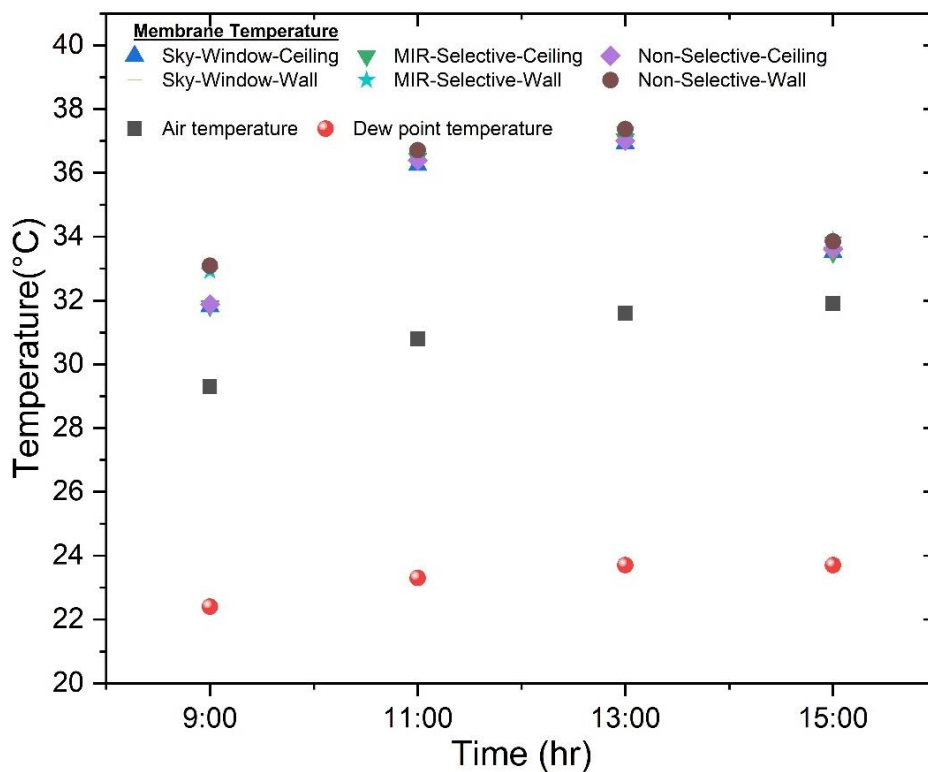


Figure 3.12 Variation of ceiling and wall panels' membrane temperature, and their corresponding ambient air and dew point temperatures at different times of the day

3.3.4 Practical Implications of the Prototype Design

The LOCH prototype is intended to provide comfort for a single occupant. The heat extraction of the prototype for the investigated membrane configurations over the day is shown in Figure 3.13. Due to the selective transparency of the sky-window selective membrane demonstrating superior cooling performance, it has the lowest heat extraction compared to other membrane configurations, irrespective of the time of the day. Their heat extraction is 33 to 44.6% and 38 to 44% lower than MIR and non-selective membranes respectively. The difference in the total heat extraction between MIR and non-selective membrane is noticeable at 9:00 hr, due to higher solar heat load on non-selective membrane configuration, i.e., 0.93 kW of heat absorbed by non-selective, where 0.79 kW absorbed by MIR selective membrane. For the rest of the studied hours, the total heat extraction rate of MIR-selective is the same as the non-selective membrane case. Considering the cooling system operation from 9:00 to 15:00, the approximate energy consumption of the sky-window selective membrane-assisted prototype is 3.94 kWh, whereas MIR and non-selective configured prototypes are 6.4 and 6.54 kWh respectively.

The present findings confirm that sky-selective membranes are effective in terms of thermal performance for outdoor radiant cooling applications. The sky window selective membranes such as PEA and STATIC (Torgerson & Hellhake, 2020) are under the development stage, and currently, it is being manufactured only in laboratory size. As this sky-window selective membrane is getting more attention in the field of daytime radiative sky cooling, large-scale production can be expected in the future. Compared to nonselective, MIR selective membranes are effective only when the cooling panel is exposed to direct solar radiation. Additional shading is enough to avoid direct solar radiation exposure, and non-selective membranes such as LDPE membranes can be utilized effectively. In terms of cost and availability, non-selective membranes are cheap and perform the same as MIR-selective membranes, under the shaded

condition. With the advancement of technology, the cooling system operation would be effectively under control for the effective control in terms of energy and thermal comfort.

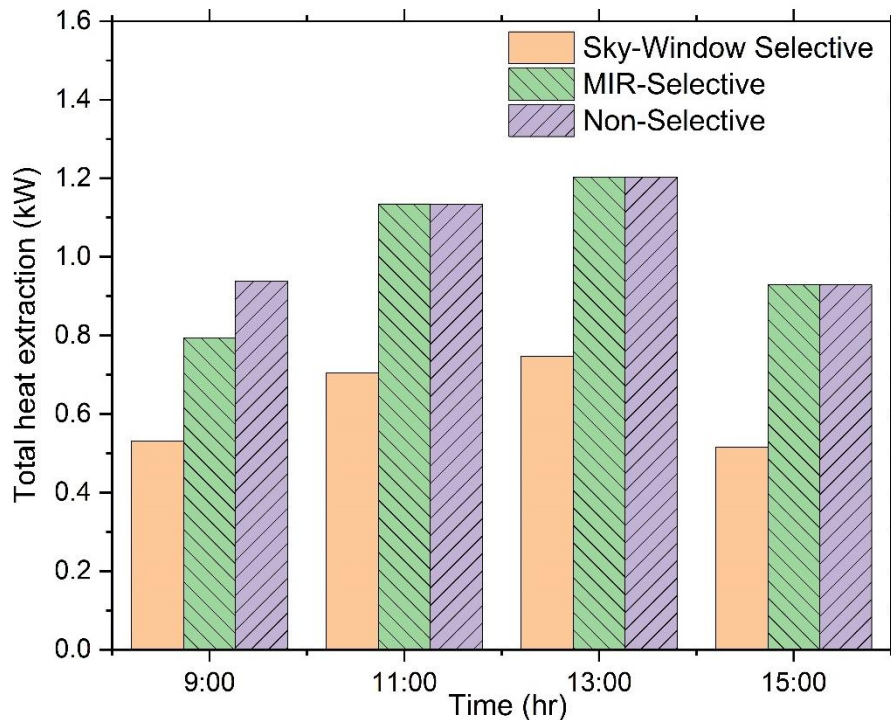


Figure 3.13 Comparison of panel heat extraction rate of the three membrane types at different times of the day

3.4 Summary

This study numerically investigated the thermal performance of a LOCH prototype equipped with membrane-assisted RCS. This chapter attempted to address the second key question related to energy consumption, and the third question associated with the design consideration for energy efficiency.

The sky window selective membrane performs best and avoids undesired heat loads, while the MIR-selective membrane-configured panels exhibit a higher heat absorption rate of 37 to 58% for the wall panel and 45 to 78% for the ceiling panel, compared with the sky-window-selective membrane-assisted panel. Non-selective membrane-configured panels allowed 1.2 times higher solar heat flux absorption than MIR-selective membrane under direct solar radiation.

The MIR-selective and non-selective membranes perform the same when the panel is not exposed to direct solar radiation. Hence, compared to MIR-selective membranes, non-selective membranes are preferred for shaded outdoor areas, as they are comparatively cheap and effective.

Sky-window membranes demonstrated superior cooling performance, offering up to 44% energy savings compared to non-selective membranes. Energy consumption estimates for a single occupant were 3.94 kWh with sky-window membranes and 6.4-6.54 kWh with MIR and non-selective membranes.

Although the sky window membranes are in the development stage, they are expected to be commercially available in the near future. Long-wave radiation from ground surfaces potentially affects the thermal performance of the panel, which can be controlled through suitable membranes and cooling structure design blocking undesirable short- and long-wave radiation to enable effective, low-energy cooling.

CHAPTER 4

Thermal Sensation Assessment - Coupling CFD and Radiation Modelling with Human Body Thermoregulation Model

The present chapter provides a novel method to assess the thermal sensation in the outdoor environment by coupling CFD and radiation modelling with the human body thermoregulation model and using the updated CBE comfort model. The objectives of the present chapter include (i) developing the CFD and radiation modelling of LOCH with the presence of CTM in an outdoor environment, (ii) establishing the coupling method between the outdoor environment modelling with human thermoregulation model, i.e., JOS-3 model (iii) analysing and comparing CFD-CTM-JOS3 coupling method with CTM-free simplified approach. The present chapter provides insights into the novel thermal sensation assessment and the effect of the proposed cooling system on human thermal sensation under the summer conditions of Hong Kong.

4.1 Research Background

In the urban outdoor environment, thermal comfort is influenced by a variety of ambient factors such as wind velocity, solar radiation, long-wave radiation from surroundings, air temperature and humidity. As these factors are constantly changing in outdoor environments, the assessment of outdoor thermal comfort is a complex and challenging task. The mainstream thermal comfort indices were originally developed to assess indoor thermal comfort, while, some of the indices were modified for the outdoor environment. There are 165 thermal comfort indices that have been developed for both indoors and outdoors (de Freitas & Grigorieva,

2017). Among them, PET, UTCI, PMV, and SET are the widely used outdoor thermal comfort indices.

Despite the variability of existing thermal comfort indices, there are still several limitations and gaps in the existing methods, UTCI, PET, and OUT_SET* were not able to provide accurate quantification of asymmetric solar radiation and dynamic wind outdoors (Huang et al., 2017). One of the main limitations of the existing outdoor comfort models is their inability to precisely account for the effects of complex thermal environmental factors such as solar radiation and wind. Solar radiation, for example, creates highly asymmetric radiation conditions for humans. Turbulent and gusty winds outdoors result in a much higher rate of convective heat transfer between the human body and the environment than indoors (Yu et al., 2020). Additionally, different body segments experience different local thermal conditions due to thermal stratification and varying exposure to solar radiation and other ambient factors. Although some of the traditional comfort models such as PET, UTCI, SET, and ET* consider the human thermoregulation system, there is a lack of accuracy due to inaccurate consideration of ambient factors (Huang et al., 2017; K. Li, Liu, & Bao, 2022). As a result, there is a need for more accurate and comprehensive methods for assessing thermal comfort outdoors.

The interface between the human thermoregulation system and the ambient environment can be established by coupling CFD simulation and the human thermoregulation model potentially, where the CFD captures the local ambient conditions and the heat exchange between a human body and the ambient. There were several studies reported on the coupling method for indoor applications early in the century (Choudhary & Udayraj, 2022; Murakami et al., 2000). One of the shortcomings of this method is that the computation cost is too high. However, the comprehensive performance of this integrated method has yet to be evaluated for the complex outdoor urban environment.

Building upon existing literature and addressing a research gap, the present study aims to enhance the interface between outdoor environment modelling and thermoregulation models and proposes a methodology to assess outdoor thermal sensation. The methodology couples CFD and radiation modelling of the outdoor environment, along with a detailed geometry of a CTM, with the JOS-3 thermoregulation model (Takahashi et al., 2021b) to assess the human physiological response. The simulated physiological response is then utilized to assess thermal sensation using the CBE comfort model (Xie et al., 2018; Hui Zhang et al., 2010). The proposed methodology considers the effects of various outdoor environmental factors including solar radiation, long-wave radiation, wind and ambient air temperature to assess thermal sensation. The proposed methodology will be applied to investigate the thermal sensation of the LOCH which is made of membrane-assisted radiant cooling panels. The objectives of the present study involve developing the urban environment modelling along with a detailed geometry of unclothed standing female CTM, establishing the coupling with the JOS-3 model and assessing the local and overall thermal sensation. The assessed thermal sensation vote (TSV) will be compared to the thermal comfort survey conducted in the experiment facility. Different ways of coupling methods within the CFD-CTM-JOS-3 coupling, based on the speed of convergence, will be analysed for various wind velocity conditions. A CTM-free simplified approach of utilizing the existing CHTC correlation to reduce the computational cost and complexity of CTM meshing will be analysed and compared with the CFD-CTM-JOS-3 coupling.

4.2 Methodology

4.2.1 Coupling of Environment Modelling and Human Thermoregulation Model

The generalized methodology to assess the thermal sensation by coupling environment modelling with a human thermoregulation model along with the CBE thermal comfort model is proposed. The environmental parameters and convective and radiative heat exchange between the human body and surroundings are modelled using CFD and radiation modelling techniques. A 3D CTM is considered in the computational domain, to estimate the heat exchanges for each local part. The JOS-3 thermoregulation model, the most updated model as of now, is employed and coupled with the CFD simulation. The converged skin temperature obtained from the coupling method is fed to the CBE thermal comfort model to predict the local and overall thermal sensation of the human body.

The coupling process between the environment modelling and the JOS-3 thermoregulation model involved various steps. The flow chart of coupling between CFD and radiation modelling and the JOS-3 thermoregulation system is shown in Figure 4.1. Based on the convective heat loss prediction of CTM, two coupling approaches are proposed, i.e., CFD-CTM-JOS-3 coupling and a CTM-free simplified approach.

(i) CFD-CTM-JOS-3 coupling method

In the first step, the outdoor environment modelling considering the CTM in the computational domain is modelled using CFD and radiation modelling. The simulation will be initiated with the assumed skin temperatures, i.e., 33.7°C, for all body segments of CTM. Considering the outdoor ambient parameters such as long-wave and solar radiations, wind velocity and air temperature, the CFD model helps to accurately capture the local heat transfer coefficients and MRT for the complex body surfaces.

The convective heat transfer coefficient (h_c) is calculated using eq. 4.1, where the convective heat loss (Q_c) is obtained from the CFD simulation. The local air temperature (T_{air}) can be assessed at different heights adjacent to the local body parts, due to the vertical temperature gradient. The higher ground surface temperature has a significant temperature gradient in proximity.

$$h_c = \frac{Q_c}{(T_{sk} - T_{air})} \quad [4.1]$$

The MRT is influenced by long-wave radiation from the surrounding building surfaces, ground surfaces, and direct and diffused solar radiation. Hence, the MRT is calculated using radiation fluxes, i.e., both long-wave and short-wave components obtained from radiation modelling. The radiative heat transfer coefficient (h_r) for each body segment is calculated using eq.4.2, where the radiative heat flux ($Q_{r(lw+Solar)}$) and MRT (T_{mrt}) are obtained from the simulation.

$$h_r = \frac{Q_{r(lw+Solar)}}{(T_{sk} - T_{mrt})} \quad [4.2]$$

In the next step, the convective and radiative heat transfer coefficients, environmental factors such as MRT, air velocity and air temperatures from the CFD simulation are provided as the input to the JOS-3 thermoregulation model to simulate the physiological responses, i.e., local skin temperature. The constant relative humidity is defined in the JOS-3 model to determine the latent heat loss from the skin. For the remaining parameters, the default values from the JOS-3 model are considered. Further, the local skin temperature obtained from the JOS-3 model will be feedback to the CFD model as boundary conditions, and this iteration will be continued until the mean skin temperature difference between the consecutive iterations is less than 0.1°C.

In this study, two hypotheses, namely one-way coupling (without feedback) and two-way coupling (with feedback until convergence), have been explored and compared, based on the

faster convergence reported by Liang et al. (H. Liang, Tanabe, & Niu, 2023) for the coupling method in the outdoor environment. In the final step, the local and overall thermal sensations are assessed using the advanced CBE thermal comfort model, which has been updated for the outdoor environment (Xie et al., 2020). The obtained skin temperature is processed to predict the thermal sensation using the CBE thermal comfort model.

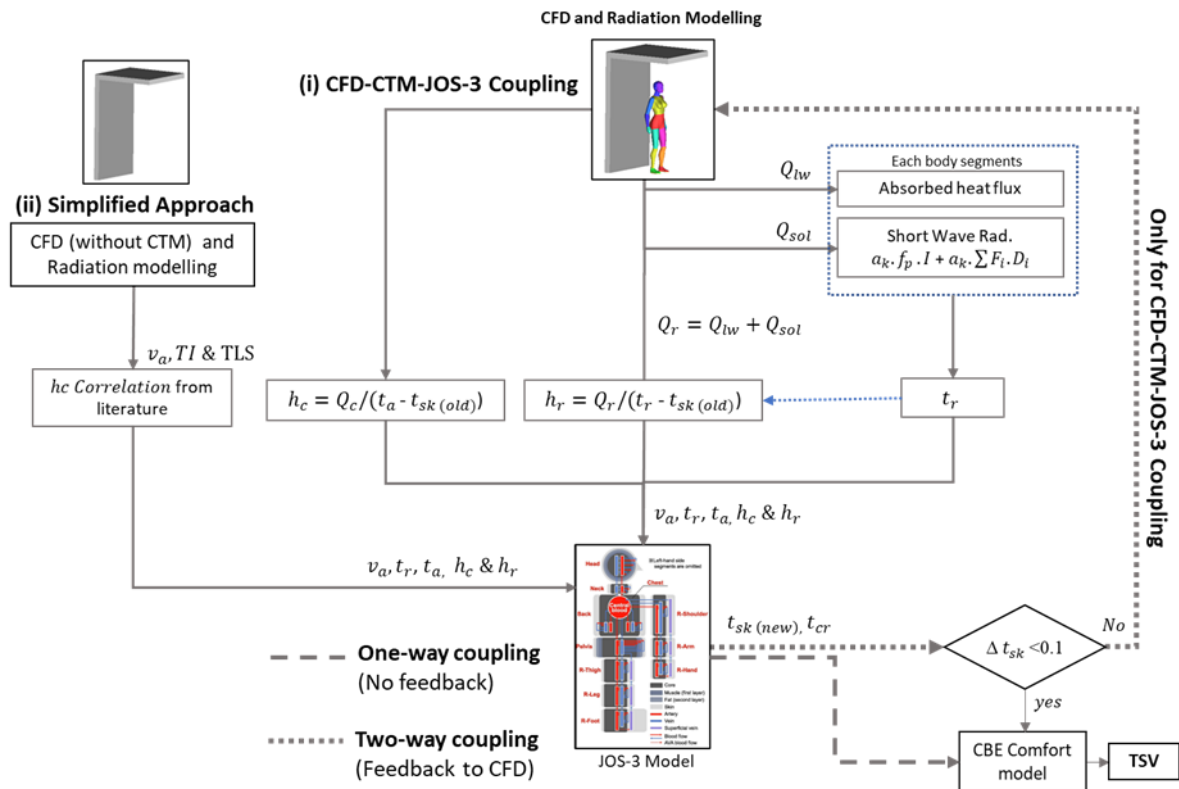


Figure 4.1 Flow chart of coupling methods (i) CFD-CTM-JOS-3 method (Both one-way and two-way coupling) (ii) CTM-free simplified approach (one-way coupling only)

(ii) CTM-free simplified approach

To eliminate the complexity involved in the mesh generation around the CTM and reduce the computation cost of CFD simulation, a CTM-free simplified approach is proposed (Figure 4.1). In the CFD-CTM-JOS-3 coupling method, the effect of wind parameters is simulated using CFD, while in the CTM-free simplified approach, the CHTC is calculated from the developed correlations reported in the literature. In both methods, the effect of solar and long wave

radiation is simulated by radiation modelling using Ansys Fluent. The CTM-free simplified approach needs the turbulence parameters, i.e., turbulence intensity (TI) and the turbulent length scale (TLS), at the CTM position, to determine the local CHTC of CTM. The turbulence parameter defined at the velocity inlet will not be the same at the CTM position due to physical and numerical dissipations. Therefore, an LES model is employed to simulate the wind condition in a computation domain without CTM. The correlations reported in the literature (eqns. 4.3 and 4.4) accounting for turbulent parameters can be used for the local CHTC calculation, considering the limitations of the study.

$$h_c = Au^n(1 + B.TI.u^{0.5}) \quad [4.3]$$

$$h_c = Au^n(1 + B.TI.u^{0.5}).(L/D)^\beta. \quad [4.4]$$

Where, h_c represents the heat transfer coefficients, A , B , n and β are the constants. D is the diameter of the human body. u , L , and TI represent wind velocity, turbulence length scale and turbulent intensity respectively.

4.2.2 JOS-3 Thermoregulation Model

The JOS-3 model divides the human body into 17 segments and consists of 85 nodes in total, including the blood compartment. The schematic of the human thermoregulation model is shown in Figure 4.2. The head and pelvis are composed of core, muscle, fat, skin, artery, and vein nodes. The chest, neck, and back regions consist of the core, skin, artery, and vein nodes, while the remaining parts additionally include a superficial vein. Equation 4.5 shows the generalized heat balance equation for the nodes.

$$Cap_{j(i)} \frac{d}{dt} (T_{j(i)}) = Q_{j(i)} + B_{j(i)} - D_{j-j(i)} - (C_{j(i)} + R_{j(i)}) - E_{j(i)} - RES_{j(i)} \quad [4.5]$$

Where, Cap , T and t are the heat capacity, temperature, and time respectively. The subscripts i , j , and j represent the segment number, tissues, and adjacent body tissues, respectively. Q is

the heat production, and B, D, C, R, E and RES are the heat exchange by blood flow, conduction, convection, radiation, evaporation, and respiration respectively. The sensible and the latent heat loss at the skin surface are expressed by eqns.4.6 and 4.8.

$$(C_{(i)} + R_{(i)}) = h_{t(i)} \cdot (T_{sk(i)} - T_{o(i)}) \cdot BSA_{(i)} \quad [4.6]$$

$$\frac{1}{h_{t(i)}} = 0.155 \cdot I_{cl(i)} + \frac{1}{f_{cl(i)} \cdot (h_{c(i)} + h_{r(i)})} (T_{sk(i)} - T_{o(i)}) \cdot BSA_{(i)} \quad [4.7]$$

$$E_{(i)} = w_{(i)} \cdot h_{et(i)} \cdot (P_{ssk(i)} - P_{a(i)}) \cdot BSA_{(i)} \quad [4.8]$$

$$\frac{1}{h_{et(i)}} = \frac{0.155 \cdot I_{cl(i)}}{L_R \cdot i_{cl(i)}} + \frac{1}{f_{cl(i)} \cdot L_R \cdot h_{c(i)}} \quad [4.9]$$

Where h is the heat transfer coefficient (W/m^2K), and its subscripts t , c , r , et represent total, convective, radiative and total evaporative respectively. The subscripts sk and o represent the skin and operative temperatures respectively. I_{cl} and f_{cl} are the clothing insulation and the clothing area factor. BSA is body surface area (m^2), w is skin wittedness, L_R is Lewis ratio, and i_{cl} is clothing vapour permeation efficiency. P_{ssk} and P_a are the saturated water vapour pressure at skin temperature and water vapour pressure in the ambient air.

As the JOS-3 model is suitable for the human physiological responses in non-uniform and transient environments, and the consideration of solar radiation, this model attempted to be used for outdoor applications. The environmental parameters such as local air temperature, mean radiant temperature and the convective and radiative heat transfer coefficients are obtained from the outdoor CFD modelling considering CTM in the computational domain. The relative humidity is assumed to be uniform throughout the body, i.e., RH: 60%. The person-related parameters are metabolic rate: 1.25 met, height: 1.584 m, sex: female, basal metabolic rate equation: Japanese, weight: 60 kg, age: 30 years old, and other input values are set as default values of the JOS-3 model. As the simulation is performed for a steady state, the simulation time is chosen to be 120 min.

Despite being an updated thermoregulation model, the JOS-3 model exhibits several limitations. These include a lack of sufficient experimental data to fully validate the model, the absence of ethnic considerations, the omission of conduction heat exchange between body segments, and the neglect of clothing material factors such as heat capacity, moisture absorption and release. The model has not yet been validated for outdoor environments. The convective and radiative asymmetries in a single element have not been accounted for in this model, which limits the consideration of actual fluid filled around the segments. The effect of wind and body movements in the conductive and evaporative heat transfer in the clothing-covered body surface needed to be integrated into the model, for better accuracy in sweat loss prediction (Parsons, et al., 1999; Hui Zhang et al., 2010). Nevertheless, it is anticipated that future updates of the JOS model series will address and overcome these limitations.

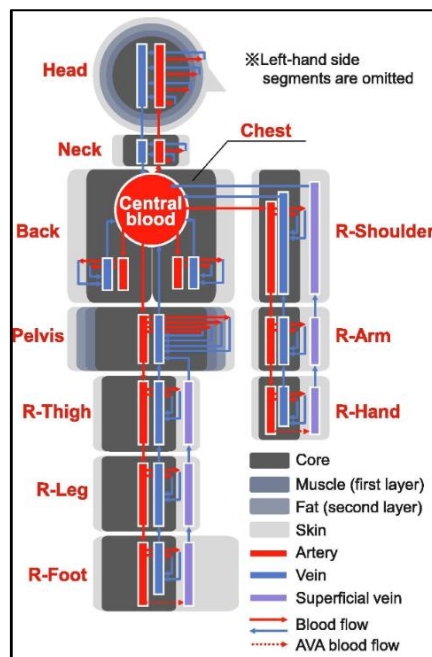


Figure 4.2 Schematic of human thermoregulation model (Takahashi et al., 2021b)

4.2.3 Thermal Sensation Assessment

To correlate subjective perceptions with physiological parameters obtained from the human thermoregulation model, a thermal sensation model is needed. In this study, the CBE model

(Hui Zhang et al., 2010) which is one of these advanced multi-nodal thermal sensation models with broad application was used.

For the determination of human thermal sensation responses, thermoreceptors located in the skin play a crucial role. These thermoreceptors detect the temperatures of the surrounding tissues and transmit signals to the brain, enabling the interpretation of the environment as a thermal sensation. Accordingly, the CBE model developed a local thermal sensation model by using the logistic regression function to link local skin temperatures and thermal sensations from experimental data from human subjects (Hui Zhang et al., 2010). In this model, the thermal sensation results are mainly determined by the bias between the local skin temperature and its corresponding set point. The set point for a specific body part is treated as the local skin temperature at which the sensation for that body part is thermally neutral (TSV = 0). The influence of whole-body level sensation on local sensations is also considered in the CBE model by using mean skin temperature and mean set point. The equation for local sensation calculation is shown as follows:

$$Local\ Sensation = 4 \left(\frac{2}{1 + e^{[-(C1+K1)(T_{skin,i} - T_{skin,i,set}) + K1(T_{skin,m} - T_{skin,m,set})]}} - 1 \right) \quad [4.10]$$

where $T_{skin,i}$ is the skin temperature for a body part i , and $T_{skin,m}$ is the mean skin temperature calculated by the seven-site method. T_{skin} with the subscript, set illustrates the skin temperature as a set point. $C1$ and $K1$ are coefficients of slope controls in the logistic function.

Due to the retention effect of thermal sensation and the inevitable slight fluctuation of local skin temperature in outdoor conditions, the concept of a null zone, a range of local skin temperatures, was used instead of a specific set point. The updated local thermal sensation

equation for the outdoor environment and the conditions of the local skin temperature deviation from the null zone are shown in eqns. 4.11 and 4.12.

$$Local\ Sensation = 4 \left(\frac{2}{1 + e^{[-(C1+K1)(T_{skin,i} - T_{skin,i,null\ zone}) + K1(T_{skin,m} - T_{skin,m,null\ zone})]}} - 1 \right) \quad [4.11]$$

$$T_{skin} - T_{skin,null\ zone} = \begin{cases} T_{skin} - T_{skin,null\ zone,upper} & T_{skin} \geq T_{skin,null\ zone,upper} \\ T_{skin} - T_{skin,null\ zone,lower} & T_{skin} \leq T_{skin,null\ zone,lower} \\ 0 & otherwise \end{cases} \quad [4.12]$$

The null zone temperature range for females and the coefficients for each body part are provided in Table 4.1 To obtain the overall sensations from local sensations, in the CBE model, local sensation groups are categorized into seven models including the high-level warm (cold) model, low-level warm (cold) model, opposite warm (cold) model and opposite-dominated cold model. The calculation methods will differ according to which model a sensation group belongs.

Table 4.1 Null zone skin temperature range and coefficients of body parts for the updated CBE comfort model (Xie et al., 2020; Y. Zhao, Zhang, Arens, & Zhao, 2014)

Body Segments	Female_ Tskin, Null zone		C1_warm	K1_warm
	Lower limit	Upper limit		
Head	33.41	34.57	1.3	0.2
Face	33.41	34.57	0.7	0.1
Neck	33.41	34.57	0.6	0.2
Abdomen	33.88	35.08	1.25	0.15
Chest	33.18	34.25	1	0.1
Back	34.60	35.71	1	0.1

Body Segments	Female_ Tskin, Null zone		C1_warm	K1_warm
	Lower limit	Upper limit		
Pelvis	32.74	34.84	0.4	0.15
L_UpperArm	29.76	31.11	0.4	0.1
L_LowerArm	31.06	32.79	0.7	0.1
L_Hand	29.45	33.18	0.45	0.15
R_UpperArm	29.76	31.11	0.29	0.11
R_LowerArm	31.06	32.79	0.4	0.1
R_Hand	29.45	33.18	0.26	0.15
L_Thigh	30.85	32.51	0.4	0.1
L_Leg	30.41	31.14	0.7	0.1
L_Foot	29.48	33.84	0.45	0.15
R_Thigh	30.85	32.51	0.29	0.1
R_Leg	30.41	31.14	0.4	0.1
R_Foot	29.48	33.84	0.26	0.15

The pieced overall thermal sensation calculation model exhibits discontinuity, leading to noticeable jumps when local sensations undergo smooth transitions across different calculation models. To mitigate these sudden jumps in the overall sensation results, the sigmoid function is employed. This smoothing function ensures the continuity of result values when a sensation group is in the critical state between two distinct pieced calculation models.

4.3 Thermal Sensation Assessment in Localised Outdoor Cooling Hub

4.3.1 CFD Modelling of Localised Outdoor Cooling Hub

The influence of ambient parameters and the LOCH on the CTM is modelled using CFD techniques. In numerical modelling, the effect of solar radiation, long-wave radiation and

outdoor wind parameters need to be considered. As the study was performed in an open space, the boundary conditions should be close enough to represent the real ambient condition of the study location. Therefore, the solar radiation and ambient conditions are obtained from the weather file of Hong Kong (Betti et al., 2022) and the corresponding ground surface temperature is obtained by energy and radiation modelling using the Ladybug and Honeybee plug-in of Grasshopper, following a methodology similar to that used in Chapter 3.

Ansys Fluent was utilized for the CFD model, simulating a CTM subjected to a localised radiant cooling station in an outdoor setting. The comfort performance of the proposed cooling station is being analysed at the worst-case scenario, i.e., 13:00 hr on a typical summer day (July 21) in Hong Kong.

The computational domain size of the model representing the outdoor environment is designed based on AIJ guidelines (Tominaga et al., 2008) (Figure 4.3). The domain size independent study has been carried out to ensure the accuracy of radiation modelling. To analyse the local thermal sensation parameters of the human, a CTM is included in the computational domain. A standing unclothed woman's CTM model has been obtained from the open access source from Kyushu University (Ito) (http://www.phe-kyudai.jp/research_01.html, accessed on November 2023). The CTM consists of 17 body segments, i.e., indicated by different colours in Table 4.2, with a height of 1.584 m. The CTM has been validated against Ito et al.'s wind tunnel experiment (Kazuhide et al., 2015) and a detailed explanation of the model validation is provided in Appendix B.

As the CFD model has been modelled for the outdoor environment, the wind parameters and short-wave and long-wave parameters need to be taken care of. The combined geometry and meshing are generated using ICEM software. Steady Reynolds-Averaged Navier Stokes (RANS) approach used for solving the governing equation. For the turbulence modelling, the

SST $k-\omega$ model is used for the current study, as it has better prediction accuracy in predicting convective heat transfer from CTM (Kazuhide et al., 2015). The y^+ value of the entire CTM surface is maintained below 1.

Table 4.2 Description of local body parts of CTM

Body Part	Area (m ²)
Foot (left and right)	0.035
Leg (left and right)	0.088
Thigh (left and right)	0.124
Hand (left and right)	0.024
Arm (left and right)	0.040
Shoulder (left and right)	0.058
Pelvis	0.212
Chest	0.139
Back	0.084
Face	0.046
Neck	0.076

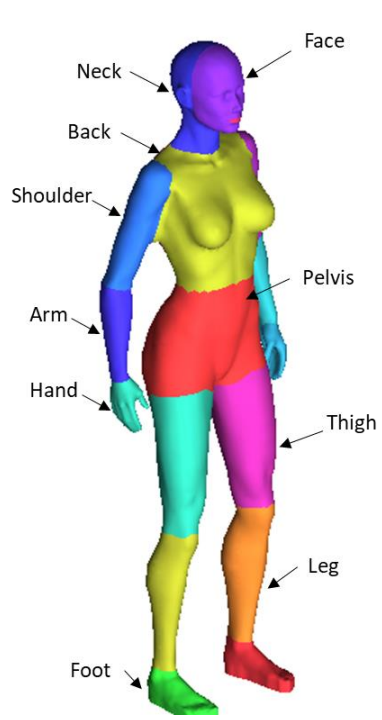
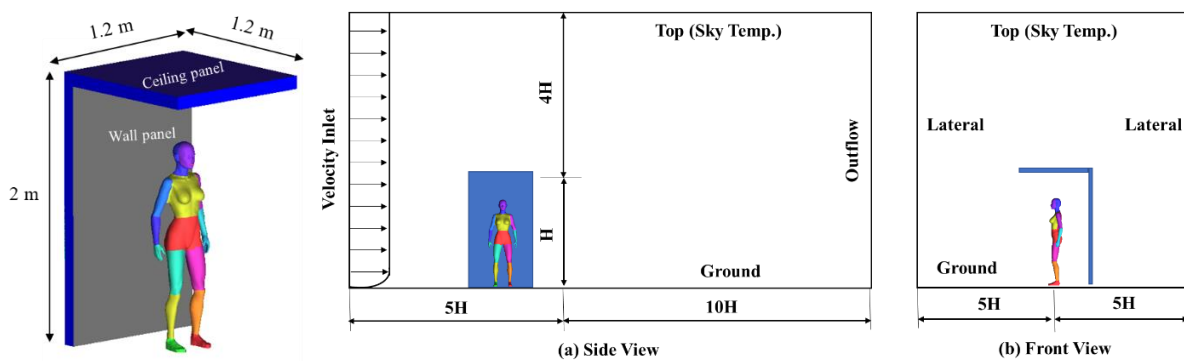



Figure 4.3 Schematic of the computational domain and radiant cooling structure

The DO radiation model has been considered for radiation modelling. The boundary conditions of the CFD model are tabulated in Table 4.3. For the solar radiation model, the solar ray tracing approach is utilized.

Table 4.3 Boundary conditions of the CFD model

Boundaries	Boundary Condition	Description
Inlet	Velocity inlet	v: 1.5 m/s, TI: 29 %, TLS: 6.6 (Zou et al., 2021), T _{air} :31.6°C*
Ground	Isothermal	T: 54.96°C *, ε: 0.8
Panel	Isothermal	T: 10°C, ε:0.95
Membrane	Coupled	semi-transparent, ε:0.124
CTM	Isothermal	Initial temp.: 33.7°C, ε: 0.95
Top surface	Isothermal	T _{sky} :258 K (Gliash et al., 2011), ε: 0.7 (Pandey et al., 1995)
Side surfaces	Symmetry	-
Outlet	Outflow	-

* Obtained from weather file and energy and radiation modelling (from Rhino Grasshopper)

The finite volume scheme was employed to discretize the governing equations. The pressure-velocity coupling utilized the coupled algorithm. Second-order discretization was applied to the convective and diffusion terms, as well as the DO radiation. A double-precision solver was chosen for the simulation. The convergence criteria for the normalized residual errors were set at 10^{-9} for the energy equation and 10^{-6} for other equations.

4.4 Result and Discussion

The proposed methodology to evaluate the outdoor thermal sensation of humans under the LOCH is analysed. The simulation was performed for the time of 13:00 hr on 21st July in Hong

Kong. This case study has been simulated and compared for the hypotheses, one-way coupling (without feedback) and two-way coupling (with feedback until convergence) process (Figure. 4.1). The thermal sensation assessed by the coupling method is compared with the thermal comfort survey results from the experiment facility of the outdoor cooling hub. The thermal sensation assessed by the CTM-free simplified approach is compared with the CFD-CTM-JOS3 coupling method, and their limitations are also discussed.

4.4.1 Convective and Radiative Heat Transfer

The outdoor environment modelling accounting for CTM and outdoor ambient parameters is modelled for outdoor radiant cooling applications. The parameters influencing the heat transfer from skin to the ambient, i.e., MRT and convective and radiative heat transfer, for each body segment for the one-way coupling (0th iteration) and two-way coupling (nth iterations) are shown in Figure 4.4. For each iteration, the local skin temperature obtained from the JOS-3 model will be transferred to environment simulation as the local boundary condition. The local MRT and air temperatures represent the outdoor ambient environment. In this study, the ambient air temperatures are measured at intervals of 0.05 m vertically (ranging from 0 to 1.6 m) and at a distance of 0.5 m horizontally in the upstream direction from the CTM centre position. The averaged air temperature from adjacent points is mapped to each local body part for further processing. There is a moderate deviation in the local MRTs between one-way and two-way coupling, due to the influence of adjacent segments' skin temperature update. The heat transfer coefficients calculated from the simulation results are the function of skin temperature, hence they keep updated for each iteration. The local CHTC of the right-side segments of CTM, i.e., windward side, have higher coefficients than left-hand side segments, i.e., leeward side. The higher incident wind velocity helps to increase the convective heat loss on the windward side. The deviation in the CHTC between one-way and two-way coupling is

less than 5%. It reveals the faster convergence and dominant influence of wind velocity on the convective heat transfer.

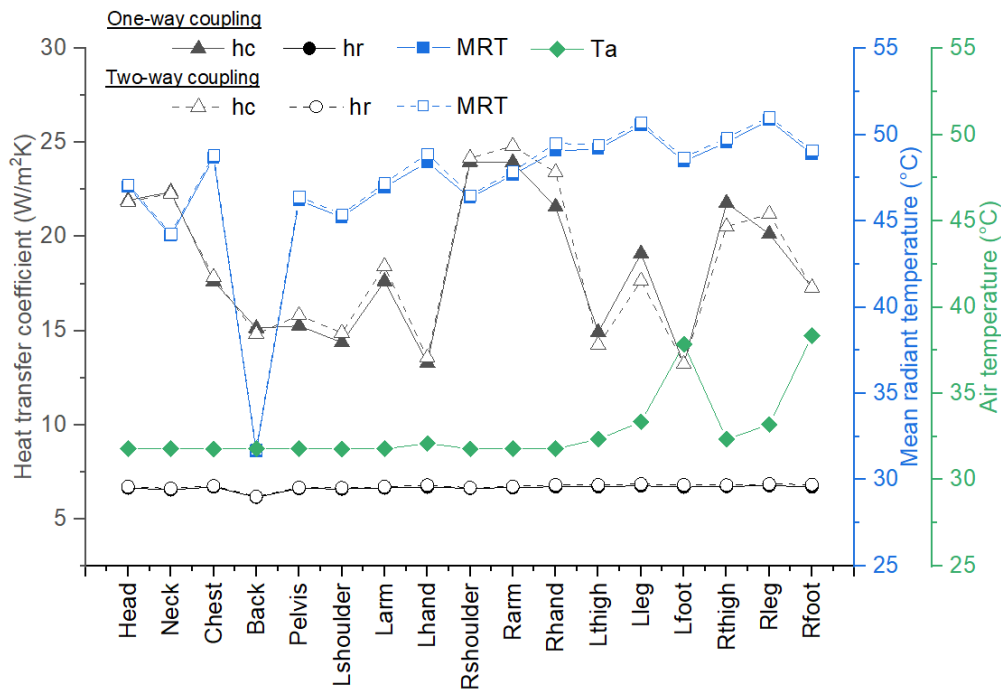


Figure 4.4 Local heat transfer coefficients, MRT and air temperature variation for the one-way and two-way coupling method

4.4.2 Thermal Sensation Assessment using the CFD-CTM-JOS-3 Coupling

Method

The local and overall skin temperatures for the one-way and two-way coupling of the CFD-CTM-JOS-3 coupling method are shown in Figure 4.5. The local and overall skin temperatures are captured once the steady state is achieved in the JOS-3 model for the specified outdoor environment. The feet have the highest skin temperature due to the low wind velocity and high thermal stratification proximity to the ground surface resulting in lower convective heat loss. The lowest skin temperature was observed at the back surface due to the impact of radiant cooling. As the back-surface temperature shares a high view factor with the wall panel, the radiative heat transfer between the panel and back surface due to long-wave radiation is higher.

The deviation between one-way coupling (0th iteration) and two-way coupling (nth iterations) for the local and overall skin temperature is insignificant, i.e., $< 0.1^{\circ}\text{C}$. Consequently, the thermal sensation prediction based on the skin temperature also reveals the insignificant deviation between the local thermal sensation (Figure 4.5b). The CBE model predicts the overall thermal sensation from the local thermal sensation, represented in the 9-point thermal sensation scale. As the thermal sensations experienced by each body segment are different, and the coefficients derived from the experiments for the local thermal sensation assessment, the pattern of TSV could be different than that of skin temperature. The overall thermal sensation is dominated by the local thermal sensation of dominant body parts whenever their local TSV value is less than -1 according to the original logic framework in the CBE comfort model. In the present case, the local TSV of the back surface has a significant influence on the overall TSV. Therefore, the small deviation of local TSV of back between the one-way and two-way coupling has a moderate influence on the overall TSV, i.e., increases from -0.06 to 0.3. However, this observation is based on the proposed cooling hub and its structure and may not be applicable to other outdoor applications.

In the proposed coupling method, the convergence speed is quick, i.e., one-way coupling, to predict the local and overall skin temperature and thermal sensation. The quick convergence is due to the dominant influence of outdoor ambient conditions on the skin temperature over the human thermoregulation system. Hence, it can be concluded that the one-way coupling is adequate to predict the skin temperature and human thermal sensation in the outdoor environment with a wind velocity higher than 1.5 m/s. Further, the influence of wind velocity on the coupling method is discussed in the upcoming section.

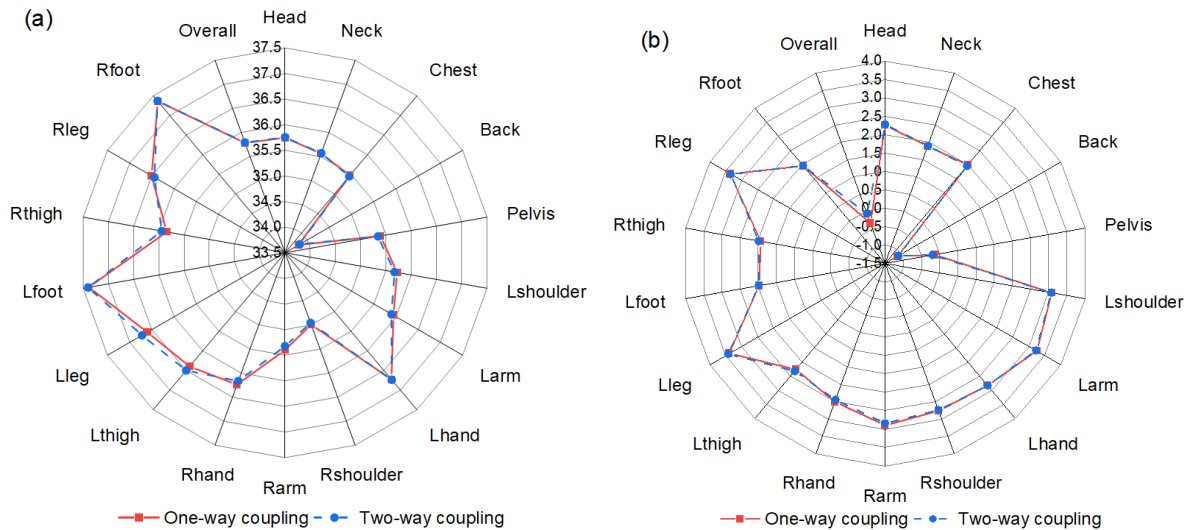


Figure 4.5 (a) Local and overall skin temperature and (b) predicted thermal sensation from one-way and two-way coupling methods (CFD-CTM-JOS-3 coupling)

4.5 Comparison of Thermal Sensation Vote between CFD-CTM-JOS-3 Coupling Method and Thermal Comfort Survey

The local and overall thermal sensation vote assessed by the coupling method is compared with the thermal comfort survey conducted from the outdoor radiant cooling hub experiment facility for similar environmental conditions (Yang et al., 2024). It is important to note that the present section is about the comparison of prediction for similar ambient conditions and average radiant panel temperature. Due to the difficulty in replicating the exact wind field around the human in the transient and non-uniform environment and limited computational sources, a single case with mean ambient conditions has been compared with the comfort survey. On the other hand, due to the lack of skin temperature measurement during the comfort survey, the prediction of human physiological responses is not compared in this study.

The experiment facility is located on the terrace of one of the buildings, i.e., Z-block, on the premises of The Hong Kong Polytechnic University, Hong Kong. The experiment facility consists of three membrane-assisted radiant cooling panels, i.e., one is on the ceiling and the

other two are installed for the wall, as shown in Figure 4.6. The average radiant cooling panel temperature of around 14°C and the survey conducted from 11:30 to 14:30 hr are considered for comparison. The thermal comfort survey was conducted from May to September, which is categorised as hot season as per the measured weather data, where the air temperature ranges from 29.4 to 35.9°C. The details of the human subject and outdoor ambient condition range of the comfort survey are shown in Table 4.4. The local skin temperatures were not measured on the subjects during the thermal comfort survey. The survey was conducted after 10 minutes of stay in the outdoor radiant cooling hub. The clothing insulation considered for the chest, back, pelvis, shoulder, thigh, leg, and feet are 0.57, 0.355, 0.93, 0.42, 0.52, 0.23, and 1.369 clo respectively, and 0 clo was considered for the rest of the body parts.

The survey results were compared with the TSV predicted from the CFD-CTM-JOS3 Coupling method and default JOS-3 model for mean outdoor ambient parameters during the survey (Figure 4.6). The most local parts' thermal sensation was assessed by the coupling method within the standard deviation of the thermal comfort survey data. The local TSV predicted by default- JOS-3 is also within the standard deviation, however, the overall TSV prediction is overpredicted compared to the mean survey results. The local TSV values predicted by the coupling method are closer to the mean value of the comfort survey for several local body parts, compared to the TSV predicted from default JOS-3. While the overall thermal sensation predicted by the coupling method has a close match with the mean of the comfort survey data. The CBE comfort model focuses on detecting the dominant thermal effects and assigns comparatively less weight to the other body parts based on the logical flow of evaluation (Hui Zhang et al., 2010). As a result, the overall thermal sensation predicted by the coupling method is comparatively closer to the mean survey results, irrespective of TSV deviations in the local parts.

Table 4.4 Details of participants and ambient conditions of the comfort survey

Human Subjects Details	
Sample size	17
Ethnic group	Chinese
Age	18-29
Clothing	0.37 clo (with STD:0.09)
Female/male ratio	1.05
BMI	18.5 - 24.9
Range of outdoor weather conditions (May – September)	
Ambient temperature	$32.3 \pm 2.13^{\circ}\text{C}$
Globe Temperature	$38.05 \pm 3.66^{\circ}\text{C}$
RH	$60.7 \pm 6.03 \%$
Wind velocity	$0.7 \pm 0.32 \text{ m/s}$
Solar Radiation	$509.8 \pm 292.43 \text{ W/m}^2$
Panel Temperature	$14.3 \pm 2.4^{\circ}\text{C}$ (Ceiling panel) $13.8 \pm 2.3^{\circ}\text{C}$ (Wall panel)

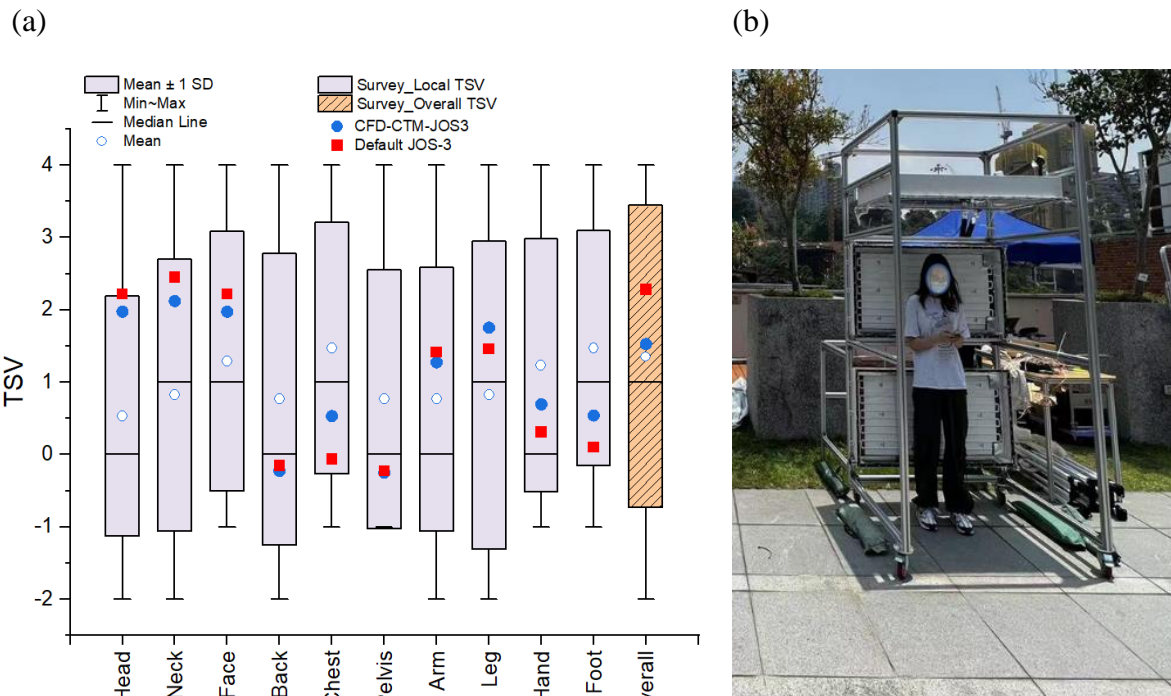


Figure 4.6 (a) Comparison of local and overall TSV between predicted by the CFD-CTM-JOS-3 coupling method and default JOS-model with thermal comfort survey (b) onsite survey of the human subject (Yang et al., 2024)

4.6 Impact of Wind Velocity on the CFD-CTM-JOS-3 Coupling Method

Wind parameters play a crucial role in convective heat transfer from the human body outdoors. The literature suggests that the coupling method in outdoor applications converges faster compared to indoor applications (H. Liang, Tanabe, & Niu, 2023), where only one iteration is sufficient for prediction, whereas indoor applications typically require four to five iterations (Voelker & Alsaad, 2018). One of the reasons for this difference is that convective heat loss due to induced forced convection in the outdoor environment is significantly higher than natural convection in the indoor environment. Therefore, understanding the influence of wind parameters on the coupling process is essential. There were developed correlations to estimate CHTCs using ambient wind parameters such as velocity and turbulent intensity (Yu et al., 2020; Zou et al., 2021). However, the present case study has limitations in implementing these correlations due to potential disturbances caused by the cooling panel to the wind flow. It is crucial to determine the influence of wind parameters on the coupling method in such cases. In the study location of Hong Kong, the frequency of annual wind velocity less than 0.5 m/s is less than 1% (Figure 4.7). Hence, the wind velocity cases of 0.5 m/s, 1 m/s and 1.5 m/s are analysed, considering the faster convergence for the outdoor environment reported (H. Liang, Tanabe, & Niu, 2023). The wind parameters for the investigated cases are listed in Table 4.5 (Zou et al., 2021).

The local CHTC of each body part for the wind velocities of 0.5, 1 and 1.5 m/s are shown in Figure 4.8. One-way and two-way coupling methods are compared to evaluate the necessity of two-way coupling for outdoor environment simulations. For the air velocity cases of 0.5, 1.0 and 1.5 m/s, the deviation between one-way and two-way coupling is insignificant, except for the feet part. Due to the higher ground surface temperature and thermal stratification near the ground, the CHTC of the ground could not be captured accurately. In previous studies, the assumption made for the ground surface temperature is the same as the air temperature to avoid

heat transfer from the ground surface (Zou et al., 2021). In the present study, the ground surface temperature, i.e., 54.9°C, is obtained using the energy and radiation modelling, for the corresponding ambient and solar conditions. Therefore, the estimation of the local heat transfer coefficient of the feet is not reliable due to the presence of a large air temperature gradient near the feet, which makes it difficult to measure the air temperature accurately. To avoid ambiguity for further steps, the heat transfer coefficients for the feet are calculated from the correlation reported in the literature (Zou et al., 2021) for side-facing cases.

Table 4.5 Wind parameters of the different cases (Zou et al., 2021)

Cases	Wind velocity (m/s)	Turbulence Intensity (%)	Turbulent Length Scale (m)
Case-1	1.5	29	6.6
Case-2	1	30	5.0
Case-3	0.5	31	3.4

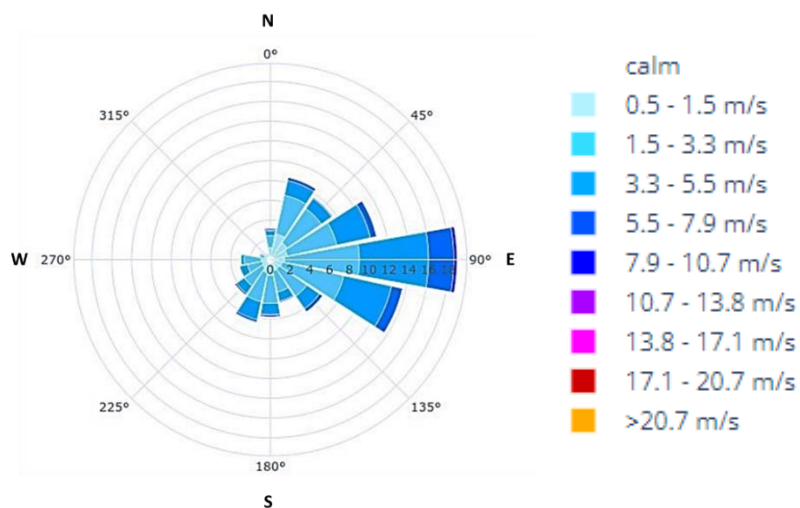


Figure 4.7 Annual Wind Rose Diagram for Hong Kong (Betti et al., 2022) (weather file: Kowloon weather station)

Exposing parts facing the wind direction, i.e., the right portion of the body parts, i.e., right hand, right thigh, right arm, right shoulder, have higher heat transfer coefficients, i.e., range from 8.4 to 25.7 W/m²K. While the local CHTCs of left body parts range from 6 to 19 W/m²K. For the investigated range of wind velocities, the local heat transfer coefficients determined from the one-way and two-way coupling methods have no significant difference, as the buoyancy effects are negligible for the studied outdoor ambient conditions. Hence, it can be concluded that in wind velocities above 0.5 m/s, the one-way coupling is adequate to determine the CHTCs for the outdoor environment.

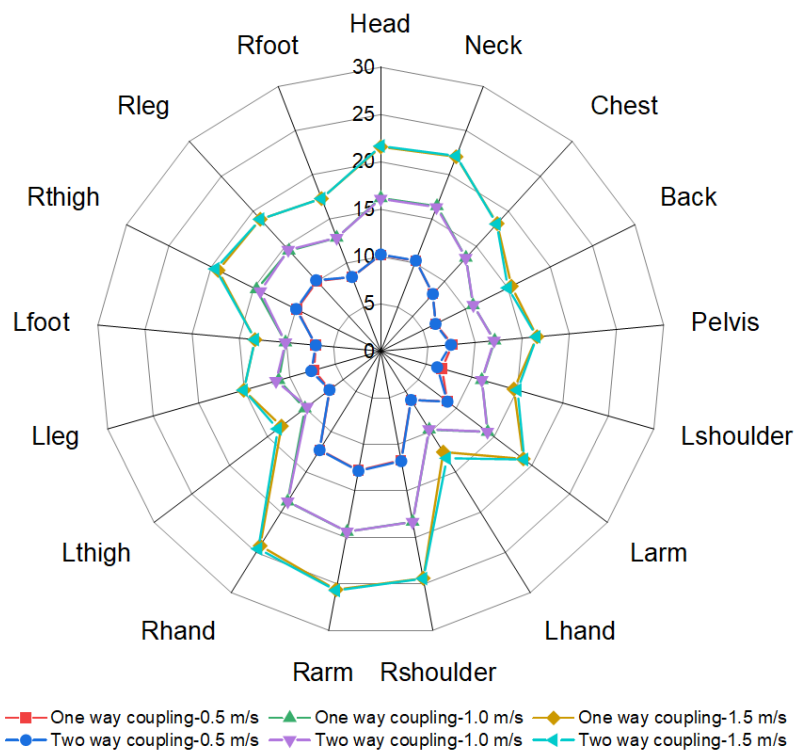


Figure 4.8 Local CHTCs (W/m²K) for the wind velocities of 0.5, 1.0 and 1.5 m/s

Further, the local and overall skin temperature and TSV of CTM for the wind velocities of 0.5, 0.5, 1 and 1.5 m/s are determined and their deviation between one-way and two-way coupling is shown in Figure 4.9. Variation in the wind velocity has a significant impact on the skin temperature and consequently thermal sensation vote. In the outdoor environment for the wind

velocity higher than 0.5 m/s, the proposed coupling method converged in the one coupling itself. Therefore, one-way coupling is sufficiently accurate for predicting the skin temperature, offering additional benefits of reduced computation time and cost.

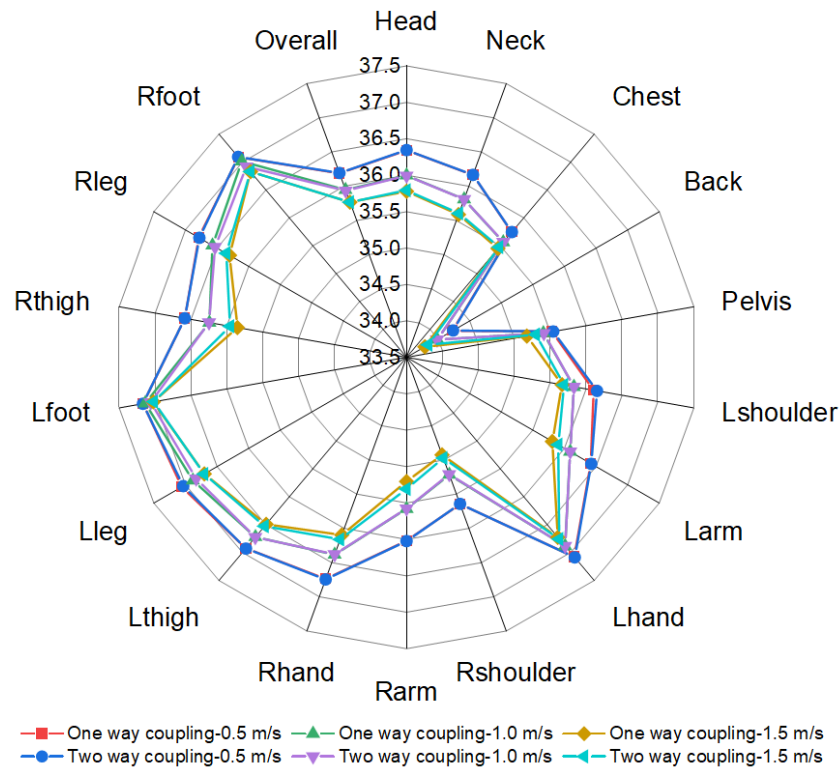


Figure 4.9 Local and mean skin temperatures assessed for the wind velocities of 0.5, 1.0 and 1.5 m/s

4.7 Comparison of the CTM-Free Simplified Approach and the CFD-CTM-JOS-3 Coupling Method

The CHTCs for the local body parts and their relation to the wind parameters have been reported in the literature (de Dear et al., 1997; Yu et al., 2020; Zou et al., 2021). However, the local RHTCs in outdoor environments have not been reported yet. Therefore, the feasibility of the combination of radiation modelling and the heat transfer coefficients from the literature (CTM-free Simplified Approach) for the thermal sensation assessment is analysed and compared with the CFD and radiation modelling (CFD-CTM-JOS-3 coupling). In this section,

convective and radiative heat transfer parameters, skin temperature and thermal sensation votes have been compared for the time of 13:00 hr in Hong Kong.

In the CTM-free simplified approach, radiation modelling was performed in the ANSYS Fluent, and the convection coefficients were derived from the correlation reported in the literature. In the present study, the correlation developed by Zou et al. (Zou et al., 2021) using CFD techniques has been considered for the side-facing scenario. Considering that the CHTC correlation developed from CFD techniques may not be accurate enough compared with that obtained from real wind environments. On the one hand, the heat transfer coefficients for the side-facing scenario are seldom reported in experimental studies, but, on the other hand, it is suggested that the correlation developed from the outdoor experiments could be considered in the future.

It is obvious that the deviations in the local and overall skin temperature between these two methods are insignificant (Figure 4.10a). The proposed cooling system has a strong cooling sensation on the back surface (Figure 4.10b). As per the CBE comfort model, the strong cooling sensation, i.e., $TSV < -1$, of dominant body parts has a significant influence on overall thermal sensation. Even though the deviation of local TSV of the back surface between these two methods is insignificant, i.e., 0.07, it influences the overall TSV, and the deviation is 0.97. The smoothing function introduced in the CBE comfort model to ensure the continuity of overall TSV might cause this deviation. It is one of the limitations of the CBE comfort model, specifically in the critical sensation group between two distinct pieced calculation models. However, considering the insignificant difference in local TSV of body parts between these methods, i.e., < 0.5 , it can be concluded that the CTM-free simplified approach could be used for the thermal sensation assessment in the outdoor wind environment. Compared to the CFD-CTM-JOS-3 coupling method, computational cost, and complex mesh generation around the

human could be relaxed. However, the limitations of the studies associated with the literature considered for hc, are also valid for the CTM-free simplified approach.

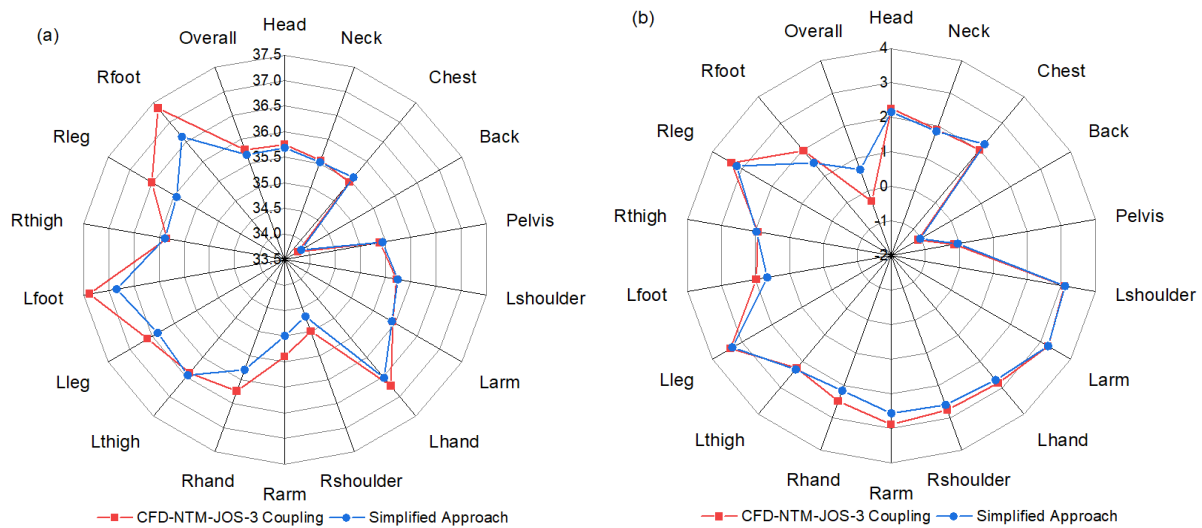


Figure 4.10 Local and overall (a) skin temperature and (b) thermal sensation vote predicted by CFD-CTM-JOS-3 coupling method and CTM-free simplified approach

The literature reported the hc as the function of wind velocity, turbulent length scale, turbulent intensity, and human orientation with respect to the wind directions. As the outdoor wind environment factors have a dominant heat transfer effect over the thermoregulation system, the CTM-free simplified approach could be suitable for outdoor wind environments at which the predominant wind velocity is more than 0.5 m/s. In other words, the CTM-free simplified approach is only suitable for one-way coupling, and not for two-way coupling where the natural convection is dominating such as indoor applications. In the present case of the radiant cooling panel with CTM, various combinations of CTM with respect to the wind direction are shown in Figure 4.11. The wind environment study reported for the CHTC has not considered the local obstacles in the surroundings. Unless the local obstacles such as the radiant panel disturb the flow approaching the CTM, the CTM-free simplified approach can be utilised for the thermal sensation assessment. For instance, in cases 2 and 3, radiant cooling panels are less likely to affect the flow near CTM. This CTM-free simplified approach could be useful for

pedestrian-level thermal comfort assessment and aids in urban design and development. For the remaining cases, the cooling panel influence the wind flow around the CTM. Hence, the CFD-CTM-JOS-3 coupling method needs to be adopted for these kinds of special cases.

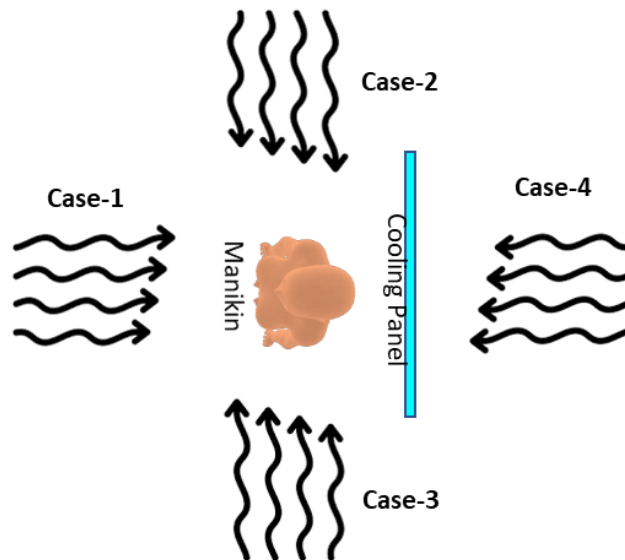


Figure 4.11 Different wind direction and manikin orientation configurations of the outdoor radiant cooling hub

4.8 Summary

The study proposes a coupling method that integrates CFD and radiation modelling with the human thermoregulation system and CBE comfort model. This integrated approach aims to assess the physiological responses and thermal sensations in outdoor environments while considering the effects of solar radiation, long-wave radiation, and wind.

The outdoor radiant cooling hub has been investigated for the coupling method. The CTM is included in the environment modelling, and the boundary conditions representing real outdoor environments are specified. It is found that the coupling method converges quickly, i.e., the skin temperature in the first iteration itself. It indicates that the influence of the outdoor environment has the dominant effect on the heat transfer over the human thermoregulation system. The effects of outdoor wind conditions on the coupling method reveal that one-way

coupling is adequate for a wind velocity of 0.5 m/s and above. As the CTM-free simplified approach is valid only for one-way coupling, it can be concluded that the simplified approach can be used for wind environments with velocities greater than 0.5 m/s. This approach also shows good agreement with the CFD-CTM-JOS3 coupling method. The CTM-free simplified approach reduces the computational cost and complicated mesh generation process, making it a practical tool for the evaluation of thermal comfort at the pedestrian level in the outdoor environment. The proposed coupling and simplified method to assess the thermal sensation has the potential to be used for many outdoor applications and urban design and development.

The CTM-free simplified approach employs heat transfer coefficients derived from the correlation developed by CFD techniques. However, this method is not suitable for indoor applications where the natural convection is dominating, nor it is suitable for scenarios involving local obstacles that disrupt the flow approaching CTM. In future studies, the CHTCs based on field measurements should also be considered. There are certain limitations associated with the JOS-3 model and CBE model and they are expected to be addressed and updated in the near future. These updates will allow for further refinement of the coupling method, resulting in a closer reflection of reality.

CHAPTER 5

Thermal and Comfort Performance Analysis of Outdoor Radiant Cooling System

This chapter evaluates the thermal and comfort performance of a LOCH prototype in street canyon environments typical of dense urban areas like Hong Kong. As LOCHs are intended primarily for bus stop applications situated along major city streets, it is important to analyze their performance within a street canyon context. The objectives of the present chapter include (i) assessing the heat extraction rate and thermal sensation experienced by the occupants for different street canyon orientations and times of day using CFD techniques and CFD-CTM-JOS3 coupling method (ii) assessing and comparing the effect of the cooling system versus a convention bus stop shelter on the thermal sensation experienced by the occupants. The present chapter aims to provide insights into the comfort offered by the proposed cooling system, as well as opportunities for optimization and enhancement in terms of both energy use and comfort levels. The findings could guide standards for effective LOCH design and placement within street networks.

5.1 Methodology

The methodology used in this study builds upon the framework developed in Chapter 4, with specific modifications to the geometry and computational domain for the street canyon configuration (Figure 5.1). Initially, energy and radiation modelling using the Rhino-Grasshopper is used to simulate the building and ground surface temperatures for the street canyon configurations. Key inputs to this modelling included the local weather data, street canyon geometry, and material properties. The resulting ground and building surface

temperatures were then used as boundary conditions for the subsequent CFD simulations. As the one-way coupling method is suitable for the outdoor environment, the ambient parameters and heat transfer coefficients acquired in the CFD simulation were directly input to the JOS-3 model to simulate the skin temperature. Finally, the obtained skin temperature data will be post-processed for the thermal sensation assessment using the CBE comfort tool.

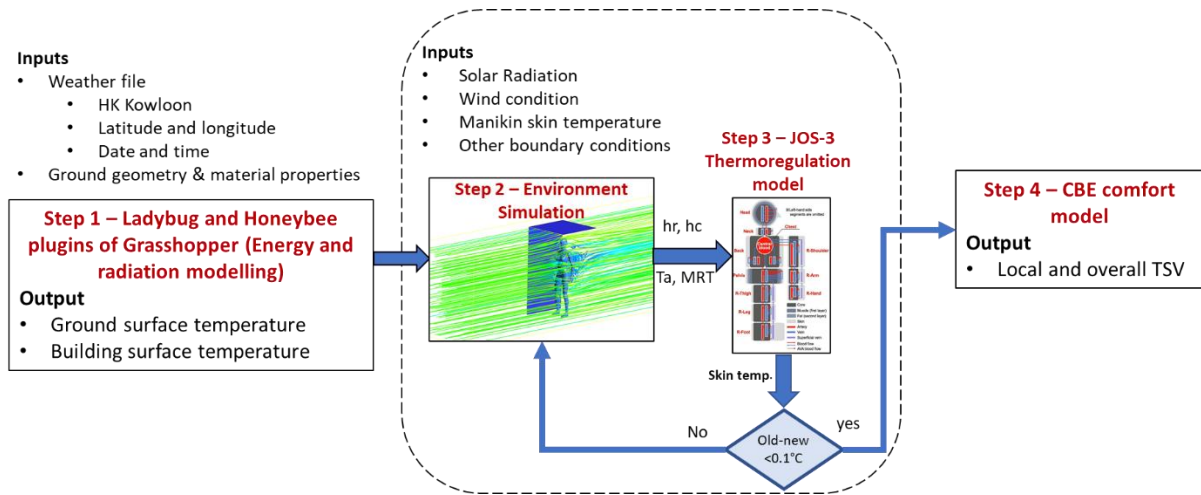


Figure 5.1 Framework of the methodology to assess the heat extraction rate and thermal sensation

The geometry of the street canyon used in the energy and radiation modelling using Rhino-grasshopper and the sun path associated with the street canyon orientations are shown in Figure 5.2. The weather file associated with the Kowloon weather station, in Hong Kong, is accessed from the open-source tool called Clima tool developed by UC Berkeley (Betti et al., 2022). The North-South and East-West orientations of the street canyon were analyzed for various times of the day, i.e., 9:00, 11:00, 13:00 and 15:00 hr. The building and ground surface temperature from the Rhino-grasshopper along with the ambient factors extracted from the weather file for the investigated date and times of the day are listed in Table 5.1. These data serve as the boundary conditions for the computational modelling.

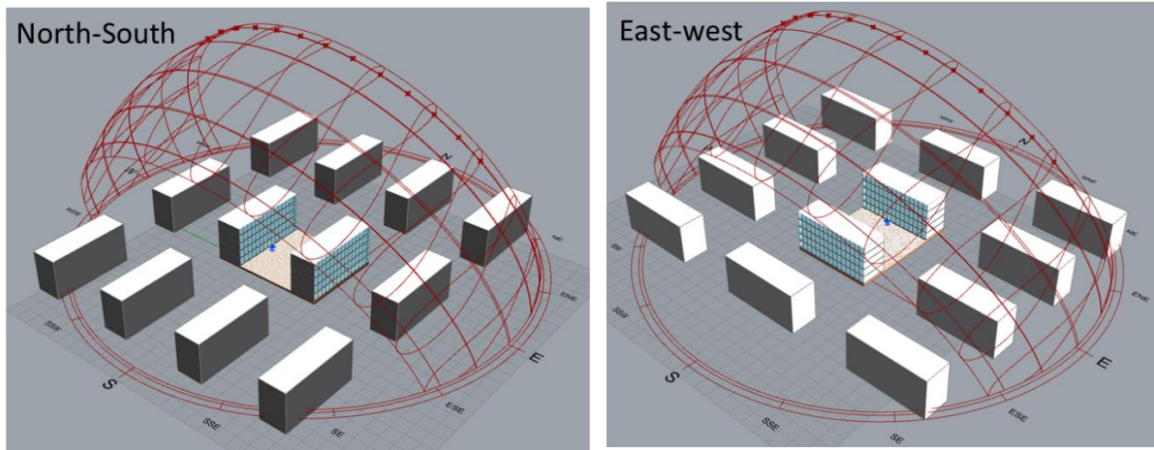


Figure 5.2 Street orientation and respective solar path diagram of Hong Kong

Table 5.1 Ambient factors and ground and building surface temperatures of the investigated times of the day

Hong Kong, 21 st July (Kowloon weather file)							
Time (hr)	Ta (°C)	Solar radiation (W/m ²)		Orientation	Surface temperature (°C)		
		Direct	Diffused		Building 1	Building 2	Ground
9:00	29.3	402	350	NS	33.09	37.80	35.45
				WE	40.52	41.75	40.88
11:00	30.8	613	326	NS	41.64	50.24	45.81
				WE	51.31	51.08	50.42
13:00	31.6	591	266	NS	51.23	46.02	49.57
				WE	54.42	53.56	53.1
15:00	31.9	388	200	NS	44.87	41.09	43.16
				WE	49.37	49.83	48.75

A steady-state 3D CFD model of the LOCH with the unclothed standing female CTM in the outdoor environment is modelled. The schematic of the computational domain considered for

the street canyon and the boundary conditions are shown in Figure 5.3. The wind direction is assumed to be along the street orientation. The average ground and building surface temperature obtained from energy and radiation modelling (Table 5.1) is provided as the boundary conditions of the domain. The boundary condition details are provided in Table 5.2. The LOCH is considered to be located on the sidewalk of the street canyon, with its structure design remaining consistent with the previous studies. The dimensions of the computational domain are shown in Figure 5.3. An unclothed female CTM is included in the computational domain to capture the heat loss components and local ambient factors of each body part. The details of the CTM have been already discussed in Chapter 4.

Table 5.2 Boundary conditions of the computational domain

Boundaries	Boundary Condition	Description
Inlet	Velocity Inlet	V: 1.5 m/s, TI: 29 %, TLS:6.6, T:BES*, ϵ :0.95
Ground	Isothermal	T: BES*, ϵ : 0.8
Radiant Panel	Isothermal	T: 10°C, ϵ : 0.95
Membrane	Coupled	semi-transparent, non-selective, ϵ : 0.124
CTM	Isothermal	T _{initial} : 33.7°C , ϵ ; 0.95
Top surface	Isothermal	T _{sky} : 258 K, ϵ : 0.7
Lateral surfaces	Building Surfaces	T: BES*
Outlet	Outflow	-

*BES – Building energy simulation and radiation modelling from Rhino Grasshopper (Table 5.1)

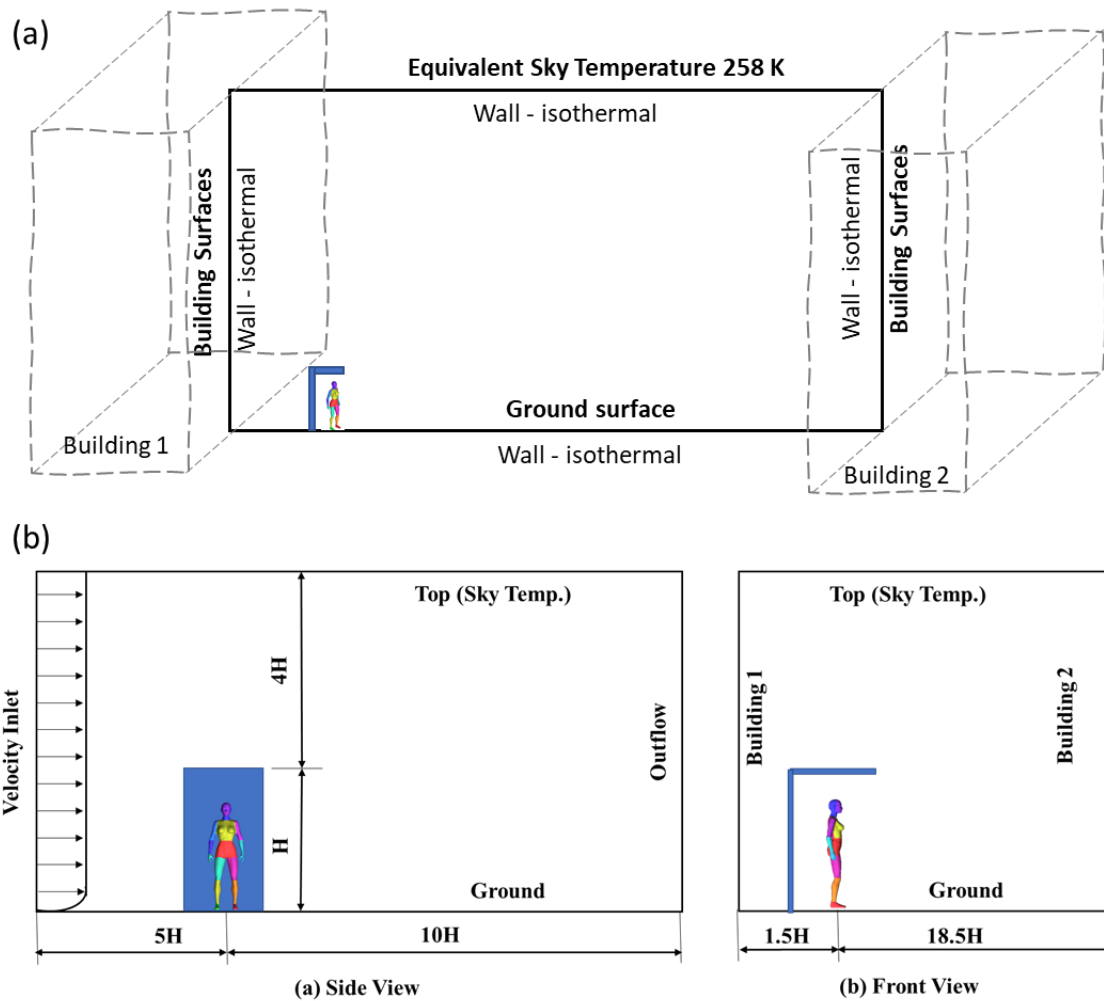


Figure 5.3 Schematic of the computational domain and boundary condition of Street Canyon

The numerical analysis is based on the conservation of mass, momentum, and energy equations, as shown in Equations 3.1, 3.2, and 3.3 (Chapter 3). A three-dimensional, steady-state numerical model was developed using the ANSYS Fluent 19.0 software. The RANS modelling approach was employed for the flow analysis, which is commonly used. The Boussinesq approximation was applied to account for variable air density in the buoyancy term of the momentum equation. This allows for analysis of buoyancy-driven airflow patterns resulting from temperature differences.

For turbulence modelling, the SST $k-\omega$ model was used. Previous studies have found this model provides better predictions of convective heat loss from CTM compared to other options. The

discrete Ordinates (DO) radiation model is utilized for the radiation modelling, as it demonstrated higher accuracy in solving complex optical problems, and the solar ray tracing approach used for the solar load. The coupled algorithm is employed for the pressure-velocity coupling. The second-order discretization is applied for the pressure, convective and diffusion terms of the governing equations, and DO radiation terms. A double-precision solver was selected. The convergence criteria for the normalized residual errors are set to 10^{-9} for the energy equation and 10^{-6} for the other equations.

In the thermoregulation model, i.e., the JOS-3 model, the relative humidity is considered to be 60% which is uniform throughout the body. As mentioned in the coupling method reported in Chapter 4, the heat transfer coefficients and ambient air temperature, MRT obtained from the CFD are provided as input to the JOS-3 model, and the person-related parameters used in the analysis are Metabolic rate: 1.25 met, Height: 1.584 m, Sex: Female, Basal metabolic rate equation: Japanese, Weight: 60 kg, and Age: 30 years. The other input values are set to the default values of the JOS-3 model. Since the simulation is performed for a steady-state condition, the simulation time is chosen to be 120 minutes.

5.2 Model Validation with Chamber Test

Due to the uncontrolled and transient environment outdoors, a chamber test was utilized for the model validation in a steady state condition. The schematic of the chamber test environment and the pictorial view of the experiment setup are shown in Figure 5.4. The climatic chamber, with specifications of 4 m (L) x 2.7 m (W) x 2.9 m (H), is equipped with a primary air unit (PAU). The airflow rate and temperature can be controlled via the PAU's controller. The prototype of the LOCH is erected in the chamber and the unclothed female thermal manikin is employed. As shown in Figure 5.4, the cooling hub consists of three panels, i.e., two walls and one ceiling panel, and the panel size of 1.2 m (L) x 0.6 m (B) x 0.1 m (t). The membrane-

assisted radiant cooling panel is comprised of a 20-micron LDPE membrane cover, a lightweight metal frame, and copper coil lines embedded in a white aluminium baseplate. The design of the panels ensures good thermal conductivity and uniform emissivity, aiming to achieve a consistent panel surface temperature. All the panels are connected to the chiller section in parallel arrangement to the chiller unit located outside the climate chamber. The chiller has an inbuilt thermostat to control the supply water temperature. Additionally, the system includes a 40-litre water tank and two water pumps to facilitate the circulation of the chilled water. Each pipeline is thermally insulated and connected through a control valve with a flow meter for the flow adjustment. The supply water temperature and flow rate are set to 10°C and 80 LPH. The supply air temperature and airflow rate of the chamber are adjusted to 24°C and 124.3 L/s. The thermal manikin's surface heat flux is set to be 50 W/m² at each body segment to avoid overheating, with the maximum surface temperature limited to 38°C.

5.2.1 Monitoring Facility

The monitoring facility includes environmental, radiant cooling systems, and thermal manikin monitoring. The climatic chamber environment is monitored using a wet-bulb globe temperature (WBGT-2010SD) meter and a portable mini-weather station at a height of 1.6 m. The WBGT meter measures the globe temperature near the thermal manikin, while the mini-weather station records various environmental parameters, including air temperature, relative humidity, and wind speed. In addition, the interior surface temperatures of all six walls were measured using T-type thermocouples. Furthermore, air temperatures at various heights within the chamber are recorded specifically at 0.6 m, 1.1 m, 1.6 m, and 2.4 m to enhance understanding of the temperature distribution inside the chamber. For the membrane-assisted radiant cooling panels system, each panel's surface temperature is measured with nine uniformly distributed T-type thermocouples, and the membrane temperature is measured with three ultra-fine K-type thermocouples. The PT100 sensors are used for measuring the inlet and

outlet water temperature of each panel. The thermal manikin, standing and consisting of 20 segments with the heating element is uniformly embedded beneath the skin surface allowing for individual control of temperature and heat input. Data collection for the thermal manikin is facilitated by thermal manikin manufacturer PT Teknik-supported data logger software, which monitors the temperature and heat flux of each segment. During the experiment, the whole system was made to run for at least 4 to 6 hours to reach the steady state conditions. Measurements from the thermal manikin are taken every minute, whereas other parameters are recorded every second. Due to the set point temperature of the water chiller, a periodic fluctuation in the supply water temperature can be observed, which in turn causes fluctuations in the panel's cooling capacity.

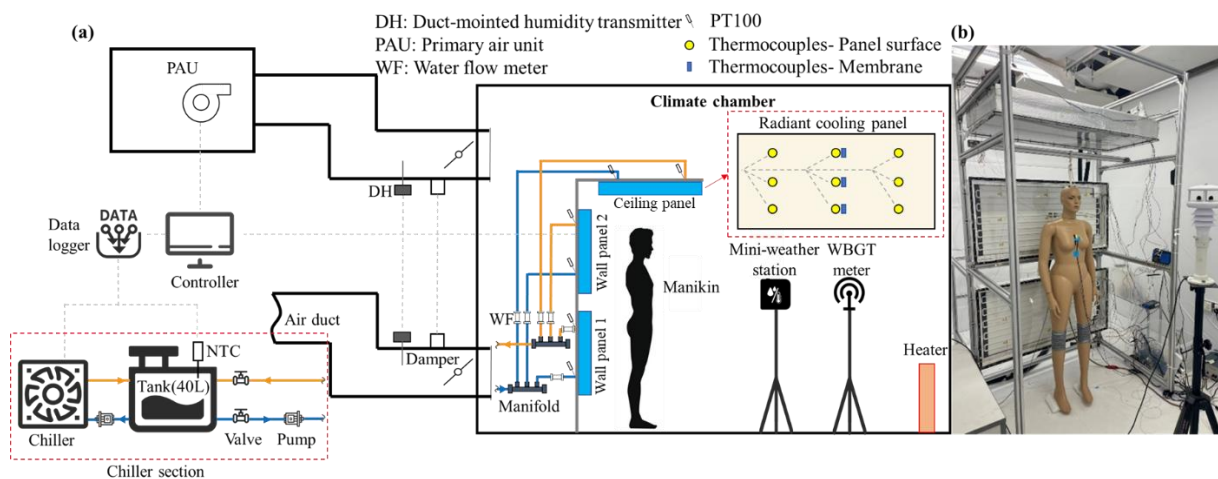


Figure 5.4 (a) Schematic of the chamber test environment and (b) Pictorial view of experiment setup

5.2.2 Comparison of Model Results and Chamber Test Results

A computational model of the LOCH with CTM in a chamber has been developed. The average panel temperature, once the system reaches a steady state within the chamber is used to define the isothermal boundary conditions for the panels. The heat flux values obtained from the thermal manikin are provided as constant heat flux boundary conditions to the CTM body parts.

The boundary conditions for all remaining boundaries are set to match those used in the experimental setup.

The model results for the total heat extraction rate of wall and ceiling cooling panels were validated against the experimental values, as illustrated in Figure 5.5. Due to the fluctuation in the supply water temperature, the cooling capacity of each panel exhibits periodic fluctuation. For validation purposes, the cooling capacity after the steady state is achieved, i.e., after 5 hours of chamber and cooling system started. The experimental values are shown in a box plot, while the simulation results are indicated by red dots. It is observed that the heat extraction rate of the wall cooling panel obtained from CFD simulation shows good agreement with the mean experimental values, exhibiting a relative error within 5%. Although the simulation results for the ceiling panel deviate from the mean experimental value, they fall within the standard deviation of the experimental results.

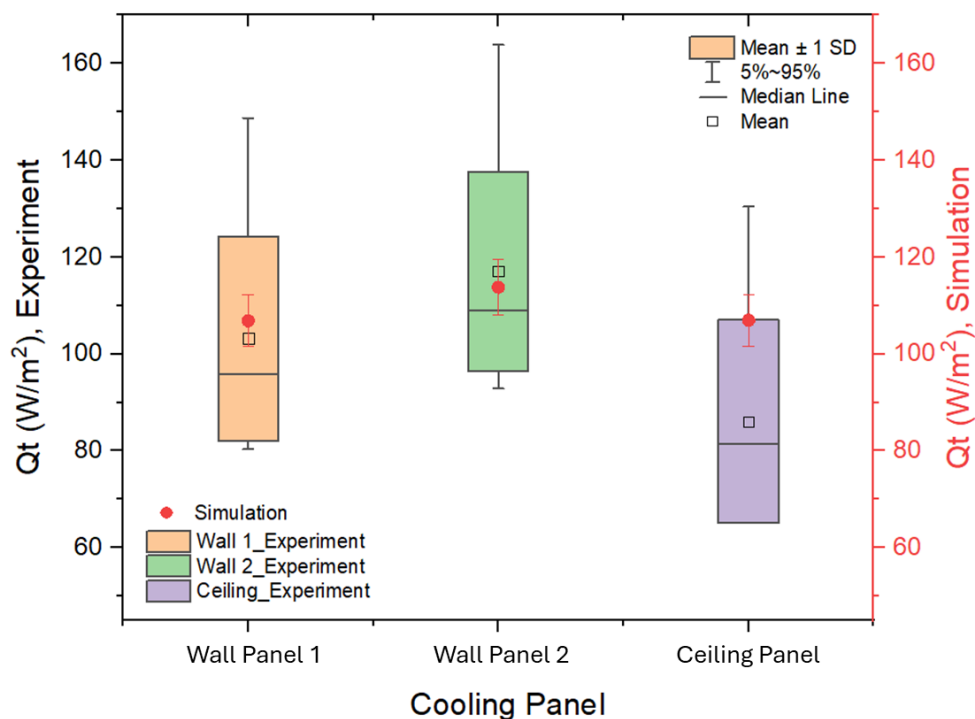


Figure 5.5 Comparison of total heat extraction rate between chamber test and CFD

A comparison of local skin temperatures obtained from the simulation and chamber test is shown in Figure 5.6. The skin temperatures of most body parts from simulation results are within the 5% relative error compared to the experimental results, except for hands and feet. The maximum relative error observed between the experimental and simulation at feet and hands is 11%. The complicated shapes of the hands including fingers, and surface area inconsistencies between CTM and thermal manikin might be the reason for this deviation.

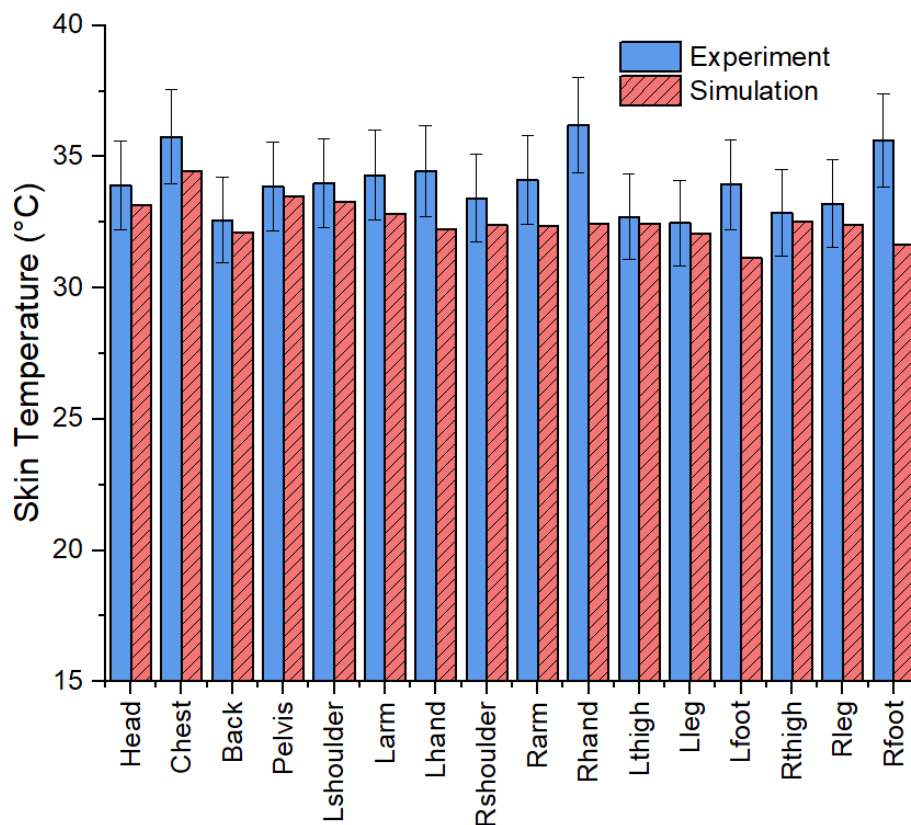


Figure 5.6 Comparison of skin temperatures of local body parts between simulation and chamber test

5.3 Results and Discussion

The thermal and comfort performance is assessed in terms of heat extraction rate and thermal sensation vote respectively. While the thermal performance of the LOCH has been explored for open spaces in previous chapters, the heat loads within a street canyon context could differ

due to the radiative effects and shading from surrounding buildings. This can impact the cooling load of the system and the occupants' thermal sensation. Hence, the proposed LOCH in a street canyon is investigated for a typical summer day in Hong Kong.

5.3.1 Thermal Performance of the System

The heat extraction rate of the radiant cooling system is analyzed at different times of the day (9:00, 11:00, 13:00, and 15:00 hr) and for both North-South (NS) and West-East (WE) street canyon orientations. For the NS orientation, the analysis focuses on East-facing LOCH, while for the WE orientation, South-facing LOCH are considered. Figure 5.7 illustrates the solar path and shading of the east and south-facing LOCH without any surrounding buildings. Figure 5.8 shows the total heat extraction rate (Q_t), radiative heat flux (Q_r), convective heat flux (Q_c) and solar heat flux (Q_s) handled by the radiant cooling panels for different times of the day and NS and WE orientation cases. For both scenarios, the ceiling panel is not exposed to solar radiation, as it is facing the downside, while the wall panel is self-shaded by its structure all the time, except at 9:00 hr in NS orientations.

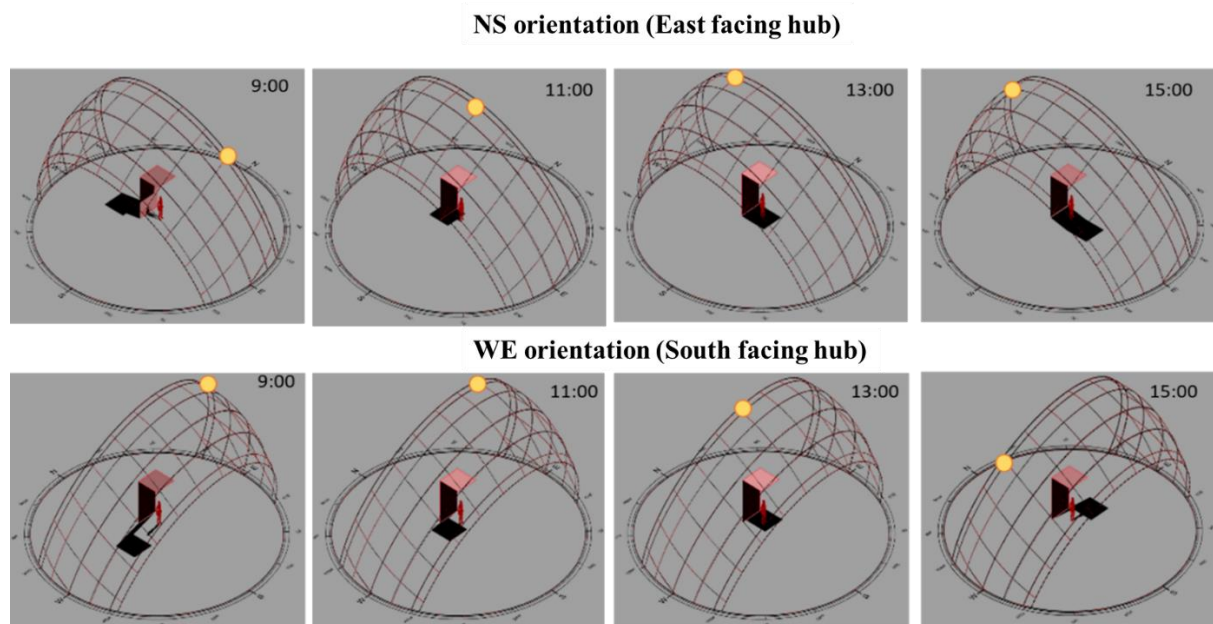


Figure 5.7 Solar exposure of the LOCH for NS (East-facing hub) and WE (South-facing hub)

orientations for 9:00, 11:00, 13:00 and 15:00 hr

Although the different orientations have different building surface and ground surface temperatures, no significant difference in the total heat extraction rate was observed between NS and WE orientation cases. The maximum heat extraction rate observed at the time of 13:00 hr, i.e., 277.9 and 280.50 W/m² of energy consumed by radiant panels for the NS and WE orientation cases respectively.

In the present study, a MIR-selective membrane has been employed, which does not allow direct solar radiation. It can be seen that during morning hours, i.e., 9:00 hr, there is not much deviation in the heat extraction rate between NS and WE orientation cases, even the major surface of the wall radiant panel exposed to direct solar radiation. Since the LDPE membrane is widely used for radiant cooling applications, as well as economic solutions, it will allow solar radiation, and overshoot the heat extraction rate at 9:00 hr in NS orientations. It can be eliminated by designing the structure considering maximum shading on the given locations and surroundings. On the other hand, the height of the buildings and the width of the streets play an important role in providing shading on the side pavements during morning and evening hours. However, it can reduce the solar heat load, and the radiative load from the buildings and ground surfaces contributes a significant percentage to the total heat extraction rate. In the present study, it was observed that the maximum solar heat flux observed is 21% of the total heat extraction rate. The absorption of direct solar radiation by surrounding surfaces increases the surface temperature and, consequently, increases the undesired radiative heat loads for the panel. The radiative heat load contributes 56-63% to the total heat extraction rate for the investigated times of the day. There is an energy-saving potential in the radiative heat load parts, as the majority of heat loads are from surroundings, rather than occupants.

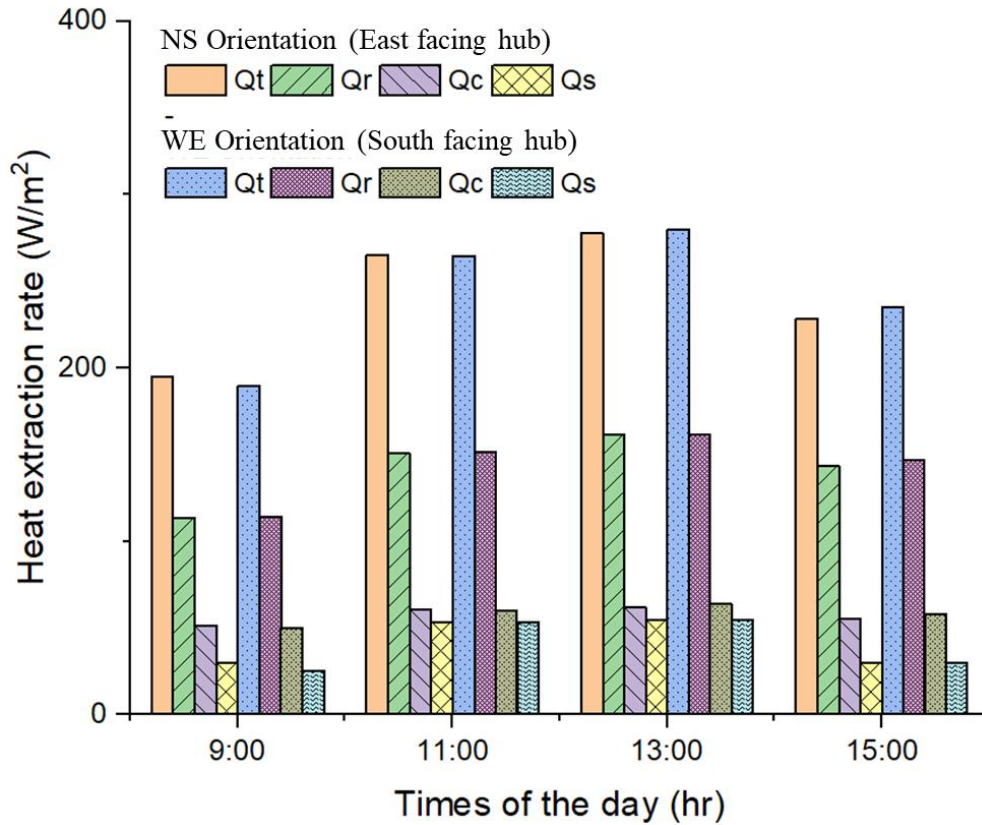


Figure 5.8 Comparison of heat load components between WE and NS orientation cases

One of the limitations of the proposed cooling system is the current structure design. The radiant cooling panels exchange the cooling energy with occupants only by radiation and no convection. With the current design, radiant cooling panels share 7.5% of the view factor with the occupant standing under LOCH. Consequently, only 8% of radiative heat exchanges with occupants. In future studies, this limitation should be addressed through structure design, to maximise the view factor shared with the occupants, while minimizing the surrounding environment. It improves energy efficiency as well as improves the comfort.

5.3.2 Comfort Performance of the System

The comfort performance of the proposed cooling system is evaluated in terms of thermal sensation vote assessed by the CFD-CTM-JOS-3 coupling method. The solar heat flux is one of the primary influencing parameters on thermal sensation. The contour of solar heat flux on

the CTM body parts for the different times of the day for the case of NS orientation is shown in Figure 5.9a. During the afternoon hours, specifically at 13:00 and 15:00, the entire body of the CTM is covered by shade. In contrast, in remaining cases, part of the body is exposed to solar radiation, which influences the local skin temperature and, in turn, affects the local and overall thermal sensation of the body.

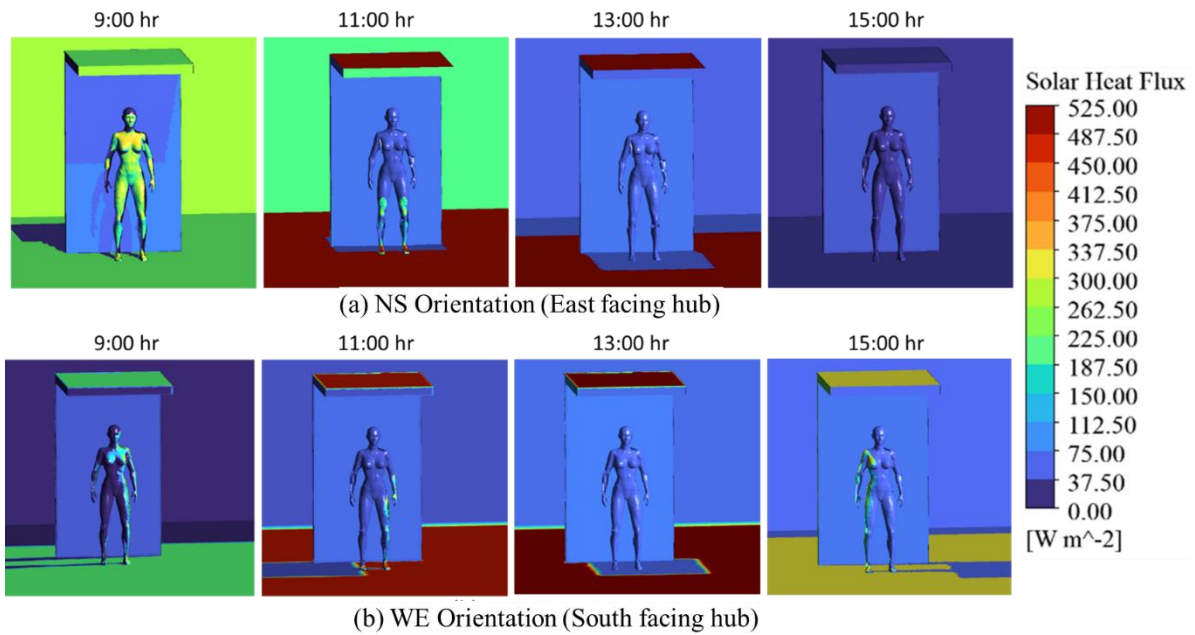


Figure 5.9 Solar heat flux contour of CTM and radiant cooling panel (a) NS and (b) WE orientation cases

Figure 5.10 shows the skin temperature and the thermal sensation of the human body under the LOCH for the case of NS orientation. At the time of 9:00 hr, the front part of the body was exposed to direct solar radiation (Figure 5.9a). It should be an undoubtedly thermally discomfort situation, and it is visible from the predicted skin temperature and local thermal sensation of the chest, i.e., 3.4 (hot sensation). However, the proposed cooling system cools down the back surface which influences the overall thermal sensation. Even though the whole front body is exposed to solar radiation, a strong cool thermal sensation felt by the back part, i.e., TSV_{back} : -1.8, of the body dominates the overall thermal sensation, i.e., $TSV_{Overall}$: -1.8.

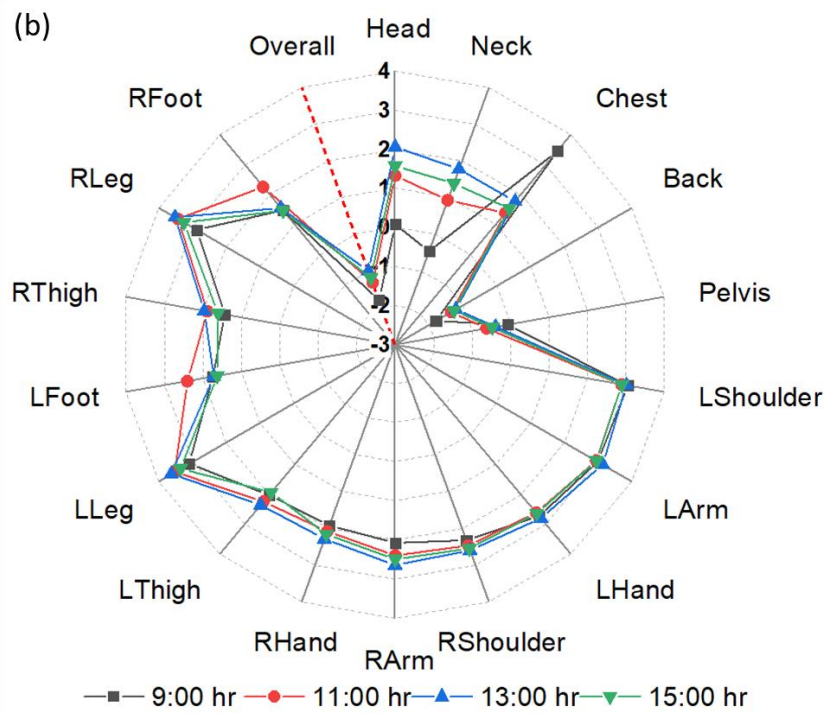
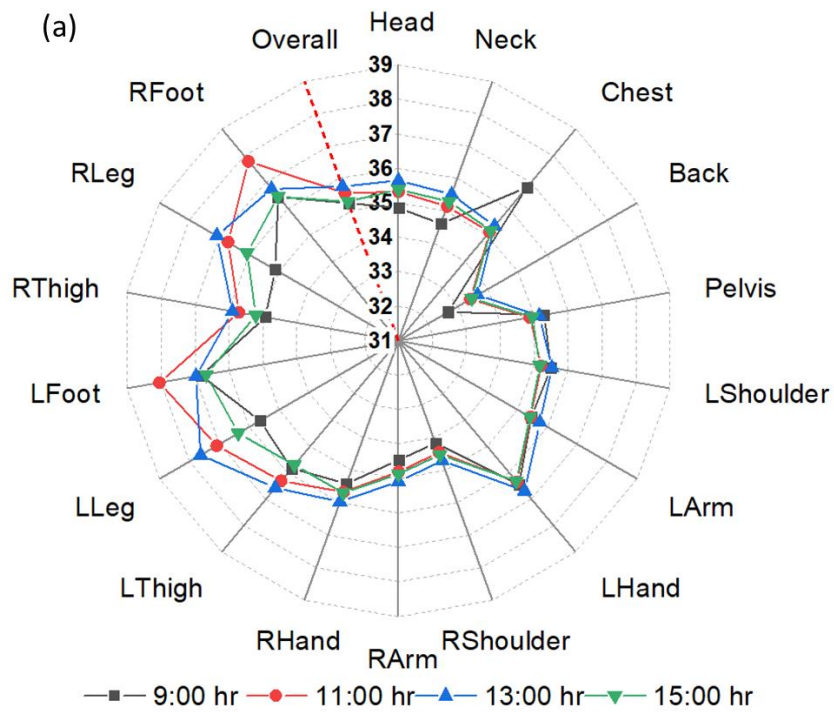


Figure 5.10 Local and overall (a) skin temperature and (b) thermal sensation vote in the LOCH for the case of NS orientation

At the time of 11:00 hr, the lower part of the body, the front part of the legs, thighs and feet are exposed to solar radiation. At 13:00, the entire body is completely shaded, and the local thermal

sensation of all dominant body parts including the forehead, chest, abdomen, and pelvis, except for the back, is comparatively warmer than the other cases. Consequently, the overall thermal sensation experienced is comparatively warmer at the time of 13:00 hr, i.e., -0.99 (slightly cool thermal sensation). In the peak time of a typical summer day, with an ambient air temperature of 31.6°C and RH of 60%, the LOCH provides a comfortable cooling spot with a slightly cool thermal sensation. At the time of 15:00 hr, the building at the back side of LOCH provides shade for part of the street. It improves the local thermal sensation for most of the body parts compared to the noon time cases, i.e., 11:00 and 13:00 hr cases. In the comfort performance analysis of NS orientation of street and east-facing LOCH, the overall thermal sensation observed for the investigated time, 9:00, 11:00, 13:00 and 15:00 hr are -1.8, -1.3, -0.99, and -1.7 respectively.

The comfort performance of WE orientation of street canyon and south-facing LOCH has been analysed, and corresponding skin temperature and thermal sensation for various times of the investigated day are shown in Figure 5.11a & b respectively. As shown in Figure 5.9b, the left side of the body is exposed to direct solar radiation during morning hours, i.e., 9:00 and 11:00 hr, while the right side of the body is exposed at evening hours, i.e., 15:00 hr, complete shade on the human observed at the time of 13:00 hr.

At the time of 9:00 hr, the left side of the body has a higher skin temperature compared to the right side. Chest and right shoulder exposed to direct solar exposure only for this time case. Hence, the local thermal sensations experienced by them are warmer than other investigated times of the day. The skin temperature for most of the body parts is lower than at other times and lower than that of the NS orientation case, due to a comparatively lower amount of solar radiation absorption. In turn, the overall thermal sensation experienced at the time of 9:00 is lowest, i.e., -1.51, compared to all other times and orientation cases.

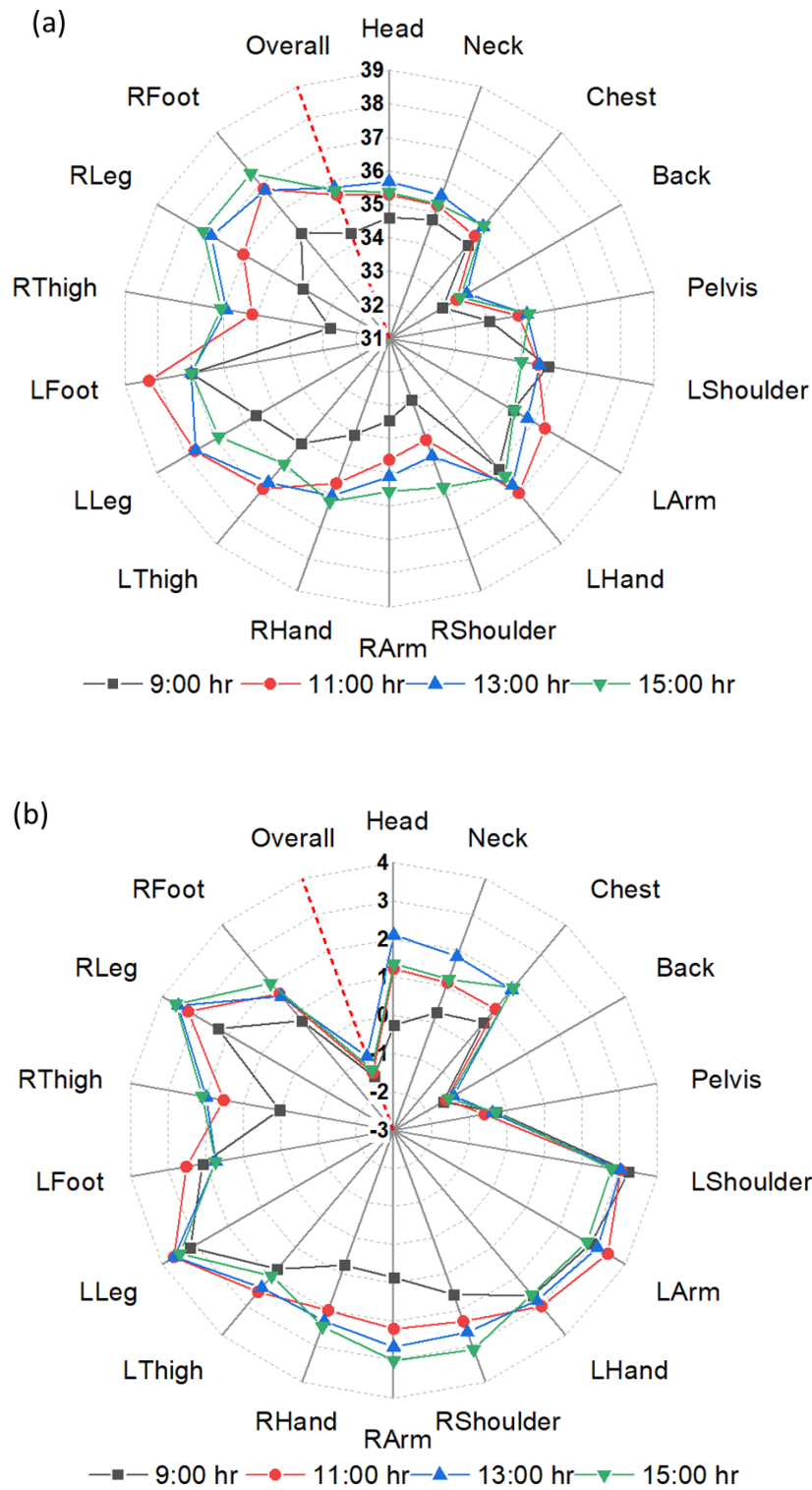


Figure 5.11 Local and overall (a) skin temperature and (b) thermal sensation vote in the LOCH for the case of WE orientation

For the case of 11:00 hr, the left arm, hand, thigh, and leg have higher skin temperature compared to other cases, due to the direct solar exposure. Even though it is completely shaded

at 13:00 hr, the skin temperature for most of the body parts is higher than the shaded body parts in other cases, because of the higher diffused radiation component and long wave radiation absorption. This observation is also noted in NS orientation cases. Head, neck, and back body parts are always shaded. A higher amount of diffused solar radiation absorption on the head and neck at the time of 13:00 hr caused warmer local sensation compared to other cases. In the 15:00 hr case, as the right side of the body was exposed to solar radiation, a comparatively warmer thermal sensation was experienced in all right parts of the body.

The proposed structure of the cooling system could provide a cool thermal sensation for the typical summer day in Hong Kong, independent of orientations of the street canyon. However, the extreme local thermal sensation was observed in the parts exposed to solar radiation. The proposed prototype design is made for a single person, but, in real cases, the structure should accommodate a minimum of 3 to 5 persons. In that case, with WE orientations people standing on the extreme side will be exposed to solar radiation during morning and evening hours, which leads to local discomfort. While, remaining people standing in the cooling hub, should be experienced comparatively improved thermal sensation. In the NS orientation, either morning or evening hours depending on the LOCH facing direction, all the occupants may be exposed to the sun if the building on the opposite is not tall enough. Hence, the primary modification should be made to provide maximum shading throughout the day. During noon hours, even the all the occupants are completely standing in the shaded hub, due to the higher diffused solar radiation load, the occupant may feel a warm or hot thermal sensation. With the current prototype design, the occupants share a large view factor with the surroundings, which causes higher radiative transfer leading to discomfort. It can be addressed by modifying the prototype design such that occupants share a higher view factor with the cooling panel, and vice versa, rather than the surroundings. This strategy not only improves the comfort but also improves the energy efficiency of the cooling system.

5.3.3 Cooling Effect Comparison: LOCH Bus Stop and Conventional Bus Stop

A comparatively warmer overall thermal sensation was experienced at the time of 13:00 hr for both orientation cases. Hence, the comfort performance of the LOCH bus stop has been compared and analyzed against that of a conventional bus stop, i.e., just shading, at 13:00 hr for the NS orientation of street canyons and East-facing bus stop scenario.

Figure 5.12 shows the comparison of skin temperature and thermal sensation vote for the investigated cases. A significant difference of 1.7°C is observed at the back surface of the body between the LOCH and conventional bus stops, while the differences in the remaining body parts are less than 0.5°C . The proposed cooling system has a dominant influence on the back, head, and neck parts of the body. In the aspect of the local thermal sensation experienced at the back-body surface, a marginal difference was observed between LOCH and the cooling spot. The reason is that the predicted skin temperature at the back is within the acceptable skin temperature range, i.e., within the null zone range (Xie et al., 2020). However, the local thermal sensation of the back for the LOCH exhibits a strong negative thermal sensation, i.e., $\text{TSV} < -1$. The local thermal sensation of the dominant body parts, i.e., forehead, chest, abdomen, back and pelvis, with TSV value lesser than -1 , have a strong influence on the overall thermal sensation. With the strong contribution of the cooling sensation of the back, the overall thermal sensation experienced in the LOCH is slightly cool, i.e., $\text{TSV}: -0.99$.

The small skin temperature deviation at the head and neck between the conventional bus stop and LOCH, i.e., 0.4 and 0.5°C respectively, cause significant differences in local thermal sensation vote, i.e., 0.7 and 1.0 respectively. In the conventional bus stop, the local discomfort experienced at the head and neck, with TSV values of 2.8 and 2.7 respectively, has a dominant influence. As a result, the overall TSV at the conventional bus stop is 3.57 (hot sensation), while in the LOCH, it is -0.99 (slightly cool sensation).

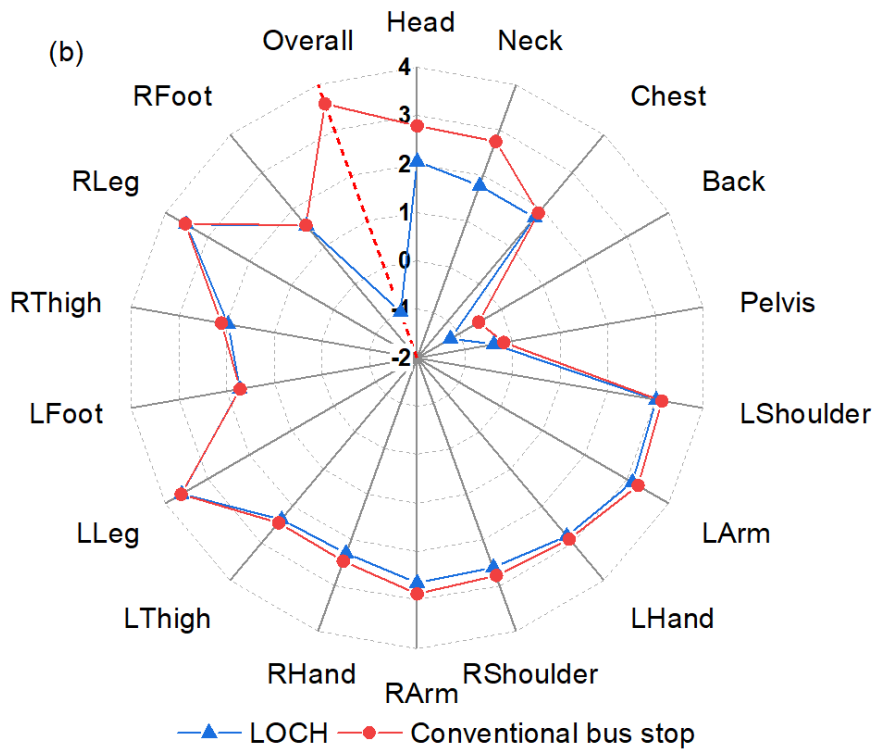
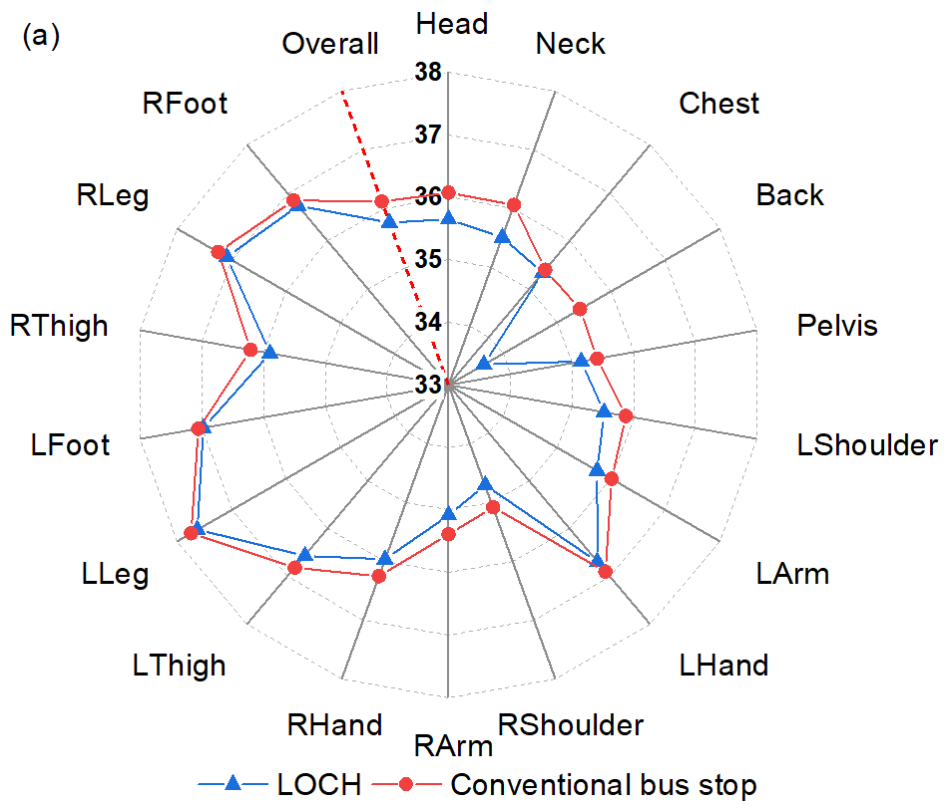


Figure 5.12 Comparison of (a) skin temperature and (b) thermal sensation vote between LOCH and conventional bus stop for NS orientation case (East-facing bus stops) at 13:00 hr

For a better understanding, the radiative heat flux and total heat flux contours of the CTM for the NS orientation at the time of 13:00 hr are shown in Figure 5.13 and Figure 5.14. In the aspect of radiative heat flux, the blue contours on the back parts of the CTM indicate that cooling energy is provided by the radiant panels by radiative heat transfer. Compared to the conventional bus stop, minimal heat is exchanged from the upper part of the chest to the panel. For the remaining front side of the body parts, there is no notable difference between the LOCH and conventional bus stop cases.

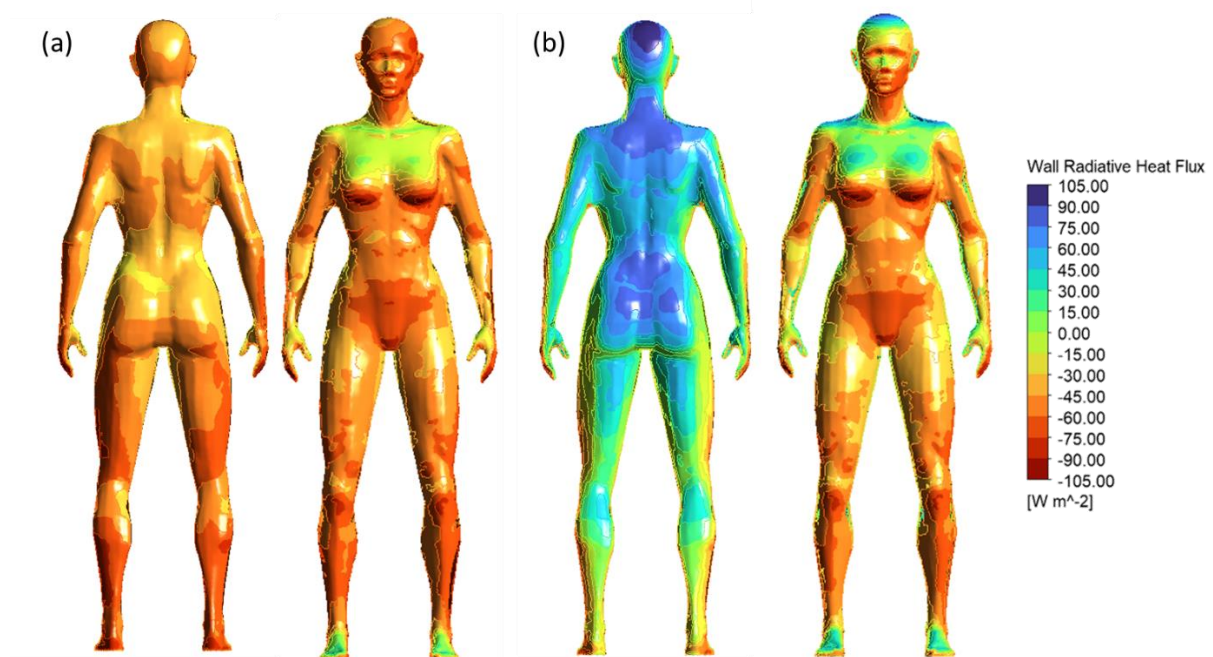


Figure 5.13 Comparison of radiative heat flux contour for (a) conventional bus stop and (b) LOCH for NS orientation case (East-facing bus stops) at 13:00 hr

Due to the orientation of the body's right side towards the wind direction, the influence of approaching wind from the right side, result in a pronounced combined effect of convective and radiative heat flux on the right side of the body compared to the left side. It can be noticed in both cases (Figure 5.14). From these contours, it can be concluded that the proposed cooling system helps to cool down the back, head and neck body parts, in turn, improves the thermal

comfort. This finding aligns with the conclusion of Yang et al. (Yang et al., 2024), which suggests that cooling spots can effectively cool back trunk, thereby improving thermal comfort.

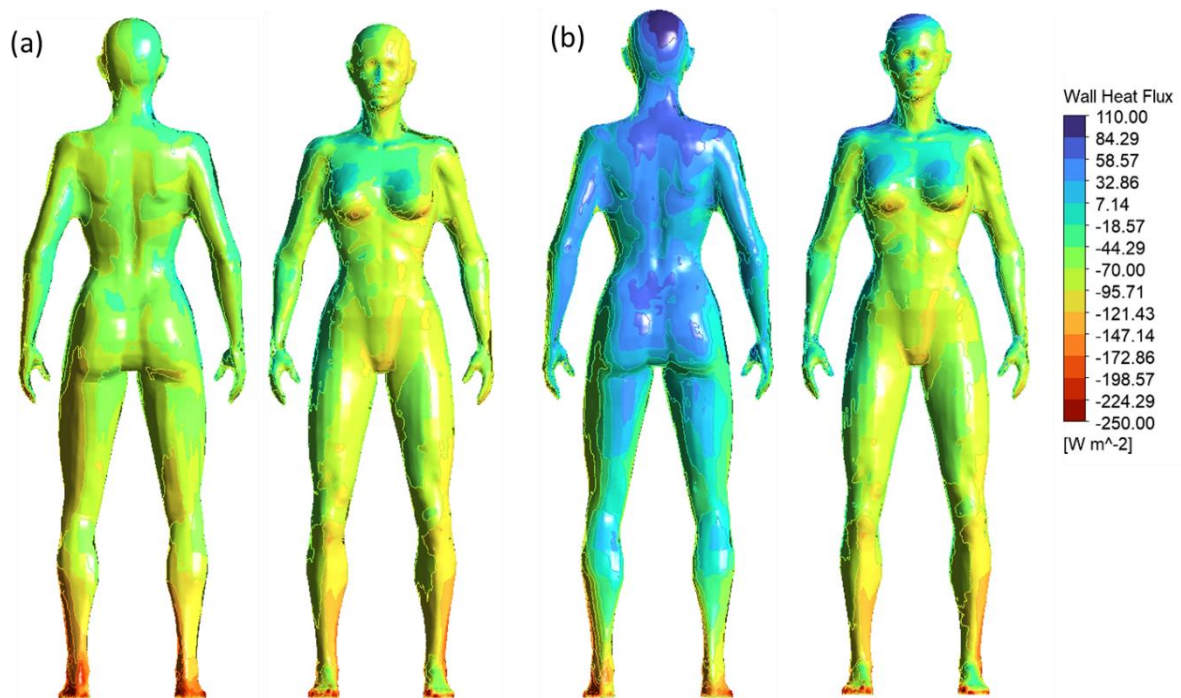


Figure 5.14 Comparison of total heat flux contour for (a) conventional bus stop and (b) LOCH for NS orientation case (East-facing bus stops) at 13:00 hr

5.4 Summary

The thermal and comfort performance of the LOCH is investigated for North-South (NS) and West-East (WE) orientations of the street canyon, with East-facing and South-facing hubs, respectively, at various times throughout a typical summer day in Hong Kong. The comfort performance has been analysed in terms of skin temperature and thermal sensation vote, assessed by the CFD-CTM-JOS-3 coupling method.

The radiant panel temperature is considered to be 10°C for all the cases. With this condition, the orientation has a very minimal impact on the heat extraction rate of the system. The maximum heat extraction rate of the proposed structure design of LOCH is 298.15 and 301.35

W/m² for the NS orientation (East-facing hub) and WE orientation (South-facing) cases, respectively.

The solar heat flux on the human is a primary influencing factor on the thermal sensation. The proposed cooling system greatly cools down the back skin temperature, in turn improving the local thermal sensation. Independent of the ambient conditions, the dominant cooling sensation on the back influences the overall thermal sensation. The orientation affects the local thermal sensation of the different body parts. During morning and evening hours, the exposure of parts to solar radiation causes strong local discomfort. At the time of 13:00 hr, the current design of LOCH provides shading for occupants, and still, the impact of diffused solar radiation, and long wave radiation causes a comparatively warmer thermal sensation. However, overall, a slightly cool thermal sensation (TSV: -0.99) was achieved even at the peak time of a typical summer day in Hong Kong (Ta: 31.6°C, RH: 60%).

The comparison of comfort performance between LOCH and conventional bus stops reveals the importance of LOCH for a hot summer day. It was found that the conventional bus stop failed to provide comfort conditions where the occupant experienced a hot thermal sensation at 13:00 hr. While LOCH provides a slightly cool thermal sensation in this condition.

The research findings from this study are limited to Hong Kong and geolocations near the equator. Another limitation is that clothing insulation was not considered in the simulation due to the complexities involved in CFD modelling. In future studies, the clothing can be considered with the updated thermoregulation model. It is believed that the considerations of clothing effect will not affect the findings of this study, but deviation in the skin temperature and thermal sensation is unavoidable. The current structure design limits the radiative heat transfer efficiency to only 8%, as it shares a very small view factor with the occupant, i.e., 7.5. Therefore, the future design should consider maximising view factors between radiant panels

and surroundings, which not only improves efficiency but also improves human comfort. On the other hand, the proposed design should also consider the maximised shading effect, especially during the summertime of a given location.

In light of the current trend of increasing heat wave events and extreme temperatures, it is essential to investigate the performance of the membrane-assisted radiant cooling system in locations with high temperatures. The current structure design may not provide comfort in this condition, as well as the longwave radiation from the surroundings affects the efficiency of the system. However, with the improved design and appropriate membrane material, the proposed cooling system can perform well in all climatic conditions. In future studies, the proposed cooling system will be integrated with low-grade energy sources, such as radiative cooling, and solar cooling.

CHAPTER 6

Conclusions and Recommendations for Future Study

Extreme heat is a global threat and there is a need to care for the vulnerable in outdoor environments and protect workers. Last year 2023 was considered the hottest in the history of many cities across the world, but 2024 is more scorching. Record-breaking temperatures, (52°C in India and China) increased the rate of heat-related health complaints, and deaths all around the world, and heat-related incidents such as 1301 deaths on the Hajj pilgrimage in Mecca due to extreme temperature forced the researchers to address this issue with high priority.

The CS-RCS is believed to be the updated version of the radiant cooling system and would be the better alternative for conventional air conditioning systems. It could be energy energy-efficient and comfortable cooling solution for both indoor and outdoor spaces. This research aimed to address the key questions about implementing membrane-assisted radiant cooling systems for outdoor applications.

In this research, a comprehensive review of the membrane-assisted radiant cooling system has been conducted, including membrane properties and their impacts on system performance, advantages and limitations, heat transfer models, thermal comfort, and energy-saving potential. The heat transfer characteristics and thermal performance of the proposed cooling system on LOCH have been investigated for the outdoor urban space of Hong Kong. Additionally, the impact of various kinds of membrane material, including non-selective, MIR-selective and sky window selective on the thermal performance has been analysed.

To assess the thermal sensation in the outdoor environment, a novel methodology has been adopted to overcome the limitations of existing outdoor thermal comfort models. A coupling

method of CFD with human thermoregulation has been established to predict the physiological parameters of the human body in the outdoor environment. It will be processed to assess the local and overall thermal sensation of the body using the updated CBE comfort model. Based on the literature, one-way and two-way coupling methods, and a CTM-free simplified approach have been analysed on the application of a LOCH.

To analyse the performance of the proposed cooling system in the street canyons in Hong Kong, the thermal and comfort performance has been investigated for various orientations of the street canyon for various times of a typical summer day. Additionally, the thermal efficiency and efficacy of the current design of the cooling system are discussed in Appendix A. The salient discussions, findings and future studies are summarized in the following subsections.

6.1 Cover Shield-assisted Radiant Cooling System

A detailed literature review was conducted on cover shield-assisted radiant cooling systems to better understand the state-of-the-art in this emerging technology, and the salient points are summarized below.

- LDPE membrane is a commonly used low-cost material with excellent infrared transparency for radiant cooling applications. However, thin LDPE membranes have poor mechanical properties and tend to tear and wrinkle easily. There is a need to develop IRT membranes with good mechanical properties to make the cooling system suitable for real-world use. Providing a thin wire mesh over the membrane can temporarily protect it from harsh ambient conditions.
- Membrane-assisted RCS has similarities to daytime radiative sky cooling, so materials used for that application can potentially be utilized. However, these advanced membrane and material solutions are still in the laboratory stage and not commercially available.

- Several heat transfer models have been developed to demonstrate the cooling capacity improvement over conventional radiant cooling systems. However, an in-depth energy model for the whole membrane-assisted RCS is yet to be explored.
- The membrane functions as a barrier, preventing moisture transfer from the ambient environment to the air gap, as well as minimizing convective heat loss from the panel to the surrounding atmosphere. Therefore, a membrane-assisted RCS has the potential to be coupled with natural ventilation and ambient wind, which is much more energy efficient to convectively cool the human body, and also help to reduce the transmission risks of air-borne diseases such as COVID-19, to improve thermal comfort in open and semi-open built environments, such as bus stops, community parks.
- Although the temperature of cooling water for the membrane-assisted RCS can be much lower than the conventional radiant cooling system, the possibility of integrating the membrane cooling system with passive cooling options, such as evaporative cooling, earth tunnel cooling, and nocturnal cooling, is still worth to be explored in the future.

6.2 Thermal Performance Assessment in the Outdoor Urban Environment

This study numerically investigated the thermal performance of a LOCH equipped with membrane-assisted RCS. The non-selective, MIR-selective, and sky-window selective membranes have been analysed for their thermal performance of the cooling hub. The salient findings from the investigation are as follows:

- The implementation of membrane on the radiant cooling panel reduces the equivalent CHTC down to 2.6 and 2.2 W/m²K for the ceiling and wall panels respectively, whereas the RHTC ranges from 5.8 to 6.1 W/m²K for both ceiling and wall panels.
- Among them, the sky window selective membrane performs best and avoids undesired heat loads. The MIR-selective membrane-configured panels exhibit a higher heat

absorption rate, i.e., ranging from 37 to 58% for the wall panel and 45 to 78% for the ceiling panel, compared with the sky-window-selective membrane-assisted panel.

- Non-selective membrane-configured panels allow direct solar radiation to reach the panel surface; resulting in 1.2 times higher solar heat flux absorption than MIR-selective panels when exposed to direct solar radiation. The MIR-selective and non-selective membranes perform the same when the panel is not exposed to direct solar radiation. Hence, compared to MIR-selective membranes, non-selective membranes are preferred for shaded outdoor areas, as they are comparatively cheap and effective.
- Sky-window-selective membrane configuration demonstrated superior cooling performance throughout the daytime, i.e., 9:00, 11:00, 13:00, and 15:00 hrs. By eliminating undesired ambient radiant load components, they offer significant energy savings of up to 44% compared with non-selective membranes. Although, these membranes are in the development stage, they are expected to be commercially available in the near future.
- The energy consumption for the LOCH prototype for a single occupant is estimated for the operation from 9:00 to 15:00 hrs. With the sky-window selective membrane configurations, the prototype effectively consumes energy of 3.94 kWh. While MIR and non-selective configured prototypes consume 6.4 and 6.54 kWh of energy respectively.

It is worth noting that, the radiation emitted from the ground surface potentially affects the performance of the cooling system, as the panel shares significant view factors with the ground surface. It can be controlled by the usage of suitable membranes and designing a cooling structure that blocks undesirable short and long-wave radiation from surroundings may result in effective cooling with low energy consumption.

6.3 Thermal Sensation Assessment (Coupling of CFD and Human Thermoregulation)

The study compared different coupling methods that integrate outdoor environment modelling with the human thermoregulation model and the CBE comfort model. The aim was to assess the physiological responses and thermal sensations in outdoor environments by considering the effects of solar radiation, long-wave radiation, and wind. The proposed coupling methods are used to assess the thermal sensation experienced under LOCH at peak time of summer day in Hong Kong. The notable findings from the study are given below.

- The coupling process inputs the local heat transfer coefficients, MRT, and air temperatures from environment modelling to the JOS-3 model. The obtained skin temperature feedback to the CFD as the boundary condition for CTM. The converged skin temperature is further processed for thermal sensation prediction.
- A case study of an outdoor radiant cooling hub is used to demonstrate the coupling methods. The two-way coupling method converges quickly with only one iteration needed, as the convection coefficient at typical outdoor wind conditions is not much influenced by the skin temperature.
- The thermal comfort survey has been performed for the outdoor radiant cooling experiment facility. The predicted thermal sensation from the coupling method is compared with the survey results, and it is found to be within the standard deviation of the survey results.
- The use of the CHTC from the literature as a CTM-free simplified approach has good agreement with the CFD-CTM-JOS-3 coupling method. The simplified approach avoided the complicated CTM mesh generation process and reduces the computational cost, making it a practical tool for the evaluation of thermal comfort at the pedestrian level in the outdoor environment.

- The CTM-free simplified approach employs heat transfer coefficient correlations developed for outdoor wind conditions, and more reliable correlations are yet to be developed. The CTM-free simplified approach is not suitable for indoor applications where natural convection is dominating, or for scenarios involving local obstacles that disrupt the flow approaching a human body.
- The CTM-free simplified approach helps urban designers and practitioners to consider and predict the comfort level in a comparatively more accurate way.
- There are certain limitations associated with the JOS-3 model and CBE model, and they are expected to be addressed and updated in the near future.

6.4 Thermal and Comfort Performance of the Cooling System

The study investigates the thermal and comfort performance of the LOCH system for different street canyon orientations and times of the day for the tropical climate of Hong Kong. The thermal sensation was assessed by the CFD-CTM-JOS3 coupling method. This study evaluates the LOCH design's real-world cooling performance to improve occupant experience. The findings could guide standards for effective LOCH design and placement within street networks to maximize occupant heat relief in urban transportation hubs like bus stops located in canyons between buildings. The major outcomes of the present study are given below.

- The radiant panel temperature is set to 10°C, and the orientation has a minimal impact on the heat extraction rate of the system. The maximum heat extraction rate of the proposed LOCH structure is 277.9 and 280.50 W/m² for NS (East-facing hub) and WE (South-facing hub) orientations, respectively.
- Solar heat flux on the human is a primary influencing factor on the thermal sensation. The proposed cooling system significantly cools down the back skin temperature,

improving the local thermal sensation. Dominant negative sensation on the back influences the overall thermal sensation, independent of ambient conditions.

- The orientation affects the local thermal sensation of different body parts, with strong local discomfort during morning and evening hours due to solar radiation exposure. At 13:00 hr, the LOCH design provides shading, but the impact of diffused solar radiation and long-wave radiation causes a comparatively warmer thermal sensation. An overall thermal sensation of slightly cool (TSV: -0.99) is achieved even at the peak time of a typical summer day in Hong Kong (T_a : 31.6°C, RH: 60%).
- The comparison of comfort performance between LOCH and a conventional bus stop reveals the importance of LOCH for hot summer days. The conventional bus stop fails to provide comfort, with the occupant experiencing a hot thermal sensation at 13:00 hr, while LOCH provides a slightly cool thermal sensation.
- The current study does not consider the effect of clothing, which can be addressed in future studies. The current LOCH design limits the radiative heat transfer efficiency to only 8%, due to a small view factor sharing with the occupant. Future designs should consider maximizing the view factor between the radiant panel and the surroundings to improve efficiency and comfort. The design should also consider maximizing the shading effect, especially during the summer.

6.5 Scope of Future Research

The applications of the membrane-assisted radiant cooling system for outdoor shelters have large space for future research for further improvements in energy efficiency and comfort in high temperatures weather. The following research directions can be addressed in future.

Cover shield material development

Advancing MIR-selective and sky-window selective membranes beyond the laboratory stage aids in improving the cooling performance of the panel. In the interim, the robustness and durability of the membrane used for the radiant cooling system need to be addressed for future design improvements without compromising the required IR transparency. For the time being, developing the protective structure or coating on the currently used membrane could be a viable solution to shield them from the harsh outdoor ambient and human interaction.

Cooling shelter design

Optimising the view factor sharing between panel and occupants for better cooling distribution, and panel energy efficiency needed to be analysed. While, the structure design ensures visibility to the environment, maximum shading hours, and wind flow to the occupants for the given geo-location.

Thermal comfort and energy efficiency

In addition to redesigning the cooling structure, integrating the other low-grade energy sources such as sky-radiative cooling and solar energy cooling, will be the sustainable solution for the liveable cities. Integration of daytime radiative sky cooling with phase change energy storage for the cooling water requirement for radiant panels will be the next phase of this research.

The optimized cooling structure design with additional passive cooling such as fan cooling or mist cooling to further improve the heat loss from the human body needed to be investigated, particularly with the locations or climate regions exceeding 45°C of ambient air temperature.

Feasibility analyses

As the radiant cooling system is limited to treating sensible heat load, the thermal and comfort performance will vary with the climate zones. In humid climates, the performance could be

lower. Therefore, the quantification of its performance around the world could help urban planners design outdoor cooling systems.

Coupling between CFD and thermoregulation model

In the current coupling method, there are some limitations associated with modelling, the JOS-3 model, and the CBE comfort tool. Clothing has a significant impact on the convective and radiative heat loss from humans, but incorporating clothing with CTM in the CFD modelling will increase the computational cost. Additionally, the JOS-3 model has to make some improvements in clothing modelling.

The null-zone range limits in the CBE comfort model associated with the present study are based on the outdoor thermal comfort survey conducted in Hong Kong. It could be refined with more subjects across the world, which makes wider use of the comfort model.

In the coupling method, the heat transfer coefficients, MRT and T_a have been fed from CFD to the JOS-3 model. In future studies, the JOS-3 model will be updated to receive the convective and radiative heat flux directly from the CFD modelling to improve the coupling method.

Appendix A Thermal Efficiency and Efficacy Analysis

The sensitivity analysis of the panel temperature on the thermal and comfort performance of the LOCH has been investigated. It is further extended to analyse the thermal efficacy and efficiency of the system. A steady-state 3D CFD model of the LOCH with the standing female CTM in the outdoor environment is modelled. The thermal sensation under the LOCH is assessed by the CFD-CTM-JOS-3 coupling method and CBE comfort model. The thermal efficiency and efficacy of the proposed cooling hub design are assessed at the peak time of a typical summer day in Hong Kong, i.e., 13:00 hr on 21st July.

The methodology adopted in Chapter 5 to investigate the thermal sensation is utilized in this investigation. The computational model of LOCH with CTM in an open space has been adopted for the study. The heat extraction rate was assessed from the computational modelling and the thermal sensation was assessed using the CFD-CTM-JOS-3 coupling method and CBE comfort model. It is used to investigate the radiative heat transfer efficiency of the system and to analyse the thermal efficacy of the system.

Radiative energy efficiency defines the quantity of the radiative heat observed by the human ($Q_{r(panel-CTM)}$) compared to the surroundings ($Q_{r,panel_total}$) and is calculated by eq. A.1. The reason to consider only the radiative heat is the cooling panel exchanges the cooling energy with the occupants only by radiative heat transfer, which is considered to be useful energy output.

$$\eta = \frac{Q_{r(panel-CTM)}}{Q_{r,panel_total}} \quad [A.1]$$

Thermal efficacy defines the effective heat extraction needed for human thermal comfort. It is represented by the energy efficacy index, ranging from 0 to 1, where 1 represents the adequate cooling energy for the acceptable overall thermal sensation, i.e., -0.5 to 0.5, and values towards

zero represent insufficient or excessive cooling energy. The energy efficacy index (*EEI*) is calculated using the eq. A.2.

$$EEI = \begin{cases} 1 - \frac{[q]_{OTSV=i} - [q]_{OTSV=0.5}}{[Q]_{OTSV=0.5}} & (0.5 < i < 4) \\ 1 & (-0.5 < i < 0.5) \\ 1 - \frac{[q]_{OTSV=-0.5} - [q]_{OTSV=i}}{[q]_{OTSV=-0.5}} & (-4 < i < -0.5) \end{cases} \quad [A.2]$$

Where the *q* and OTSV represent the total heat extraction rate (W/m²) of radiant cooling panels and overall thermal sensation vote respectively. The limitation of the index is that the $[q]_{OTSV=0.5}$ (or) -0.5 is the function of ambient factors. The thermal comfort survey conducted in the experimental facility analysed the neutral range with respect to UTCI, which is a combined index of the outdoor parameters. Due to the limited computation source of numerical analysis, the energy efficacy was assessed for various panel temperatures at the peak time of a typical summer day.

Results and Discussion

Sensitivity Analysis – Cooling Panel Temperature

The sensitivity analysis is performed for different panel surface temperatures, ranging from 4 to 24°C. The local and overall skin temperatures were assessed for various panel temperatures shown in Figure A.1a. For a better understanding, the comfort performance of the No-cooling scenario to replicate the conventional bus stops was also compared with the LOCH. The variations of the local skin temperature between various panel surface temperatures are insignificant, except for the back surface. Compared to the No-Cooling scenario, with localised cooling it reduces the back surface considerably. It reveals that the potential of the proposed LOCH structure dominantly cools down the back surface compared to other body parts. This

is due to the large view factor of the back surface shared with the radiant cooling panel. A decrease in the panel surface temperature from 24 to 4°C reduces the back surface temperature from 34.4 to 33.4°C. Other than the back body surface, the head and neck parts of the body have been significantly influenced by the change in panel temperature. However, the panel temperature has an insignificant influence on the skin temperature of the remaining body parts. Compared to the cooling cases, the no-cooling case exhibits higher skin temperature for all the body part surfaces, and the cooling cases exhibit a strong variation in the skin temperature of the back, neck, and head body parts. From the sensitivity analysis, it can be concluded that the proposed cooling system with its current structure design, predominantly cools down the back, head and neck.

The variation of thermal sensation votes for various panel temperature cases and no cooling cases, shown in Figure A.1b. Even in a No-Cooling scenario, the back body surface feels the negative local thermal sensation, i.e., slightly cool thermal sensation. This is due to the higher null zone upper limit, i.e., 35.71°C for the back surface in the outdoor environments (Xie et al., 2020). However, it could not help with improving overall thermal sensation. The overall thermal sensation experienced in the No-Cooling Scenario is 3.41, i.e., above hot. Reducing the panel temperature below 14°C shows a favourable overall thermal sensation response, i.e., overall TSV < 1 (slightly warm). The panel temperature below 10°C provides a slightly cool environment (TSV < -1) even at the investigated ambient conditions.

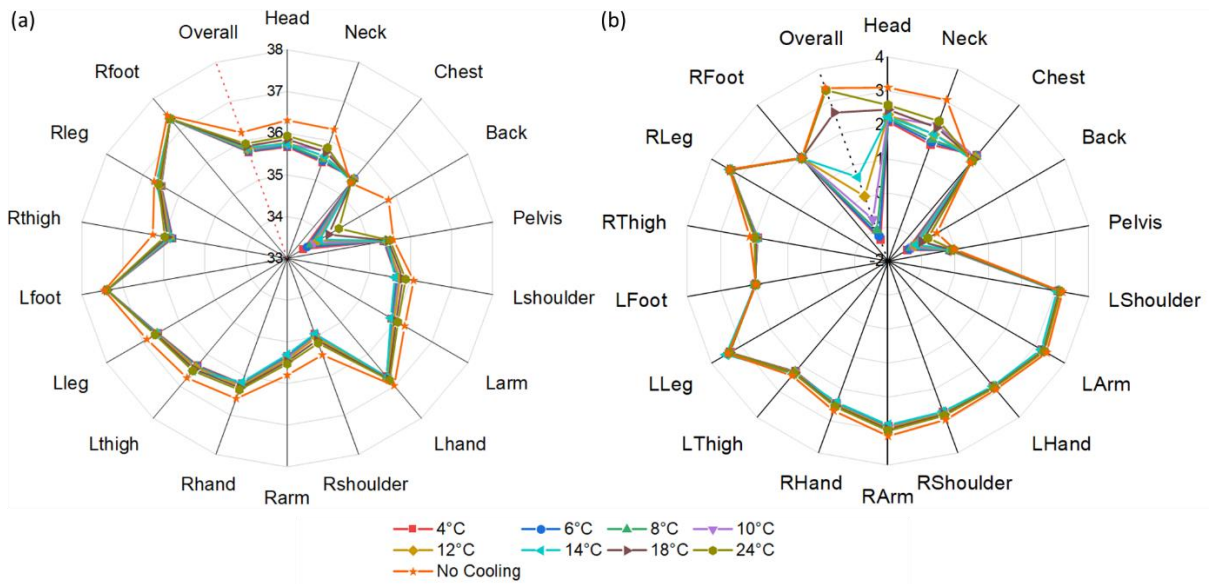


Figure A.1 Variations of local and overall (a) skin temperature and (b) thermal sensation vote for different cooling panel temperatures and no-cooling case

Thermal Efficiency and Efficacy

In the present study, the radiative energy efficiency does not change significantly with the panel temperature. The radiative energy efficiency of the current structure design is only 8%. The reason is that the view factor of the cooling panels shared with the human body is only 7.5. It shows the inefficiency of the current structure design and also indicates the huge energy-saving potential in the radiative heat transfer part. It could be improved by two strategies, i.e., adopting a sky-window selective membrane, and redesigning the structure for the maximized view factor with occupants. The proposed prototype is designed for a single occupant but in real cases, the cooling hub will be designed for the occupancy of at least 3 to 5 persons. In that case, there is a chance of blocking the panel view of the surrounding buildings by occupants, which may improve the heat exchange between the wall panel to occupants.

The energy efficacy of the proposed LOCH structure is analysed for the open space at 13:00 hr, to analyse it for the worst-case scenario. Figure A.2, shows the heat extraction of the panel, overall thermal sensation and energy efficacy index with the variation of panel surface

temperature. Lowering the panel temperature from 24 to 4°C reduces the local skin temperature of the back from 34.4 to 33.43°C, consequently, the overall thermal sensation vote (TSV) in the 9-point scale reduces from 3.3 to -1.3. The analysis revealed that achieving a 0.1°C reduction in the CTM’s back skin temperature required a minimum energy consumption of 50W by the cooling system. For the investigated ambient condition, the panel surface temperature between 11 to 13°C provides the neutral overall thermal sensation, i.e., -0.5 to 0.5, where the efficacy index in this range is 1. The total energy consumption of the panel for the neutral TSV condition is 1260 to 1320 W for the investigated ambient conditions. An Increase and decrease in the panel temperature beyond or lower than this range result in undercooling or overcooling respectively. The limitation of the present study is that the efficacy evaluation in this study has been analysed for specific ambient conditions. It needed to be evaluated for different ambient conditions for the summer conditions, and it will be beneficial to design an efficient cooling system to meet the comfort with optimal energy consumption.

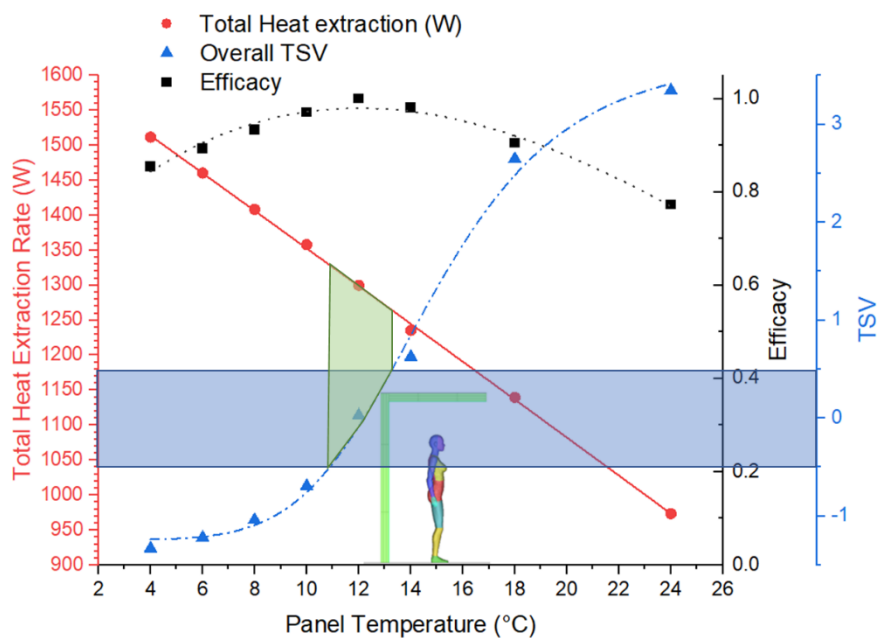
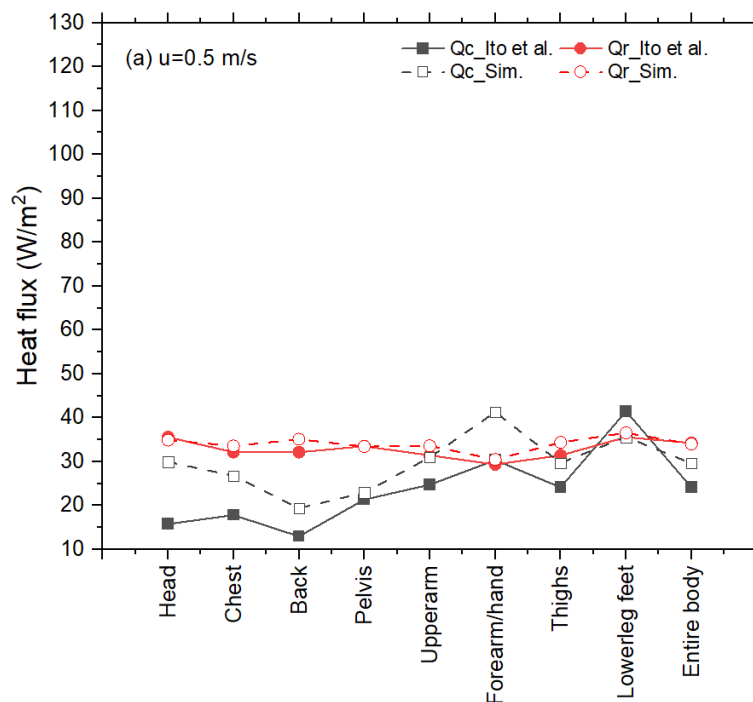


Figure A.2 Variation of heat extraction rate, overall thermal sensation vote and energy efficacy for different cooling panel temperature

Appendix B - Computational Thermal Manikin (CTM) Validation

The CTM is validated with the wind tunnel experiments and the inlet wind conditions are considered as per the experiment (Kazuhide et al., 2015). The simulation was performed for the three different inlet wind conditions. The local convective and radiative heat fluxes have been compared with the experiment results, as shown in Figure B.1. The radiative heat flux for the three cases is in good agreement with the experiment results and the percentage error is less than 5%. The simulation results of local convective heat flux for all the cases follow a similar trend against the experimental results, however, the average deviation between them is around 25%. The CTM used for the simulation has a lesser surface area compared to the manikin used in the wind tunnel. It is one of the reasons for this deviation. On the other hand, as per Gao et al., (S. Gao et al., 2019) reproducing the experimental airflow field in CFD simulations has proven to be challenging, despite extensive efforts to maintain numerical boundary conditions consistent with the experimental conditions. Accordingly, the deviation between the CFD simulation of CTM and the experiment is deemed acceptable.



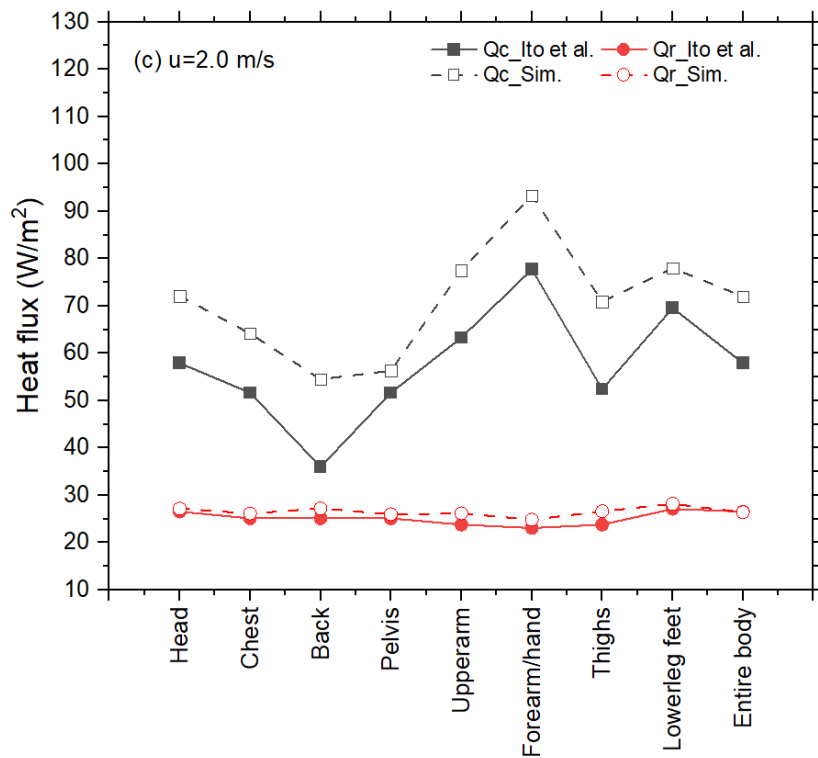
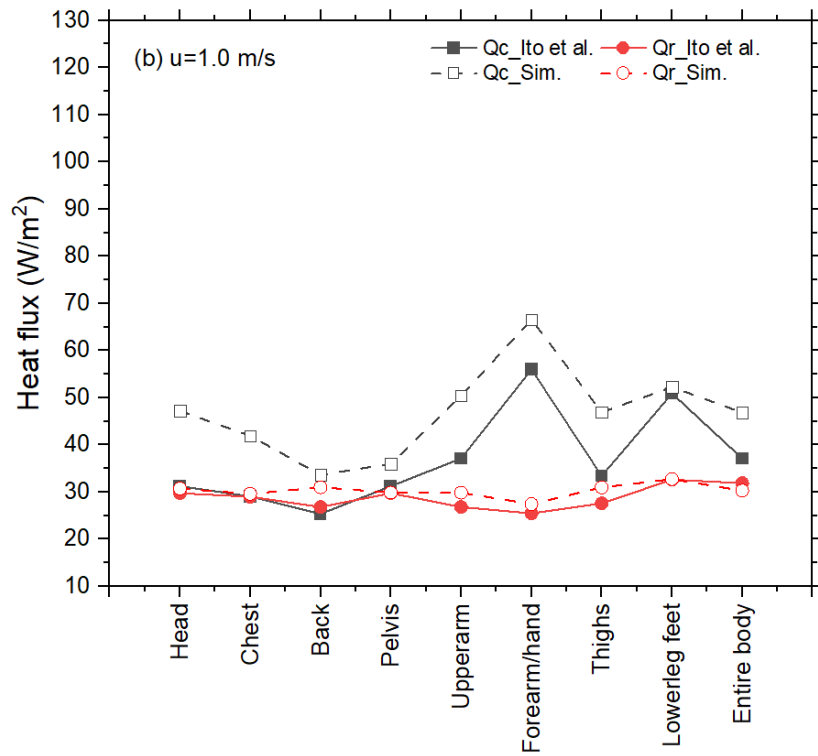


Figure B.1 Convective and radiative heat flux validation of CTM against the wind tunnel experiments for the velocities of (a) 0.5 m/s (b) 1.0 m/s and (c) 2.0 m/s

References

- Abdel-Bary, E. M. (2003). *Handbook of plastic films*: iSmithers Rapra Publishing.
- Albuja, R., Foliaco, B., Bula, A., & Gonzalez-Quiroga, A. (2022). Potential of hybrid radiant cooling with infrared-transparent membranes to improve thermal comfort in hot and humid climate. *International Journal of Thermofluids*, 16. doi:10.1016/j.ijft.2022.100214
- Alfano, F. R. D. A., Palella, B. I., & Riccio, G. (2024). THERMODE 2023: Formulation and Validation of a new Thermo-physiological Model for Moderate Environments. *Building and Environment*, 252, 111272.
- Ali, A. H. H., Saito, H., Taha, I. M. S., Kishinami, K., & Ismail, I. M. (1998). Effect of aging, thickness and color on both the radiative properties of polyethylene films and performance of the nocturnal cooling unit. *Energy Conversion and Management*, 39(1-2), 87-93.
- Allegrini, J., & Carmeliet, J. (2017). Coupled CFD and building energy simulations for studying the impacts of building height topology and buoyancy on local urban microclimates. *Urban Climate*, 21, 278-305. doi:10.1016/j.uclim.2017.07.005
- Al-Mogbel, A., & Chaturvedi, S. (2003, June). A coupled model for predicting heat and mass transfer from a human body to its surroundings. In *36th AIAA thermophysics conference* (p. 4211).
- ANSI/ASHRAE. (2013). Standard 55-2013, Thermal environmental conditions for human occupancy. In Atlanta, GA, USA: American National Standards Institute, American Society of Heating, Refrigerating and Air-Conditioning Engineers.

- Arens, E., & Zhang, H. (2006). The skin's role in human thermoregulation and comfort. In *Thermal and Moisture Transport in Fibrous Materials* (pp. 560-602).
- Aviv, D., Chen, K. W., Teitelbaum, E., Sheppard, D., Pantelic, J., Rysanek, A., & Meggers, F. (2021). A fresh (air) look at ventilation for COVID-19: Estimating the global energy savings potential of coupling natural ventilation with novel radiant cooling strategies. *Appl Energy*, 292, 116848. doi:10.1016/j.apenergy.2021.116848
- Ballester, J., Quijal-Zamorano, M., Méndez Turrubiates, R. F., Pegenaute, F., Herrmann, F. R., Robine, J. M., . . . Achebak, H. (2023). Heat-related mortality in Europe during the summer of 2022. *Nature medicine*, 29(7), 1857-1866.
- Balocco, C., Mercatelli, L., Azzali, N., Meucci, M., & Grazzini, G. (2018). Experimental transmittance of polyethylene films in the solar and infrared wavelengths. *Solar Energy*, 165, 199-205.
- Betti, G., Tartarini, F., Nguyen, C., & Schiavon, S. (2022). CBE Clima Tool: a free and open-source web application for climate analysis tailored to sustainable building design. *arXiv preprint arXiv:2212.04609*.
- Blazejczyk, K., Epstein, Y., Jendritzky, G., Staiger, H., & Tinz, B. (2012). Comparison of UTCI to selected thermal indices. *International Journal of Biometeorology*, 56, 515-535.
- Brake, R., & Bates, G. (2002). A valid method for comparing rational and empirical heat stress indices. *Annals of occupational hygiene*, 46(2), 165-174.
- Castellani, M. P., Rioux, T. P., Castellani, J. W., Potter, A. W., Notley, S. R., & Xu, X. (2023). Finite element model of female thermoregulation with geometry based on medical images. *J Therm Biol*, 113, 103477. doi:10.1016/j.jtherbio.2023.103477

- Castellani, M. P., Rioux, T. P., Castellani, J. W., Potter, A. W., & Xu, X. (2021). A geometrically accurate 3 dimensional model of human thermoregulation for transient cold and hot environments. *Computers in Biology and Medicine*, *138*, 104892.
- Chatzidimitriou, A., & Yannas, S. (2015). Microclimate development in open urban spaces: The influence of form and materials. *Energy and Buildings*, *108*, 156-174.
- Chen, G., Rong, L., & Zhang, G. (2020). Comparison of urban airflow between solar-induced thermal wall and uniform wall temperature boundary conditions by coupling CitySim and CFD. *Building and Environment*, *172*. doi:10.1016/j.buildenv.2020.106732
- Chen, H., Ooka, R., Huang, H., & Tsuchiya, T. (2009). Study on mitigation measures for outdoor thermal environment on present urban blocks in Tokyo using coupled simulation. *Building and Environment*, *44*(11), 2290-2299. doi:https://doi.org/10.1016/j.buildenv.2009.03.012
- Chen, K. W., Teitelbaum, E., Meggers, F., Pantelic, J., & Rysanek, A. (2020). Exploring membrane-assisted radiant cooling for designing comfortable naturally ventilated spaces in the tropics. *Building Research & Information*, *49*(5), 483-495. doi:10.1080/09613218.2020.1847025
- Chen, Y.C., & Matzarakis, A. (2018). Modified physiologically equivalent temperature—Basics and applications for western European climate. *Theoretical and applied climatology*, *132*, 1275-1289.
- Chen, Z., Zhu, L., Raman, A., & Fan, S. (2016). Radiative cooling to deep sub-freezing temperatures through a 24-h day–night cycle. *Nature Communications*, *7*(1), 13729.

- Cheng, V., Ng, E., Chan, C., & Givoni, B. (2012). Outdoor thermal comfort study in a subtropical climate: a longitudinal study based in Hong Kong. *International Journal of Biometeorology*, 56, 43-56.
- Cheung, P. K., & Jim, C. Y. (2018). Comparing the cooling effects of a tree and a concrete shelter using PET and UTCI. *Building and Environment*, 130, 49-61. doi:<https://doi.org/10.1016/j.buildenv.2017.12.013>
- Choudhary, B., & Udayraj. (2022). A coupled CFD-thermoregulation model for air ventilation clothing. *Energy and Buildings*, 268. doi:10.1016/j.enbuild.2022.112206
- Coles, R., McDowell, D., & Kirwan, M. J. (2003). Food packaging technology (Vol. 5): CRC press.
- Cook, M., Yang, T., & Cropper, P. (2011). Thermal comfort in naturally ventilated classrooms: application of coupled simulation models. In *Building Simulation 2011 conference*.
- Crawley, D. B., Lawrie, L. K., Pedersen, C. O., & Winkelmann, F. C. (2000). Energy plus: energy simulation program. *ASHRAE journal*, 42(4), 49-56.
- Cropper, P. C., Yang, T., Cook, M., Fiala, D., & Yousaf, R. (2010). Coupling a model of human thermoregulation with computational fluid dynamics for predicting human–environment interaction. *Journal of Building Performance Simulation*, 3(3), 233-243. doi:10.1080/19401491003615669
- Dai, Q., Xing, D., Fang, X., & Zhao, Y. (2017). Numerical research on the thermal performance of high altitude scientific balloons. *Applied Thermal Engineering*, 114, 51-57.

- de Dear, R. J., Arens, E., Hui, Z., & Oguro, M. (1997). Convective and radiative heat transfer coefficients for individual human body segments. *Int J Biometeorol*, 40(3), 141-156. doi:10.1007/s004840050035
- de Freitas, C. R., & Grigorieva, E. A. (2017). A comparison and appraisal of a comprehensive range of human thermal climate indices. *International Journal of Biometeorology*, 61, 487-512.
- Desa, U. N. (2014). World urbanization prospects. *Population Division, department of economic and social affairs, United Nations Secretariat*.
- Dharmasastha, K., Zhong, Z., Niu, J., & Liang, H. (2023). A comprehensive review of cover-shield-assisted radiant cooling system. *Energy and Buildings*, 291. doi:10.1016/j.enbuild.2023.113121
- Do, H. Q., Luther, M. B., Amirkhani, M., Wang, Z., & Martek, I. (2022). Radiant conditioning retrofitting for residential buildings. *Energies*, 15(2), 449.
- Dodla, V. B., Satyanarayana, G. C., & Desamsetti, S. (2017). Analysis and prediction of a catastrophic Indian coastal heat wave of 2015. *Natural Hazards*, 87(1), 395-414. doi:10.1007/s11069-017-2769-7
- Du, K., Wu, H., Guo, Y., Huang, G., Xu, X., & Liu, Y. (2022). Improving Cooling Capacity of Condensation-Free Radiant Cooling for Low-Emissivity Chilled Ceiling via Adaptive Double-Skin Infrared Membranes. *Frontiers in Thermal Engineering*, 2. doi:10.3389/fther.2022.905015
- Du, K., Wu, H., Huang, G., Xu, X., & Liu, Y. (2021). Condensation-free radiant cooling with double-skin infrared-transparent membranes. *Building and Environment*, 193. doi:10.1016/j.buildenv.2021.107660

- Dugaria, S., Bortolato, M., & Del Col, D. (2018). Modelling of a direct absorption solar receiver using carbon based nanofluids under concentrated solar radiation. *Renewable Energy*, 128, 495-508. doi:<https://doi.org/10.1016/j.renene.2017.06.029>
- Dzyuban, Y., Hondula, D. M., Coseo, P. J., & Redman, C. L. (2022). Public transit infrastructure and heat perceptions in hot and dry climates. *International Journal of Biometeorology*, 66(2), 345-356. doi:10.1007/s00484-021-02074-4
- Edward, N. (2009). Wind and heat environment in densely built urban areas in Hong Kong. *Wind and Heat Environment in Densely Built Urban Areas in Hong Kong*, 13(2), 169-178.
- Fanger, P. O. (1970). Thermal comfort. Analysis and applications in environmental engineering. *Copenhagen: Danish Technical Press.*
- Fanger, P. O., Ipsen, B. M., Langkilde, G., Olesen, B. W., Christensen, N. K., & Tanabe, S. (1985). Comfort limits for asymmetric thermal radiation. *Energy and Buildings*, 8(3), 225-236.
- Fiala, D., Lomas, K. J., & Stohrer, M. (1999). A computer model of human thermoregulation for a wide range of environmental conditions: the passive system. *Journal of applied physiology*, 87(5), 1957-1972.
- Fiala, D., Lomas, K. J., & Stohrer, M. (2001). Computer prediction of human thermoregulatory and temperature responses to a wide range of environmental conditions. *International Journal of Biometeorology*, 45, 143-159.
- FLUENT, A. (2009). ANSYS FLUENT 12.0. *Theory Guide*, 67.
- Franke, J., Hellsten, A., Schlunzen, K. H., & Carissimo, B. (2011). The COST 732 Best Practice Guideline for CFD simulation of flows in the urban environment: a summary. *International Journal of Environment and Pollution*, 44(1-4), 419-427.

- Fu, M., Yu, T., Zhang, H., Arens, E., Weng, W., & Yuan, H. (2014). A model of heat and moisture transfer through clothing integrated with the UC Berkeley comfort model. *Building and Environment*, 80, 96-104.
- Gagge, A. P., Fobelets, A. P., & Berglund, L. (1986). A standard predictive index of human response to the thermal environment. *ASHRAE Transactions*.
- Gao, N., Niu, J., & Zhang, H. (2006). Coupling CFD and Human Body Thermoregulation Model for the Assessment of Personalized Ventilation. *HVAC&R Research*, 12(3), 497-518. doi:10.1080/10789669.2006.10391191
- Gao, S., Ooka, R., & Oh, W. (2019). Formulation of human body heat transfer coefficient under various ambient temperature, air speed and direction based on experiments and CFD. *Building and Environment*, 160. doi:10.1016/j.buildenv.2019.106168
- Gentle, A. R., Dybdal, K. L., & Smith, G. B. (2013). Polymeric mesh for durable infra-red transparent convection shields: Applications in cool roofs and sky cooling. *Solar Energy Materials and Solar Cells*, 115, 79-85. doi:10.1016/j.solmat.2013.03.001
- Gliah, O., Kruczek, B., Etemad, S. G., & Thibault, J. (2011). The effective sky temperature: an enigmatic concept. *Heat and Mass Transfer*, 47(9), 1171-1180. doi:10.1007/s00231-011-0780-1
- Gobatti, L., Bach, P. M., Scheidegger, A., & Leitão, J. P. (2023). Using satellite imagery to investigate Blue-Green Infrastructure establishment time for urban cooling. *Sustainable Cities and Society*, 97, 104768.
- Golaka, A., & Exell, R. H. B. (2007). An investigation into the use of a wind shield to reduce the convective heat flux to a nocturnal radiative cooling surface. *Renewable Energy*, 32(4), 593-608.

- Gong, N., Tham, K. W., Melikov, A. K., Wyon, D. P., Sekhar, S. C., & Cheong, K. W. (2006). The Acceptable Air Velocity Range for Local Air Movement in The Tropics. *HVAC&R Research*, 12(4), 1065-1076. doi:10.1080/10789669.2006.10391451
- Gordon, R. G., Roemer, R. B., & Horvath, S. M. (1976). A mathematical model of the human temperature regulatory system-transient cold exposure response. *IEEE Transactions on Biomedical Engineering*(6), 434-444.
- Goyal, M. K., Singh, S., & Jain, V. (2023). Heat waves characteristics intensification across Indian smart cities. *Scientific Reports*, 13(1), 14786. doi:10.1038/s41598-023-41968-8
- Gu, J. A., Wu, H., Zhang, G., Du, K., Guo, Y., Huang, G., . . . Ma, H. (2023). Numerical study of the integrated heat transfer of a condensation-free radiant cooling panel covered with multiple interlayer infrared membranes. *Journal of Building Engineering*, 63. doi:10.1016/j.job.2022.105460
- Guo, Y., Wu, H., Du, K., Huang, G., & Xu, X. (2023). Experimental study on radiant cooling with double-skin infrared-transparent membranes. *Energy and Buildings*, 278. doi:10.1016/j.enbuild.2022.112654
- He, R., Liao, Y., Huang, J., Cheng, T., Zhang, X., Yang, P., . . . Liu, K. (2021). Radiant air-conditioning with infrared transparent polyethylene aerogel. *Materials Today Energy*, 21. doi:10.1016/j.mtener.2021.100800
- Höpfe, P. (1999). The physiological equivalent temperature—a universal index for the biometeorological assessment of the thermal environment. *International Journal of Biometeorology*, 43, 71-75.

- Houchois, N., Teitelbaum, E., Chen, K. W., Rucewicz, S., & Meggers, F. (2019). The SMART sensor: fully characterizing radiant heat transfer in the built environment. *Journal of Physics: Conference Series*, 1343(1). doi:10.1088/1742-6596/1343/1/012073
- Hsu, P.C., Song, A. Y., Catrysse, P. B., Liu, C., Peng, Y., Xie, J., . . . Cui, Y. (2016). Radiative human body cooling by nanoporous polyethylene textile. *Science*, 353(6303), 1019-1023.
- Hu, R., & Niu, J. L. (2012). A review of the application of radiant cooling & heating systems in Mainland China. *Energy and Buildings*, 52, 11-19. doi:10.1016/j.enbuild.2012.05.030
- Huang, T., Li, J., Xie, Y., Niu, J., & Mak, C. M. (2017). Simultaneous environmental parameter monitoring and human subject survey regarding outdoor thermal comfort and its modelling. *Building and Environment*, 125, 502-514. doi:10.1016/j.buildenv.2017.09.015
- Huizenga, C., Hui, Z., & Arens, E. (2001). A model of human physiology and comfort for assessing complex thermal environments. *Building and Environment*, 36(6), 691-699. doi:10.1016/s0360-1323(00)00061-5
- Ichihara, M., Saitou, M., Nishimura, M., & Tanabe, S.-i. (1997). Measurement of Convective and Radiative Heat Transfer Coefficients of Standing and Sitting Human Body by Using a Thermal Manikin. *Journal of Architecture and Planning (Transactions of AIJ)*, 62(501), 45-51. doi:10.3130/aija.62.45_5
- Ignatov, I., Mosin, O., & Drossinakis, C. (2014). Infrared thermal field emitted from human body. thermovision. *Journal of Medicine, Physiology and Biophysics*, 1, 1-12.

- International Organization for, S. (2007). ISO 20473: 2007. Optics and photonics—Spectral bands.
- Iqbal, S. (2019). Thermal Comfort and Energy-Use in Urban Transitional Spaces-Bus stop in Slovenia. *Master Thesis*, Lund University, Scandinavia.
- Iso, B. S. I. (2015). 20473: 2007 Optics and Photonics—Spectral Bands. In: British Standards Institution (BSI).
- Issa, F. S., & Alrusayni, Y. A. (2024). 100 - Heat Wave. In G. Ciottone (Ed.), *Ciottone's Disaster Medicine (Third Edition)* (pp. 621-624). New Delhi: Elsevier.
- Ito, K. Virtual Manikin (Computer Simulated Person) Library. Retrieved from http://www.phe-kyudai.jp/research_01.html
- Jiang, Y., Xie, Y., & Niu, J. (2024). Short-term dynamic thermal perception and physiological response to step changes between real-life indoor and outdoor environments. *Building and Environment*, 251. doi:10.1016/j.buildenv.2024.111223
- Joshi, A., Wang, F., Kang, Z., Yang, B., & Zhao, D. (2022). A three-dimensional thermoregulatory model for predicting human thermophysiological responses in various thermal environments. *Building and Environment*, 207, 108506.
- Joshi, A., Wang, F., Kang, Z., Yang, B., & Zhao, D. (2022). A three-dimensional thermoregulatory model for predicting human thermophysiological responses in various thermal environments. *Building and Environment*, 207. doi:10.1016/j.buildenv.2021.108506
- Kántor, N., & Unger, J. (2011). The most problematic variable in the course of human-biometeorological comfort assessment — the mean radiant temperature. *Open Geosciences*, 3(1), 90-100. doi:10.2478/s13533-011-0010-x

- Karmann, C., Schiavon, S., & Bauman, F. (2017). Thermal comfort in buildings using radiant vs. all-air systems: A critical literature review. *Building and Environment*, 111, 123-131. doi:10.1016/j.buildenv.2016.10.020
- Kazuhide, I., Kiao, I., Takashi, K., Toshikatsu, U., Tomoyuki, E., Toshiaki, O., . . . Jiyuan, T. (2015). CFD Benchmark Tests for Indoor Environmental Problems: Part 3 Numerical Thermal Manikins. *International Journal of Architectural Engineering Technology*, 2(1), 50-75. doi:10.15377/2409-9821.2015.02.01.3
- Keeping Bus Stops Cool! - Demonstration Experiment of the "Green Air Conditioner" in Fujisawa SST. (2017). Retrieved from <https://news.panasonic.com/global/topics/5141>
- Kilic, M., & Sevilgen, G. (2008). Modelling airflow, heat transfer and moisture transport around a standing human body by computational fluid dynamics. *International Communications in Heat and Mass Transfer*, 35(9), 1159-1164. doi:10.1016/j.icheatmasstransfer.2008.05.006
- Kingma, B. R. M. (2012). Human thermoregulation : a synergy between physiology and mathematical modelling. *PhD Thesis, Universitaire Pers Maastricht*, Netherlands.
- Kingma, B. R. M., Schellen, L., Frijns, A. J. H., & van Marken Lichtenbelt, W. D. (2012). Thermal sensation: a mathematical model based on neurophysiology. *Indoor Air*, 22(3), 253-262.
- Knowlton, K., Rotkin-Ellman, M., King, G., Margolis Helene, G., Smith, D., Solomon, G., . . . English, P. (2009). The 2006 California Heat Wave: Impacts on Hospitalizations and Emergency Department Visits. *Environmental Health Perspectives*, 117(1), 61-67. doi:10.1289/ehp.11594

- Kobayashi, Y., & Tanabe, S.-i. (2013). Development of JOS-2 human thermoregulation model with detailed vascular system. *Building and Environment*, 66, 1-10.
- Kornev, N. (2016). Coupling of human thermoregulation and URANS computation for investigation of local heat transfer and flow structures in a generic car cabin. *Flow, Turbulence and Combustion*, 97(4), 1281-1296.
- Kotharkar, R., & Ghosh, A. (2022). Progress in extreme heat management and warning systems: A systematic review of heat-health action plans (1995-2020). *Sustainable Cities and Society*, 76. doi:10.1016/j.scs.2021.103487
- Kyogoku, S., & Takebayashi, H. (2023). Experimental Verification of Mist Cooling Effect in Front of Air-Conditioning Condenser Unit, Open Space, and Bus Stop. *Atmosphere*, 14(1). doi:10.3390/atmos14010177
- La, D., Dai, Y. J., Li, Y., Wang, R. Z., & Ge, T. S. (2010). Technical development of rotary desiccant dehumidification and air conditioning: A review. *Renewable and Sustainable Energy Reviews*, 14(1), 130-147. doi:10.1016/j.rser.2009.07.016
- Lai, A., Maing, M., & Ng, E. (2017). Observational studies of mean radiant temperature across different outdoor spaces under shaded conditions in densely built environment. *Building and Environment*, 114, 397-409.
- Lei, Y., He, Y., Li, X., Tian, Y., Xiang, X., & Feng, C. (2024). Experimental comparison on the performance of radiative, reflective and evaporative cooling in extremely hot climate: A case study in Chongqing, China. *Sustainable Cities and Society*, 100, 105023.
- Leroy, A., Bhatia, B., Kelsall, C. C., Castillejo-Cuberos, A., Di Capua, H. M., Zhao, L., . . . Wang, E. N. (2019). High-performance subambient radiative cooling enabled by

optically selective and thermally insulating polyethylene aerogel. *Sci Adv*, 5(10), eaat9480.
doi:10.1126/sciadv.aat9480

- Leroy, A., Bhatia, B., Njike, U. T., Vaartstra, G., & Wang, E. N. (2021). Zinc sulfide-pigmented polyethylene aerogel covers for daytime radiative cooling. *Journal of Photonics for Energy*, 11(4), 042110-042110.
- Li, C., & Ito, K. (2014). Numerical and experimental estimation of convective heat transfer coefficient of human body under strong forced convective flow. *Journal of Wind Engineering and Industrial Aerodynamics*, 126, 107-117.
doi:10.1016/j.jweia.2014.01.003
- Li, K., Liu, X., & Bao, Y. (2022). Evaluating the performance of different thermal indices on quantifying outdoor thermal sensation in humid subtropical residential areas of China. *Frontiers in Environmental Science*, 10, 1071668.
- Li, Z., Chen, Q., Song, Y., Zhu, B., & Zhu, J. (2020). Fundamentals, materials, and applications for daytime radiative cooling. *Advanced Materials Technologies*, 5(5), 1901007.
- Li, Z., Zhang, H., Wen, C.-Y., Yang, A.-S., & Juan, Y.-H. (2020). Effects of frontal area density on outdoor thermal comfort and air quality. *Building and Environment*, 180.
doi:10.1016/j.buildenv.2020.107028
- Liang, H., Tanabe, S. I., & Niu, J. (2023). Coupled simulation of CFD and human thermoregulation model in outdoor wind environment. In *E3S Web of Conferences* (Vol. 396, p. 05008). EDP Sciences.

- Liang, H., Yu, Y., & Niu, J. (2023). Large eddy simulation of convective heat transfer around human body in outdoor environments. In *International Heat Transfer Conference Digital Library*. Begel House Inc..
- Liang, Y., Zhang, N., Wu, H., Xu, X., Du, K., Yang, J., . . . Huang, G. (2021). Thermal environment and thermal comfort built by decoupled radiant cooling units with low radiant cooling temperature. *Building and Environment*, 206. doi:10.1016/j.buildenv.2021.108342
- Liang, Y., Zhang, N., Wu, H., Xu, X., Yang, J., & Huang, G. (2022). Cooling load characteristics of indoor spaces conditioned by decoupled radiant cooling unit with low radiant temperature. *Building Simulation*, 15(12), 2067-2079. doi:10.1007/s12273-022-0919-7
- Lin, T.-P., Matzarakis, A., & Huang, J. J. (2006). Thermal comfort and passive design strategy of bus shelters. In *23rd International Conference on Passive and Low Energy Architecture, PLEA 2006*.
- Liu, J., & Niu, J. (2016). CFD simulation of the wind environment around an isolated high-rise building: An evaluation of SRANS, LES and DES models. *Building and Environment*, 96, 91-106.
- Liu, L., Zhang, X., Liang, H., Niu, J., & Wu, J.-Y. (2022). Cooling storage performance of a novel phase change material nano-emulsion for room air-conditioning in a self-designed pilot thermal storage unit. *Applied Energy*, 308, 118405.
- Masterton, J. M., & Richardson, F. A. (1979). *Humidex: a method of quantifying human discomfort due to excessive heat and humidity*: Environment Canada, Atmospheric Environment.

- Mirzaei, P. A., & Haghighat, F. (2010). Approaches to study Urban Heat Island – Abilities and limitations. *Building and Environment*, 45(10), 2192-2201. doi:<https://doi.org/10.1016/j.buildenv.2010.04.001>
- Moghimi, M. A., Craig, K. J., & Meyer, J. P. (2015). A novel computational approach to combine the optical and thermal modelling of Linear Fresnel Collectors using the finite volume method. *Solar Energy*, 116, 407-427. doi:<https://doi.org/10.1016/j.solener.2015.04.014>
- Mokhtari, R., & Ghasempour, R. (2023). Feasibility study of integration of radiative cooling and hydronic radiant system for free cooling of single-family houses. *Applied Thermal Engineering*, 220. doi:[10.1016/j.applthermaleng.2022.119629](https://doi.org/10.1016/j.applthermaleng.2022.119629)
- Mokhtari, R., & Jahangir, M. H. (2021). The effect of occupant distribution on energy consumption and COVID-19 infection in buildings: A case study of university building. *Building and Environment*, 190, 107561. doi:<https://doi.org/10.1016/j.buildenv.2020.107561>
- Mokhtari, R., Ulpiani, G., & Ghasempour, R. (2022). The Cooling Station: Combining hydronic radiant cooling and daytime radiative cooling for urban shelters. *Applied Thermal Engineering*, 211. doi:[10.1016/j.applthermaleng.2022.118493](https://doi.org/10.1016/j.applthermaleng.2022.118493)
- Morse, R. N. (1963). Radiant Cooling. *Architectural Science Review*, 6(2), 50-53. doi:[10.1080/00038628.1963.9696068](https://doi.org/10.1080/00038628.1963.9696068)
- Murakami, S., Kato, S., & Zeng, J. (2000). Combined simulation of airflow, radiation and moisture transport for heat release from a human body. *Building and Environment*, 35(6), 489-500. doi:[https://doi.org/10.1016/S0360-1323\(99\)00033-5](https://doi.org/10.1016/S0360-1323(99)00033-5)

- Naghshine, B. B., & Saboonchi, A. (2018). Optimized thin film coatings for passive radiative cooling applications. *Optics Communications*, 410, 416-423. doi:10.1016/j.optcom.2017.10.047
- Nilsson, N. A., Eriksson, T. S., & Granqvist, C. G. (1985). Infrared-transparent convection shields for radiative cooling: Initial results on corrugated polyethylene foils. *Solar Energy Materials*, 12(5), 327-333.
- Ning, B., Chen, Y., Liu, H., & Zhang, S. (2016). Cooling capacity improvement for a radiant ceiling panel with uniform surface temperature distribution. *Building and Environment*, 102, 64-72. doi:https://doi.org/10.1016/j.buildenv.2016.03.009
- Omori, T., Yang, J. H., Kato, S., & Murakami, S. (2004). Coupled simulation of convection and radiation on thermal environment around an accurately shaped human body. *In RoomVent 2004, 9th international conference in University of Coimbra*.
- Pandey, D. K., Lee Iii, R. B., & Paden, J. (1995). Effects of atmospheric emissivity on clear sky temperatures. *Atmospheric Environment*, 29(16), 2201-2204.
- Park, H., Yoo, S. J., Seo, J., Eisaku, S., Hiroshi, H., Kuga, K., & Ito, K. (2024). Integration of computer-simulated persons with multi-node thermoregulation model that considers the effect of clothing for skin surface temperature distribution analysis. *Building and Environment*, 248, 111105.
- Parsons, K. C., Havenith, G., Holmér, I., Nilsson, H., & Malchaire, J. (1999). The effects of wind and human movement on the heat and vapour transfer properties of clothing. *Annals of Occupational Hygiene*, 43(5), 347-352.

- Peel, M. C., Finlayson, B. L., & McMahon, T. A. (2007). Updated world map of the Köppen-Geiger climate classification. *Hydrology and earth system sciences*, 11(5), 1633-1644.
- Pickup, J., & de Dear, R. (2000). An outdoor thermal comfort index (OUT_SET*)-part I- the model and its assumptions. In *Biometeorology and urban climatology at the turn of the millenium. Selected papers from the Conference ICB-ICUC* (Vol. 99, pp. 279-283).
- Pieters, J. G., & Deltour, J. M. (1997). Performances of greenhouses with the presence of condensation on cladding materials. *Journal of Agricultural Engineering Research*, 68(2), 125-137.
- Pollet, I. V., & Pieters, J. G. (2000). Condensation and radiation transmittance of greenhouse cladding materials, part 2: results for a complete condensation cycle. *Journal of Agricultural Engineering Research*, 75(1), 65-72.
- Post, C. (2021). Qatar opens first-ever air conditioned jogging track. Retrieved from <https://www.coolingpost.com/world-news/qatar-opens-first-ever-air-conditioned-jogging-track/>
- Potsis, T., Tominaga, Y., & Stathopoulos, T. (2023). Computational wind engineering: 30 years of research progress in building structures and environment. *Journal of Wind Engineering and Industrial Aerodynamics*, 234. doi:10.1016/j.jweia.2023.105346
- Qu, Y., Milliez, M., Musson-Genon, L., & Carissimo, B. (2012). Numerical study of the thermal effects of buildings on low-speed airflow taking into account 3D atmospheric radiation in urban canopy. *Journal of Wind Engineering and Industrial Aerodynamics*, 104-106, 474-483. doi:<https://doi.org/10.1016/j.jweia.2012.03.008>

- Rakha, T., & Zhandand Christoph Reinhart, P. (2017, August). A framework for outdoor mean radiant temperature simulation: Towards spatially resolved thermal comfort mapping in urban spaces. In *Building Simulation 2017* (Vol. 15, pp. 2414-2420). IBPSA.
- Ramesh Babu, A., Sebben, S., Chronéer, Z., & Etemad, S. (2024). An adaptive cabin air recirculation strategy for an electric truck using a coupled CFD-thermoregulation approach. *International Journal of Heat and Mass Transfer*, 221, 125056. doi:<https://doi.org/10.1016/j.ijheatmasstransfer.2023.125056>
- Rhee, K.-N., & Kim, K. W. (2015). A 50 year review of basic and applied research in radiant heating and cooling systems for the built environment. *Building and Environment*, 91, 166-190. doi:[10.1016/j.buildenv.2015.03.040](https://doi.org/10.1016/j.buildenv.2015.03.040)
- Riffat, J., Kutlu, C., Tapia-Brito, E., Su, Y., & Riffat, S. (2022). A preliminary experimental study of a novel incorporation of chilled ceiling with phase change materials and transparent membrane cover. *International Journal of Low-Carbon Technologies*, 17, 258-265. doi:[10.1093/ijlct/ctab104](https://doi.org/10.1093/ijlct/ctab104)
- Robine, J.-M., Cheung, S. L. K., Le Roy, S., Van Oyen, H., Griffiths, C., Michel, J.-P., & Herrmann, F. R. (2008). Death toll exceeded 70,000 in Europe during the summer of 2003. *Comptes Rendus Biologies*, 331(2), 171-178. doi:<https://doi.org/10.1016/j.crvi.2007.12.001>
- Roshan, G., Moghbel, M., & Attia, S. (2020). Evaluating the wind cooling potential on outdoor thermal comfort in selected Iranian climate types. *Journal of Thermal Biology*, 92, 102660. doi:<https://doi.org/10.1016/j.jtherbio.2020.102660>

- Saber, E. M., Tham, K. W., & Leibundgut, H. (2016). A review of high temperature cooling systems in tropical buildings. *Building and Environment*, 96, 237-249. doi:10.1016/j.buildenv.2015.11.029
- Santamouris, M. (2020). Recent progress on urban overheating and heat island research. Integrated assessment of the energy, environmental, vulnerability and health impact. Synergies with the global climate change. *Energy and Buildings*, 207, 109482. doi:https://doi.org/10.1016/j.enbuild.2019.109482
- Santamouris, M., Ding, L., & Osmond, P. (2019). Urban Heat Island Mitigation. In P. Newton, D. Prasad, A. Sproul, & S. White (Eds.), *Decarbonising the Built Environment: Charting the Transition* (pp. 337-355). Singapore: Springer Singapore.
- Schellen, L., Loomans, M., Kingma, B. R. M., De Wit, M. H., Frijns, A. J. H., & van Marken Lichtenbelt, W. D. (2013). The use of a thermophysiological model in the built environment to predict thermal sensation: coupling with the indoor environment and thermal sensation. *Building and Environment*, 59, 10-22.
- Shan, X., Liu, L., Wu, Y., Yuan, D., Wang, J., Zhang, C., & Wang, J. (2022). Aerogel-functionalized thermoplastic polyurethane as waterproof, breathable freestanding films and coatings for passive daytime radiative cooling. *Advanced Science*, 9(20), 2201190.
- Sheppard, D. (2020). Integrating Membrane-Assisted Radiant Cooling Panels in Building Energy Simulation. *Master Thesis*, The University of British Columbia.
- Shinoda, J., Kazanci, O. B., Tanabe, S.-i., & Olesen, B. W. (2019). A review of the surface heat transfer coefficients of radiant heating and cooling systems. *Building and Environment*, 159. doi:10.1016/j.buildenv.2019.05.034

- Siegel, R. (1996). Two-flux method for transient radiative transfer in a semitransparent layer. *International Journal of Heat Mass Transfer*, 39(NAS 1.15: 112492).
- Siegel, R., & Spuckler, C. M. (1996). Temperature distributions in semitransparent coatings-A special two-flux solution. *Journal of Thermophysics and Heat Transfer*, 10(1), 39-46.
- Smith, P., & Twizell, E. H. (1984). A transient model of thermoregulation in a clothed human. *Applied Mathematical Modelling*, 8(3), 211-216.
- Sofotasiou, P., Hughes, B. R., & Calautit, J. K. (2015). Qatar 2022: Facing the FIFA World Cup climatic and legacy challenges. *Sustainable Cities and Society*, 14, 16-30. doi:<https://doi.org/10.1016/j.scs.2014.07.007>
- Sola-Caraballo, J., Lopez-Cabeza, V. P., Roa-Fernández, J., Rivera-Gomez, C., & Galan-Marin, C. (2024). Assessing and upgrading urban thermal resilience of a Spanish MoMo neighbourhood over the span of 1960–2080. *Building and Environment*, 256, 111485. doi:<https://doi.org/10.1016/j.buildenv.2024.111485>
- Steadman, R. G. (1984). A universal scale of apparent temperature. *Journal of Applied Meteorology and Climatology*, 23(12), 1674-1687.
- Stock, S., Bu, F., Fancourt, D., & Mak, H. W. (2022). Longitudinal associations between going outdoors and mental health and wellbeing during a COVID-19 lockdown in the UK. *Scientific Reports*, 12(1), 10580. doi:[10.1038/s41598-022-15004-0](https://doi.org/10.1038/s41598-022-15004-0)
- Stolwijk, J. A. (1971). A mathematical model of physiological temperature regulation in man (No. NASA-CR-1855). NASA contractor report, USA.

- Streblow, R., Müller, D., Gores, I., & Bendfeldt, P. (2008, September). A coupled simulation of the thermal environment and thermal comfort with an adapted Tanabe comfort model. In *7th International Thermal Manikin and Modelling Meeting, Portugal*.
- Su, X., Zhang, L., Liu, Z., Luo, Y., Lian, J., & Luo, Y. (2019). A computational model of an improved cooling radiant ceiling panel system for optimization and design. *Building and Environment*, *163*, 106312. doi:<https://doi.org/10.1016/j.buildenv.2019.106312>
- Sydney's Busted Bus Stops: Read our Campaign Report. (2024). Retrieved from <https://swelteringcities.org/2024/03/13/sydneys-busted-bus-stops-report/>
- Takahashi, Y., Nomoto, A., Yoda, S., Hisayama, R., Ogata, M., Ozeki, Y., & Tanabe, S.-i. (2021a). Thermoregulation model JOS-3 with new open source code. *Energy and Buildings*, *231*, 110575.
- Takahashi, Y., Nomoto, A., Yoda, S., Hisayama, R., Ogata, M., Ozeki, Y., & Tanabe, S.-i. (2021b). Thermoregulation model JOS-3 with new open source code. *Energy and Buildings*, *231*. doi:10.1016/j.enbuild.2020.110575
- Takemori, T., Nakajima, T., & Shoji, Y. (1996). A fundamental model of the human thermal system for prediction of thermal comfort. *Heat Transfer-Japanese Research*, *24*(2).
- Taleghani, M., Kleerekoper, L., Tenpierik, M., & Van Den Dobbelen, A. (2015). Outdoor thermal comfort within five different urban forms in the Netherlands. *Building and Environment*, *83*, 65-78.
- Taleghani, M., Sailor, D. J., Tenpierik, M., & van den Dobbelen, A. (2014). Thermal assessment of heat mitigation strategies: The case of Portland State University, Oregon, USA. *Building and Environment*, *73*, 138-150.

- Tan, J., Zheng, Y., Tang, X., Guo, C., Li, L., Song, G., . . . Chen, H. (2010). The urban heat island and its impact on heat waves and human health in Shanghai. *International Journal of Biometeorology*, 54(1), 75-84. doi:10.1007/s00484-009-0256-x
- Tanabe, S.-i., Kobayashi, K., Nakano, J., Ozeki, Y., & Konishi, M. (2002). Evaluation of thermal comfort using combined multi-node thermoregulation (65MN) and radiation models and computational fluid dynamics (CFD). *Energy and Buildings*, 34(6), 637-646.
- Tang, H., Liu, X.-H., Li, H., Zhou, Y., & Jiang, Y. (2016). Study on the reduction of condensation risks on the radiant cooling ceiling with superhydrophobic treatment. *Building and Environment*, 100, 135-144. doi:https://doi.org/10.1016/j.buildenv.2016.02.008
- Tang, H., Zhang, T., Liu, X., & Li, C. (2021). A novel pulse width modulation for metal radiant panels to control the condensation risk in a hot and humid environment. *Building and Environment*, 196, 107802. doi:https://doi.org/10.1016/j.buildenv.2021.107802
- Teitelbaum, E., Aviv, D., Hou, M., Li, J., Rysanek, A., & Meggers, F. (2021). Validation of radiant and convective heat transfer models of photonic membrane using non-invasive imaging of condensation pattern. *Journal of Physics: Conference Series*, 2069(1). doi:10.1088/1742-6596/2069/1/012100
- Teitelbaum, E., Chen, K. W., Aviv, D., Bradford, K., Rufenacht, L., Sheppard, D., . . . Rysanek, A. (2020). Membrane-assisted radiant cooling for expanding thermal comfort zones globally without air conditioning. *Proc Natl Acad Sci U S A*, 117(35), 21162-21169. doi:10.1073/pnas.2001678117
- Teitelbaum, E., Chen, K. W., Meggers, F., Pantelic, J., Aviv, D., & Rysanek, A. (2019). The Cold Tube: Membrane assisted radiant cooling for condensation-free outdoor comfort

in the tropics. *Journal of Physics: Conference Series*, 1343(1). doi:10.1088/1742-6596/1343/1/012080

- Teitelbaum, E., P. J., Clayton Miller, Forrest Meggers. (2019). Design with Comfort: Expanding the psychrometric chart with radiation and convection dimensions.
- Teitelbaum, E., Rysanek, A., Pantelic, J., Aviv, D., Obelz, S., Buff, A., . . . Meggers, F. (2019). Revisiting radiant cooling: condensation-free heat rejection using infrared-transparent enclosures of chilled panels. *Architectural Science Review*, 62(2), 152-159. doi:10.1080/00038628.2019.1566112
- Teufl, H., Schuss, M., & Mahdavi, A. (2021). Potential and challenges of a user-centric radiant cooling approach. *Energy and Buildings*, 246. doi:10.1016/j.enbuild.2021.111104
- Thom, E. C. (1959). The discomfort index. *Weatherwise*, 12(2), 57-61.
- Tock, R. W. (1983). Permeabilities and water vapor transmission rates for commercial polymer films. *Advances in Polymer Technology: Journal of the Polymer Processing Institute*, 3(3), 223-231.
- Tominaga, Y., Mochida, A., Yoshie, R., Kataoka, H., Nozu, T., Yoshikawa, M., & Shirasawa, T. (2008). AIJ guidelines for practical applications of CFD to pedestrian wind environment around buildings. *Journal of Wind Engineering and Industrial Aerodynamics*, 96(10-11), 1749-1761. doi:10.1016/j.jweia.2008.02.058
- Torgerson, E., & Hellhake, J. (2020). Polymer solar filter for enabling direct daytime radiative cooling. *Solar Energy Materials and Solar Cells*, 206, 110319. doi:https://doi.org/10.1016/j.solmat.2019.110319

- Turnow J., K. S., Kewitz R. & N. Kornev (2016). Coupling of human thermoregulation and URANS computation for investigation of local heat transfer and flow structures in a generic car cabin. *Flow, Turbulence and Combustion*, 97(4), 1281-1296.
- Unnikrishnan, G., Hatwar, R., Hornby, S., Laxminarayan, S., Gulati, T., Belval, L. N., . . . Reifman, J. (2021). A 3-D virtual human thermoregulatory model to predict whole-body and organ-specific heat-stress responses. *European Journal of Applied Physiology*, 121(9), 2543-2562.
- Voelker, C., & Alsaad, H. (2018). Simulating the human body's microclimate using automatic coupling of CFD and an advanced thermoregulation model. *Indoor Air*, 28(3), 415-425. doi:10.1111/ina.12451
- Waiting for a bus becomes cool. (2017). Retrieved from <https://www.coolingpost.com/features/waiting-for-a-bus-becomes-cool/>
- Wang, J. (2005). Experiment and simulation of system combining displacement ventilation with cooling ceiling with high long wave transmittance film. *PhD thesis*, Tongji University, China.
- Wang, Y., Huang, Z., Lu, Y., Zhao, M., & Li, J. (2013). Heat transfer properties of the numerical human body simulated from the thermal manikin. *Journal of the Textile Institute*, 104(2), 178-187. doi:10.1080/00405000.2012.707901
- Wong, N. H., & Khoo, S. S. (2003). Thermal comfort in classrooms in the tropics. *Energy and Buildings*, 35(4), 337-351.
- Xie, Y., Huang, T., Li, J., Liu, J., Niu, J., Mak, C. M., & Lin, Z. (2018). Evaluation of a multi-nodal thermal regulation model for assessment of outdoor thermal comfort:

Sensitivity to wind speed and solar radiation. *Building and Environment*, 132, 45-56.
doi:10.1016/j.buildenv.2018.01.025

- Xie, Y., Niu, J., Zhang, H., Liu, S., Liu, J., Huang, T., . . . Mak, C. M. (2020). Development of a multi-nodal thermal regulation and comfort model for the outdoor environment assessment. *Building and Environment*, 176. doi:10.1016/j.buildenv.2020.106809
- Xing, D., & Li, N. (2021). Thermal performance improvement for the ceiling radiant cooling panel with an inbuilt air gap by the convection shield. *Sustainable Energy Technologies and Assessments*, 44. doi:10.1016/j.seta.2021.101012
- Xing, D., Li, N., Cui, H., Zhou, L., & Liu, Q. (2020). Theoretical study of infrared transparent cover preventing condensation on indoor radiant cooling surfaces. *Energy*, 201. doi:10.1016/j.energy.2020.117694
- Xing, D., Li, N., Zhang, C., & Heiselberg, P. (2021). A critical review of passive condensation prevention for radiant cooling. *Building and Environment*, 205. doi:10.1016/j.buildenv.2021.108230
- Xu, J., Psikuta, A., Li, J., Annaheim, S., & Rossi, R. M. (2019). Influence of human body geometry, posture and the surrounding environment on body heat loss based on a validated numerical model. *Building and Environment*, 166. doi:10.1016/j.buildenv.2019.106340
- Yaglou, C. P., & Minaed, D. (1957). Control of heat casualties at military training centers. *Arch. Indust. Health*, 16(4), 302-316.
- Yang, A.-S., Juan, Y.-H., Wen, C.-Y., & Chang, C.-J. (2017). Numerical simulation of cooling effect of vegetation enhancement in a subtropical urban park. *Applied Energy*, 192, 178-200. doi:10.1016/j.apenergy.2017.01.079

- Yang, J., Liang, Y., Zhong, Z., Dharmasastha, K., Xie, Y., & Niu, J.-L. (2024). Thermal comfort investigation of membrane-assisted radiant cooling in outdoor settings. *Sustainable Cities and Society*, *113*, 105634. doi:<https://doi.org/10.1016/j.scs.2024.105634>
- Yang, J., Ni, S., & Weng, W. (2017). Modelling heat transfer and physiological responses of unclothed human body in hot environment by coupling CFD simulation with thermal model. *International Journal of Thermal Sciences*, *120*, 437-445.
- Yang, J., Wang, Z.-H., Kaloush, K. E., & Dylla, H. (2016). Effect of pavement thermal properties on mitigating urban heat islands: A multi-scale modeling case study in Phoenix. *Building and Environment*, *108*, 110-121.
- Yang, J., Weng, W., & Zhang, B. (2014). Experimental and numerical study of physiological responses in hot environments. *Journal of Thermal Biology*, *45*, 54-61.
- Yang, J., Weng, W., Wang, F., & Song, G. (2017). Integrating a human thermoregulatory model with a clothing model to predict core and skin temperatures. *Applied ergonomics*, *61*, 168-177.
- Yang, J., Wong, M. S., Menenti, M., & Nichol, J. (2015). Modeling the effective emissivity of the urban canopy using sky view factor. *ISPRS Journal of Photogrammetry and Remote Sensing*, *105*, 211-219. doi:<https://doi.org/10.1016/j.isprsjprs.2015.04.006>
- Yang, M., Zou, W., Guo, J., Qian, Z., Luo, H., Yang, S., . . . Wiersma, D. S. (2020). Bioinspired “skin” with cooperative thermo-optical effect for daytime radiative cooling. *ACS Applied Materials & Interfaces*, *12*(22), 25286-25293.

- Yu, Y., Liu, J., Chauhan, K., de Dear, R., & Niu, J. (2020). Experimental study on convective heat transfer coefficients for the human body exposed to turbulent wind conditions. *Building and Environment*, 169. doi:10.1016/j.buildenv.2019.106533
- Zhang, H. (2003). Human thermal sensation and comfort in transient and non-uniform thermal environments. *PhD Thesis, University of California, Berkeley*.
- Zhang, H., Arens, E., Huizenga, C., & Han, T. (2010). Thermal sensation and comfort models for non-uniform and transient environments: Part I: Local sensation of individual body parts. *Building and Environment*, 45(2), 380-388. doi:10.1016/j.buildenv.2009.06.018
- Zhang, J., Yuan, J., Liu, J., Zhou, Z., Sui, J., Xing, J., & Zuo, J. (2021). Cover shields for sub-ambient radiative cooling: A literature review. *Renewable and Sustainable Energy Reviews*, 143. doi:10.1016/j.rser.2021.110959
- Zhang, N., Liang, Y., Wu, H., Xu, X., Du, K., Shao, Z., . . . Huang, G. (2021). Heat transfer modeling and analysis of air-layer integrated radiant cooling unit. *Applied Thermal Engineering*, 194. doi:10.1016/j.applthermaleng.2021.117086
- Zhang, N., Wan, H., Liang, Y., Wu, H., Xu, X., Suen, S. M., & Huang, G. (2023). Principle and application of air-layer integrated radiant cooling unit under hot and humid climates. *Cell Reports Physical Science*, 4(2). doi:10.1016/j.xcrp.2023.101268
- Zhang, Y., & Yang, T. (2008). Simulation of human thermal responses in a confined space. *In Indoor Air 2008, Copenhagen, Denmark*.
- Zhao, K., Liu, X.-H., & Jiang, Y. (2016). Application of radiant floor cooling in large space buildings – A review. *Renewable and Sustainable Energy Reviews*, 55, 1083-1096. doi:10.1016/j.rser.2015.11.028

- Zhao, Y., Zhang, H., Arens, E. A., & Zhao, Q. (2014). Thermal sensation and comfort models for non-uniform and transient environments, part IV: Adaptive neutral setpoints and smoothed whole-body sensation model. *Building and Environment*, 72, 300-308. doi:<https://doi.org/10.1016/j.buildenv.2013.11.004>
- Zhong, Z., Ma, W., Yao, S., Xu, X., & Niu, J. (2022). Enhancing the cooling capacity of radiant ceiling panels by latent heat transfer of superhydrophobic surfaces. *Energy and Buildings*, 263. doi:10.1016/j.enbuild.2022.112036
- Zhu, S., Kato, S., Ooka, R., Sakoi, T., & Tsuzuki, K. (2008). Development of a computational thermal manikin applicable in a non-uniform thermal environment—Part 2: Coupled simulation using Sakoi's human thermal physiological model. *HVAC&R Research*, 14(4), 545-564.
- Zou, J., Liu, J., Niu, J., Yu, Y., & Lei, C. (2021). Convective heat loss from computational thermal manikin subject to outdoor wind environments. *Building and Environment*, 188. doi:10.1016/j.buildenv.2020.107469